AN EXPERIMENTAL INVESTIGATION OF THE EFFECTS OF LEADING EDGE MODIFICATIONS ON THE POST-STALL CHARACTERISTICS OF AN NACA 0015 WING

by

Jugal Kishore Saini

Thesis submitted to the Faculty of the Graduate School
of the University of Maryland in partial fulfillment
of the requirements for the degree of
Master of Science
1979

ABSTRACT

Title of Thesis: An Experimental Investigation of the Effects of Leading Edge Modifications on the Post-Stall Characteristics of an NACA 0015 Wing

Jugal Kishore Saini, Master of Science, 1979

Thesis directed by: Dr. Everett Jones
Associate Professor
Department of Aerospace Engineering

and

Dr. Allen E. Winkelmann
Assistant Professor
Department of Aerospace Engineering

The effects of leading edge modifications on the stalling characteristics of an NACA 0015 panel wing model were investigated in a series of low speed wind tunnel tests. The modification typically consisted of adding a 14% Clark Y glove onto a portion of the leading edge. Six-component balance data, pressure distribution measurements and oil flow visualization tests were completed at a Reynolds number based on chord of 2.0×10^6 for increasing and decreasing angles of attack from 0^o to 50^o.

The leading edge modifications produce stabilizing vortices at stall and beyond. These vortices have the effect of fixing the stall pattern of the wing such that various portions of the wing upper surface stall nearly symmetrically. This results in a higher lift on the modified wing as compared to the lift on the unmodified wing in the post-stall region. The lift curve slope of the modified and unmodified wings remained essentially constant at 0.071 per degree. Two lift-coefficient peaks were obtained for the baseline NACA 0015 wing at angles of attack

of 17° and 30°. The twin-peak behavior of the lift curve was also observed on the modified wings. The drag coefficient obtained with several modified configurations was smaller than the drag coefficient of the baseline NACA 0015 wing in the pre-stall region. Also a smaller center of pressure shift with angle of attack was observed with several modified configurations. Considering a smoother variation of lift, pitching moment, rolling moment at stall and a smaller drag and center of pressure movement to be desired criteria, the best configuration tested consisted of placing the glove on the entire leading edge except for a gap at 25% to 50% of the semispan.

To my parents,

brother Krishan and

friend Padmanabhan

ACKNOWLEDGEMENTS

I wish to express my wholehearted gratefulness to Dr. Everett Jones for his constant encouragement and valuable advice. I am sincerely thankful to Dr. Allen E. Winkelmann who as a co-advisor has been of immense help during the research work. I also express my gratitude to Dr. Jewel B. Barlow and Dr. John D. Anderson, Jr., for their valuable suggestions.

To Mr. S. Agrawal, a fellow graduate student, a special word of thanks for working together with me. I acknowledge and appreciate the help of fellow graduate students Messrs. P. Sampath and K.N. Parthasarathy in computer programming and related aspects.

I am indebted to the staff of the Wind Tunnel Operations Department for all the help I received during this study. In particular I wish to thank Mr. C.W. Lessig and Ms. Janet T. Redpath for making the wing gloves. To Mr. James Deveney of the Aerospace Shop, a note of appreciation for his help during construction of models.

Special thanks are due to Ms. Vicki Brewer for her careful and efficient typing of this report.

The present work was supported in part by NASA Contract Number NSG 1570. Financial support received from the Minta Martin Foundation of the University of Maryland is deeply appreciated.

TABLE OF CONTENTS

TABLE OF CONTENTS (continued)

LIST OF TABLES

LIST OF SYMBOLS

a	Wing lift curve slope
ALPHA	Angle of attack measured with reference to basic wing chord
b	Wing semispan
c	Mean aerodynamic chord (mac)
C_D,CD	Drag coefficient, $\frac{D}{q_\infty S}$
C_L,CL	Lift coefficient, $\frac{L}{q_\infty S}$
C_M,CM	Pitching moment coefficient defined about 25% mac, $\frac{M}{q_\infty S\ c}$
CN	Yawing moment coefficient, $\frac{N}{q_\infty S\ b}$
C_p,CP	Pressure coefficient, $\frac{p - p_\infty}{q_\infty}$
CR	Rolling moment coefficient, $\frac{R}{q_\infty S\ b}$
CY	Side force coefficient, $\frac{Y}{q_\infty S}$
D	Drag
L	Lift
M	Pitching moment defined about 25% mac
N	Yawing moment
p	Local pressure
p_∞	Free stream pressure
q_∞	Free stream dynamic pressure, $\frac{1}{2}\rho_\infty U_\infty^{\ 2}$
R	Rolling moment
Re_c	Reynolds number based on chord of basic wing
S	Projected area of wing
t	Maximum thickness of airfoil
U_∞	Free stream velocity
V	Wing volume

X	Chordwise location of center of pressure measured from leading edge of mac
Y	Side force
Y1	Spanwise location of center of lift measured from wing root
Y2	Spanwise location of center of drag measured from wing root
α	Angle of attack
ε	Blockage correction factor
ρ_∞	Free stream density

LIST OF FIGURES

CHAPTER 1

INTRODUCTION

Stalls and spins have continued to be a major cause of accidents involving general aviation aircraft. Recent studies (References 1-3) have suggested that modifications to the leading edge of the wing can reduce the tendency of light aircraft to enter a spin after stall. The modifications typically consist of adding a drooped glove onto a portion of the leading edge. This results in a sharp and discontinuous change in airfoil shape in the spanwise direction. Vortices which are shed at the leading edge discontinuities serve to preserve lift on the wing to very large angles of attack. The resulting flat top lift curve would produce gradual and nearly symmetrical post-stall changes in the wing span loading about the aircraft rolling and yawing axes. Consequently, very gentle adverse accelerations occur. It has been hypothesized that these characteristics will help prevent inadvertent spin entry after a stall (Reference 2).

The theoretical basis for the concept of leading edge modifications was the modelling of three-dimensional wings using a nonlinear-lifting-line approach with a simulated stalled wing section (Reference 1). This study suggested that the local leading edge type separation produced a much stronger induced angle of attack distribution than trailing edge separation. The strong vortices shed at the edge of the stalled section stabilized (localized) separation and helped fix the stall pattern of the wing such that the various portions of the wing upper surface stalled nearly symmetrically. The post-stall lift curve of the wing could be tailored as a function of angle of attack by controlling the stall at local points along the span.

The induced effects, of the flow separation at stall for a basic (unmodified) wing, cause upper surface stagnation (counter rotating) vortices to be shed. The strength of the vortex cell, illustrated in Figure 1, implies the level of lift loss. The inboard vortex may not exist in the event of absence of upper surface lift at stall.

In order to obtain a better understanding of the flow field in the post-stall regimes and the effects of leading edge modifications on these flow fields, an experimental research program has been carried out at the University of Maryland. Two series of tests were performed. The first series consisted of force and flow visualization tests on a small scale NACA 0015 wing in the Aerospace Boundary Layer Research Tunnel. Data were obtained for increasing and decreasing angles of attack from 0° to 50° and at a Reynolds number based on chord of $Re_c = 350{,}000$. The second series consisted of force, pressure measurement and flow visualization tests on a large scale NACA 0015 panel wing model in the Glenn L. Martin Wind Tunnel. These tests were also made for increasing and decreasing angles of attack from 0° to 50° and at a Reynolds number based on chord of $Re_c = 2.0 \times 10^6$.

In the following chapter, a description of the experimental program will be given. The results of both series of tests will then be presented in Chapter 3. Chapter 4 will summarize the major findings of this study and recommendation for future work will be outlined in Chapter 5.

CHAPTER 2

EXPERIMENTAL PROGRAM

The experiments were completed in two wind tunnels; the Aerospace Boundary Layer Research Tunnel and the Glenn L. Martin Subsonic Wind Tunnel. Details of model construction, test procedure, error assessment and data reduction are also given in this chapter.

2.1 Test Facilities

The Aerospace Boundary Layer Research Tunnel is an open circuit, variable speed (from 4.57 m/sec to 45.72 m/sec) facility with a rectangular test section measuring 43.94 cm by 115.83 cm. Lift, drag and pitching moment measurements are made with a three-component strain-gage balance. A further description of the tunnel is given in Reference 4.

The Glenn L. Martin Wind Tunnel is a closed circuit 2.36 m by 3.35 m subsonic tunnel. The test section velocity could be varied from 0 m/sec to 91.44 m/sec. It is equipped with a six-component balance. The data are obtained by a real time computer controlled data-acquisition system and recorded on digital magnetic tape. The system also has a real time plotting capability. For further details of the wind tunnel see Reference 5.

2.2 Models and Leading Edge Gloves

The two-dimensional 12.7-cm-chord wing model tested in the Aerospace Boundary Layer Research Tunnel had an NACA 0015 airfoil section. The coordinates of this section are given in Reference 6. The model was constructed of laminated mahogany. The surface of the model was lacquered, sanded with No. 400 carborundum paper, painted black and finally buffed to obtain an aerodynamically smooth surface. The maximum deviation of the model coordinates from the specified coordinates was 0.127 mm. The model spanned the 43.94 cm dimension of the tunnel. A 0.635 mm gap was allowed between the ends of the model and the tunnel walls to insure freedom of movement.

As will be discussed in the next chapter, serious questions arose during the two-dimensional tests about the validity of the data in the post-stall region. Hence the two-dimensional model was later tested as a three-dimensional reflection plane model by decreasing its span to 80% tunnel width. The selection of the maximum span of the three-dimensional model was based on the conclusions of References 7-9 which showed that the tunnel wall interference for three-dimensional tests in a rectangular test section is minimum when the ratio of span of the wing to width of the test section is about 0.8. A sketch of the installation of the model in the test section is shown in Figure 2.

The 45.72-cm-chord, 137.16-cm-semispan NACA 0015 reflection plane model tested in the Glenn L. Martin Wind Tunnel had five rows of pressure orifices and a segmented flap as shown in Figure 3. This was an existing laminated mahogany wing model which was previously constructed by the wind tunnel. The pressure orifices were connected by plastic tubes to a pressure transducer through a scanivalve.

The large scale wing was modified by bolting on wooden leading edge gloves which were installed in segments so as to produce an unmodified gap of varying width at various spanwise positions. The gloves, eight in number, were of equal lengths. The glove was designed by matching the nose of a 14% thick 48.77-cm-chord Clark Y airfoil to the leading edge of the wing such that the upper surfaces of the two airfoils coincide from 8.5% to 40% of chord. The lower surface of the Clark Y airfoil was faired flat from 12% to 35% of chord so that it blended with the lower surface of the wing. This resulted in a camber at the nose as well as a smaller leading edge radius. A sketch of the airfoil with leading edge glove is shown in Figure 3.

2.3 Test Procedures

The experimental procedures followed in the two series of tests are described below:

A) Two- and Three-Dimensional Tests in the Aerospace Boundary Layer Research Tunnel

The tests conducted on the horizontally mounted 12.7-cm-chord NACA 0015 wing consisted of measurements of lift, drag, quarter-chord pitching moment and flow visualization tests at a Reynolds number based on chord of $Re_c = 350{,}000$. The data were obtained at increasing and decreasing angles of attack from 0^o to 50^o, at intervals of 5^o or less.

The three-component strain-gage balance was calibrated at the beginning and end of each test. A simple but quite accurate procedure was employed for calibrations. This involved replacing the wing with an aluminum rod, which was held in position in the balance and extended to the middle of test section. Simulated loads were applied in small increments to the lift/drag/moment calibrating fixture. The strain gage output was amplified 900 times and read on a digital time integrating millivoltmeter. Possible interference between the three components of the balance was also checked during calibration and was found to be negligible. Typical slopes of the calibration curves for lift, drag and pitching moment were 88 mv/228 gm, 69 mv/50 gm and 279 mv/50 ft-gm respectively. The speed of the tunnel for different attitudes of the model was held constant by varying the opening of control vanes. Fluctuations in lift, drag and moment were large in the post-stall region. In order to read the values correctly, the time integrating constant of the millivoltmeter was set at 10 seconds.

Oil flow visualization tests were made using a mixture of mineral oil and titanium dioxide, in approximate ratio of 1:1 by volume. A small amount of oleic acid was added to control the degree of coagulation of particles.

It was originally intended to study the effects of leading edge modifications on the small scale models before doing tests on the large scale panel wing model. However, because of time constraints, tests of the large scale wing were performed before the small scale tests were completed.

B) Reflection-Plane Model Tests in the Glenn L. Martin Wind Tunnel

The tests on the 45.72-cm-chord NACA 0015 wing with and without leading edge modifications included six-component balance measurements, pressure distribution measurements and oil flow visualization tests at increasing and decreasing angles of attack from 0° to 50°. These tests were conducted at a Reynolds number (based on the chord of the unmodified wing) of $Re_c = 2.00 \times 10^6$. The model was mounted vertically on the floor of test section. Wind off data were obtained for -5° through 55° and were taken into account for test data correction. The force and pressure data were measured simultaneously and recorded by the data-acquisition system. An oil mixture, consisting of 20 weight motor oil and fluorescent green C.H. 185% dye, in the ratio of 250:1 by weight, was used in the flow visualization tests. Figure 4 shows the various modified leading edge configurations which were tested.

2.4 Error Assessment of Data

In this section, an assessment is made of the errors involved in the force, pressure and angle of attack measurements. For convenience, these have been listed in Table 1.

Column (a) in Table 1 contains error assessment for the data obtained in the Aerospace Boundary Layer Research Tunnel. The percentage errors in the force and the moment coefficients were calculated from the maximum variations and the average values of the force and the moment at $\alpha = 18^{\circ}$. The variations (fluctuations) of the force and the moment data were essentially zero in the pre-stall range.

Column (b) shows the error assessment of the data obtained in the Glenn L. Martin Wind Tunnel. The variations in the force and the moment coefficients given in this column were calculated from the maximum possible variation in the force and the moment measurements non-dimensionalized with respect to the basic wing.

2.5 Data Reduction

The procedures used to reduce the data obtained from the tests in the Aerospace Boundary Layer Research Tunnel and the Glenn L. Martin Wind Tunnel are outlined as follows:

A) Two- and Three-Dimensional Tests in the Boundary Layer Research Tunnel

The lift, drag and quarter-chord pitching moment data obtained in millivolts from the digital millivoltmeter were converted to forces in grams and moments in foot-grams through calibration curves. The room pressure, temperature and atmospheric density were used to calculate tunnel speed from the speed micromanometer reading. From the lift, drag, quarter-chord moment and speed as obtained above, the lift, drag and moment coefficients were calculated. These coefficients were then corrected for wind tunnel wall corrections as given below:

1) Two-Dimensional Wind Tunnel Wall Corrections:

The following expressions, contained in Reference 7, were used to correct the force and moment data for the effects of the solid blockage caused by the constriction of the flow past the model, for the effects of blockage caused by the wake and for the distortion of the lift distribution caused by the induced curvature of the flow. Horizontal buoyancy corrections were neglected since the pressure gradients along the wall were very small due to a slight test section divergence.

$$\alpha = \alpha' + 0.022354\ (C_L' + 4\ C_M')$$

$$C_L = C_L'(0.996002 - 0.10917\ C_D')$$

$$C_D = C_D'(0.997677 - 0.10917\ C_D')$$

$$C_M = C_M'(0.998452 - 0.10917\ C_D') + 0.0006125\ C_L'$$

where the primed quantities represent the coefficients measured in the tunnel.

2) Three-Dimensional Wind Tunnel Wall Corrections:

Corrections accounting for the effects of solid blockage, wake blockage and streamline curvature were used as given in Reference 7. The downwash correction factor, 0.215, determined from Reference 9 was used for the angle of attack correction. The various three-dimensional correction-expressions are given below:

$$V = 0.7\ t\ c\ b$$

$$\varepsilon = 0.0644V + 0.04544\ S\ C_D'$$

$$\alpha = \alpha' - 2.46284\ S\ C_L'$$

$$C_L = C_L'(1 - 2\varepsilon) - 0.223895\ C_L'\ a$$

$$C_D = C_D'(1 - 2\varepsilon) + 0.039074\ S\ (C_L')^2$$

$$C_M = C_M'(1 - 2\varepsilon) + 0.055974\ S\ C_L'\ a$$

where the primed quantities represent the coefficients measured in the tunnel.

B) Three-Dimensional Tests in the Glenn L. Martin Wind Tunnel

The force data obtained in this tunnel were corrected for solid blockage, wake blockage, tunnel wall constriction effects and downwash effects before recording them on to digital magnetic tape (Reference 10). Data were available both in body and wind axes systems. The pitching moment data as recorded were about the axis of rotation of the turn table on which the model was mounted. An offset of 3.02 cm, which existed between the axis of rotation and the quarter-chord line of the basic wing, was taken into consideration while reducing the pitching moment data. The pressure distribution data obtained in millivolts were also recorded on the magnetic tape. Force and pressure data were transferred from the magnetic tape to a file on the University's UNIVAC 1108 computer facility for further data reduction.

A computer program was written to calculate and plot force and moment coefficients. For each configuration, the appropriate projected wing area, mean aerodynamic chord and wing span were used for non-dimensionalizing the forces and moments. The pitching moments were calculated at the quarter-mean-aerodynamic-chord. This program also incorporated calculation and plotting of chordwise location of center of pressure and spanwise locations of centers of lift and drag which were derived as follows:

$$X = \left(- \frac{M_B}{L_B} + \frac{c}{4} \right) / c$$

$$Y1 = \left(\frac{R_W}{L_W} \right) / b$$

$$Y2 = \left(- \frac{N_W}{D_W} \right) / b$$

where subscript B stands for body axes system and W for wind axes system.

Another program was written to calculate the pressure coefficients and to plot the pressure coefficients in two dimensions and three dimensions. A listing of the programs is given in Appendix A.

CHAPTER 3

RESULTS AND DISCUSSION

The results obtained from tests on the small 12.7-cm-chord NACA 0015 wing model are presented in Section A. The results of experiments on the large 45.72-cm-chord NACA 0015 wing model are contained in Section B.

A. 12.7-cm-Chord NACA 0015 Wing Model Results

Two- and three-dimensional aerodynamic characteristics (lift, drag and pitching moment) of the 12.7-cm-chord NACA 0015 wing are presented in Figures 5-7. The tests were completed at a Reynolds number based on chord of $Re_c = 350{,}000$ for angles of attack from 0^o to 50^o. Hysteresis effects were apparent when the angle of attack was reduced from the deep post-stall region.

As shown in Figures 5a and 5b, the section lift curve for the NACA 0015 airfoil is not linear at lower angles of attack. However, the section lift curve slope of 0.096/degree is obtained by a straight line fit between angles of attack of $\alpha = 0^o$ and $\alpha = 8^o$. A maximum section lift coefficient of 1.03 occurs at $\alpha = 15^o$ and a second peak, having a value of 1.05, occurs at $\alpha = 45^o$. For the three-dimensional wing of aspect ratio 5.54, an average lift curve slope of 0.066/degree is obtained. The initial lift-coefficient peak of 0.93 occurs at $\alpha = 16^o$ and the second peak of 0.78 occurs at $\alpha = 45^o$. In the post-stall region the three-dimensional lift is less than the two-dimensional lift.

A section lift curve slope of 0.096/degree was also obtained for an NACA 0015 airfoil at $Re_c = 1.23 \times 10^6$ in earlier tests by Pope (Reference 11). The section data from Reference 11 are shown in Figure 5c.

Comparison of the two-dimensional results in Figure 5a and 5c indicates that the effect of Reynolds number is to increase the initial lift-coefficient peak whereas the second peak does not change appreciably.

The results of tests on a three-dimensional flat plate wing (aspect ratio 5) from Reference 12 are also shown in Figure 5c. The flat plate data show only one lift-coefficient peak of 0.9 at $\alpha \approx 30^{0}$.

The results in Figure 5 show that the hysteresis in lift exists for the two-dimensional NACA 0015 wing in the vicinity of stall. In the range of α near stall, the lift for a decreasing angle of attack is less than the lift at corresponding angle when the angle of attack is increasing. The lift hysteresis also exists for the three-dimensional NACA 0015 wing. The hysteresis in drag and pitching moment exist for the two-dimensional wing as shown in Figs. 6 and 7. The drag at decreasing angles of attack is more than the drag at increasing angles of attack. The pitching moments are more negative during the decreasing angles of attack. The hysteresis in drag and pitching moment also exist for the three-dimensional wing. The hysteresis in lift, drag and pitching moment are in agreement with the results on these hysteresis reported in Reference 13.

Oil flow patterns in Figure 8 show the phenomenon of laminar separation on the NACA 0015 wing at $Re_c = 350{,}000$. The separation of a laminar flow over the NACA 0015 airfoil has been mentioned in Chapter 4 of Reference 14. Identical flow patterns were observed on the upper and lower surfaces at angle of attack $\alpha = 0^{0}$. At $\alpha = 0^{0}$, the flow on the upper surface separates at about 45% chord location as shown in Figure 8a. As the angle of attack is increased, the separation moves towards the leading edge on the upper surface and towards the trailing edge on the lower surface (Figures 8b and 8c). The locations of laminar separation on an NACA 0015 airfoil at $\alpha = 0^{o}$ and 10^{o} predicted by the airfoil computer program of Reference 15 were within 5% of locations of laminar separation observed in Figure 8. The flow on the lower surface was fully attached at $\alpha \approx 13^{o}$.

The two-dimensional flow patterns were essentially similar to the three-dimensional flow patterns before stall. As the "2-D" and 3-D wings approached stall, a pair of counter-rotating swirl patterns were observed in the oil patterns (Figures 9a and 9b). The pattern was symmetric about the centerline for the "2-D" wing but shifted towards the wall for the 3-D wing. A region of reversed flow existed over the central portion of the wings. As suggested in Reference 16, the formation of the swirl patterns may be due to a loop vortex that is attached to the wing in the centers of the swirls. In another explanation (Reference 1), these vortices are viewed as coming off the surface and going to infinity without interacting with each other. The observation of the swirl patterns on the "2-D" wing led to questions about testing such models in the post-stall region. For this reason, all later tests were conducted with reflection plane or 3-D models mounted on one wall of the tunnel.

Several tests were performed with 0.23 mm leading edge grit placed at 5% chord in order to simulate effects of higher Reynolds number. The size of the grit was determined using the criteria given in Reference 17. Grit reduced the maximum lift coefficients and the lift curve slope while increasing the minimum drag coefficient by 100%. In addition, the wing with grit was observed to stall at a lower angle of attack. The explanation for these variations is that the kinetic energy of the already turbulent flow was decreased by the use of grit (Reference 14).

The tests described above on the 12.7-cm-chord NACA 0015 wing were jointly made with a fellow graduate student Mr. S. Agrawai and are also reported in his thesis (Reference 18).

B. 45.72-cm-Chord NACA 0015 Wing Model Results

The results of tests done on the 45.72-cm-chord NACA 0015 wing with and without leading edge modifications are presented in three parts. Part 1 consists of a systematic analyses of the data (including hysteresis) obtained with various leading edge modifications. Oil flow patterns are given in part two. In part three, correlation between the surface pressure distribution, the force and the flow pattern is discussed.

1.) Six Component Force and Moment Data

The data for the 45.72-cm-chord NACA 0015 wing were obtained at Reynolds number (based on unmodified wing chord) of $Re_c = 2.0 \times 10^6$ for increasing and decreasing angles of attack from 0^o to 50^o.

The effects of varying the location and extent of the gap in the gloved leading edge over the inboard half of the reflection plane model are shown in Figures 10 to 16. The results of other modifications are given in Figures 17 to 23. The lift curve slope (0.071/degree) remains essentially the same for the baseline NACA 0015 wing and the wing with various leading edge modifications. Since the angle of attack reference line of the baseline wing is also used for the modified configurations, this results in a slight shift of data in the linear range. A maximum lift coefficient of 1.11 occurs at an angle of attack of $\alpha = 17.5^o$ for the baseline wing. There is a sharp drop in the lift coefficient at stall. A second lift-coefficient peak of 0.94 occurs at $\alpha = 30.5^o$. The drop in lift at the second peak is less abrupt than the drop in lift at the initial peak. A maximum lift coefficient of about 1.05 is obtained for configuration 3 (a gap in the leading edge glove from 37.5% to 50% semispan), configuration 4 (a gap in the glove from 25% to 50% semispan) and configuration 5 (a glove on leading edge in the outer half semispan). In addition, the stall advances to $\alpha = 17.5^{0}$ (Figure 10). The maximum lift and the stalling angle of configuration 8 (a gap in the glove from 50% to 62.5% semispan) and configuration 9 (a glove on leading edge in the inner half semispan) approach the maximum lift and the stalling angle of the baseline NACA 0015 wing (Fig. 17). However, the lift is higher on the modified wings than on the baseline wing in the post-stall region. The twin-peak characteristic is also observed on the modified wings. The second peak is higher than the initial peak in configuration 3 and configuration 4. Configuration 4 and configuration 5 exhibit a moderate drop in lift at stall. The effect of flap deflection is to increase the lift until $\alpha = 38^{0}$.

A minimum drag coefficient of 0.00875 for the baseline wing is obtained at $\alpha = 0^{0}$ as shown in Figures 11 and 18. The rate of drag coefficient change is maximum at stall, less in the post-stall region and the least in the pre-stall region. It is observed that the drag coefficient remains essentially constant for the wing with and without modifications until $\alpha \approx 11^{0}$. Data at $\alpha = 5^{0}$ for configuration 6 (gaps in the glove at 25%-37.5% and 62.5%-75% semispan) and configuration 7 (a gap in the glove from 25% to 37.5 semispan) were not taken. However, the plotting program joined the adjacent data points by a straight line. The drag is less for configurations 4, 8 and 9 between $\alpha = 11^{0}$ and respective maximum lift angles. Deflection of flaps increases the drag at all angles. Though not rechecked, the drag data point at $\alpha = 25.5^{0}$ is believed to be doubtful.

The variation of the pitching moment coefficient (about 25% mean-aerodynamic-chord) with angle of attack is plotted in Figures 12 and 19. The pitching moment is either zero or negative for all the configurations. Since the leading edge modification provides a camber to the modified wing the pitching moment decreases in pre-stall range as expected. The pitching moments of configurations 3 and 5 behave in the same manner as the pitching moment of the baseline wing. However, configurations 4 and 9 do not show the increase in pitching moments at the angles for maximum lift. Configuration 4 shows a smoothly varying pitching moment curve. When flaps are deflected, a uniform increase in the pitching moment at all angles results.

Figures 13 and 20 show the plot of the rolling moment coefficient versus angle of attack. The rolling moment which is essentially the same for the wing with and without modifications, increases linearly with angle of attack up to $\alpha = 10^{\circ}$. The slope of the rolling moment coefficient curve decreases from $\alpha = 10^{\circ}$ to the maximum lift angle. It becomes negative at stall and beyond for the baseline wing. The rolling moment decreases slightly at stall for the modified wings and then recovers. The recovery pattern is different for different configurations. Configuration 4 maintains essentially a constant rolling moment from stall until $\alpha = 41^{\circ}$. The rolling moment for the wing with flap deflected is higher in comparison to the wing with no flap. However, in the vicinity of stall and at $\alpha = 30^{\circ}$, the difference between the values with and without flap deflection decreases. The yawing moment increases with angle of attack as shown in Figures 14 and 21. A constant yawing moment between $\alpha = 12^{\circ}$ and the maximum lift angle is obtained for configurations 8 and 9. The yawing moment changes abruptly at stall in these configurations.

The side force coefficient keeps increasing with angle of attack before stall, decreases slightly at stall, increases again until $\alpha \approx 30^{o}$ and then drops as shown in Figures 15 and 22. The variation of side force with angle of attack on the baseline wing and of configuration 9 are comparable. Configuration 3 produces the maximum side force in the post-stall range.

The chordwise position of the center of pressure is plotted against angle of attack for the various wing configurations in Figures 16a and 23a. The large value of the chordwise location of center of pressure of 53% chord at $\alpha = 0$ for the baseline wing is attributed in part to the calculation accuracy using small but finite values of the lift and the pitching moment. The lift being negative, the center of pressure location is ahead of leading edge for the modified wing. The center of pressure is seen to shift towards leading edge until maximum lift angle and then moves towards the trailing edge. A similar trend has also been found on a flat plate wing and a Clark Y wing (References 12 and 19). The center of pressure for the baseline wing shifts from 25% to 47.5% of the chord. The effect of the leading edge modification is to move the center of pressure towards leading edge (compared to the center of pressure location for the baseline wing at corresponding angles of attack). The minimum chord-wise travel of the center of pressure of 27% to 42% of the mean aerodynamic chord is obtained for configuration 4. Use of flaps shifts the center of pressure towards the trailing edge, as expected for a cambered wing. The spanwise variation of the center of lift (calculated from the lift and the rolling moment), shown in Figure 16b and 23b, varies between 33% and 45% of semispan for the baseline wing. The leading edge modification and the deflection of the flap move the center of lift inboard. Figures 16c and 23c show the spanwise movement of the center of drag (calculated from drag and yawing moment).

The hysteresis effects of lift, drag and pitching moment data of the NACA 0015 wing with and without leading edge modifications are shown in Figures 24 to 26. Wherever possible, the plots are made clear by marking arrows to indicate the direction of change of angle of attack. As shown in Figure 24, the lift coefficient at a decreasing angle is less than the lift coefficient at the corresponding increasing angle in the vicinity of stall. Higher lift during the decreasing angles is observed for configuration 5 around $\alpha = 30^{\circ}$. However, the higher lift coefficients shown for the decreasing angles between $\alpha = 50^{\circ}$ and $\alpha = 33^{\circ}$ are attributed to the fact that the data were taken at a larger interval between $\alpha = 50^{\circ}$ and $\alpha = 20^{\circ}$ and that the plotting program joined the two adjacent data points by a straight line.

The hysteresis effects of drag coefficient are seen around stall in Figure 25. The drag coefficient is more for the decreasing angles of attack than the drag coefficient for the increasing angles of attack. There is essentially no hysteresis in the drag at higher angles of attack. Figure 26 shows that the hysteresis in pitching moment exists on the baseline wing at stall. The pitching moment is more negative for the decreasing angles on the baseline wing. An increase in the pitching moment is observed at maximum lift angle on the modified wings. No hysteresis exists on configuration 2 as shown in Figures 24-26.

The hysteresis shown in Figures 24-26 results from a rather complicated relationship between the pressure field around the airfoil and the retion of separated flow. The phenomenon of hysteresis may be explained as follows. The laminar boundary layer which separated near the leading edge reattaches some distance downstream as a turbulent boundary layer. This results in the formation of a short bubble near the leading edge. At stall, the short bubble bursts, and the flow separates near the leading edge. This results in a drop in the lift, increase in the drag and decrease in the pitching moment. When the angle of attack is decreasing, there is no reattachement of the flow at the stalling angle. Decrease of the incidence at first has little effect on the separated region. But at an appropriate angle, the flow reverts to the short bubble configuration as rapidly as the short bubble had burst (Reference 20). The results of the present study suggest that the airfoils which do not exhibit the leading edge short bubble separation, may not exhibit hysteresis effects.

2.) Flow Visualization Tests

The oil flow patterns on the baseline NACA 0015 wing at various angles of attack are shown in Figure 27. The phenomenon of laminar separation near the leading edge is apparent in Figures 27a and 27b. It is observed that the (laminar) separation bubble on the upper surface at $\alpha = 16.5^{o}$ has moved forward compared to the location of separation bubble at $\alpha = 10^{o}$. The trailing edge separation of the turbulent flow in the pre-stall region is also seen in these figures. Figure 27c shows the existence of two counter-rotating swirl patterns on the upper surface at stall. The presence of the tip vortices is shown by curved oil streak lines near the tip. Wall interference is also apparent in these figures. With increasing angles of attack the outboard swirl pattern moves towards the tip of the wing. At very high angle of attack, both swirl patterns move towards the trailing edge and finally appear to leave the surface.

Figure 28 shows a sequence of oil flow photographs when the 14%

Clark Y glove is added to the leading edge except for a gap at 37.5% to 50% semispan. Figure 29 shows a similar sequence when the nose glove is only on the outer 50% semispan. A comparison of the pictures in Figures 27, 28 and 29 shows that the flow patterns on all three wings are essentially the same in the pre-stall region.

The vortices which are shed by the leading edge modification alters the flow of the baseline wing at stall in such a manner that the inboard swirl pattern shifts outboard. This shift increases the area of attached flow on the inboard section of the wing which would be expected to increase the lift contribution of this area. The striking effect of the leading edge modification is to preserve the attached flow on the outboard portion of the upper surface at higher angles of attack. It is interesting to note that the flow patterns on the outboard section of configuration 5 (a glove from 50% to 100% semispan) were identical to the patterns shown in Figure 28 for configuration 3 (a gap in the glove at 37.5%-50% semispan). The unsteady nature of the flow after stall was observed during the flow visualization test on the wing shown in Figure 29. The initial flow pattern observed on the wing at $\alpha = 18.5^{\circ}$ was very similar to the pattern later observed at $\alpha = 20^{\circ}$. During the test, the oil pattern abruptly underwent a change and ended up with the pattern shown in Figure 29c.

3.) Pressure Distribution Data

The surface pressure distributions are presented in Figures 30 to 40. Figures 30 and 31 show data for the baseline NACA 0015 wing, Figure 32 to 35 for the modified wings and Figures 36 to 40 show comparisons of various modifications.

a.) The NACA 0015 Baseline Wing

Figure 30 shows the three-dimensional plot of pressure variation over the upper and the lower surfaces of the NACA 0015 baseline wing. Since the three-dimensional plotting program does not plot negative values, the pressure coefficients were uniformly increased so that the maximum negative pressure coefficient became zero.

As shown in Figure 31a and 31b, the pressure distribution over 17% to 62% semispan is constant at $\alpha = 10^{\circ}$ and gradually drops towards the tip of the wing. At $\alpha = 17.5^{\circ}$, the maximum pressure peak occurs at 39% semispan. Comparison of the pressure distributions at $\alpha = 10^{\circ}$ and 17.5° shows that the pressure (in magnitude) increases on the upper and the lower surfaces at $\alpha = 17.5^{\circ}$. This comparison also qualitatively confirms the increase in lift, drag, quarter-chord pitching moment, chordwise movement of the center of pressure towards leading edge and spanwise movement of the center of lift towards root from $\alpha = 10^{\circ}$ to $\alpha = 17.5^{\circ}$ observed in the six-component balance results (Figure 10 to 16).

The pressure distribution obtained at stall ($\alpha = 18.5^{\circ}$) on the aft part of the wing at 17%, 39% and 62% (rows 1, 2 and 3, Figure 31c) is nearly constant. The oil flow photograph taken at stall (Figure 27c) shows the presence of a 3-D separation bubble (with counter-rotating swirl patterns) over the same area of the wing. The maximum blockage to the oncoming flow of the 3-D separation bubble is noted at row 2 where the pressure peak is minimum. At row 2, the pressure decrease from 20% chord to the trailing edge indicates an increase in velocity which is obvious in the flow pattern. From Figure 31c and 31e, it is seen that the pressure on the upper surface is higher near the leading edge, lower at the rear surface and the center of lift shifts towards the tip at stall. These variations in the pressure distribution result in less lift, more drag, less pitching moment, rearward chordwise movement of the center of pressure and outboard spanwise movement of the center of lift at $\alpha = 18.5^{\circ}$. The same trends were also observed in the six-component balance results (Figures 10 to 16).

As noted in the oil flow photographs of the baseline wing beyond stall (Figure 27d), the flow over the wing near the wall appears to be fully separated. The corresponding pressure coefficeints in this region vary from -0.45 to -0.50 (Figure 31g). Around 40% semispan, the swirl near the leading edge helps keep the flow locally attached. The flow in between the two swirls located at about 75% semispan is attached as shown by the consistent recovery of pressure at row 4. The dip in the pressure distribution at 83% chord on row 5 could not be explained. It is seen from Figures 31e and 31g that the pressure increases on the lower surface at $\alpha = 30^{\circ}$. Even though the pressure peaks on rows 4 and 5 are higher at $\alpha = 30^{\circ}$, their contribution to lift is reduced because of the steep recovery of pressure. The increased pressure on most of the upper surface and the lower surface add up to increase lift, drag, pitching moment, chordwise location of center of pressure and to decrease the spanwise position of center of lift at $\alpha = 30^{\circ}$ compared to $\alpha = 18.5^{\circ}$.

The pressure increases on the lower surface and the flow separates on most of the upper surface at angles of attack beyond $\alpha = 30^{\circ}$ (Figures 27e, 31i and 31j). It is observed that the pressure coefficient in the separated regions is nearly constant at about -0.55.

The pressure distribution for increasing and decreasing angles is also compared in Figure 31 for $\alpha = 10^{\circ}$, 17.5°, 18.5° and 30°. The pressure distributions for increasing and decreasing angles are identical at

$\alpha = 10^{\circ}$. This agress with the six-component balance results which show no hysteresis effects. However, different pressure distributions are observed for increasing and decreasing angles at $\alpha = 17.5^{\circ}$, 18.5° and 30°. Hysteresis is also seen in the force results at these angles (Figure 10 to 16).

b.) The Modified NACA 0015 Wing

The pressure distributions for the modified wings are shown in Figures 32 to 35. The pressures at the orifices which were covered with the leading edge glove are not plotted in these figures. In the absence of pressure distribution on the front portion of the upper surface of the wing, which contributes substantially to the forces and moments at moderate angles of attack, even the qualitative comparison of forces/moments of the baseline wing and the modified wing on the basis of pressure distributions could not be made. Figure 32 shows the pressure distribution on the wing with a glove on the entire leading edge (configuration 2). The full recovery of pressure on the upper surface of configuration 2 indicates that the flow is attached at $\alpha = 18.5^{\circ}$ (Figure 32a). This agrees with the force test results which show that the maximum lift occurs for configuration 2 at $\alpha = 18.5^{\circ}$ (Figure 24).

Figures 28 and 29 show that the flow patterns due to the vortices shed at mid semispan are identical for configurations 3 and 5 at $\alpha = 16.5^{\circ}$ and 30°. However, the pressure distribution at row 3 (which appears to lie along most of the path of the vortices) (Figures 33, 34 and 35) are not identical for configurations 3, 4 and 5. The pressure distribution at rows 4 and 5 are identical in the post-stall region for these configurations.

The pressure distribution at row 1 on the upper surface of the baseline wing at maximum lift (Figure 31c) is constant from 75% chord to the trailing edge, suggesting a separated flow region on the inboard side. However, the flow is attached on the inboard surface of configuration 4 as shown by full recovery of the pressure on row 1 (Figure 33a). This explains in part why configuration 4 has a lower drag compared to the drag of the baseline wing in the pre-stall region.

Figure 36b shows the pressure distribution at row 1 for the baseline wing and configuration 5 at various angles of attack. At $\alpha = 17.5^{\circ}$, a constant pressure on the aft portion of the upper surface of configuration 5 implies that the flow is separated there. The abrupt changes in pressure at 75% chord on the inboard portion of the wing could not be explained. The dip in pressure coefficient at 15% chord on the upper surface of configuration 5 at $\alpha = 17.5^{\circ}$ (shown in Figure 37b) may be explained by a flow pattern similar to that which exists at row 2 for $\alpha = 20^{\circ}$ (Figure 29d). The 15% chord location appears to be the dividing line between a high shear attached flow near the leading edge and a region of reversed flow extending from the trailing edge. To the oncoming flow, the 3-D separation bubble containing the reversed flow appears somewhat as an effective bluff body mounted on the upper surface of the wing. It is of interest to note that the surface pressures measured just ahead of a circular cylinder mounted on a wind tunnel wall (Reference 21) also show a dip in pressure as observed at 15% chord. The pressure distribution for the baseline wing and configuration 8 (a gap in the glove from 50% to 62.5% semispan) and configuration 9 (a glove on 0% to 50% semispan) are shown in Figures 38-40. It is observed that the pressure distributions on the baseline wing, configuration 8 and configuration 9 are identical at angles of attack beyond 30° and the pressure coefficient (-0.50) is constant on the upper surface. Also as noted earlier, the pressure coefficient in a separated region is about -0.50 for all the configurations. A pressure coefficient of -0.42 on a flat plate wing at $\alpha = 90^{\circ}$ has been reported in Reference 22.

The decrease in pressure on the lower surface at 90% chord at $\alpha = 30^{\circ}$ and 50° (Figures 36c and 36d) is probably due to the wing-wall effects because this variation occurs only in the vicinity of wall.

A good correlation could be made between the surface pressure distributions and the flow patterns for the baseline wing. In other cases the pressure distribution does not fully agree with the flow patterns. This is attributed to the large spacing in the adjacent pressure orifices which possibly missed the high gradients in pressure associated with the swirl patterns observed on some wings.

CHAPTER 4

SUMMARY AND CONCLUSIONS

An experimental study of the aerodynamic characteristics of an NACA 0015 wing with various leading edge modifications was completed. The first series of wind tunnel tests performed in the Aerospace Boundary Layer Research Tunnel provided preliminary information on the post-stall behavior of a small scale (12.7-cm-chord) NACA 0015 wing. The first set of tests involved a "2-D" wing model that spanned the entire width of the test section. The second set of tests were completed on a reflection plane model that spanned 80% of the test section width (effective aspect ratio = 5.54). Three-component balance data and oil flow visualization photographs were obtained at a Reynolds number based on chord of Re_c = 350,000 and for increasing and decreasing angles of attack from 0^o to 50^o. The second series of tests were completed using a 45.72-cm-chord reflection plane model (effective aspect ratio of 6.0) in the Glenn L. Martin Wind Tunnel. Leading edge modifications were made by placing 14% Clark Y nose gloves onto the leading edge of the wing. In addition to six-component balance data and fluorescent oil flow visualization photographs, a limited amount of surface pressure data was obtained at $Re_c = 2.0 \times 10^6$ for increasing and decreasing angles of attack from 0^o to 50^o. The conclusions of these tests are itemized below:

1.) A lift-curve slope of 0.071/degree was obtained for the NACA 0015 wing with and without leading edge modifications. In the post-stall region, a second lift-coefficient peak was obtained on the NACA 0015 baseline wing at $\alpha = 30^o$. The values of the lift coefficient at the initial and the second peaks were 1.11 and 0.94 respectively.

2.) The leading edge modifications increased the lift coefficient in the post-stall regime. The effects of increasing the width of a gap in the leading edge glove over the inner half of semispan was to reduce the initial lift-coefficient peak to 1.05 and to advance the angle of stall by 1° to 17.5°.

3.) Configuration 4 (a gap in the glove from 25% to 50% semispan) and configuration 5 (a glove on the outer half semispan) exhibited a smoother drop in the lift coefficient at stall.

4.) The drag coefficients for configuration 4, configuration 8 (a gap in the glove from 50% to 62.5% semispan) and configuration 9 (a glove on the inner half semispan) were less than the drag coefficient of the NACA 0015 baseline wing between $\alpha = 11^{0}$ and 16.5°.

5.) An increase in the pitching moment (about the 25% mac) was observed at the maximum lift angle for the NACA 0015 wing with and without leading edge modifications. However, configuration 4 and configuration 9 did not show an appreciable change in the pitching moment at the maximum lift angle.

6.) The rolling moment coefficient increased linearly with angle of attack up to $\alpha = 10^{\circ}$, and then decreased until the angle of attack for maximum lift. The rolling moment coefficient for configuration 4 was essentially constant in the post-stall region.

7.) The behavior of the yawing moment coefficients were essentially the same for the NACA 0015 wing with and without leading edge modifications. A consistent increase in magnitude with the angle of attack was noted for every configuration.

8.) The side force coefficient kept increasing with angle of attack before stall, decreased at stall, increased until $\alpha \approx 30^{\circ}$ and then dropped.

Configuration 3 produced the maximum side force in the post-stall range.

9.) A chordwise movement of center of pressure of 25% to 47.5% chord was obtained on the NACA 0015 wing for the entire angle of attack range of 0° to 50°. The chordwise location of center of pressure for the modified wing shifted forward compared to the location of center of pressure for the unmodified wing at corresponding angles of attack. The minimum chordwise movement of center of pressure (27% to 42% mac) was obtained for configuration 4.

10.) The spanwise movement of center of lift for the NACA 0015 wing was from 33% to 45% semispan for angles of attack from 0° to 50°. The effect of the leading edge modification was to shift the center of lift inboard.

11.) The shape of the airfoil appeared to have a strong influence on the hysteresis effects. The NACA 0015 baseline wing exhibited hysteresis effects whereas the wing modified with a 14% Clark Y glove on the entire leading edge did not show appreciable hysteresis.

12.) A good correlation existed between the force/moment results, the oil flow patterns and the surface pressure distributions for the NACA 0015 wing at various angles of attack. In some cases (the baseline wing and configuration 5) an abrupt change in the pressure variation were noted in the vicinity of the counter rotating swirl patterns observed in the oil flow photographs. In other instances, however, the pressure distribution did not change even though a very distinct swirl pattern existed across the pressure taps. The failure to observe pressure changes may be attributed to the large spacing between adjacent pressure taps which caused any pressure peaks associated with the swirl patterns to be missed. A large variation in the pressure distribution in cases where no vortex or swirl patterns were observed could not be explained. It is interesting to note that $C_p \approx -0.5$ over the surface for which the flow was separated; this appeared to be independent of configuration and angle of attack beyond the stall.

13.) The use of "2-D" full span wing model to study the post-stall behavior is questionable. Oil flow patterns obtained in this study revealed the presence of a highly 3-D flow for a full span model.

14.) Considering a smoother variation of lift, pitching moment, rolling moment at stall (that would improve the aspects affecting the spin departure) and a smaller drag and center of pressure movement to be desired criteria, the best modification tested was configuration 4.

CHAPTER 5

RECOMMENDATIONS FOR FUTURE WORK

In regards to the present study, a number of recommendations for future work are given below:

1.) An extensive experimental study including flow visualization, surface pressure measurements, and flow field surveys on a finite wing would be made at stall and beyond. Tests would be specifically aimed at determining whether the apparent vortices in the 3-D separation bubble form a loop vortex above the upper surface or these vortices lift off the surface and go to infinity without interacting with each other. In addition, the wing/wall effect on the lower surface of a reflection plane model at higher angles of attack would be investigated.

2.) Flow visualization, surface pressure measurements and flow field surveys would then be performed on a finite wing with the leading edge modification for a configuration that would exhibit the most promising results in the six-component balance data.

3.) Above mentioned tests would also be made on a wing/fuselage and wing/leading edge modification/fuselage combinations.

4.) Using the results obtained from tests on a finite wing as a guide, a theoretical model of the three-dimensional flow field would be constructed.

5.) A numerical technique would be developed to predict the aerodynamic characteristics of a finite wing at stall and beyond employing the above mentioned flow model.

6.) An appropriate treatment of the wing/leading edge modification, wing/fuselage effects and wing/leading edge modification/fuselage configurations would then be incorporated in the numerical analysis.

Table 1 - Estimated Errors for Force/Pressure Measurements

a) Made in the Aerospace Boundary Layer Research Tunnel

b) Made in the Glenn L. Martin Wind Tunnel

Quantity	a	b (based on baseline wing)
α	$\pm$ 0.3 degree	$\pm$ 0.1 degree
C_L	$\pm$ 2%	$\pm$ 0.00103
C_D	$\pm$ 5%	$\pm$ 0.00026
C_M	$\pm$ 2%	$\pm$ 0.00069
CR		$\pm$ 0.00029
CN		$\pm$ 0.00029
CY		$\pm$ 0.00129
C_p		$\pm$ 0.01

```
@FLIST,M Q.
FLIST  06/14/79   22:49:30
END FLIST  23 CARDS GENERATED.

@HDG,P  ******  CUT  ******

@ELT,L Q.CUT
ELT 6B-06/14-22:49 CUT(1)
      000         SUBROUTINE CUT(XMIN,XMAX,YMIN,YMAX,ISTRX,ISTRY,IPLOT,ISY,A,B,
      000        *J,IB,KY)
      000    C
      000         DIMENSION ISTRX(5),ISTRY(2,9),ISY(6),A(35,5),B(35,5)
      000         DIMENSION IB(5)
      000    C
      000         CALL INITT(30)
      000         CALL BINITT
      000         CALL DLIMX(XMIN,XMAX)
      000         CALL DLIMY(YMIN,YMAX)
      000         CALL TYPE(IPLOT,1,ISY(1))
      000         CALL CHECK(A(1,1),B(1,1))
      000         CALL DSPLAY(A(1,1),B(1,1))
      000         CALL NOTATE(493,50,5,ISTRX)
      000         CALL NOTATE(40,410,2,ISTRY(1,KY))
      000         IF(J.EQ.1) GOTO 20
      000         DO 10 K1 = 2 , J
      000         IFAC = IB(K1-1)
      000         CALL TYPE(IPLOT,IFAC,ISY(K1))
      000    10   CALL CPLOT(A(1,K1),B(1,K1))
      000    20   CALL HDCOPY
      000         RETURN
      000         END

@HDG,P  ******  DUMP  ******

@ELT,L Q.DUMP
ELT 6B-06/14-22:49 DUMP(2)
      000         SUBROUTINE DUMP(Y,A,B,C,D,E,F,G,H,O,K)
      000    C
      000         DIMENSION Y(35,5),A(35,5),B(35,5),C(35,5),D(35,5),E(35,5),F(35,5)
      000         DIMENSION G(35,5),H(35,5),O(35,5)
      000    C
      000         GOTO(10,20,30,40,50,60,70,80,90),K
      000    10   DO 1 I = 1 , 35
      000         DO 1 J = 1 ,5
      000    1    Y(I,J)=A(I,J)
      000         RETURN
      000    20   DO 2 I = 1 , 35
      000         DO 2 J = 1 ,5
      000    2    Y(I,J) = B(I,J)
      000         RETURN
      000    30   DO 3 I = 1 , 35
      000         DO 3 J = 1 , 5
      000    3    Y(I,J) = C(I,J)
      000         RETURN
      000    40   DO 4 I = 1 , 35
      000         DO 4 J = 1 ,5
      000    4    Y(I,J) = D(I,J)
      000         RETURN
      000    50   DO 5 I = 1 , 35
      000         DO 5 J = 1 , 5
      000    5    Y(I,J) = E(I,J)
      000         RETURN
      000    60   DO 6 I = 1 , 35
      000         DO 6 J = 1 , 5
      000    6    Y(I,J) = F(I,J)
      000         RETURN
      000    70   DO 7 I = 1 , 35
      000         DO 7 J = 1 , 5
      000    7    Y(I,J) = G(I,J)
      000         RETURN
      000    80   DO 8 I = 1 , 35
      000         DO 8 J = 1 , 5
```

```
****** DUMP ******
000    8     Y(I,J) = H(I,J)
000          RETURN
000    90    DO 9 I = 1 , 35
000          DO 9 J = 1 , 5
000    9     Y(I,J) = O(I,J)
000          RETURN
000          END

WHDG,P ****** FORCE ******

WELT,L Q.FORCE
ELT 68-06/14-22:49 FORCE(23)
000          DIMENSION CLW(35,5),CDW(35,5),CMW(35,5),CNW(35,5),CRW(35,5),
000         *CYW(35,5),ALPHA(35,5),IB(5),Y(35,5)
000          DIMENSION YMIN(9),YMAX(9),ISTRY(2,9),ISTRX(5),ISY(6)
000          DIMENSION XCP(35,5),Y1CP(35,5),Y2CP(35,5)
000    C
000          DATA YMIN/-.1,0.,-.3,-.4,0.,-.1,0.,0.,0./
000          DATA YMAX/1.5,1.,.2,.1,.6,.1,1.,1.,1./
000          DATA ISTRX/65,76,80,72,65/
000          DATA ISTRY/67,76,67,68,67,77,67,78,67,82,67,89,88,0,89,49,89,50/
000          DATA IB/72,323,525,121,969/
000          DATA ISY/1,3,8,4,2,11/
000    C
000          WRITE (6,66)
000          READ (5,11) IPLOT
000    1     CALL ERASE
000          WRITE (6,44)
000          READ(5,11,END=200) J
000    5     WRITE (6,55)
000          READ(5,11) NSTART,NEND,FACS,FACC,X1,CBAR,CHORD
000          IF(NSTART.EQ.1) GOTO 100
000          I=2
000          ISTAT=0
000          J=J+1
000    10    READ(7,22) IREC
000          READ (7,77) AL,AD,AM,AN,AR,AY
000          READ(7,33) ALPHA(I,J),CLW(I,J),CDW(I,J),CMW(I,J),CNW(I,J),
000         *CRW(I,J),CYW(I,J)
000    C
000    C
000    C
000    C
000    C
000    C
000          IF(IREC.EQ.NSTART) ISTAT=1
000          IF(ISTAT.EQ.0) GOTO 10
000          CLW(I,J) = I-1
000          CDW(I,J) = I-1
000          CMW(1,J) = I-1
000          CNW(1,J) = I-1
000          CRW(1,J) = I-1
000          CYW(1,J) = I-1
000          ALPHA(1,J) = I-1
000          XCP(1,J) = I-1
000          Y1CP(1,J) = I-1
000          Y2CP(1,J) = I-1
000          CLW(I,J) = FACS*CLW(I,J)
000          CDW(I,J) = FACS*CDW(I,J)
000          CNW(I,J) = FACS*CNW(I,J)
000          CRW(I,J) = FACS*CRW(I,J)
000          CYW(I,J) = FACS*CYW(I,J)
000          CMW(1,J) = FACS*CMW(I,J)*FACC
000          ALP = ALPHA(I,J)*3.141593/180.
000          IF(NSTART.GT.800.AND.NSTART.LT.930) GOTO 20
000          ALB = AL*COS(ALP)+AD*SIN(ALP)
000          XCP(I,J) = (-AM/ALB+CHORD/4.+X1)/CHORD
000          Y1CP(I,J) = AR/(AL*4.)
000          Y2CP(I,J) = -AN/(AD*4.)
000    20    EXP1 = CLW(I,J)*COS(ALP)+CDW(I,J)*SIN(ALP)
000          EXP2 = 0.75*(FACC-1.) -X1/CBAR
000          CMW(I,J) = CMW(I,J) + EXP1*EXP2
000          IF(IREC.EQ.NEND) GOTO 5
000          I=I+1
```

```
****** FORCE ******

      000            GOTO 10
      000     C
      000     C      START PLOT
      000     C
      000     100    CONTINUE
      000            KMAX = 9
      000            IF(IREC.GT.800.AND.IREC.LT.930) KMAX = 3
      000            DO 160 K = 1 , KMAX
      000            CALL DUMP (Y,CLW,CDW,CMW,CNW,CRW,CYW,XCP,Y1CP,Y2CP,K)
      000            CALL INITT(30)
      000            CALL BINITT
      000            CALL DLIMX(-5.,50.)
      000            CALL DLIMY(YMIN(K),YMAX(K))
      000            CALL TYPE (IPLOT,1,ISY(1))
      000            CALL CHECK(ALPHA(1,1),Y(1,1))
      000            CALL DSPLAY(ALPHA(1,1),Y(1,1))
      000            IF(J.EQ.1) GOTO 155
      000            DO 150 K1 = 2 , J
      000            IFAC = IB(K1-1)
      000            CALL TYPE (IPLOT,IFAC,ISY(K1))
      000            CALL CPLOT(ALPHA(1,K1),Y(1,K1))
      000     150    CONTINUE
      000     155    CALL NOTATE(493,50,5,ISTRX)
      000            CALL NOTATE(40,410,2,ISTRY(1,K))
      000            CALL HDCOPY
      000     160    CONTINUE
      000            CALL CUT(0.,50.,.5,1.3,ISTRX,ISTRY,IPLOT,ISY,ALPHA,
      000           *CLW,J,IB,1)
      000            CALL CUT(-5.,20.,0.,.3,ISTRX,ISTRY,IPLOT,ISY,ALPHA,CDW
      000           *,J,IB,2)
      000            GOTO 1
      000     200    CALL FINITT(0,700)
      000     11     FORMAT( )
      000     22     FORMAT(I7)
      000     33     FORMAT(29X,F8.1,9X,F10.3,F10.4,4F10.3)
      000     44     FORMAT(10X,'INPUT 0 TO CONTINUE,TO STOP TYPE Q')
      000     55     FORMAT(10X,'INPUT NSTART,NEND,FACS,FACC,X1,CBAR,CHORD',/,10X,
      000           *'TO INDICATE COMPLETION OF MULTIPLE PLOT SET ',
      000           */,10X,'TYPE IN 1,1,1,.1,.1,.1,.1.  TOTAL OF 7  ONES')
      000     77     FORMAT(46X,F8.1,F10.2,4F10.1)
      000     66     FORMAT(10X,'INPUT IPLOT = 0 FOR DASHED LINES',
      000           */,10X,'INPUT IPLOT = 1 FOR LINES + SYMBOLS',
      000           *,/,10X,'INPUT IPLOT = 2 FOR SYMBOLS ONLY'
      000           *,/,10X,'USE IPLOT = 0 IF YOU ONLY WANT TO LOOK AT THE PLOTS')
      000            STOP
      000            END

@HDG,P  ******  MAIN  ******

@ELT,L Q.MAIN
ELT 6B-06/14-22:49 MAIN
      000     10     READ (5,11,END =100) I,J,K,L,Q,A,B,C,D,E,F,G,H,O
      000            WRITE (7,22) I,J,K,L,Q,A,B,C,D,E,F,G,H,O
      000     11     FORMAT( )
      000     22     FORMAT(I7,3I5,F8.2,2F8.2,F8.1,F10.2,4F10.1,F10.2)
      000            READ(5,11) A,B,C,D,E,F,G,H
      000            WRITE (7,33) A,B,C,D,E,F,G,H
      000     33     FORMAT(30X,2F8.2,F8.1,F10.2,4F10.1)
      000            READ (5,11) A,B,C,D,E,F,G,H
      000            WRITE (7,44) A,B,C,D,E,F,G,H
      000     44     FORMAT(29X,F8.1,F8.1,1X,F10.3,F10.4,4F10.3)
      000            GOTO 10
      000     100    STOP
      000            END

@HDG,P  ******  MAP  ******

@ELT,L Q.MAP
ELT 6B-06/14-22:49 MAP
      000     IN SAMPATH*TEMP.MAIN
      000     END
```

```
****** MAP ******

@HDG,P ****** MFORCE ******

@ELT,L Q.MFORCE
ELT 6B-06/14-22:49 MFORCE(2)
 000   IN WT*GRAPHICS.FORCE,.DUMP,.TYPE,.CUT
 000   LIB UOM*AG2PLOT10.
 000   END

@HDG,P ****** MPRESS ******

@ELT,L Q.MPRESS
ELT 6B-06/14-22:49 MPRESS(1)
 000   IN WT*GRAPHICS.PRESS
 000   END

@HDG,P ****** MPRES2D ******

@ELT,L Q.MPRES2D
ELT 6B-06/14-22:49 MPRES2D(1)
 000   IN WT*GRAPHICS.PRES2D,.TYPE
 000   LIB UOM*AG2PLOT10.
 000   END

@HDG,P ****** PRESS ******

@ELT,L Q.PRESS
ELT 6B-06/14-22:49 PRESS(14)
 000          DIMENSION IC(220),ICP(34,5),CP(34,5)
 000          DIMENSION INFOX(5),INFOY(15)
 000          EQUIVALENCE (IC(46),ICP(1,1))
 000   C
 000          F(A,B,L1,M1)=(B-A)*FLOAT(M1-INFOY(L1))/
 000         *FLOAT(INFOY(L1+1)-INFOY(L1))+A
 000          G(C,D,L2,M2)=(D-C)*FLOAT(M2-INFOX(L2))/
 000         *FLOAT(INFOX(L2+1)-INFOX(L2))+C
 000   C
 000          DATA INFOY/1,2,3,5,9,13,17,25,33,45,57,61,67,73,77/
 000          DATA INFOX/1,27,53,79,92/
 000          DATA IXDIM,IYDIM/92,76/
 000          READ(5,11)NSTART,NSTOP
 000   10     READ(7,22,END=100)ISTART,IQ,IA,IFAC
 000          IF(ISTART.GT.NSTOP) STOP
 000          READ(7,33)(IC(I),I=1,220)
 000          READ(7,33)ISKIP
 000          IF(ISTART.LT.NSTART)GOTO 10
 000          NPORTS=IC(1)
 000          IA = -IA/10
 000          DO 20 I = 1 , NPORTS
 000          DO 20 J = 1 , 5
 000   20     CP(I,J) = FLOAT(ICP(I,J))
 000          FAC = FLOAT(IFAC)/1000.
 000          DO 30 J = 1 , 5
 000          Q1 = CP(1,J)
 000          Q2 = CP(2,J)
 000          QVOLTS = (Q1-Q2)*FAC
 000          PST = CP(3,J)
 000          DO 30 I = 4 , NPORTS
 000   30     CP(I,J) = (CP(I,J)-PST)/QVOLTS
 000   C      WRITE (6,110)
 000   C      WRITE (6,66) ISTART,IA
 000   C      WRITE (6,55) ((I,(CP(I,J),J=1,5)),I=1,NPORTS)
 000          WRITE (15,77) IXDIM,IYDIM
 000          DO 40 IX = 1 , IXDIM
 000          DO 31 I = 1 , 5
 000   31     IF(IX.GE.INFOX(I).AND.IX.LE.INFOX(I+1)) GOTO 32
 000   32     DO 40 IY = 1 , IYDIM
 000          DO 34 J = 1 , 15
 000   34     IF(IY.GE.INFOY(J).AND.IY.LE.INFOY(J+1)) GOTO 35
 000   35     Z1 = F(CP(J+3,I),CP(J+4,I),J,IY)
```

```
 ****** PRESS ******

000                 Z2 = F(CP(J+3,I+1),CP(J+4,I+1),J,IY)
000                 Z = G(Z1,Z2,I,IX)
000         40      WRITE (15,88) Z
000                 GOTO 10
000         11      FORMAT ( )
000         22      FORMAT(I10,24X,I8,16X,I8,24X,I8)
000         33      FORMAT(10X,11I8)
000         55      FORMAT(10X,I5,5X,5E12.4)
000         66      FORMAT(10X,'START REC NO ',I7,5X,'ALPHA',I6)
000         77      FORMAT(2I3)
000         88      FORMAT(E10.3)
000         110     FORMAT(1H1)
000         100     STOP
000                 END
```

```
@HDG,P  ******  PRES2D  ******

@ELT,L Q.PRES2D
ELT 6B-06/14-22:49 PRES2D(3)
000                 DIMENSION IB(6),Y(35,5),XCL(16),XCU(15)
000                 DIMENSION SCALEX(4),SCALEY(4)
000                 DIMENSION IC(220),ICP(34,5),CP(34,5),ISTRX(5),ISTRY(3),ISY(6)
000                 EQUIVALENCE (IC(46),ICP(1,1))
000                 DATA SCALEX/3.,0.,0.,1./
000                 DATA SCALEY/3.,6.,-2.,-2./
000                 DATA IB/72,323,525,121,545,969/
000                 DATA XCL/15.,0.,.0125,.025,.05,.1,.15,.2,.3,.4,.55,.7,.75,.825,
000                *.9,.95/
000                 DATA XCU/14.,.0125,.025,.05,.1,.15,.2,.3,.4,.55,.7,.75,.825,.9,.95/
000                */
000                 DATA ISTRX/67,72,79,82,68/
000                 DATA ISTRY/45,67,80/
000                 DATA ISY/1,3,8,4,2,11/
000                 WRITE (6,99)
000                 READ (5,11) IPLOT1
000                 WRITE (6,121)
000                 DO 1 I = 1 , 5
000                 Y(1,I) = 15.
000         1       Y(17,I) = 14.
000                 JJ = 0
000         C
000         C
000                 READ(5,11)NSTART,NSTOP,ITAP,IPLOT
000         100     JJ = JJ + 1
000         10      READ(7,22,END=50)ISTART,IQ,IA,IFAC
000                 IF(ISTART.GT.NSTOP) JJ = JJ - 1
000                 IF(ISTART.GT.NSTOP) GOTO 50
000                 READ(7,33)(IC(I),I=1,220)
000                 READ(7,33)ISKIP
000                 IF(ISTART.LT.NSTART)GOTO 10
000                 NPORTS=IC(1)
000                 IA = -IA/10
000                 DO 20 I = 1 , NPORTS
000                 DO 20 J = 1 , 5
000         20      CP(I,J) = FLOAT(ICP(I,J))
000                 FAC = FLOAT(IFAC)/1000.
000                 DO 30 J = 1 , 5
000                 Q1 = CP(1,J)
000                 Q2 = CP(2,J)
000                 QVOLTS = (Q1-Q2)*FAC
000                 PST = CP(3,J)
000                 DO 30 I = 4 , NPORTS
000         30      CP(I,J) = (CP(I,J)-PST)/QVOLTS
000                 IF(IPLOT.EQ.1) GOTO 46
000                 DO 40 I = 2 , 16
000         40      Y(I,JJ) = -CP(I+2,ITAP)
000                 DO 45 I = 18 , 32
000         45      Y(I,JJ) = -CP(I,ITAP)
000                 GOTO 100
000         46      DO 47 I = 2 , 16
000                 DO 47 JK = 1 , 5
000         47      Y(I,JK) = -CP(I+2,JK)
000                 DO 48 I = 18 , 32
000                 DO 48 JK = 1 , 5
```

```
****** PRES2D ******

        000  48      Y(I,JK) = -CP(I+1,JK)
        000  50      CALL INITT(30)
        000          CALL BINITT
        000          CALL CHECK(SCALEX,SCALEY)
        000          CALL DSPLAY(SCALEX,SCALEY)
        000          IF(IPLOT.EQ.1) JJ = 5
        000          DO 60 I = 1 , JJ
        000          IFAC = IB(I)
        000          CALL TYPE (IPLOT1,IFAC,ISY(I))
        000          CALL CPLOT(XCL,Y(1,I))
        000          CALL TYPE (IPLOT1,IFAC,ISY(I))
        000          CALL CPLOT(XCU,Y(17,I))
        000  60      CONTINUE
        000          CALL NOTATE(493,50,5,ISTRX)
        000          CALL NOTATE(20,410,3,ISTRY)
        000          CALL HDCOPY
        000          CALL FINITT(0,700)
        000  11      FORMAT ( )
        000  22      FORMAT(I10,24X,I8,16X,I8,24X,I8)
        000  33      FORMAT(10X,11I8)
        000  55      FORMAT(10X,I5,5X,5E12.4)
        000  66      FORMAT(10X,'START REC NO ',I7,5X,'ALPHA',I6)
        000  77      FORMAT(2I3)
        000  88      FORMAT(E10.3)
        000  99      FORMAT(10X,'INPUT IPLOT1 = 0 FOR DASHED LINES',
        000         */,10X,'INPUT IPLOT1 = 1 FOR LINES + SYMBOLS',
        000         */,10X,'INPUT IPLOT1 = 2 FOR SYMBOLS ONLY')
        000  110     FORMAT(1H1)
        000  121     FORMAT(5X,'TYPE IN START ,END REC , TAP LOCATION & IPLOT',
        000         */,5X,'IPLOT = 1 FOR CP PLOT OF WHOLE WING',
        000         */,5X,'IPLOT=ANYTHING BUT 1 FOR SPECIFIC TAPS AT DIFF ALP'
        000         *,/,5X,'ALL ON THE SAME LINE SEPARATED BY COMMAS')
        000          STOP
        000          END

@HDG,P  ******  TYPE  ******

@ELT,L Q,TYPE
ELT 6B-06/14-22:49 TYPE
        000          SUBROUTINE TYPE (IPLOT,IFAC,IVALUE)
        000          IF(IPLOT.EQ.0) CALL LINE(IFAC)
        000          IF(IPLOT.EQ.2) CALL LINE(0)
        000          IF(IPLOT.GT.0) CALL SYMBL(IVALUE)
        000          RETURN
        000          END

@HDG,N

@RESUME,E
```

REFERENCES

1. Kroeger, R.A. and Feistel, T.W., "Reduction of Stall-Spin Entry Tendencies Through Wing Aerodynamic Design," SAE Paper 760481, April 1976.

2. Feistel, T.W. and Anderson, S.B., "A Method for Localizing Wing Flow Separation at Stall to Alleviate Spin Entry Tendencies," AIAA Paper 78-1476, 1978.

3. "Stall/Spin Flight Research Expanded," Aviation Week and Space Technology, September 11, 1978, pp. 103 and 105.

4. Winkelmann, A.E., "Experimental Studies of a Two and a Three-Dimensional Low Speed Turbulent Boundary Layer," Doctoral Dissertation, University of Maryland, 1976.

5. Information for Users of the Glenn L. Martin Institute of Technology Low Speed Wind Tunnel at the University of Maryland, Part I - Description of the Wind Tunnel.

6. Abbott, I.H. and Doenhoff, A.E., "Theory of Wing Section," McGraw Hill Book Company, Inc., 1949.

7. Pope, A. and Harper, J.J., "Low-Speed Wind Tunnel Testing," John Wiley and Sons, Inc., New York, 1966.

8. Pankhurst, R.C. and Holder, D.W., "Wind-Tunnel Technique," Sir Issac Pitman and Son, Ltd., London, 1948.

9. Glauert, H., "The Interference on the Characteristics of an Airfoil in a Wind Tunnel of Rectangular Section," Reports and Memoranda No. 1459, 1932.

10. Information for Users of the Glenn L. Martin Institute of Technology Low Speed Wind Tunnel at the University of Maryland, Part III - Data Reduction Procedures.

11. Pope, A., "Summary Report of the Forces and Moments Over an NACA 0015 Airfoil Through 180° Angle of Attack," Aero Digest, April 1949, pp. 76, 78 and 100.

12. Riegels, F.W., "Aerofoil Section," Butterworths, London, 1961.

13. Cristzos, C.C., Heyson, H.H. and Boswinkle, R.W., "Aerodynamic Characteristics of NACA 0012 Airfoil Section at Angles of Attack From 0° to 180°", NACA Technical Note 3361, January 1955.

14. Hoerner, S.F. and Borst, H.V., "Fluid-Dynamic Lift," Mrs. Lisetolle A. Hoerner, 1975.

15. Smetana, F.O., Summey, D.C., Smith, N.S. and Carden, R.K., "Light Aircraft Lift, Drag and Moment Prediction - A Review and Analysis," NASA CR-2523, May 1975.

16. Winkelmann, A.E., "Flow Visualization Studies of a Low Aspect Ratio Finite Wing Beyond Stall," TR AE-79-3, Department of Aerospace Engineering, University of Maryland, College Park, June 1979.

17. Braslow, A.L., Hicks, R.M. and Harris, R.V., "Use of Grit-Type Boundary-Layer-Transition Trips on Wind-Tunnel Models," NACA TN D-3579, September 1966.

18. Agrawal, S., "Parametric Studies of Discontinuous Leading Edge Effects on Wing Characteristics for Angles of Attack up to 50^o," M.S. Thesis, University of Maryland, 1979.

19. Knight, M. and Wenzinger, C.J., "Wind Tunnel Tests on a Series of Wing Models Through a Large Angle of Attack Range," NACA Technical Report 317, 1929.

20. Thwaites, B., "Incompressible Aerodynamics," Clarendon Press, Oxford, 1960, Chapters 1 and 5.

21. Vasanta, Ram, V., "Untersuchungen über die Eckengrenzschicht an einem Kreiszylinder mit Seitenwand," Bericht 63/46, Braunschweig.

22. Hoerner, S.E., "Fluid-Dynamic Drag," published by the author, 1965.

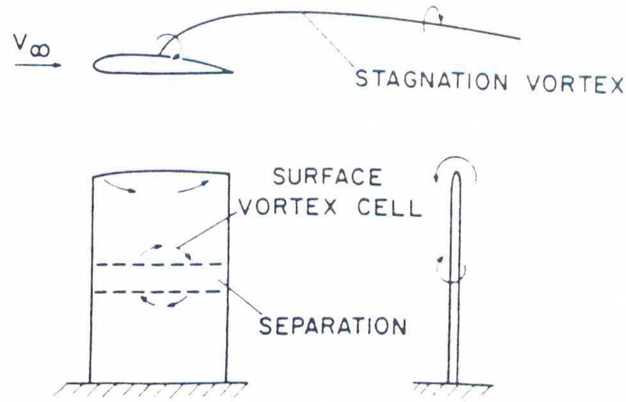

Example of a separation vortex
(from Reference 1)

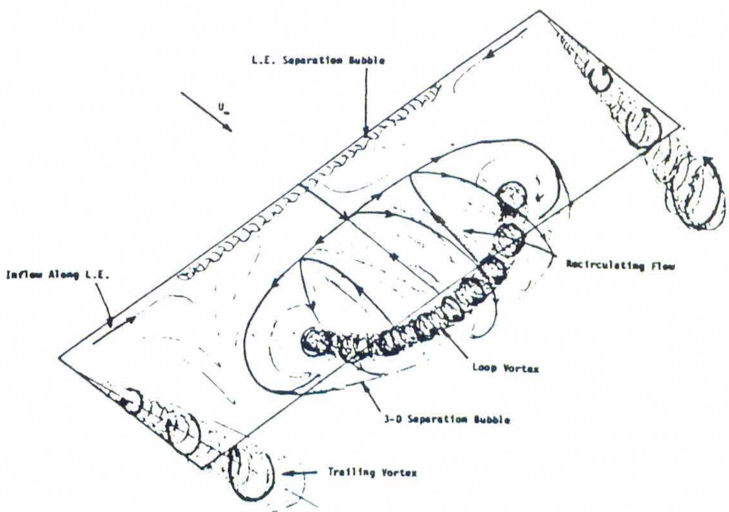

Tentative Flow Model Based on Oil Flow Patterns

(from Reference 16)

Figure 1 - Possible flow field models used to explain counter-rotating swirl patterns.

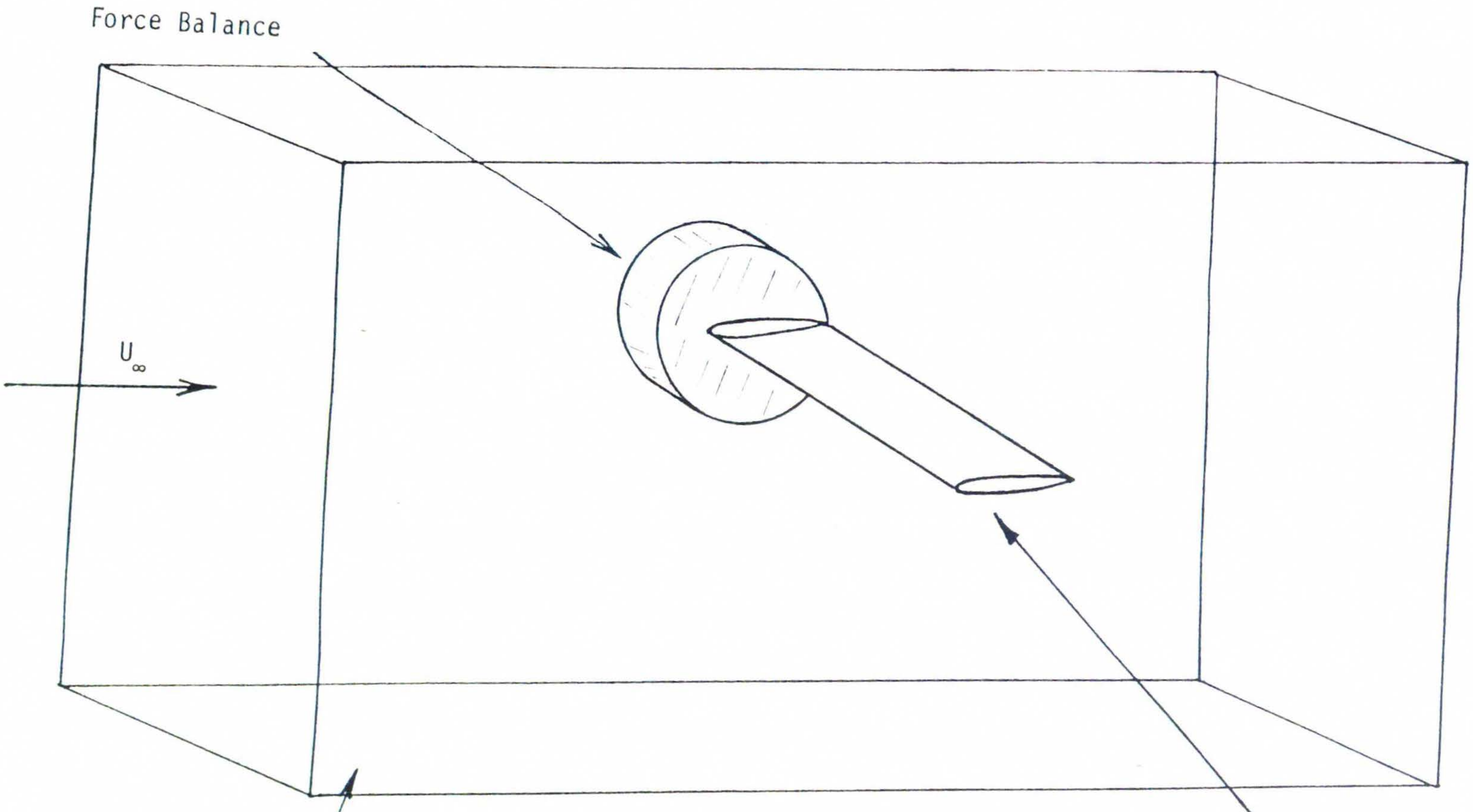

	Wing Model		
	NACA	Chord cm	Span cm
2-D	0015	12.70	43.94
3-D	0015	12.70	35.15

Figure 2 - Sketch of Wing Models in Boundary Layer Research Tunnel

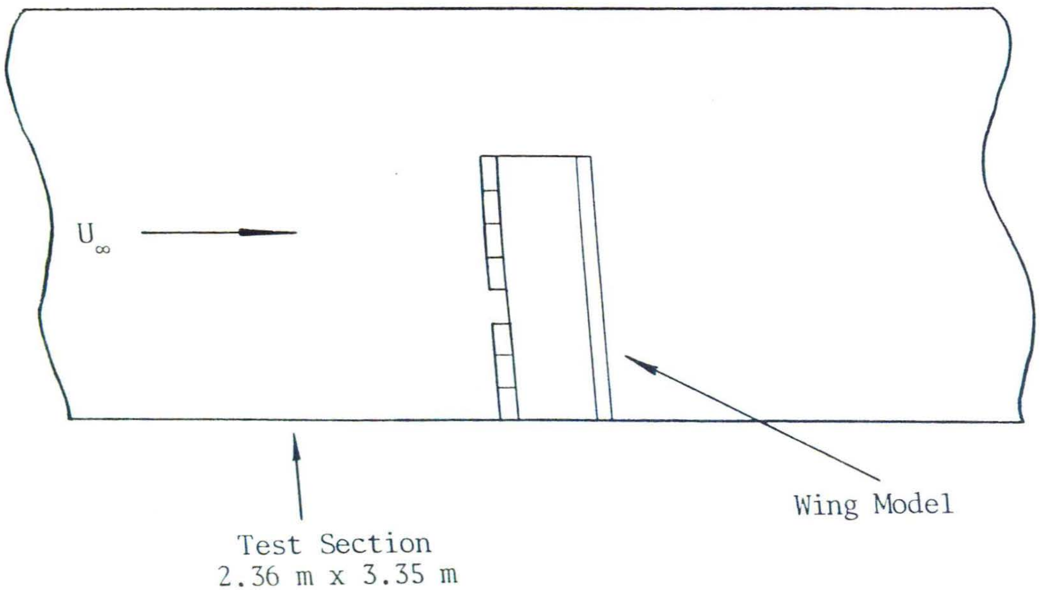

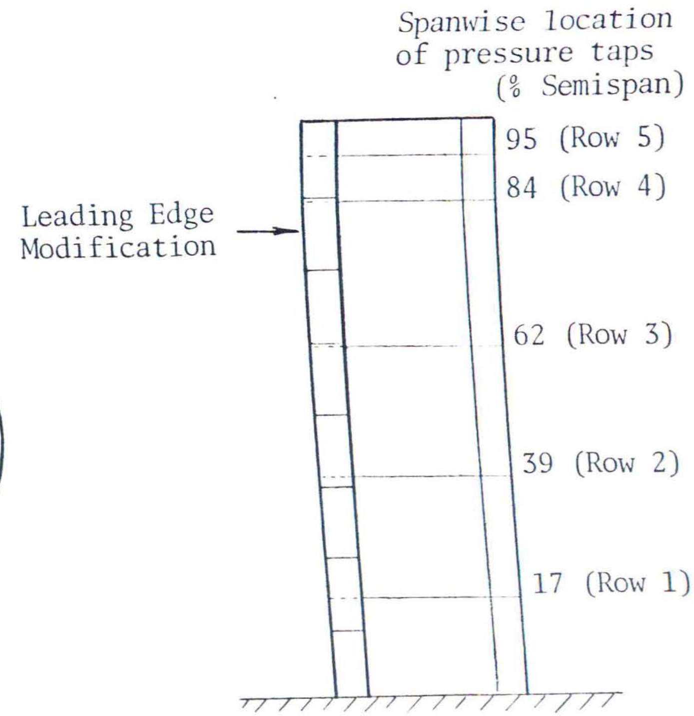

Chordwise location of pressure taps on
upper/lower surface

Tap No.	% Chord	Tap No.	% Chord
1	0	9	0.40
2	0.0125	10	0.55
3	0.025	11	0.70
4	0.050	12	0.75
5	0.10	13	0.825
6	0.15	14	0.90
7	0.20	15	0.95
8	0.30		

Figure 3 - Sketch of Wing Model in Glenn L. Martin Wind
Tunnel and Details of Leading Edge Glove

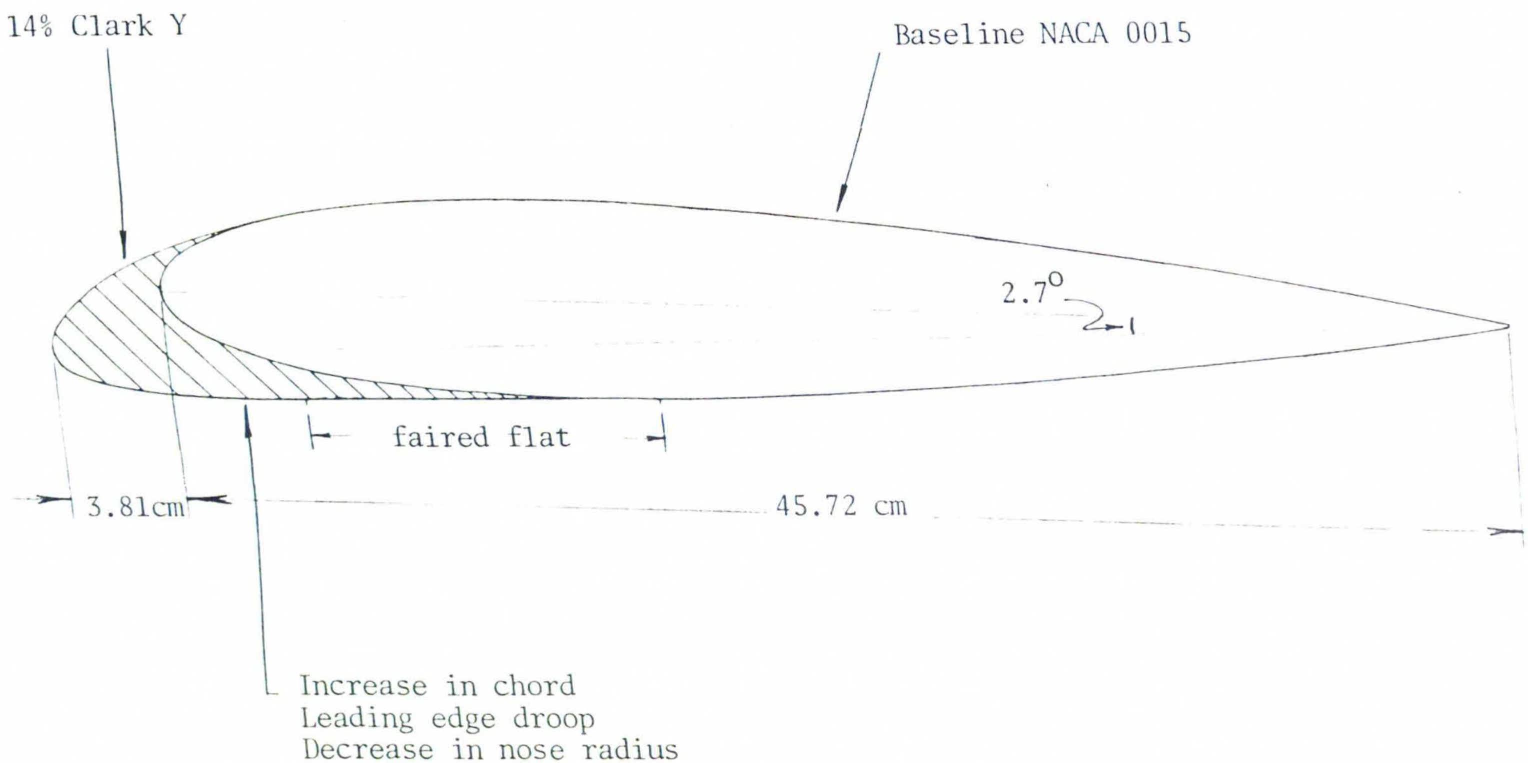

Figure 3 - Concluded.

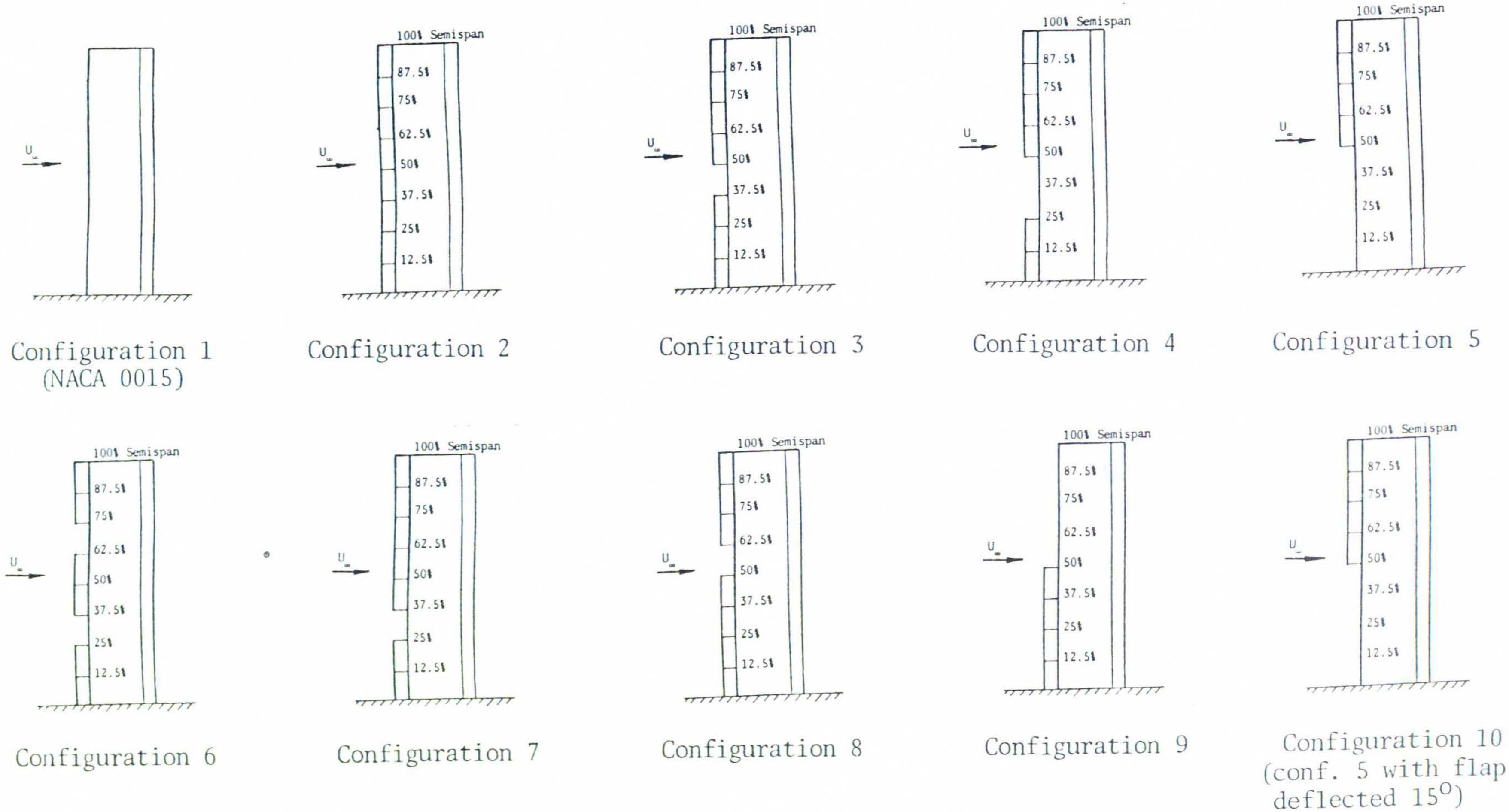

Figure 4 - Various leading edge configurations tested.

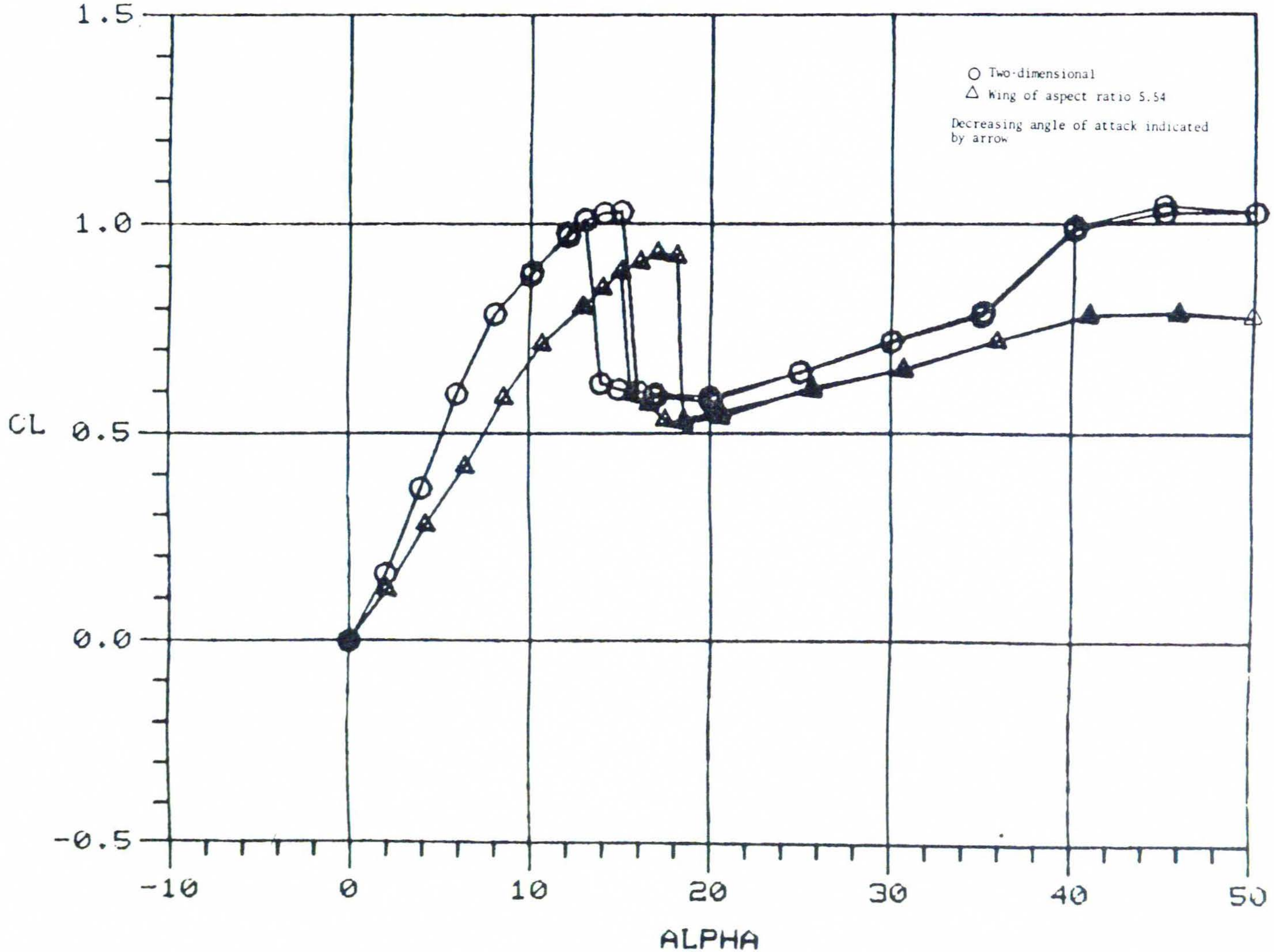

a) NACA 0015 wing, Re_c = 350,000

Figure 5 - Variation of lift coefficient with angle of attack.

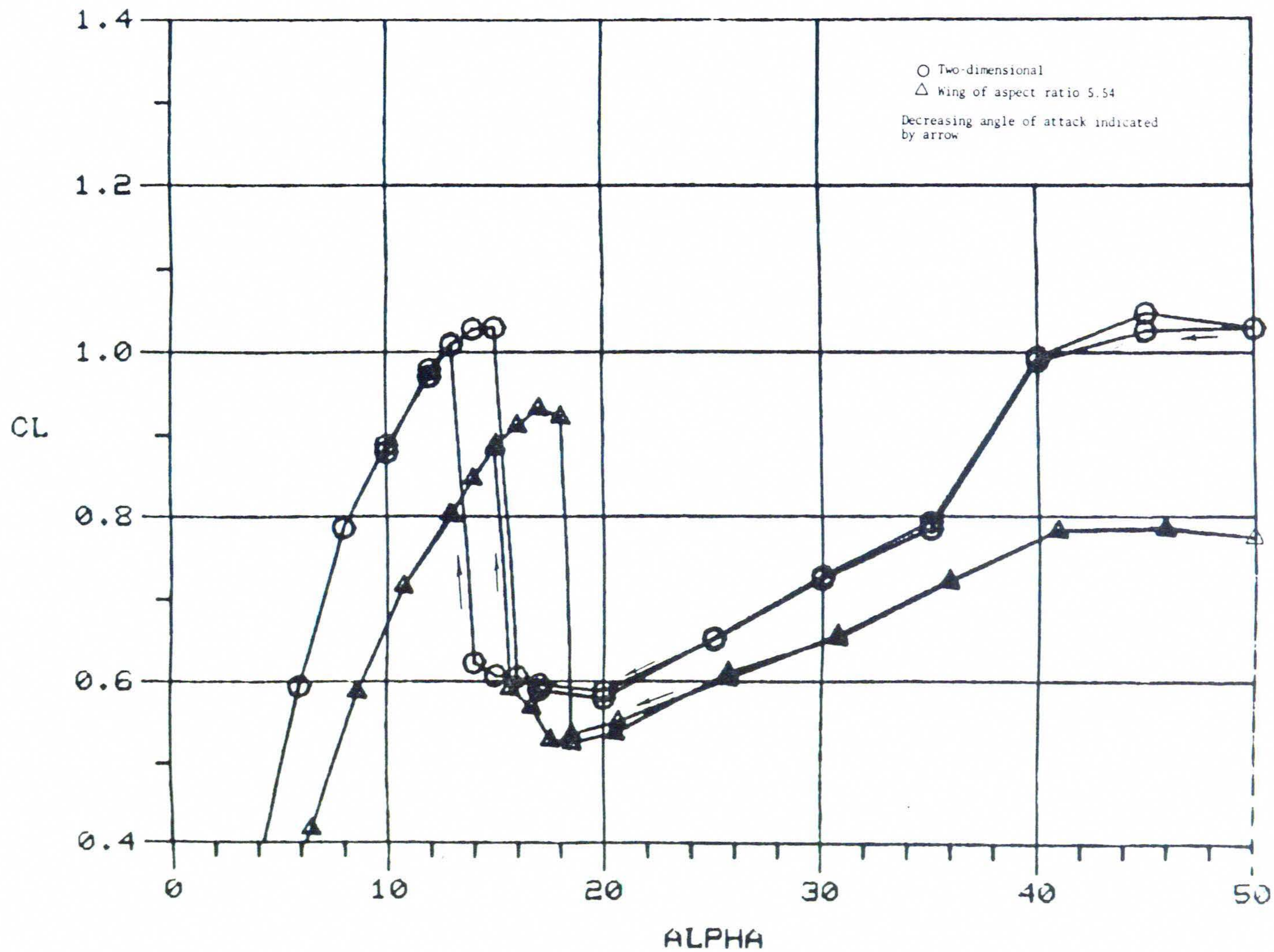

b) NACA 0015 wing. C_L expanded scale

Figure 5 - Continued.

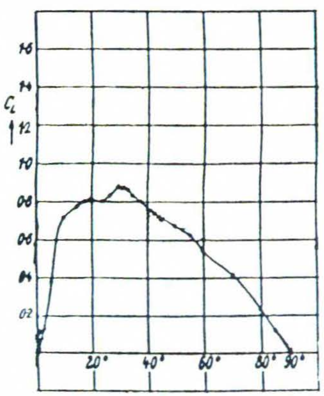

Flat plate wing, aspect ratio 5
(from Reference 12)

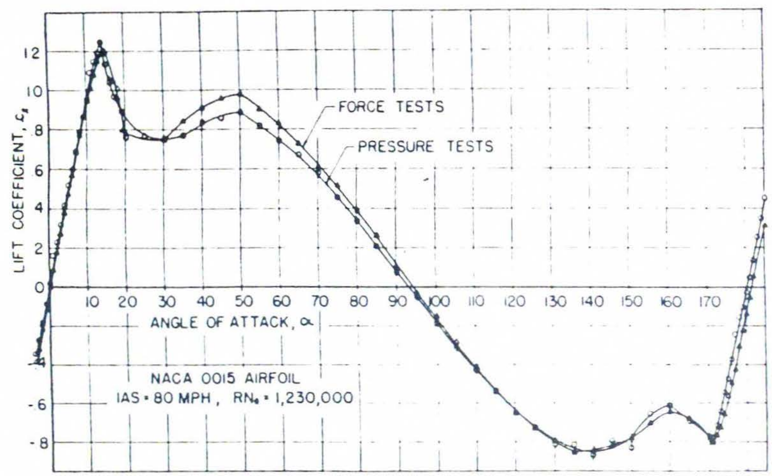

NACA 0015 Airfoil (from Reference 11)

c) Flat plate wing, aspect ratio 5 and NACA 0015 airfoil.

Figure 5 - Variation of lift coefficient with angle of attack.

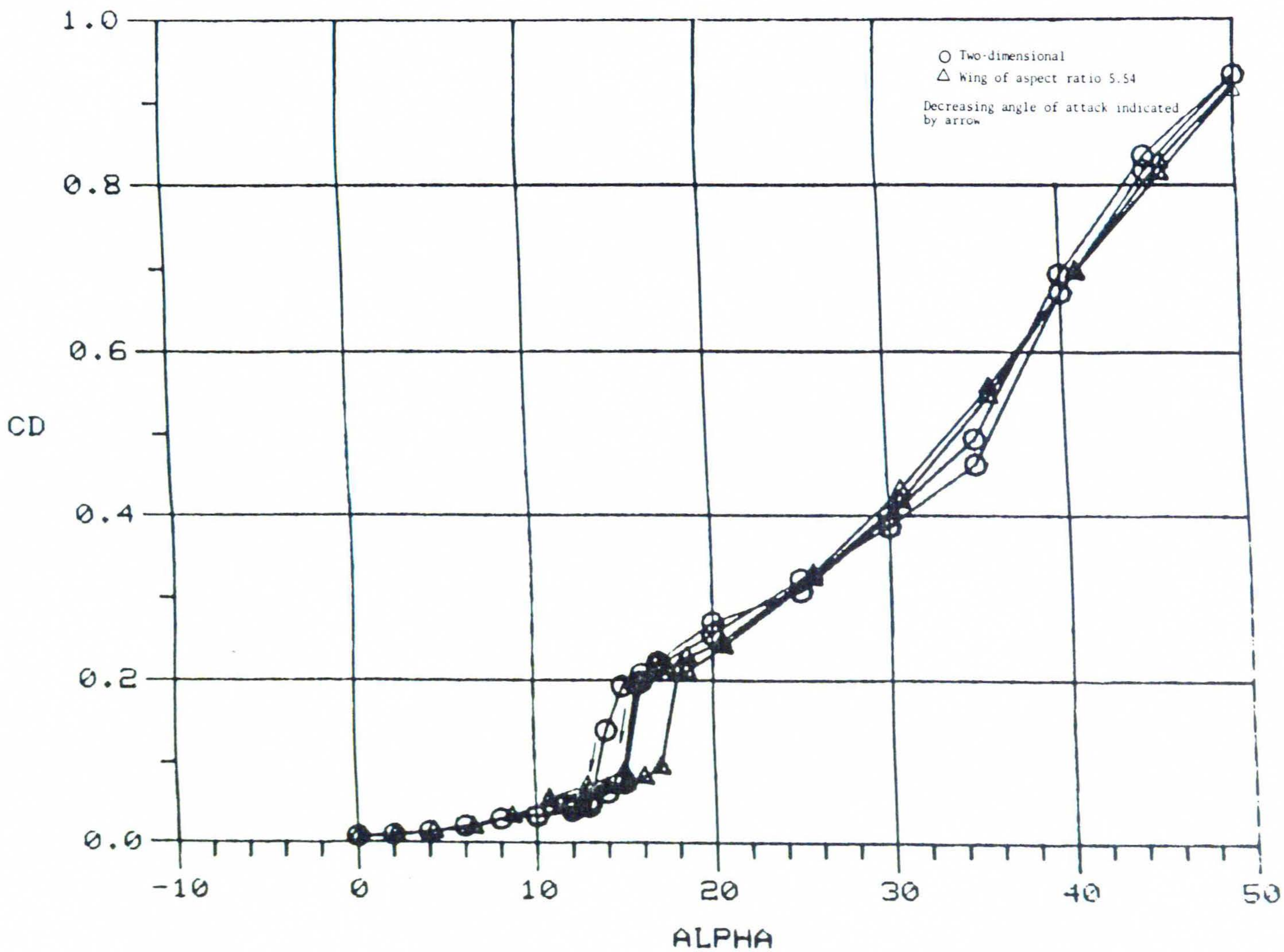

a) Data for $\alpha = 0^{\circ}$ to 50°

Figure 6 - Variation of drag coefficient with angle of attack of NACA 0015 wing, Re_c = 350,000.

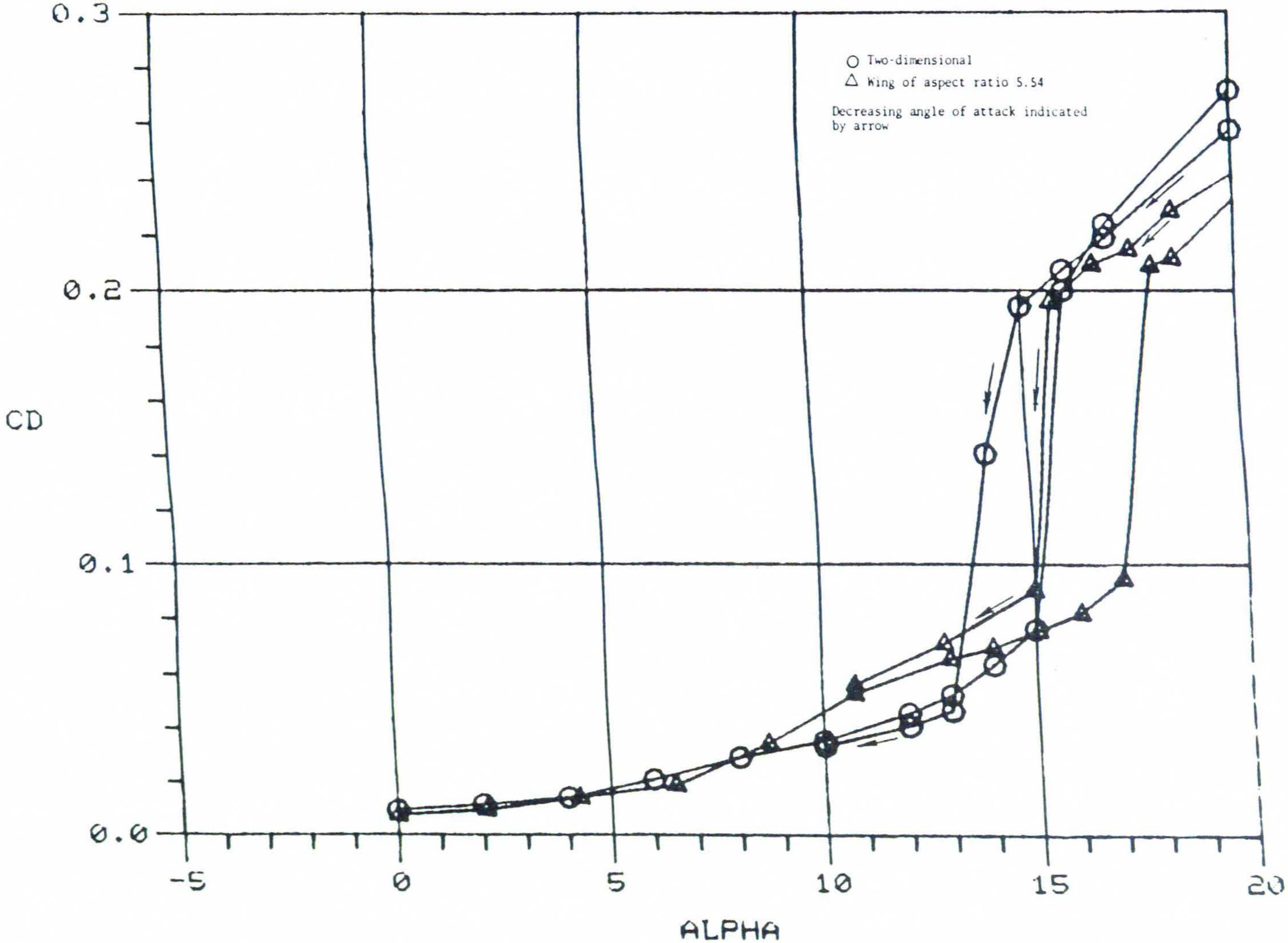

b) Data for $\alpha = 0^{o}$ to 20^{o}

Figure 6 - Concluded.

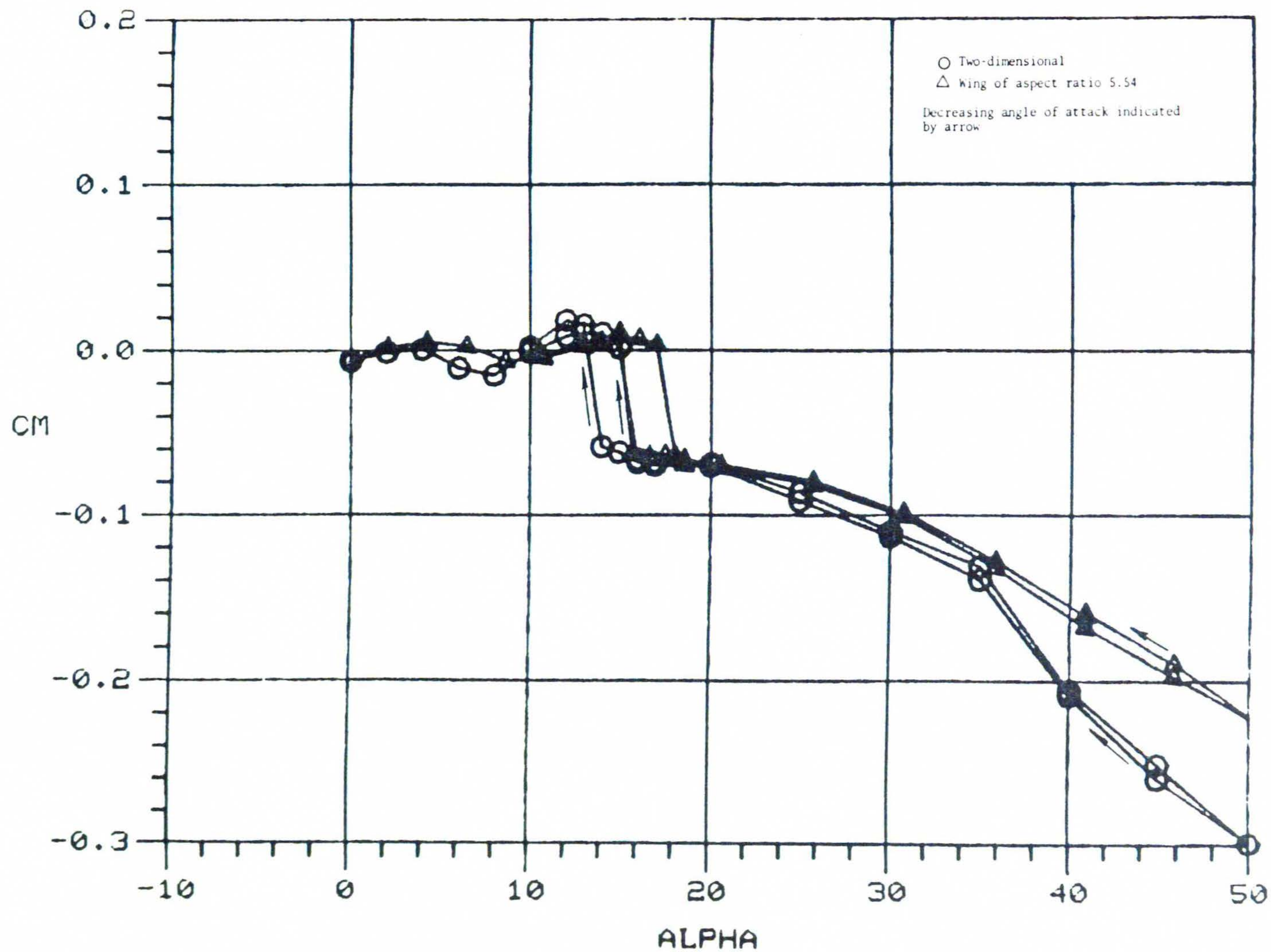

Figure 7 - Variation of pitching moment coefficients with angle of attack of NACA 0015 wing, Re_c = 350,000.

$\downarrow U_\infty$

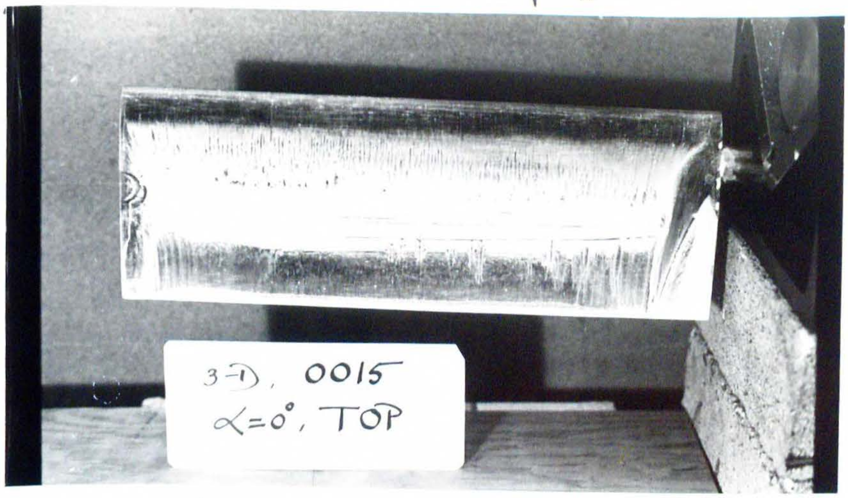

a) At $\alpha = 0^{o}$

$\downarrow U_\infty$

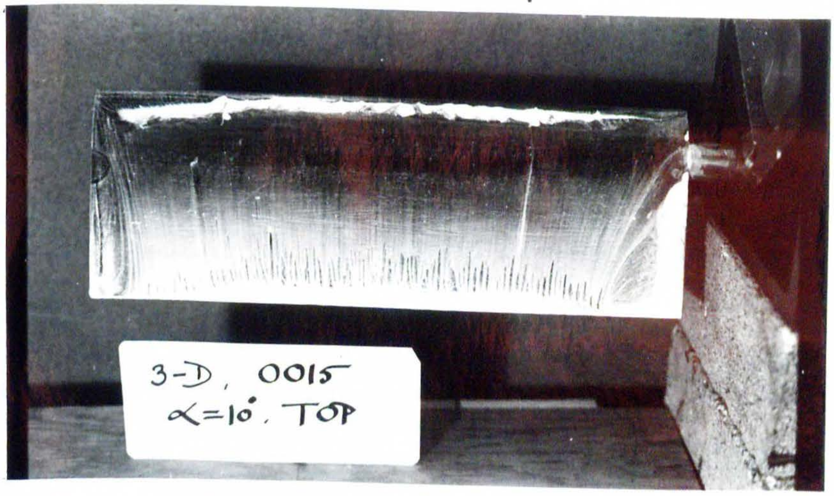

b) Upper surface at $\alpha = 10^{o}$

c) Lower surface at $\alpha = 10^{o}$ $\uparrow U_\infty$

Figure 8 - Oil flow patterns showing laminar separation on NACA 0015 wing, Re_c = 350,000.

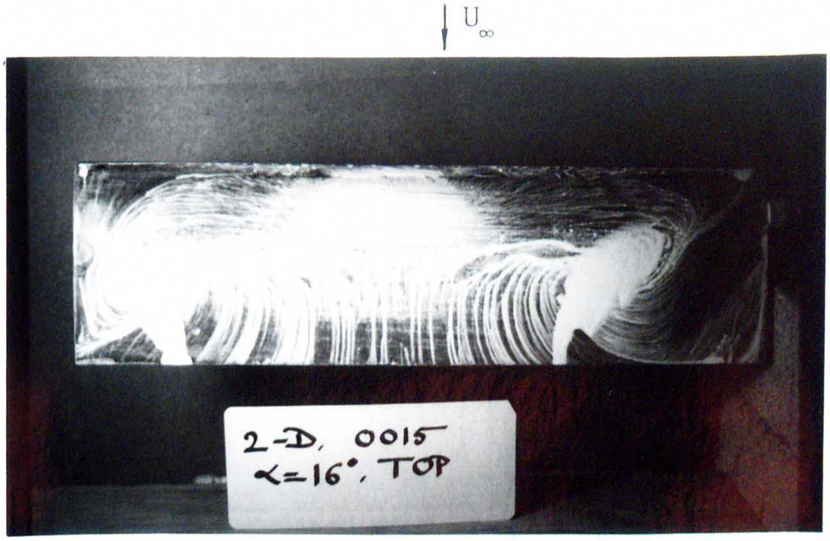

a) 2-D upper surface at $\alpha = 16^{\circ}$

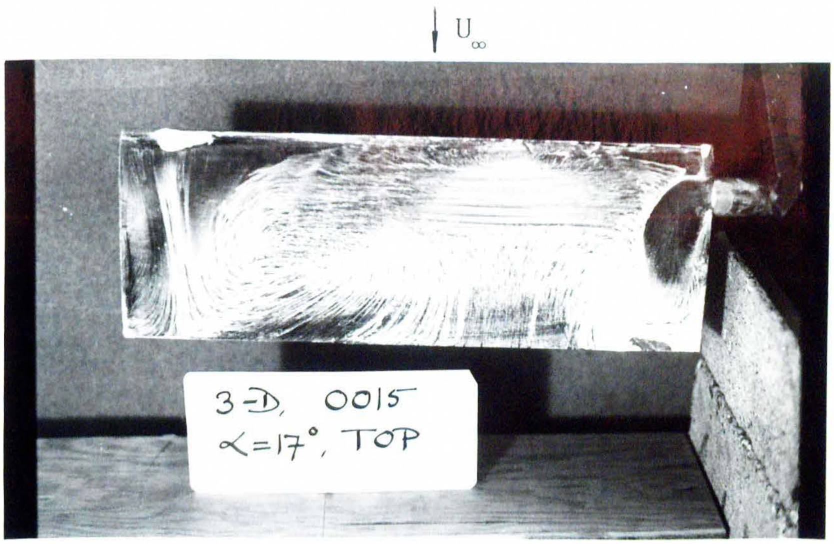

b) 3-D upper surface at $\alpha = 17^{\circ}$

Figure 9 - Oil flow patterns on NACA 0015 wing at various angles of attack, Re_c = 350,000.

$\downarrow U_\infty$

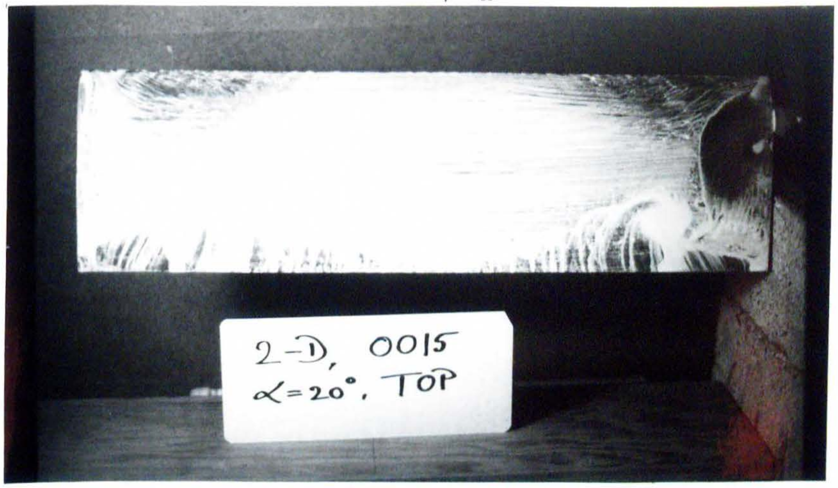

c) 2-D upper surface at $\alpha = 20^{o}$

$\downarrow U_\infty$

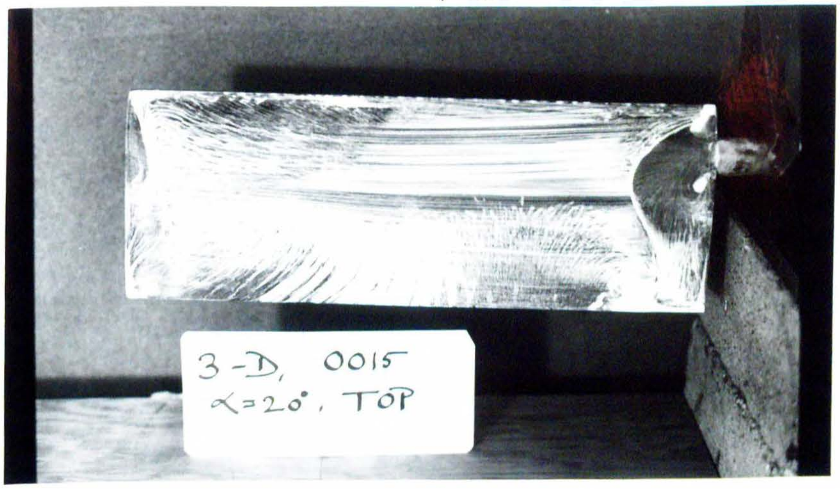

d) 3-D upper surface at $\alpha = 20^{o}$

Figure 9 - Concluded.

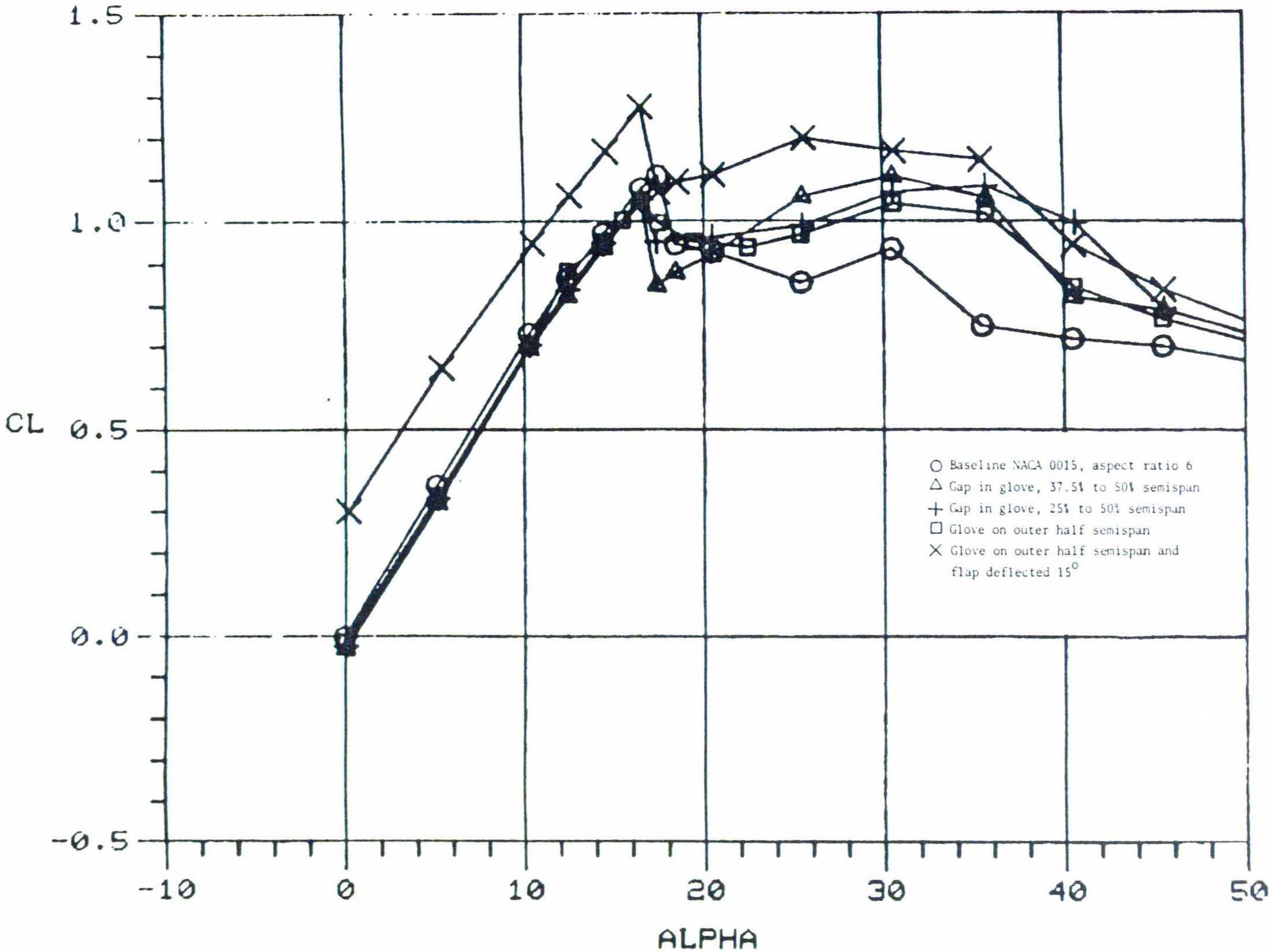

a) C_L for $\alpha = 0^{\circ}$ to 50°

Figure 10 - Lift coefficient vs. α for NACA 0015 wing with leading edge modifications on inboard half semispan, $Re_c = 2.0 \times 10^6$.

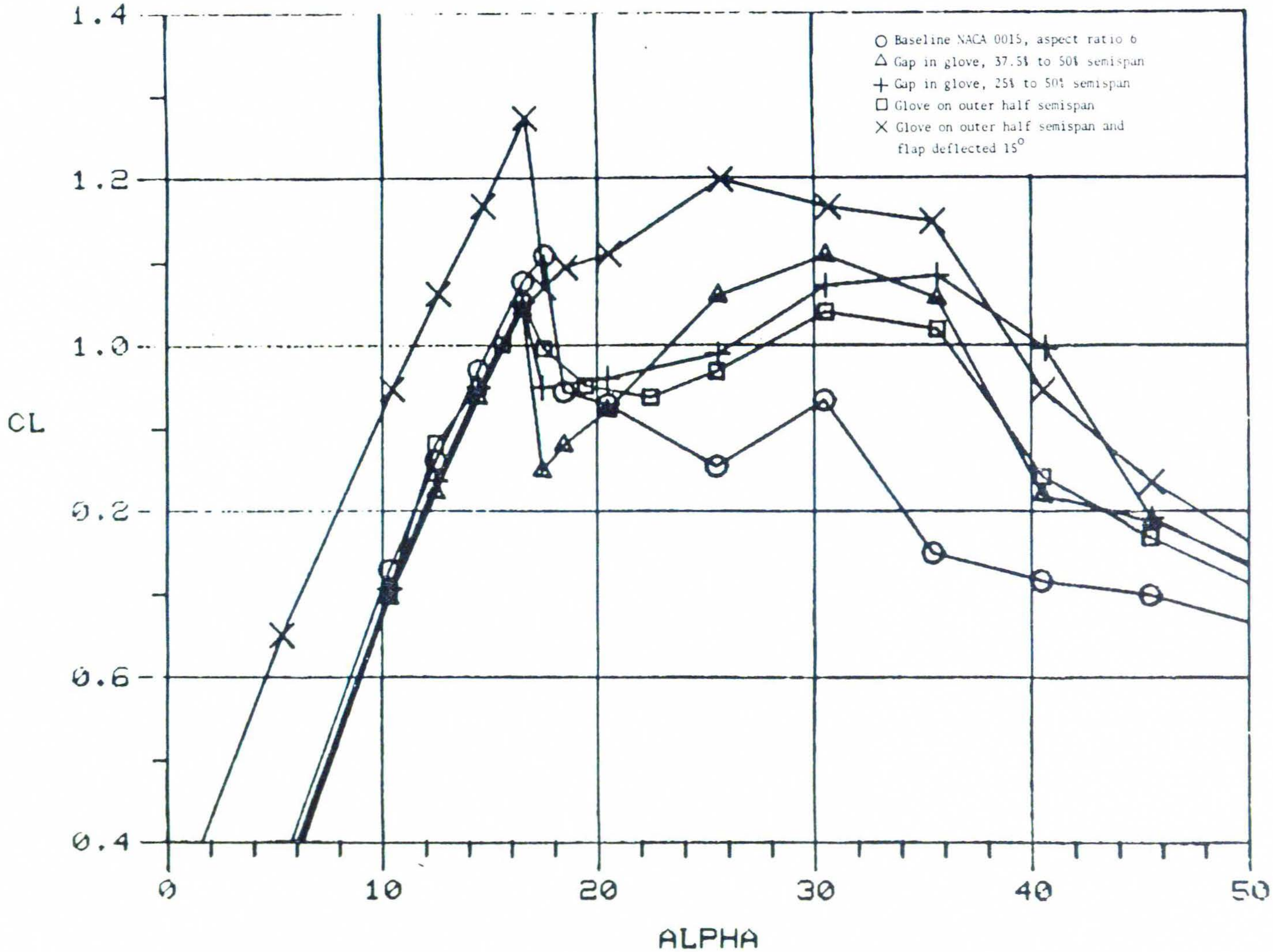

b) C_L expanded scale

Figure 10 - Concluded.

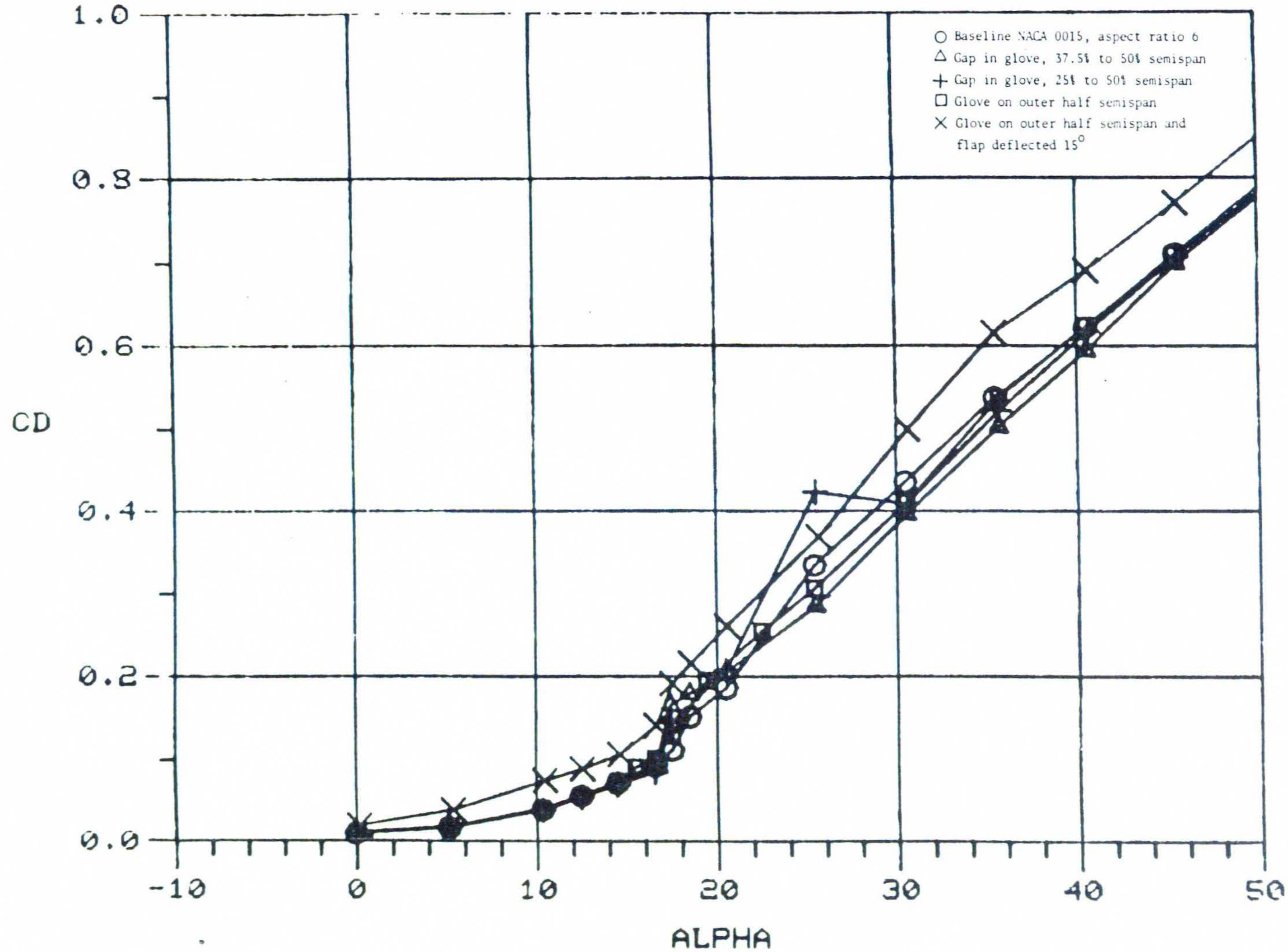

a) Data for $\alpha = 0^{\circ}$ to 50°

Figure 11 - Drag coefficient vs. α for NACA 0015 wing with leading edge modifications on inboard half semispan, $Re_c = 2.0 \times 10^6$.

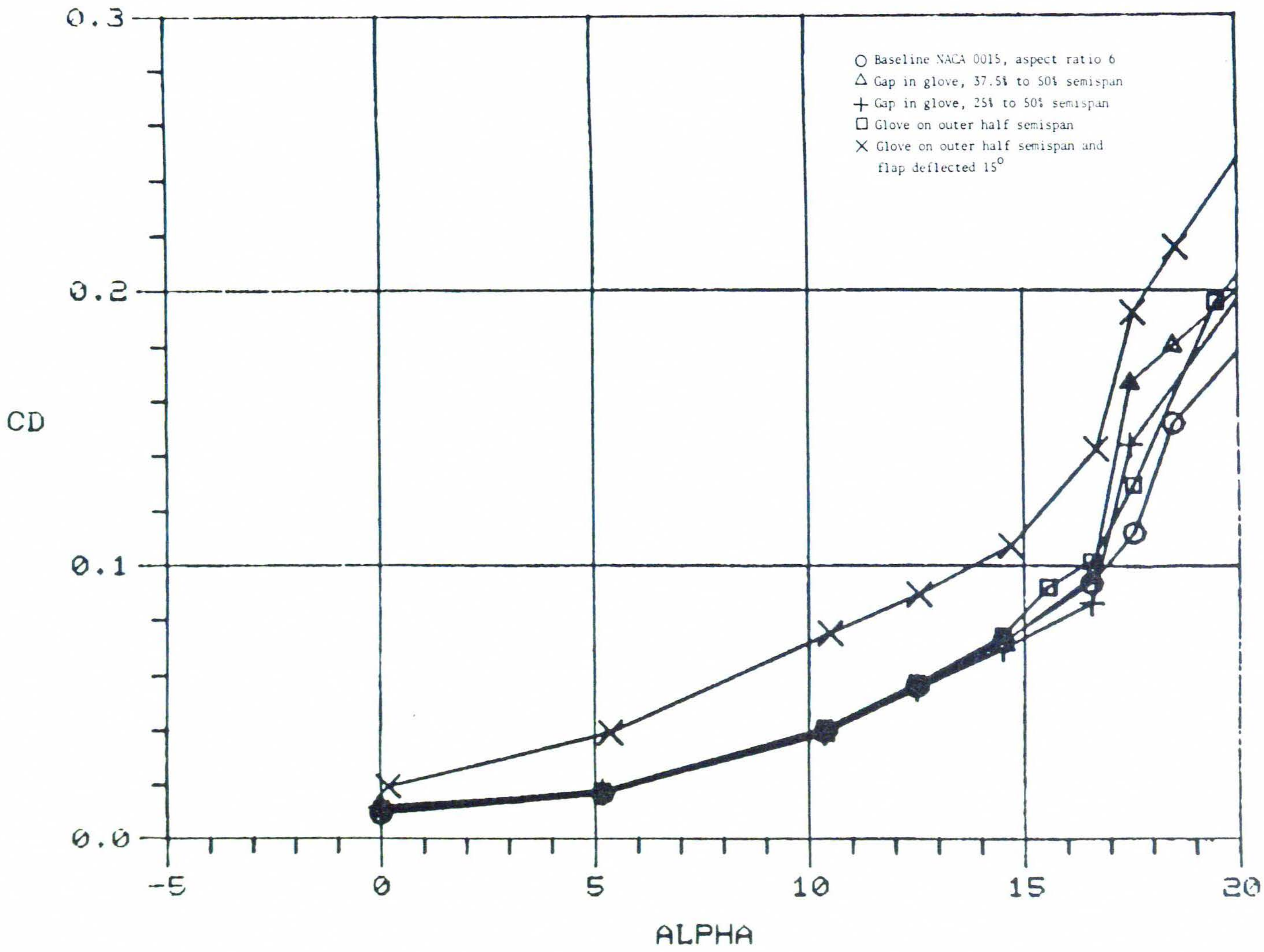

b) Data for $\alpha = 0^{\circ}$ to 20°

Figure 11 - Concluded.

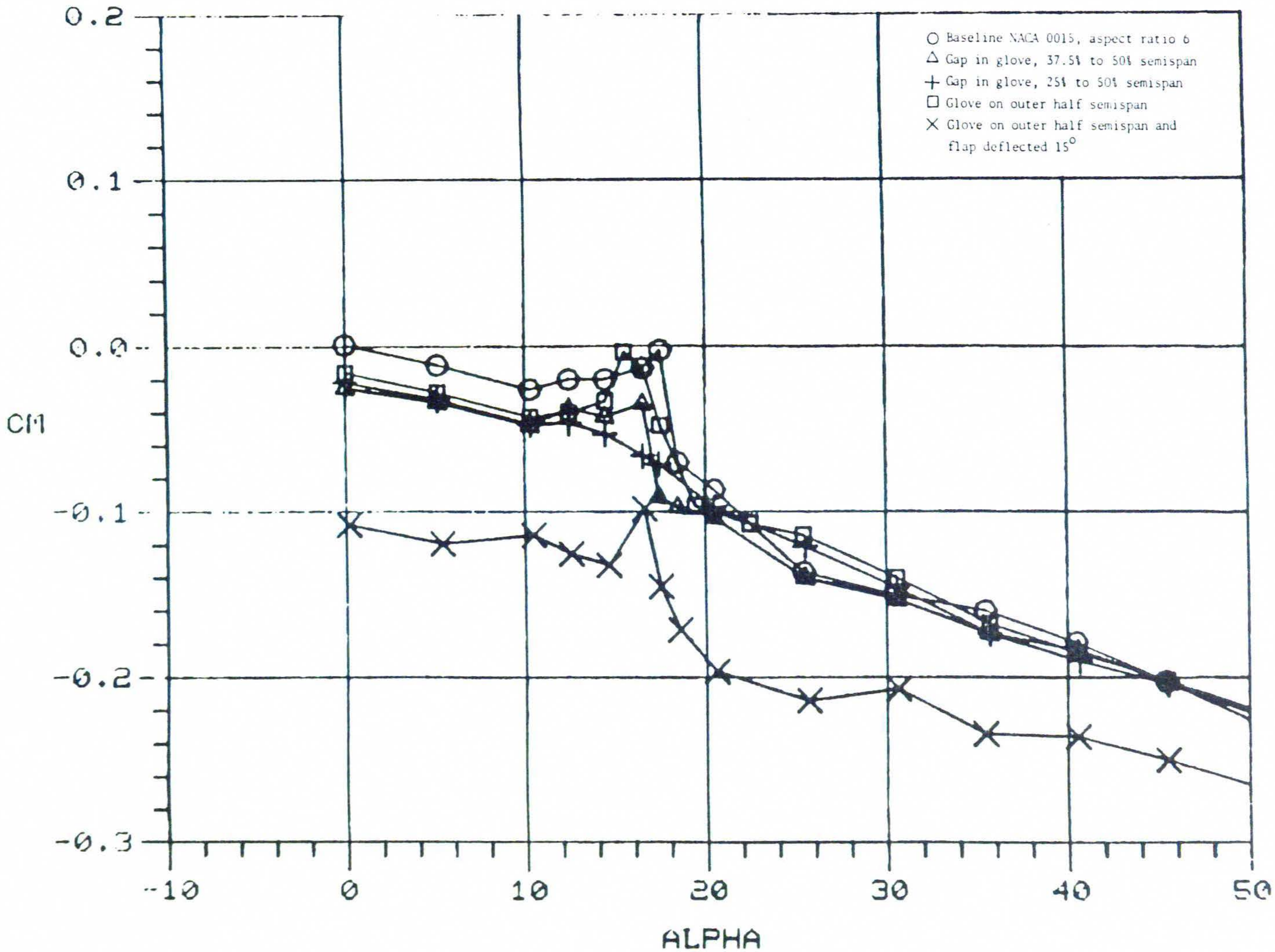

Figure 12 - Pitching moment coefficient vs. α for NACA 0015 wing with leading edge modifications on inboard half semispan, $Re_c = 2.0 \times 10^6$.

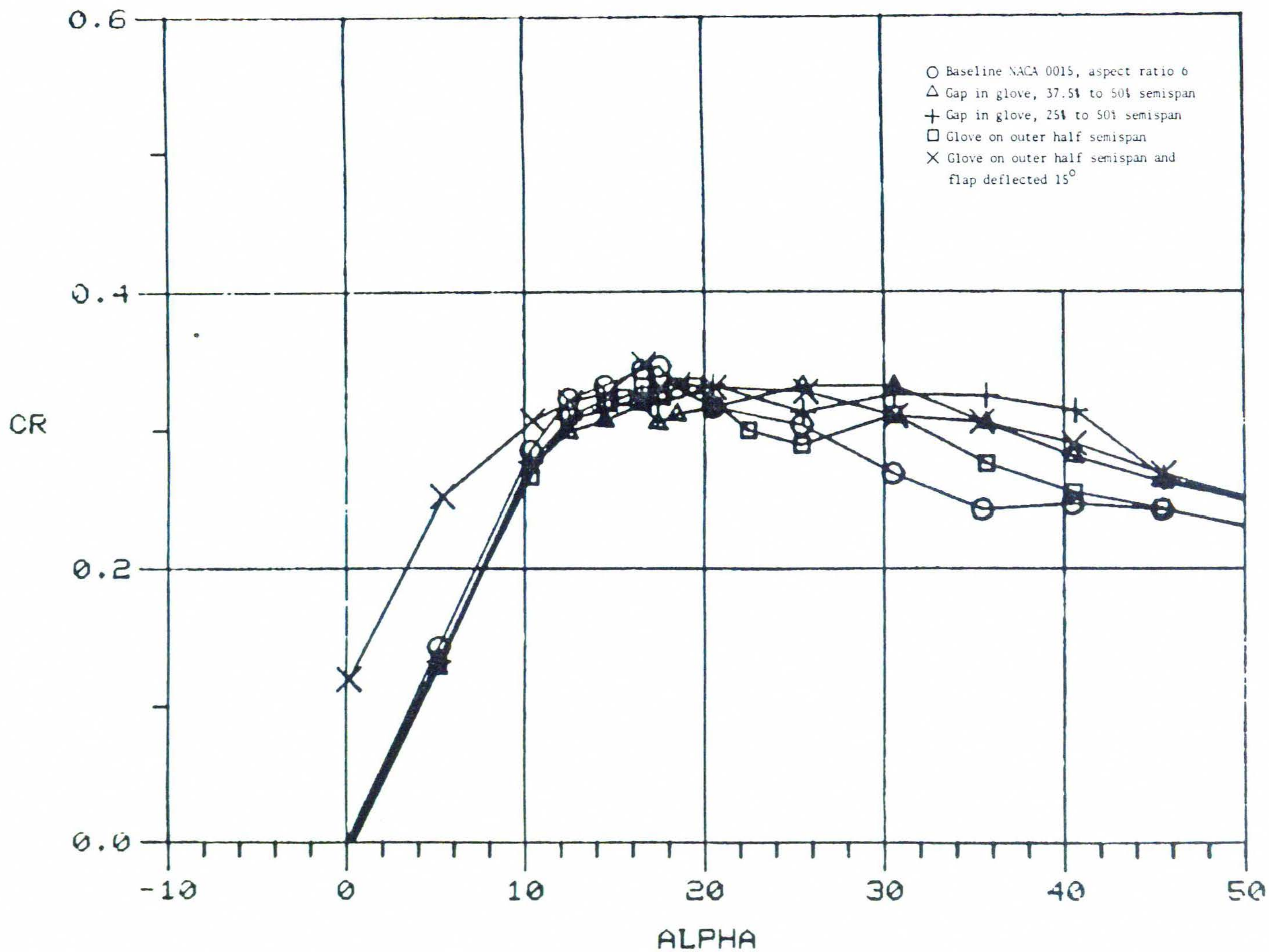

Figure 13 - Rolling moment coefficient vs. α for NACA 0015 wing with leading edge modifications on inboard half semispan, $Re_c = 2.0 \times 10^6$.

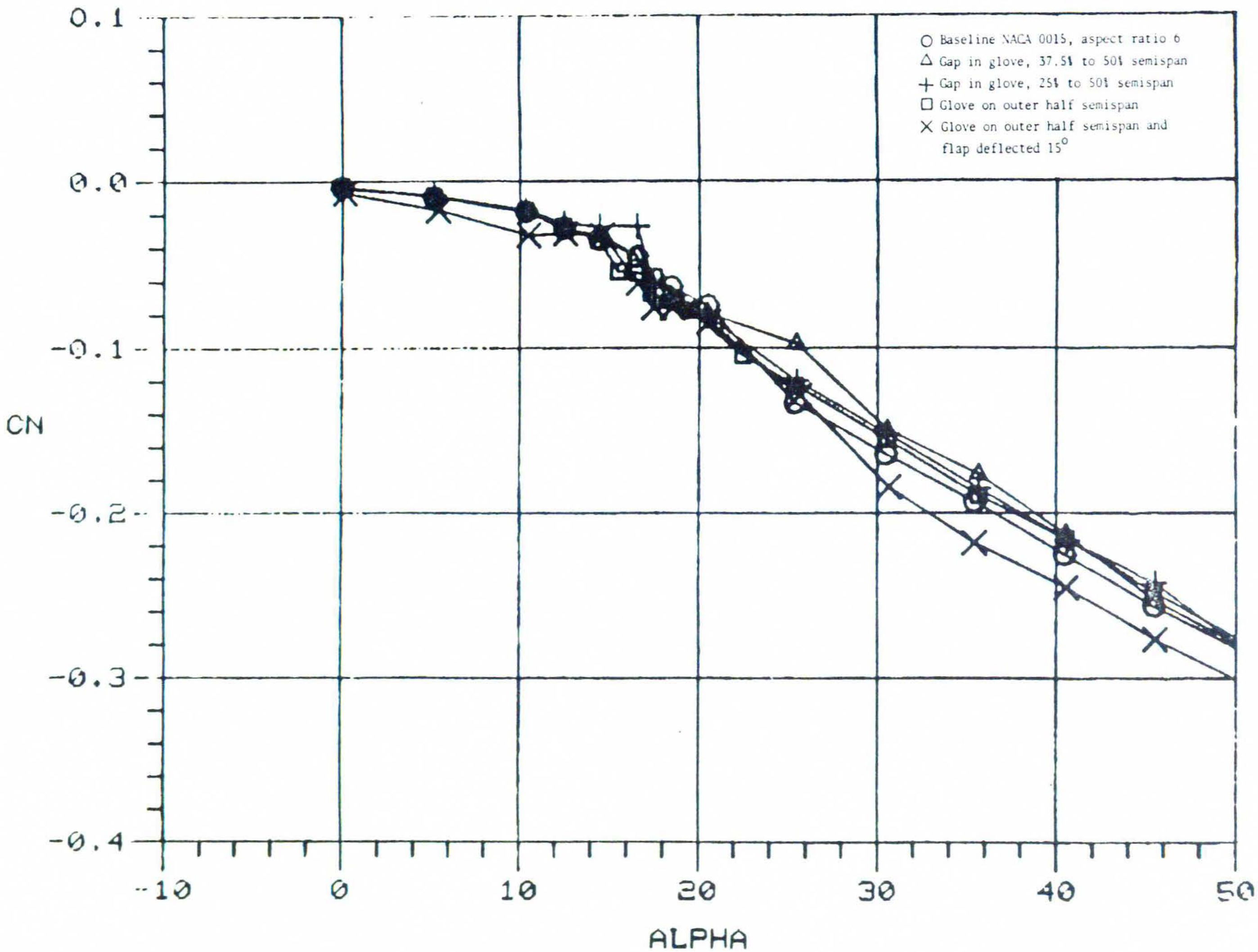

Figure 14 - Yawing moment coefficient vs. α for NACA 0015 wing with leading edge modifications on inboard half semispan, $Re_c = 2.0 \times 10^6$.

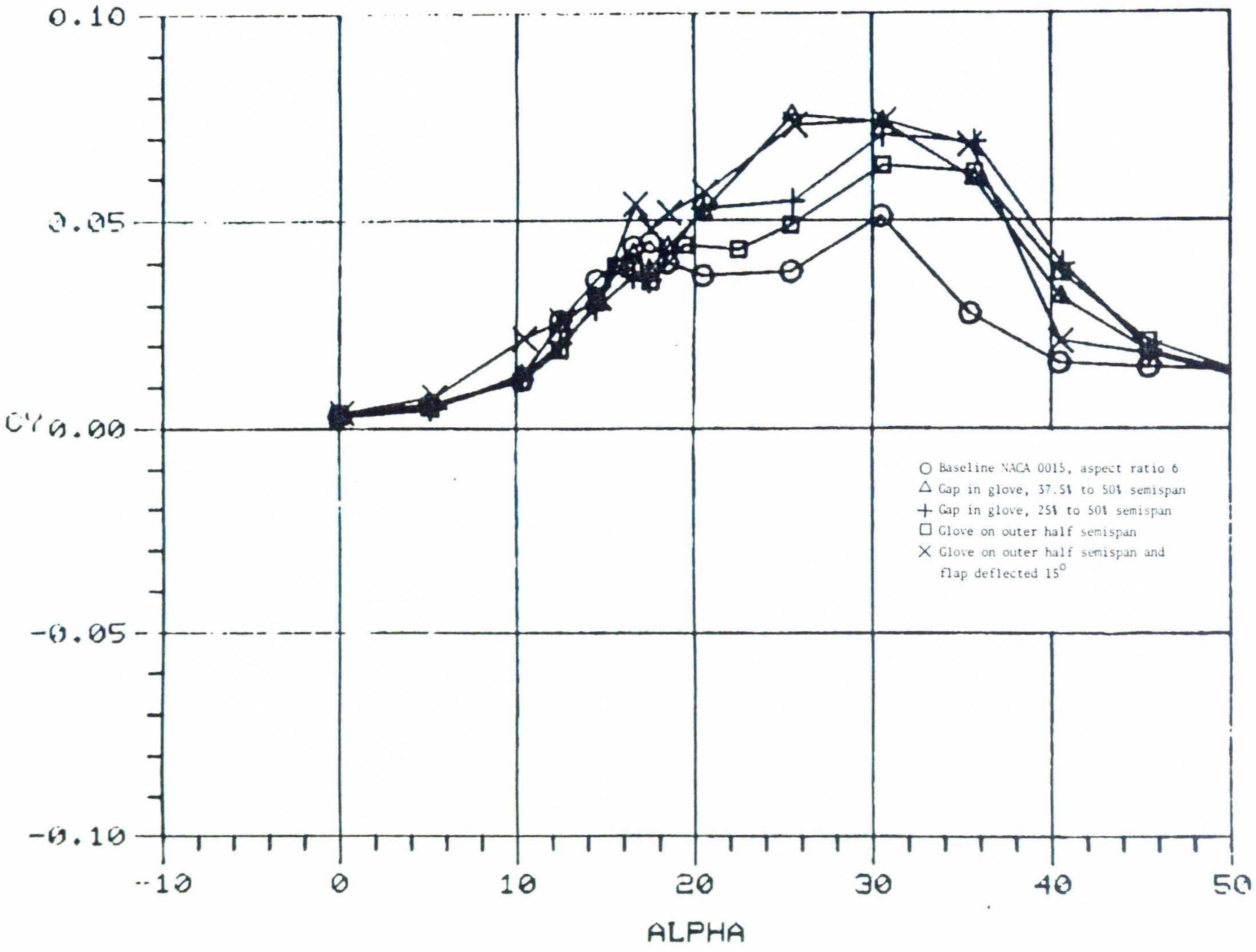

Figure 15 - Side force coefficient vs. α for NACA 0015 wing with leading edge modifications on inboard half semispan, $Re_c = 2.0 \times 10^6$.

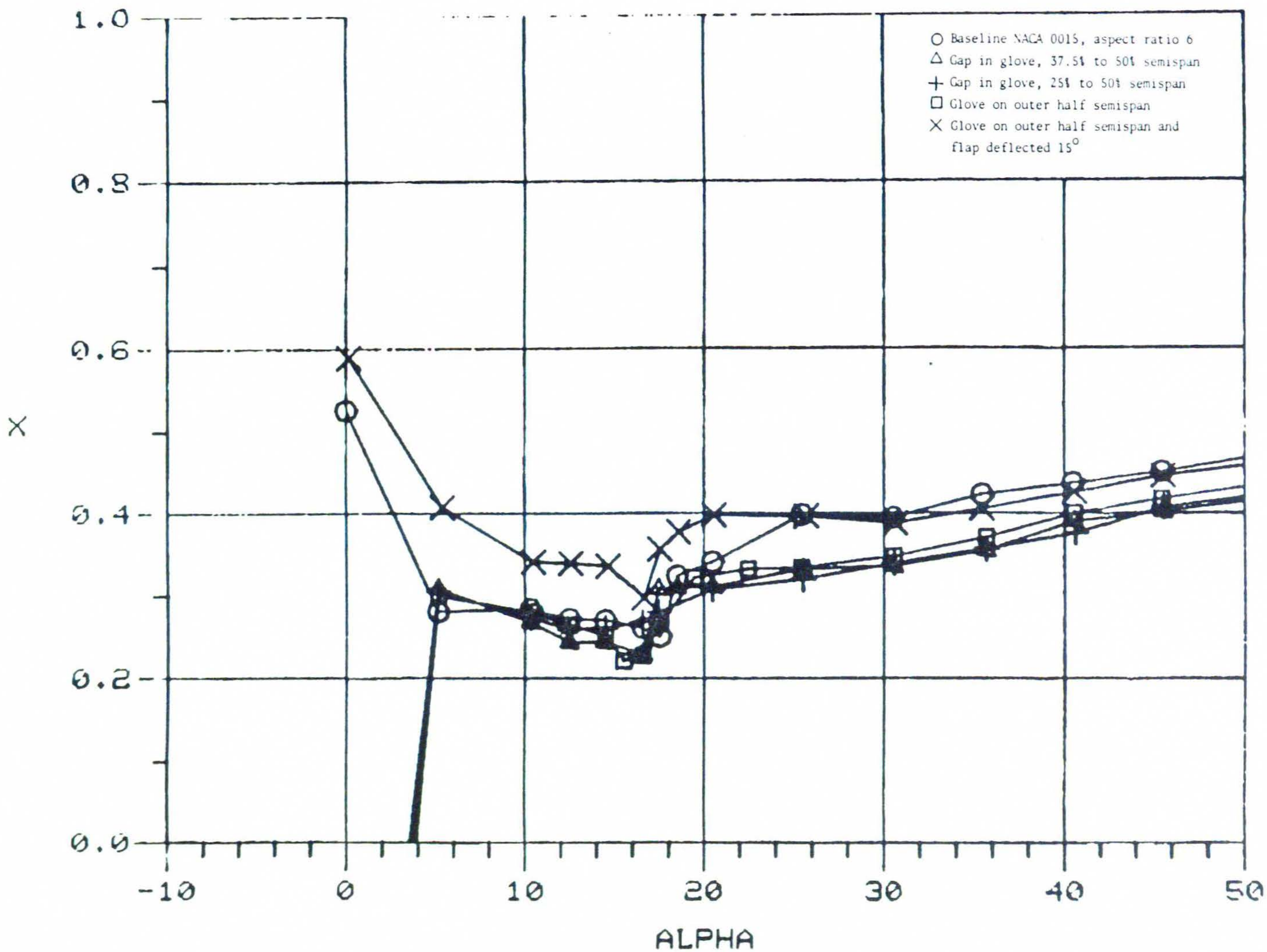

a) Chordwise location of center of pressure.

Figure 16 - Center of force location vs. α for NACA 0015 wing with leading edge modifications on inboard half semispan, $Re_c = 2.0 \times 10^6$.

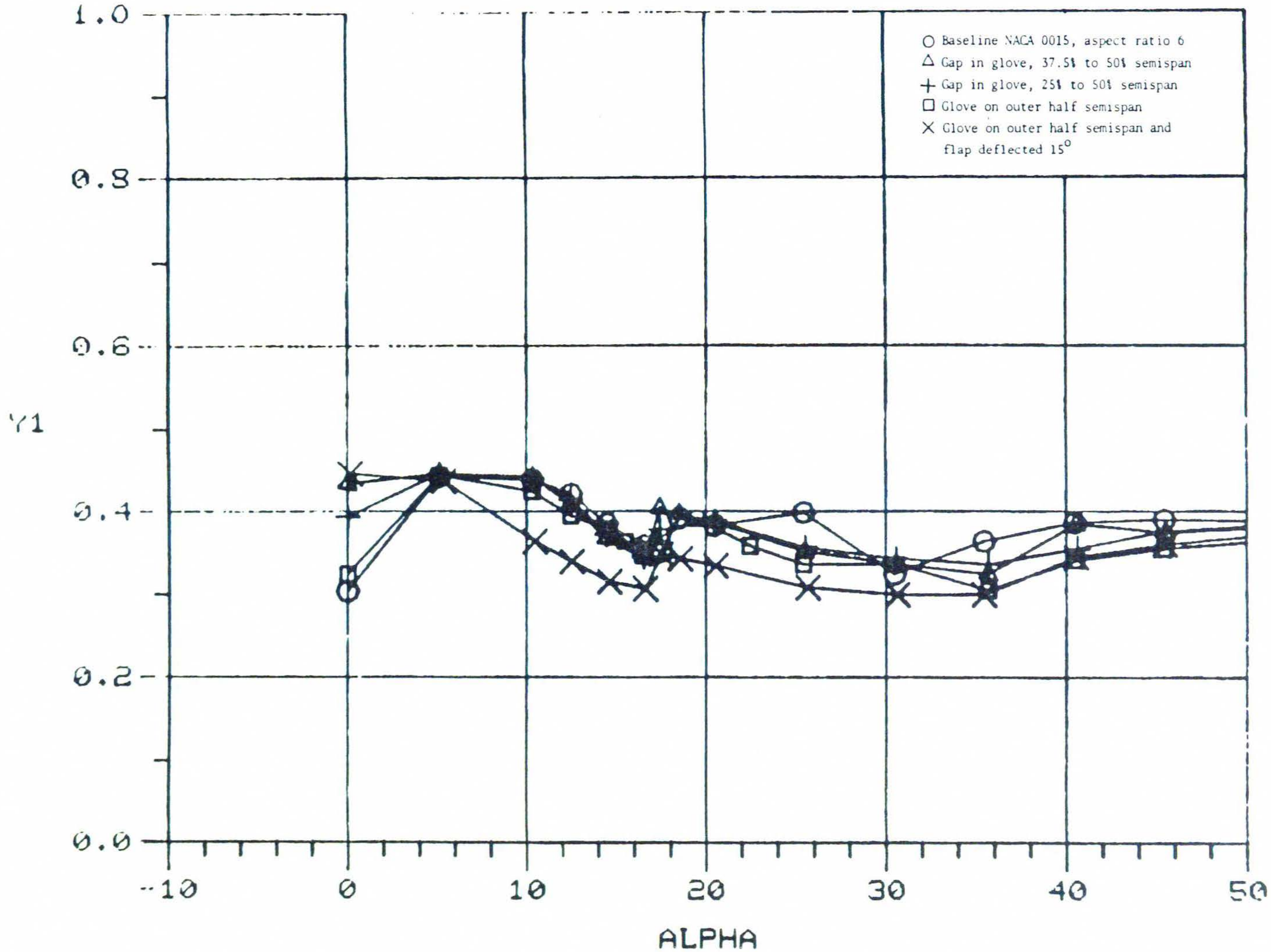

b) Spanwise location of center of lift

Figure 16 - Continued.

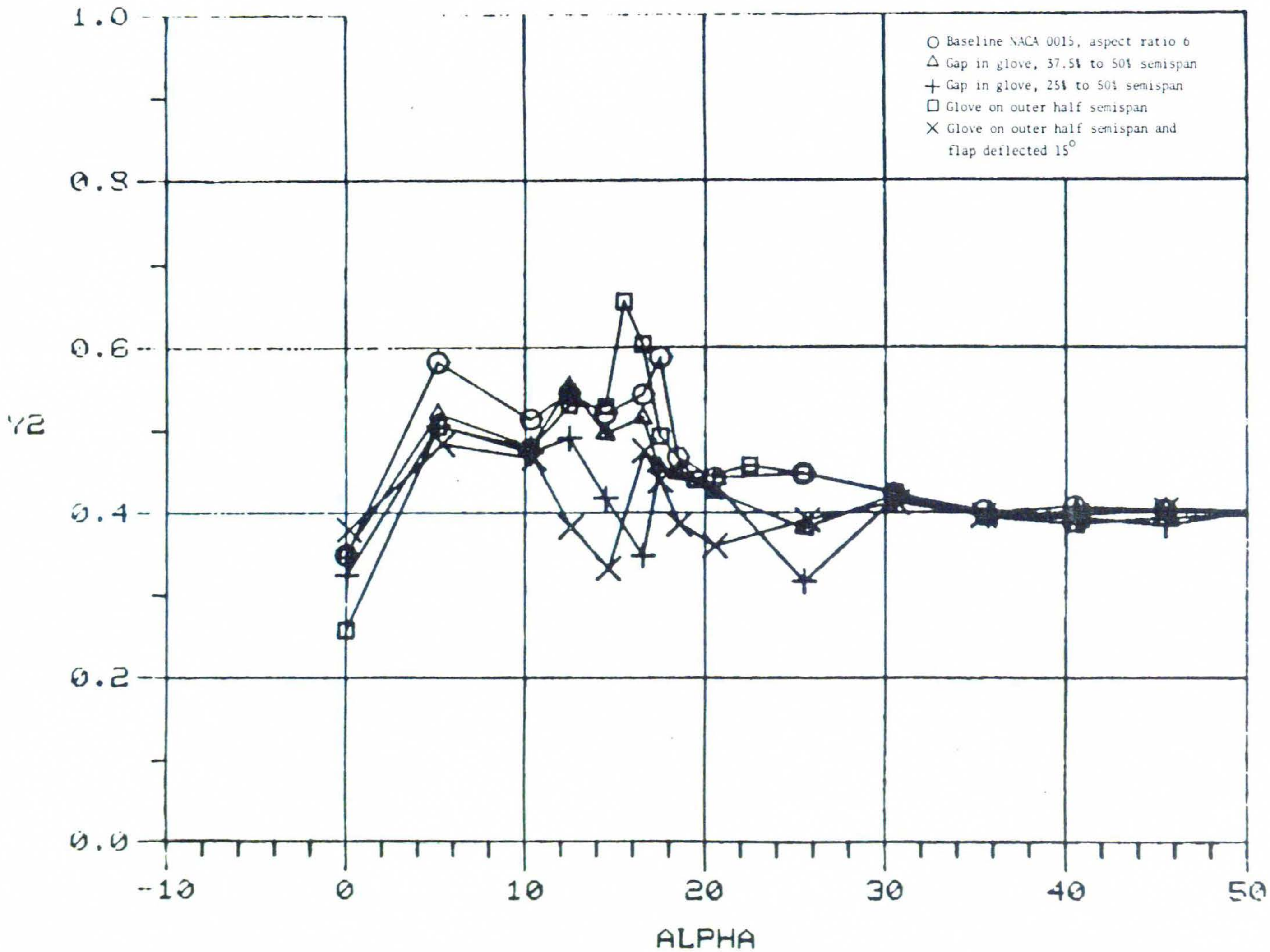

c) Spanwise location of center of drag

Figure 16 - Concluded.

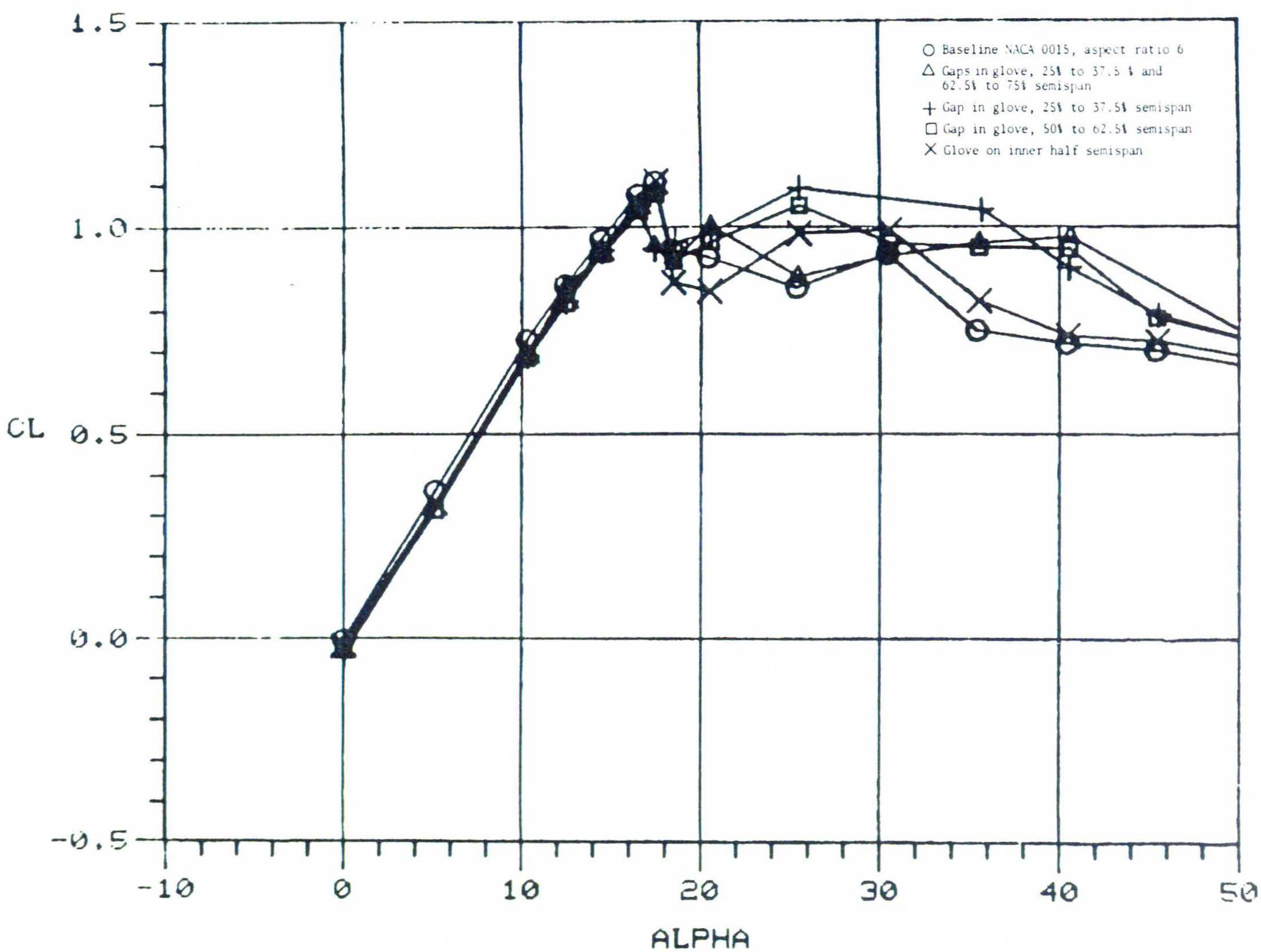

a) C_L for $\alpha = 0^{o}$ to 50^{o}

Figure 17 - Lift coefficient vs. α for NACA 0015 wing with various leading edge modifications, $Re_c = 2.0 \times 10^6$.

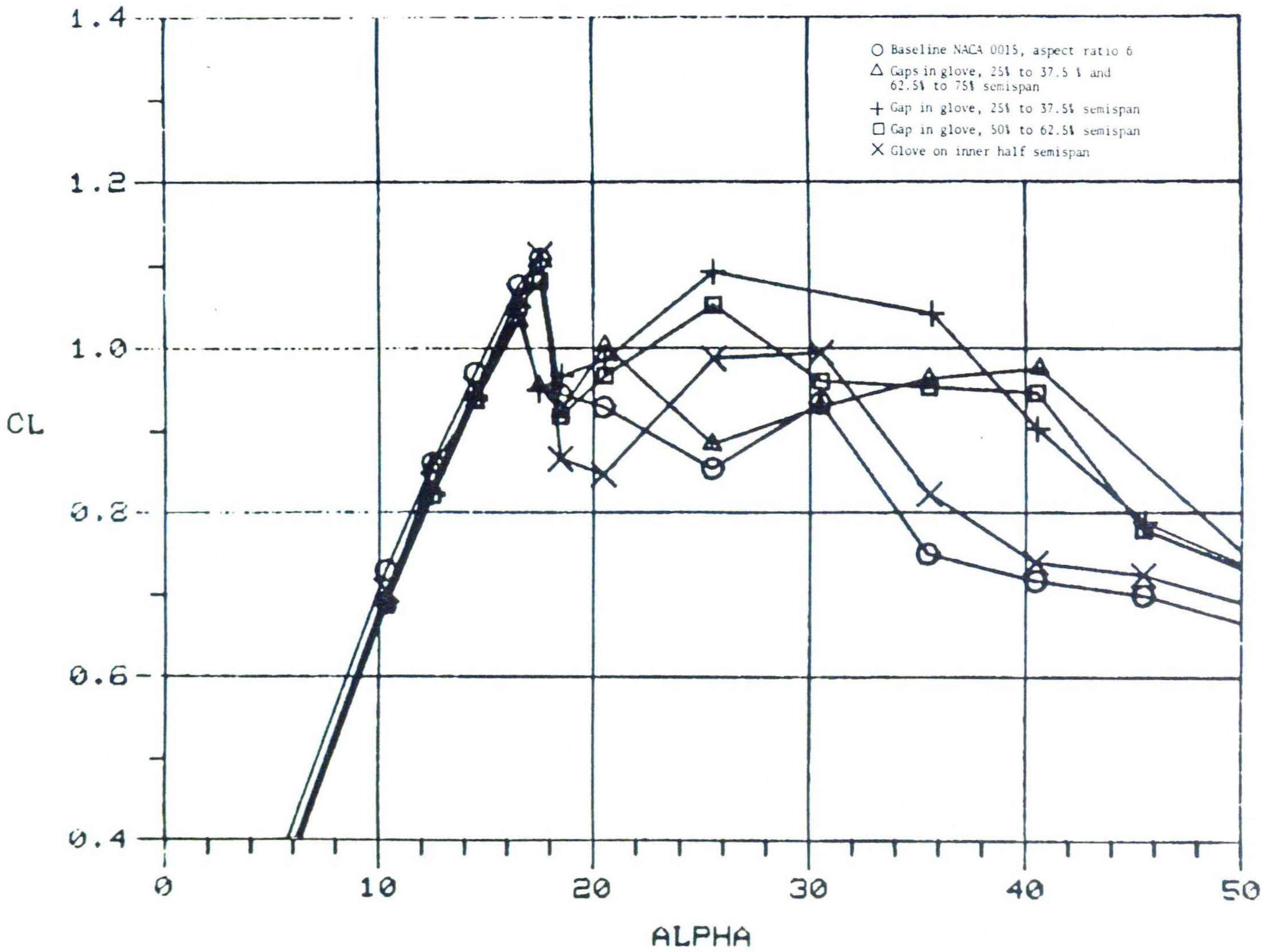

b) C_L expanded scale

Figure 17 - Concluded.

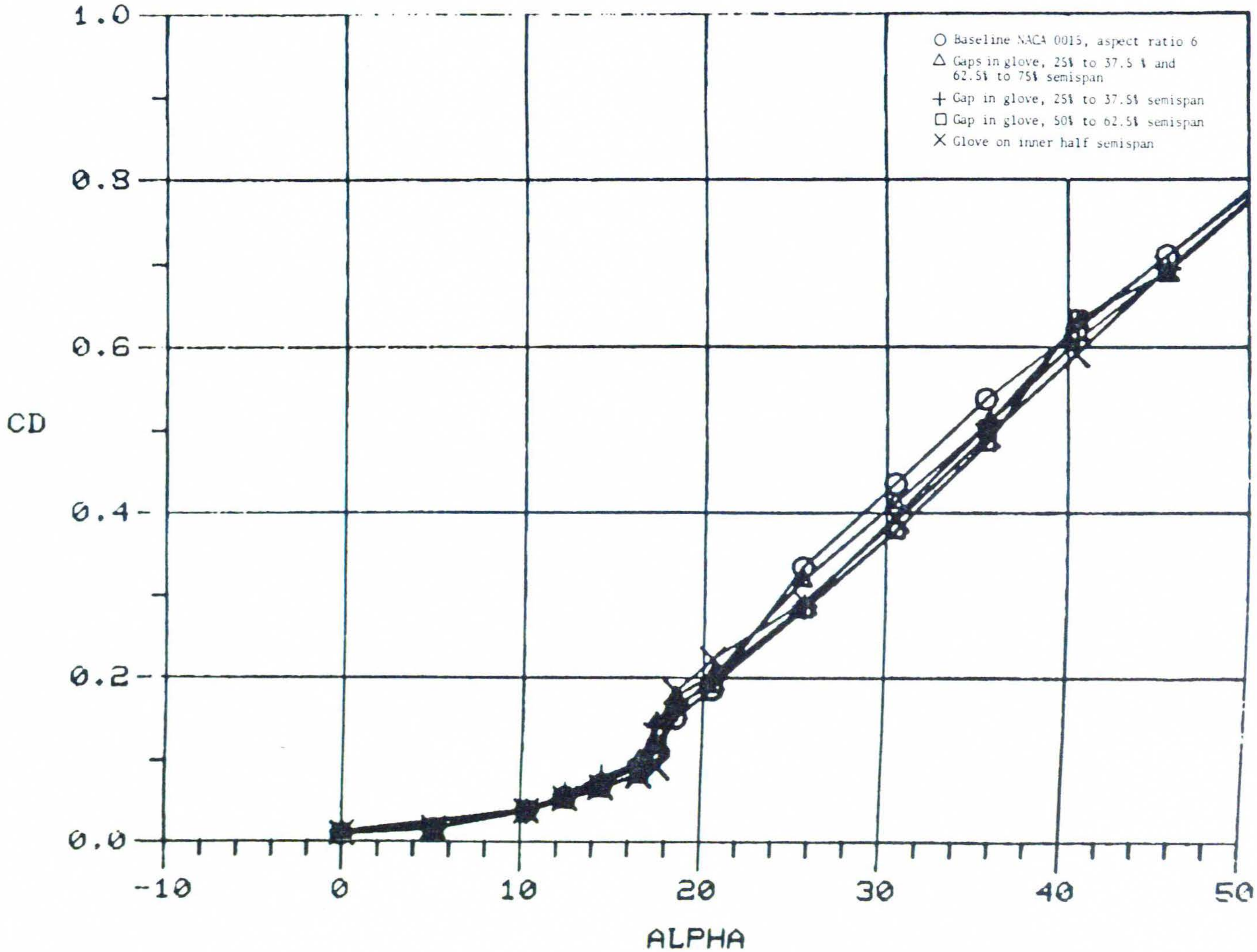

a) Data for $\alpha = 0^{o}$ to 50^{o}

Figure 18 - Drag coefficient vs. α for NACA 0015 wing with various leading edge modifications, $Re_c = 2.0 \times 10^6$.

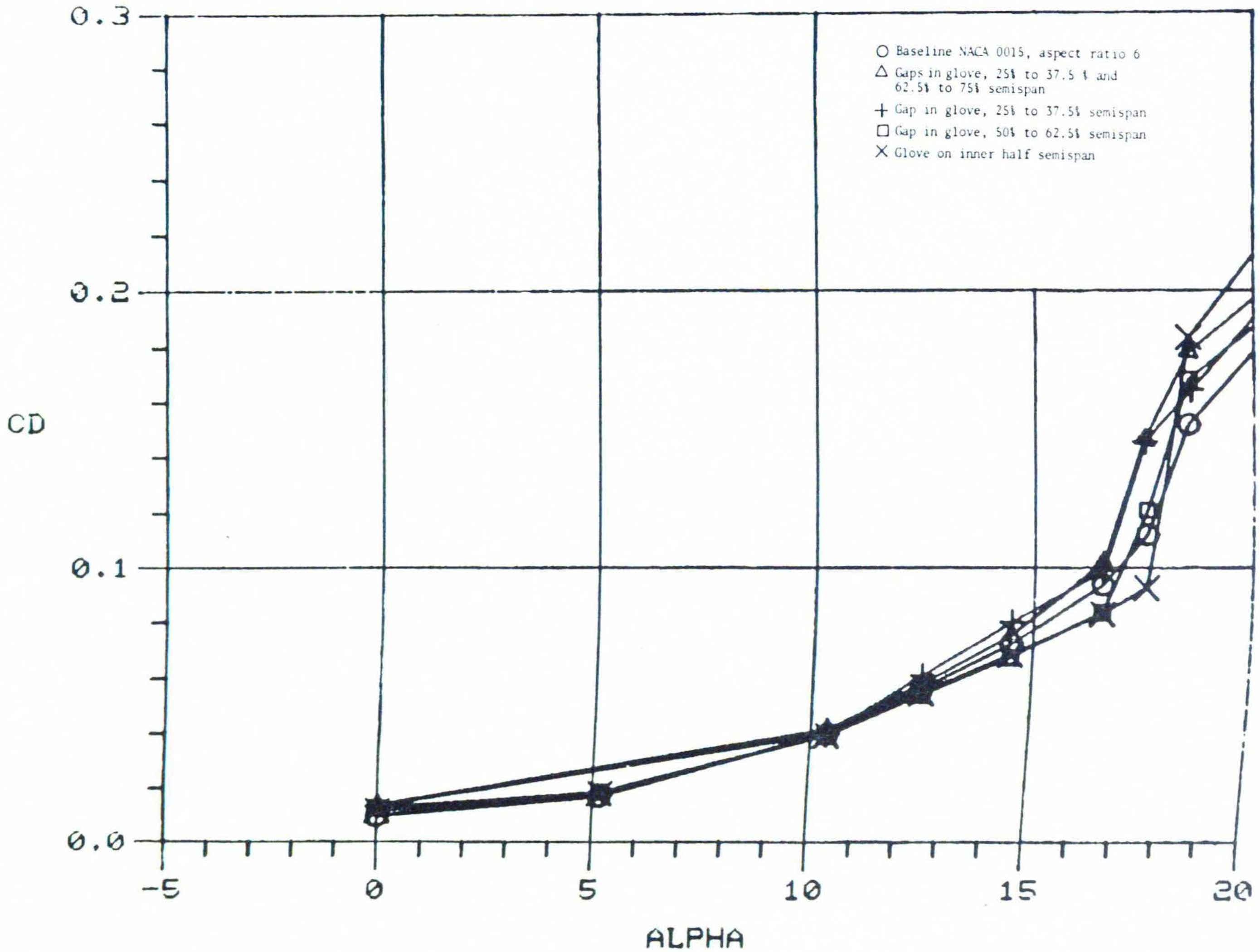

b) Data for $\alpha = 0^{\circ}$ to 20°

Figure 18 Concluded.

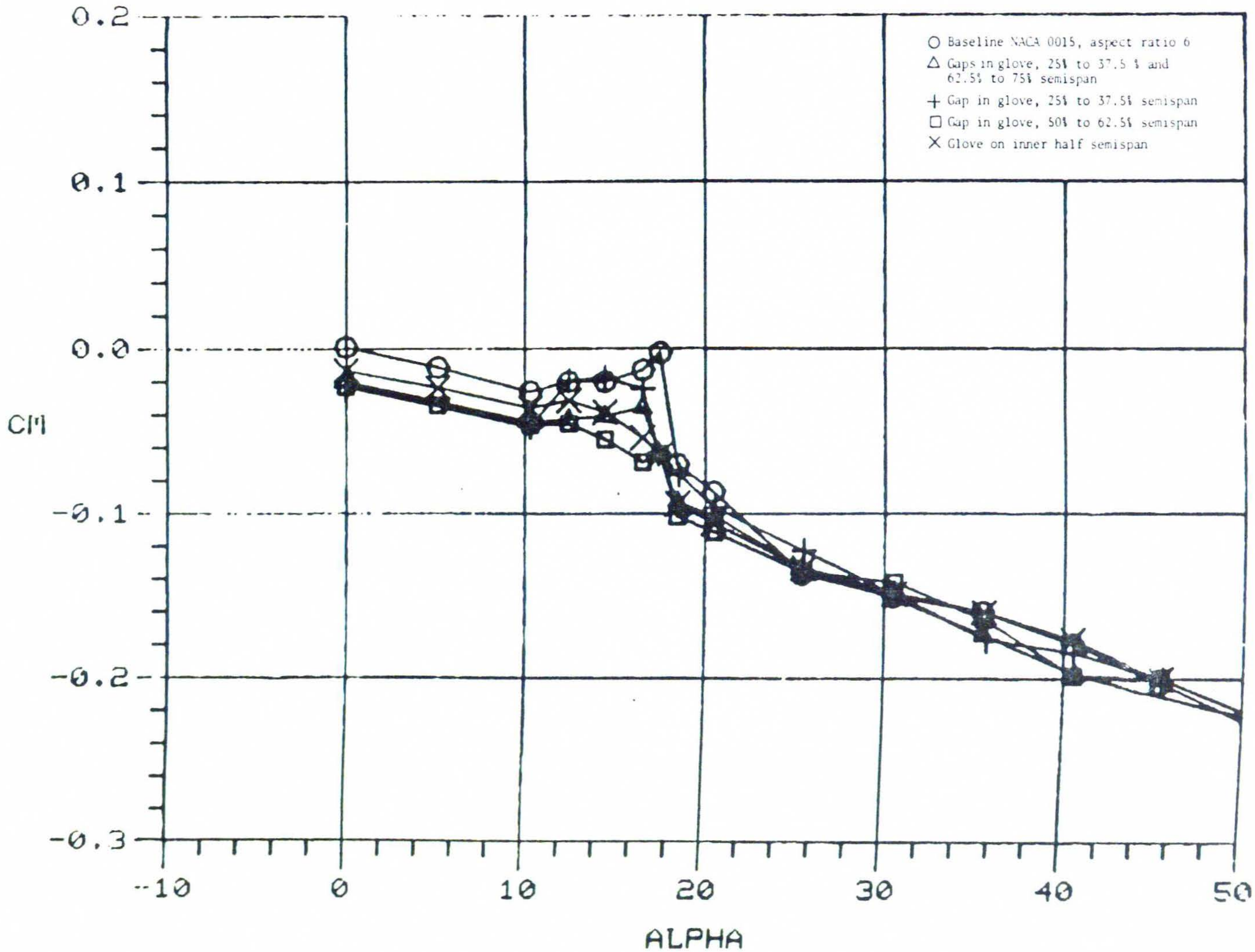

Figure 19 - Pitching moment coefficient vs. α for NACA 0015 wing with various leading edge modifications, $Re_c = 2.0 \times 10^6$.

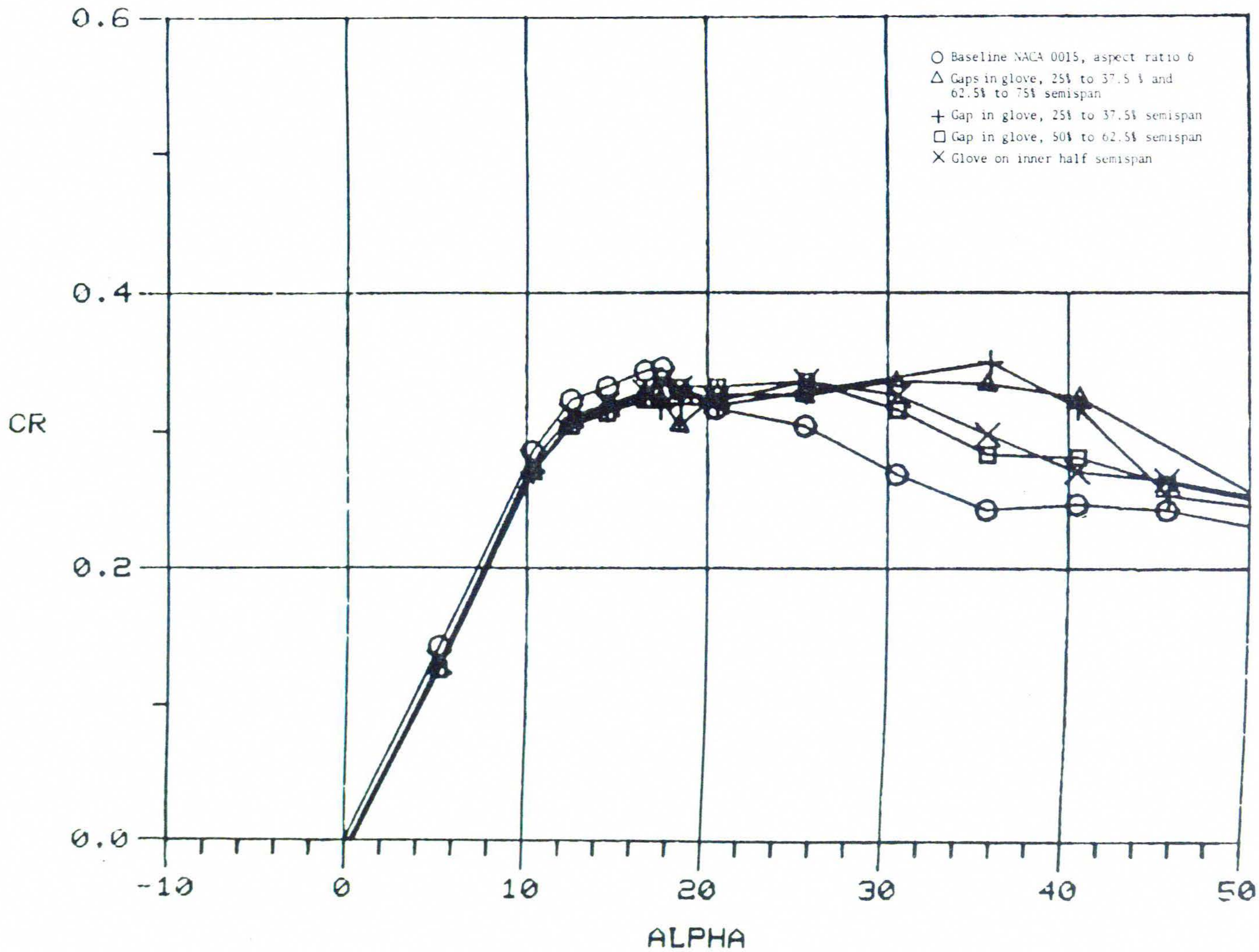

Figure 20 - Rolling moment coefficient vs. α for NACA 0015 wing with various leading edge modifications, $Re_c = 2.0 \times 10^6$.

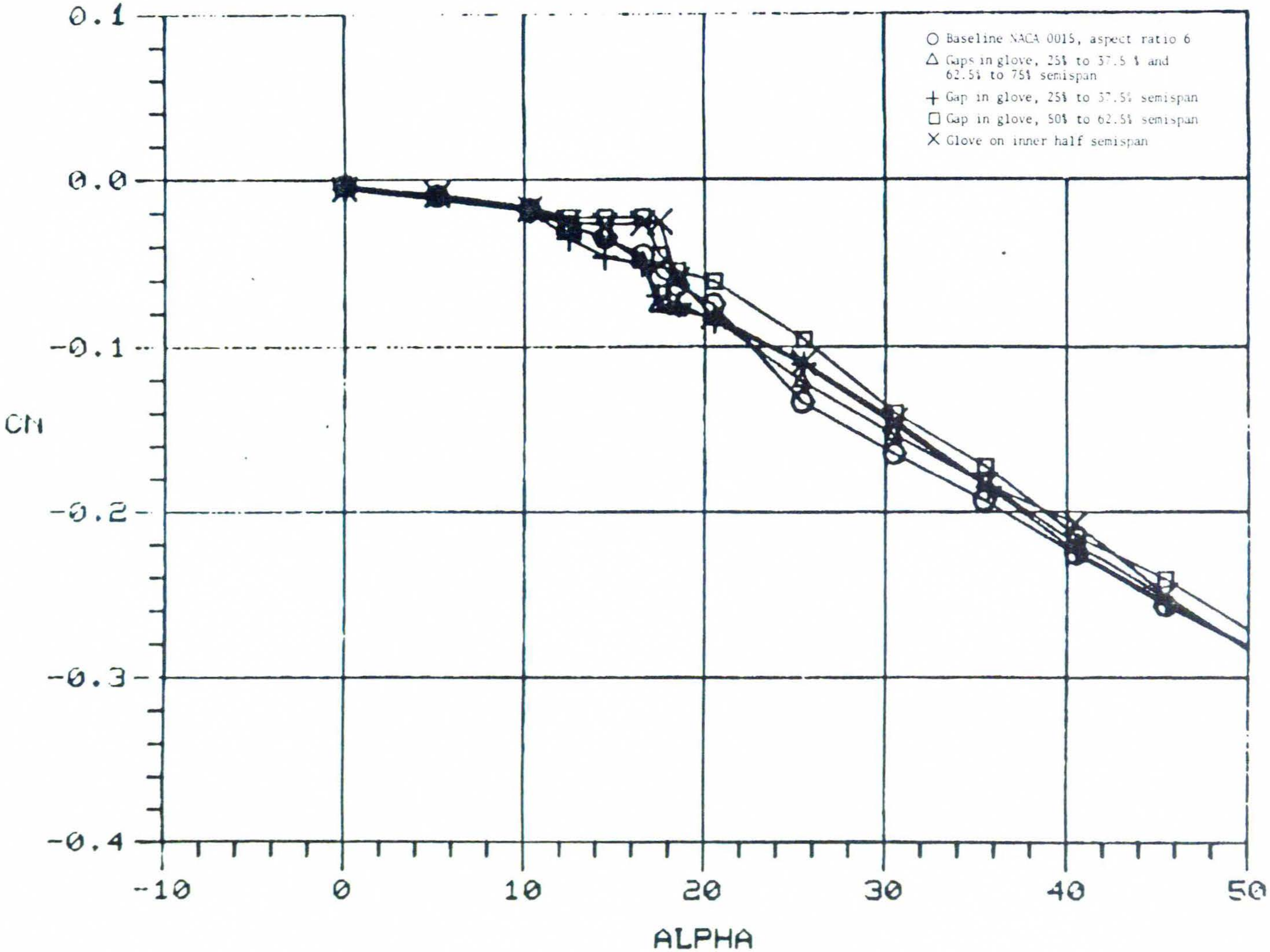

Figure 21 - Yawing moment coefficient vs. α for NACA 0015 wing with various leading edge modifications, $Re_c = 2.0 \times 10^6$.

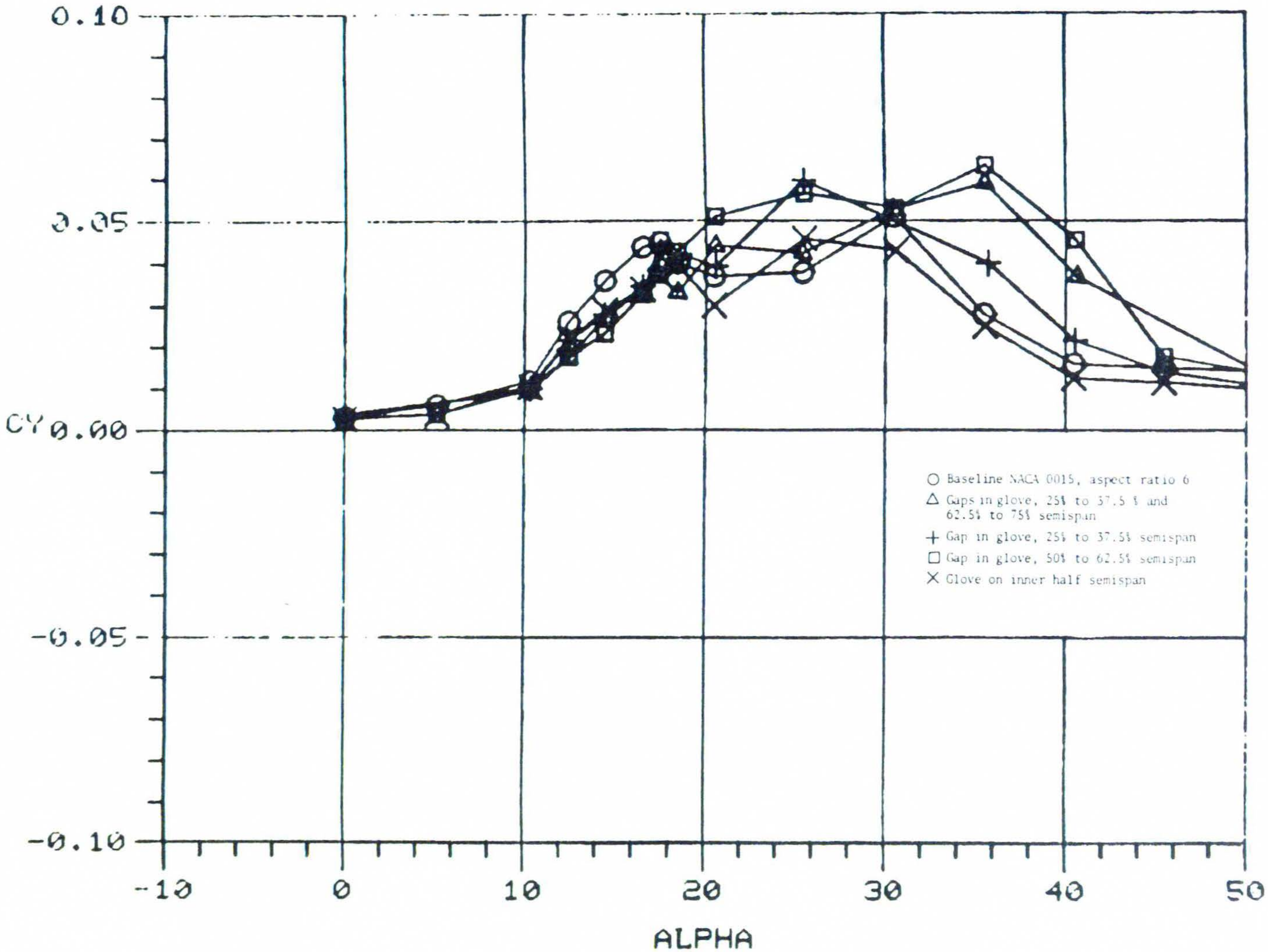

Figure 22 - Side force coefficient vs. α for NACA 0015 wing with various leading edge modifications, $Re_c = 2.0 \times 10^6$.

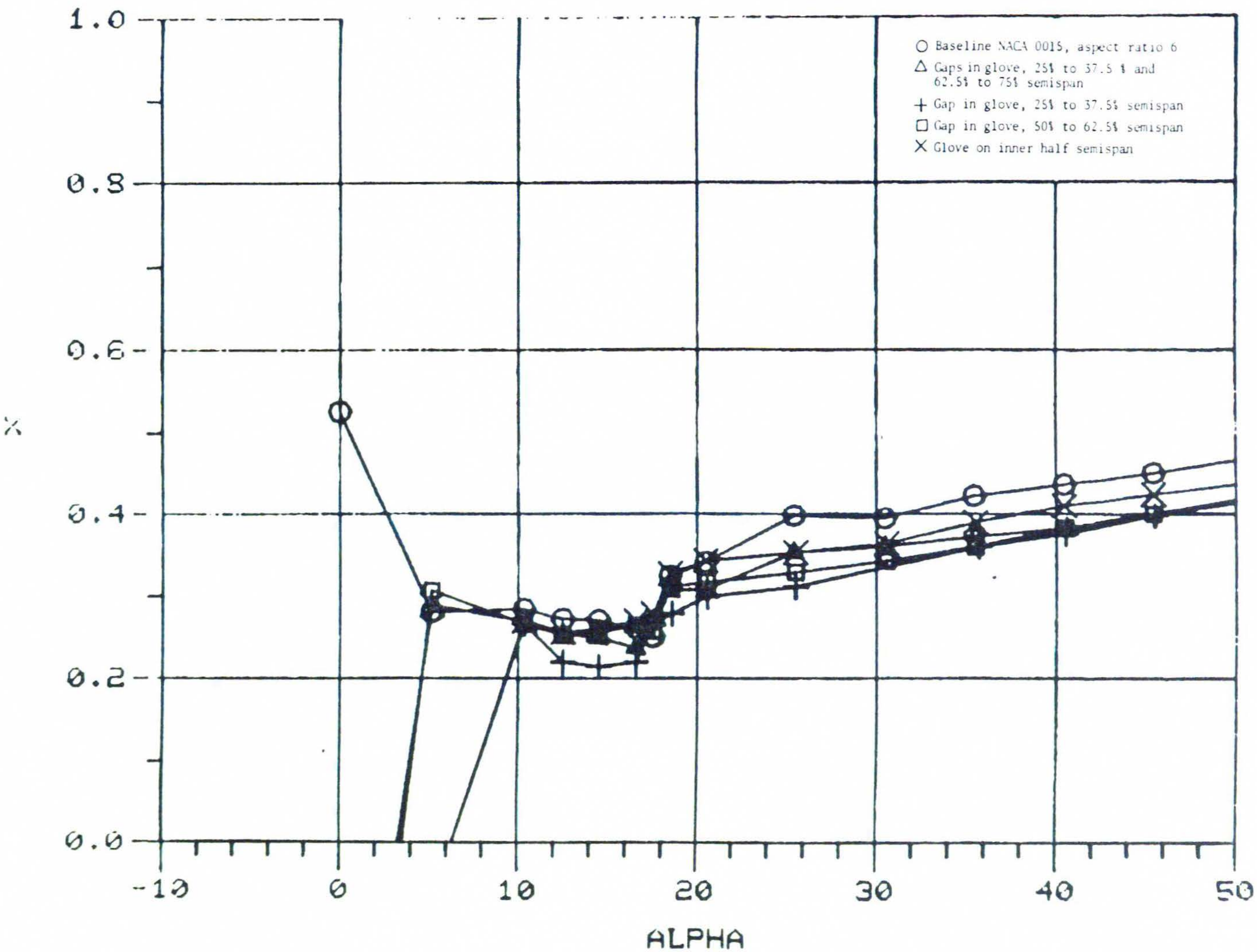

a) Chordwise location of center of pressure

Figure 23 - Center of force location vs. α for NACA 0015 wing with various leading edge modifications, $Re_c = 2.0 \times 10^6$.

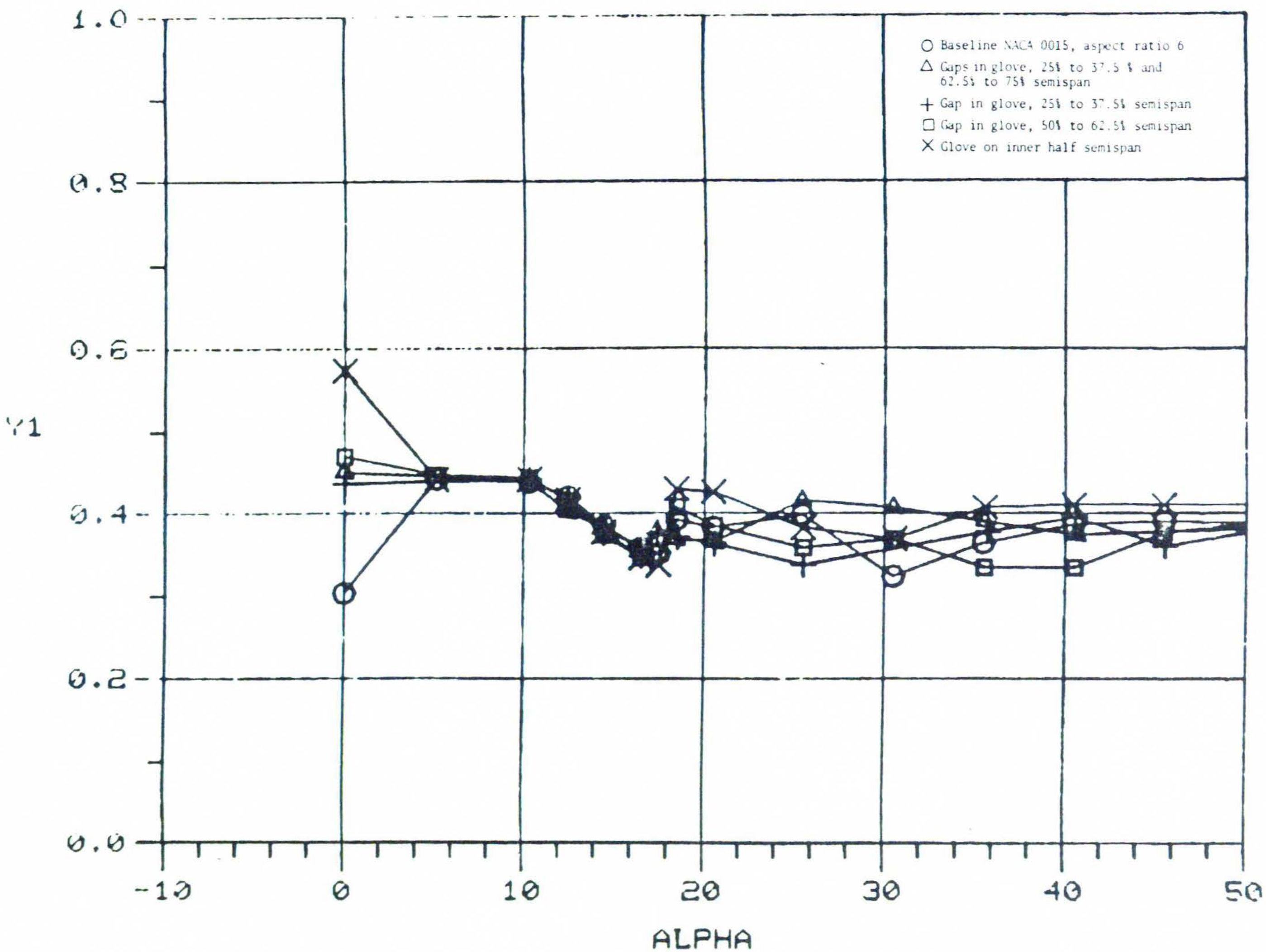

b) Spanwise location of center of lift

Figure 23 - Continued.

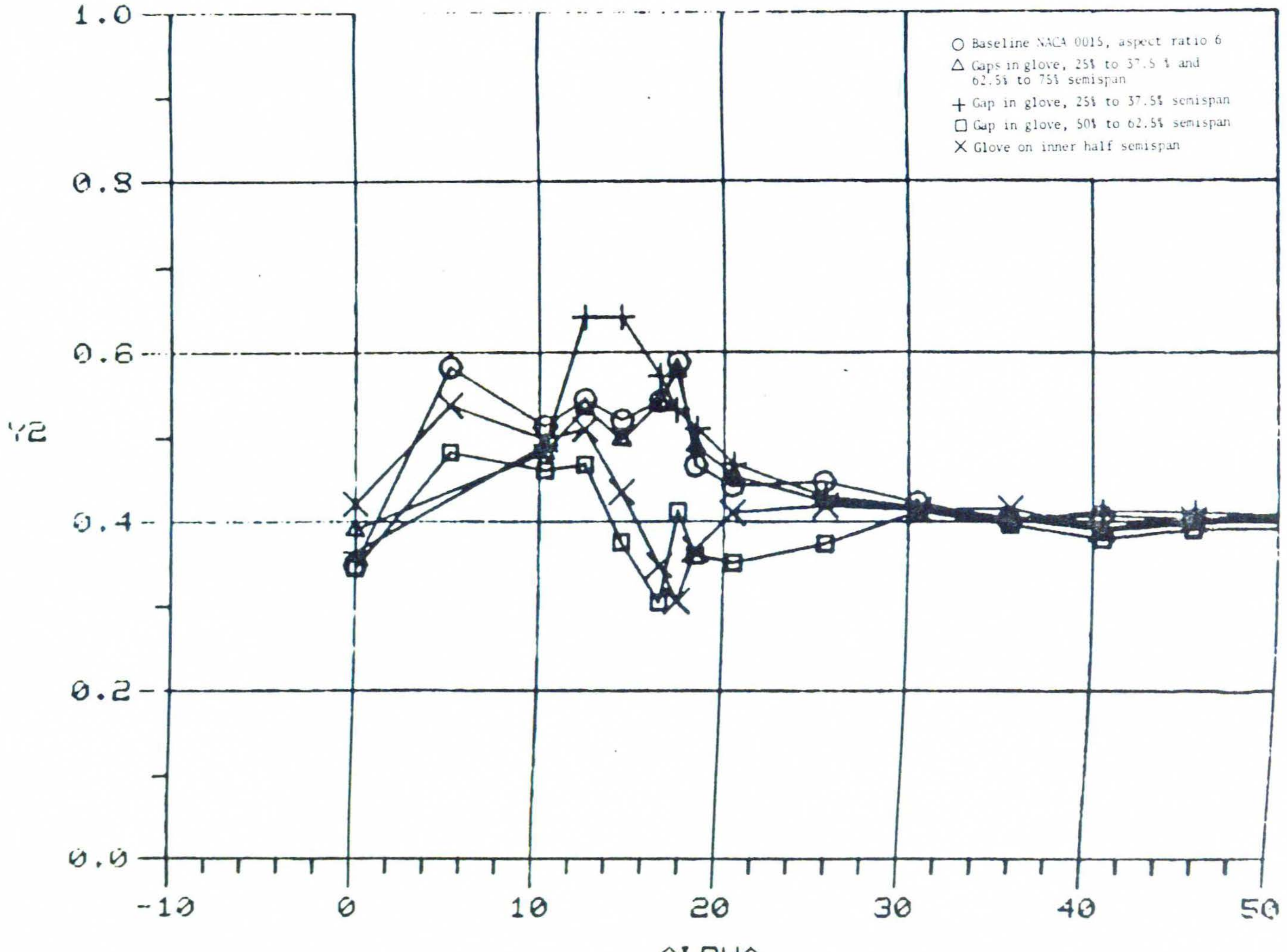

c) Spanwise location of center of drag

Figure 23 - Concluded.

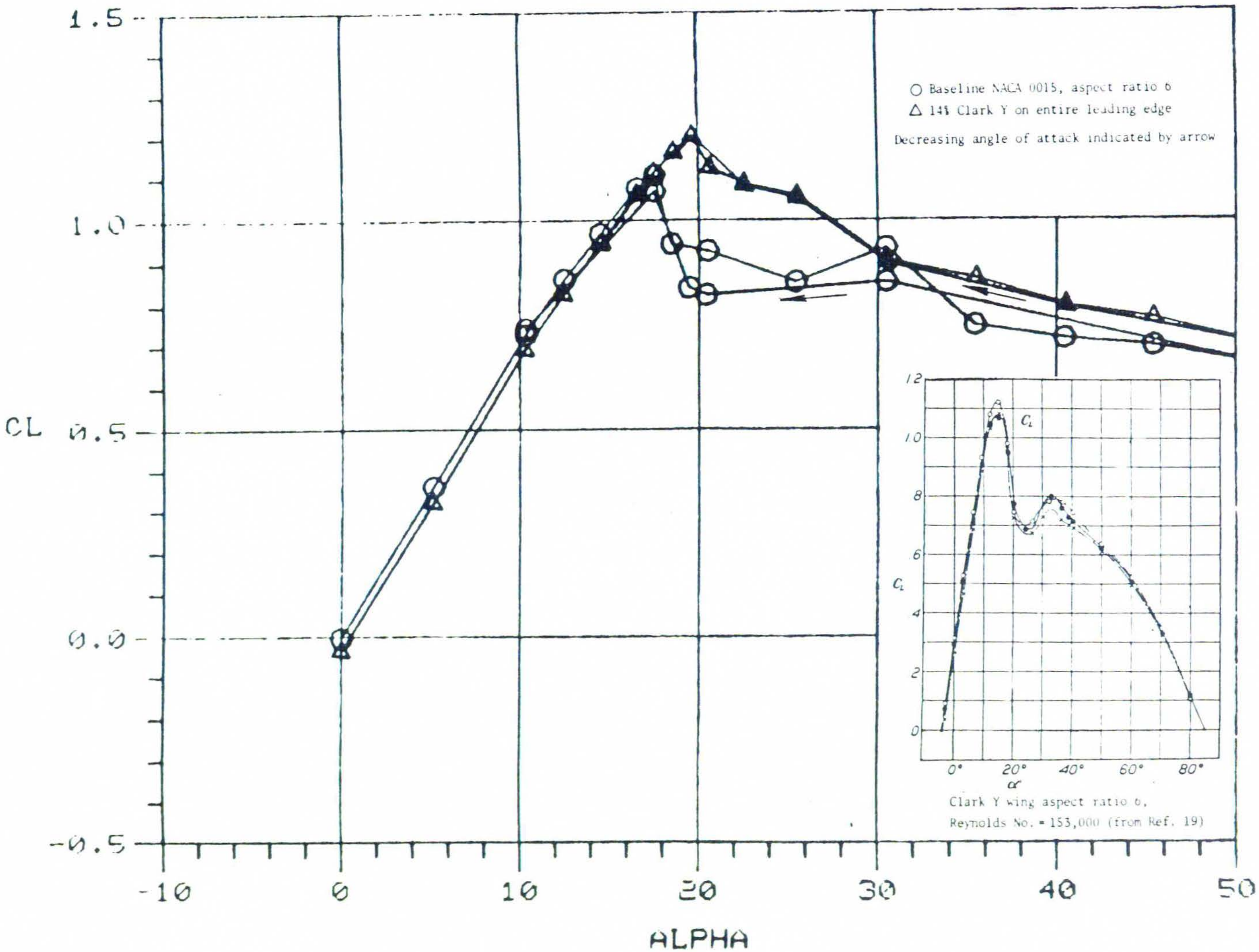

a) C_L for $\alpha = 0^{\circ}$ to 50°

Figure 24 - Lift coefficient vs. α (including hysteresis) for NACA 0015 wing with various leading edge modifications, $Re_c = 2.0 \times 10^6$.

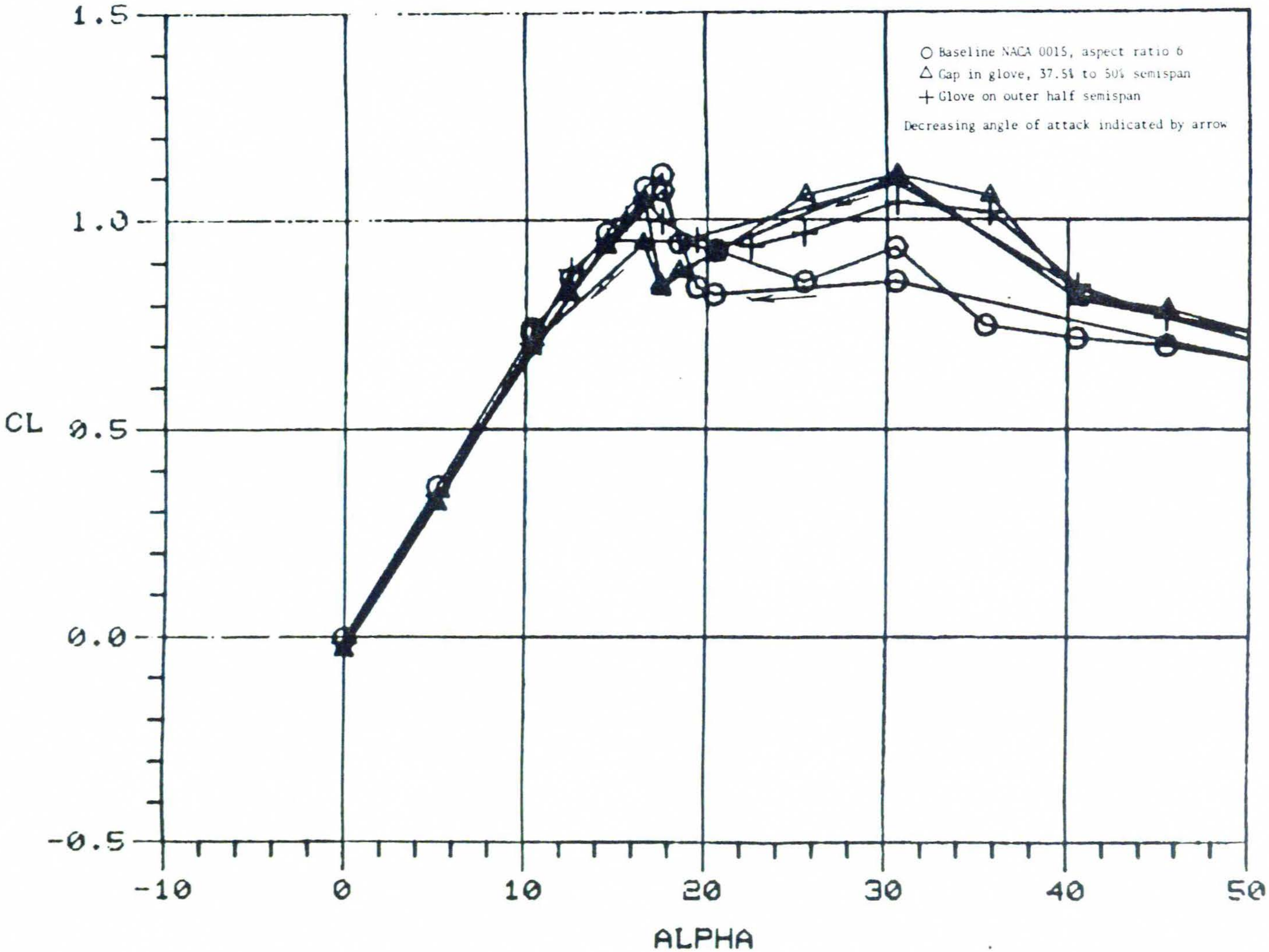

a) Concluded.

Figure 24 - Continued.

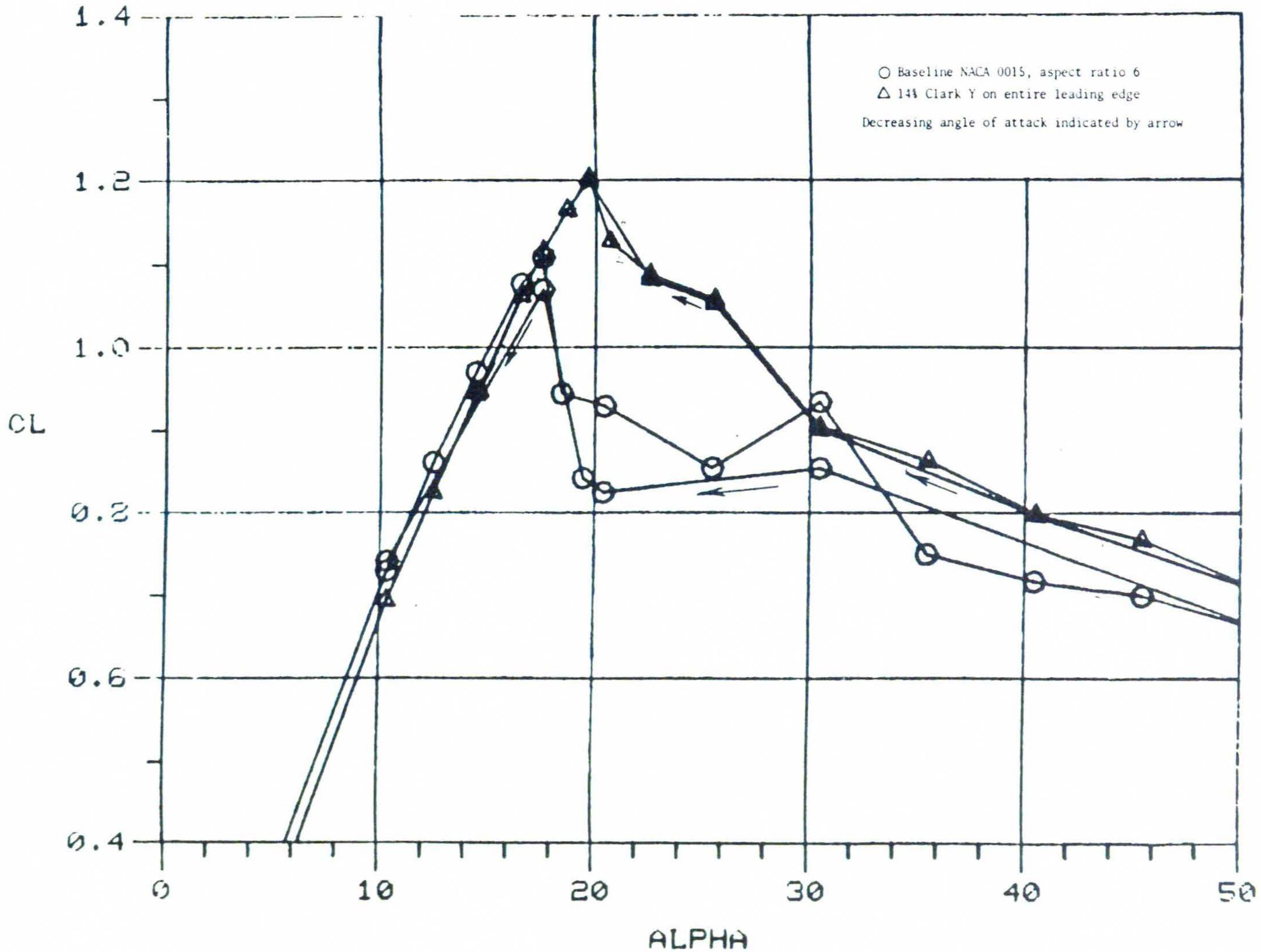

b) C_L expanded scale.

Figure 24 - Continued.

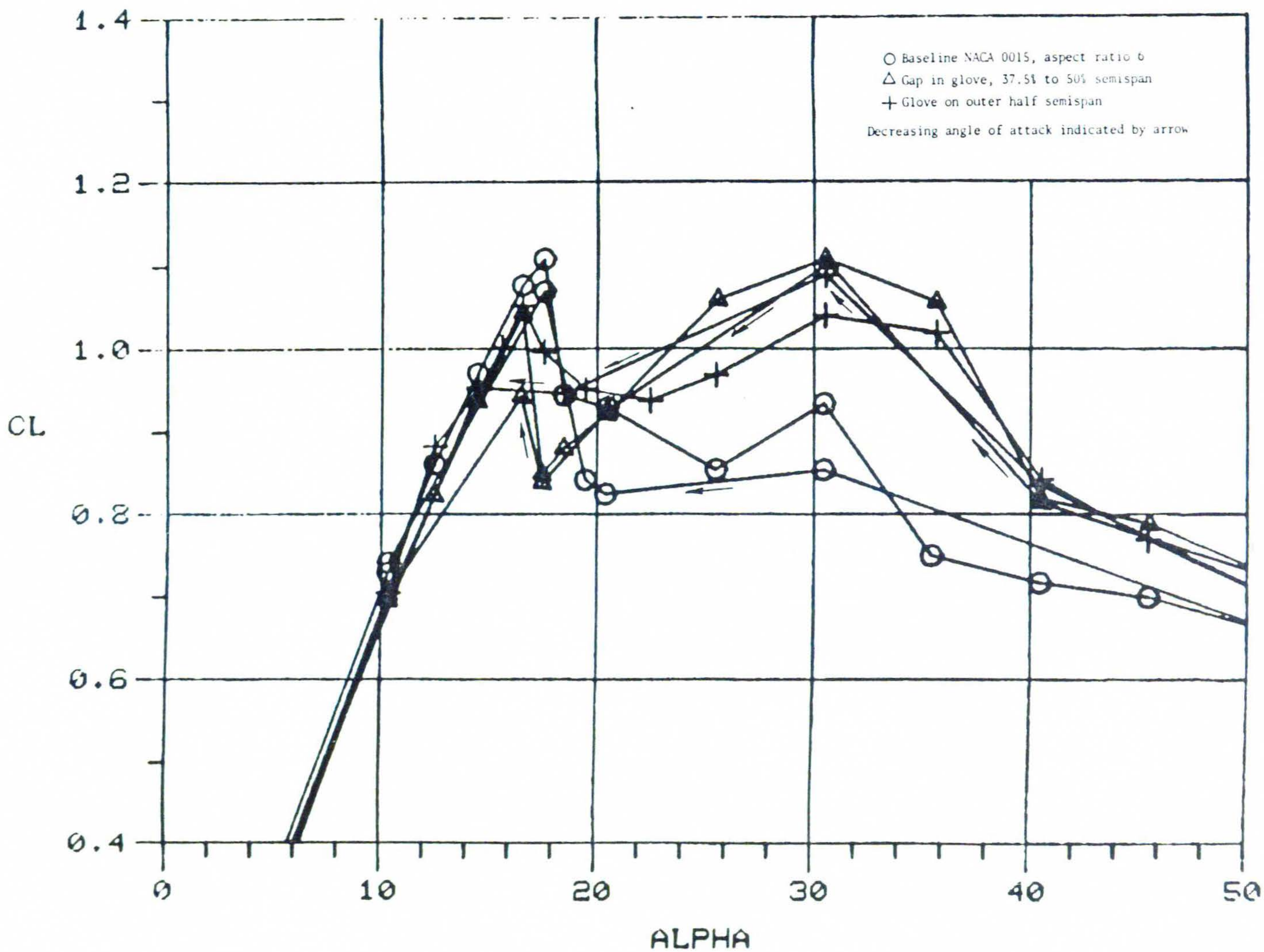

b) Concluded.

Figure 24 - Concluded.

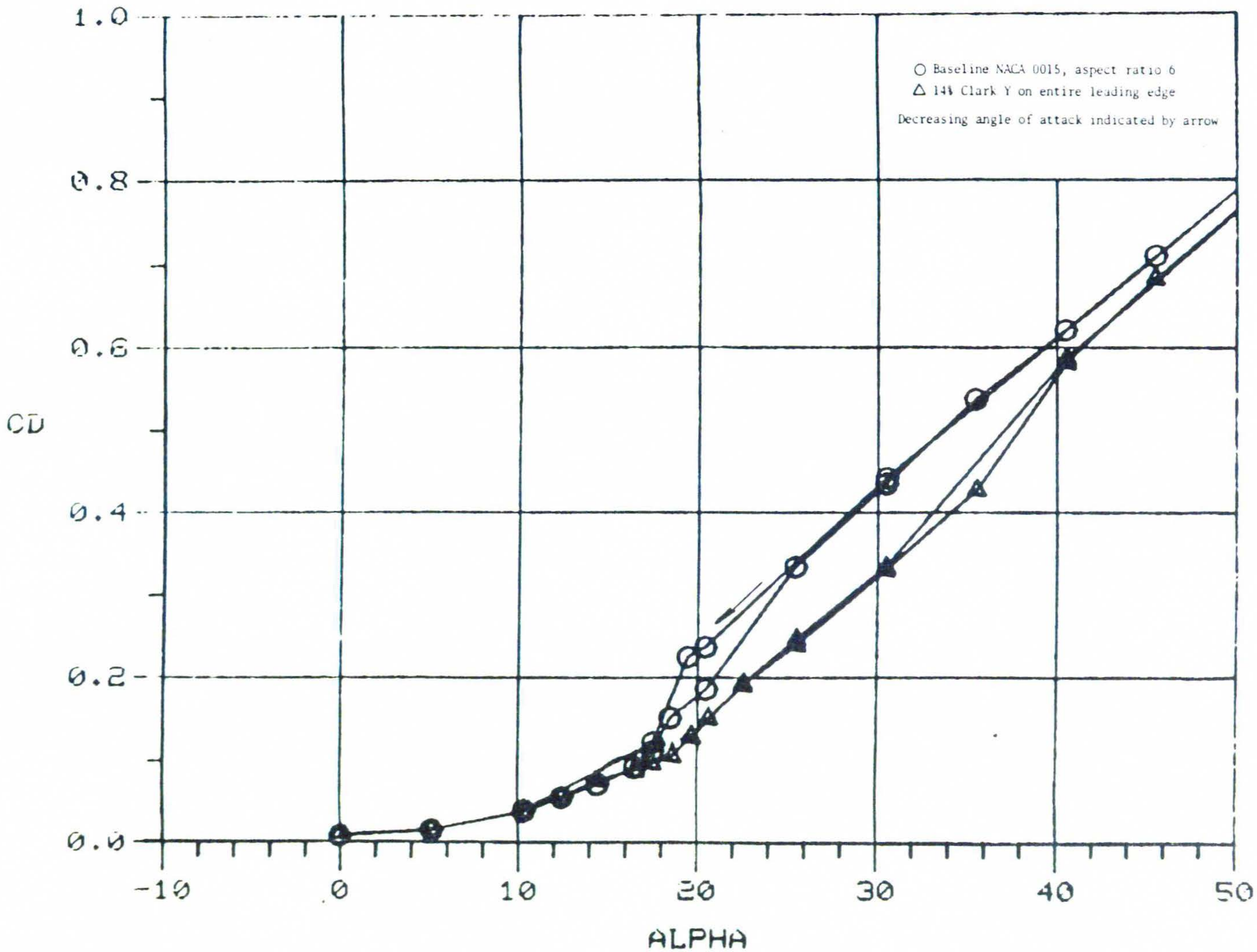

a) Data for $\alpha = 0^o$ to 50^o

Figure 25 - Drag coefficient vs. α (including hysteresis) for NACA 0015 wing with various leading edge modifications, $Re_c = 2.0 \times 10^6$.

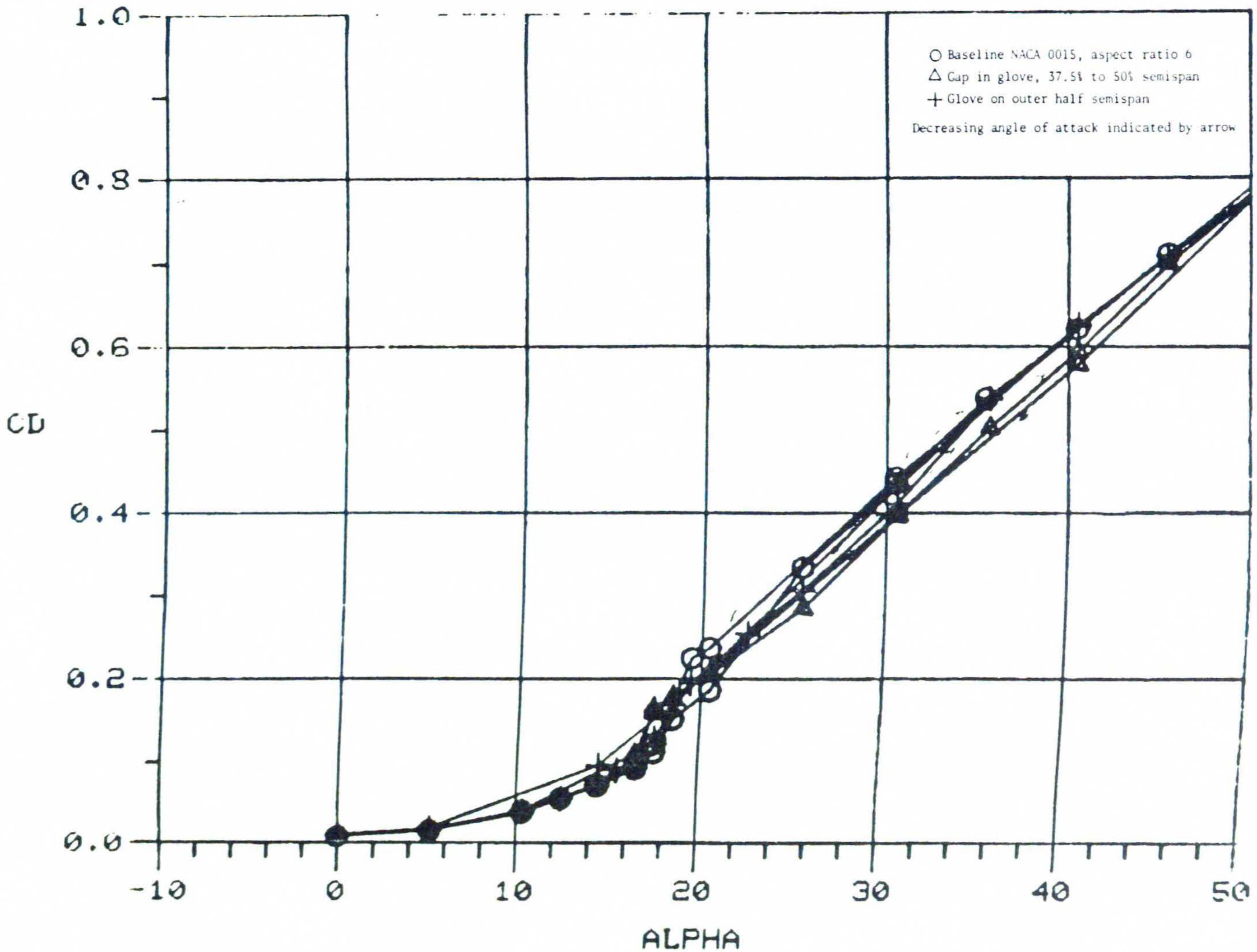

a) Concluded

Figure 25 - Continued.

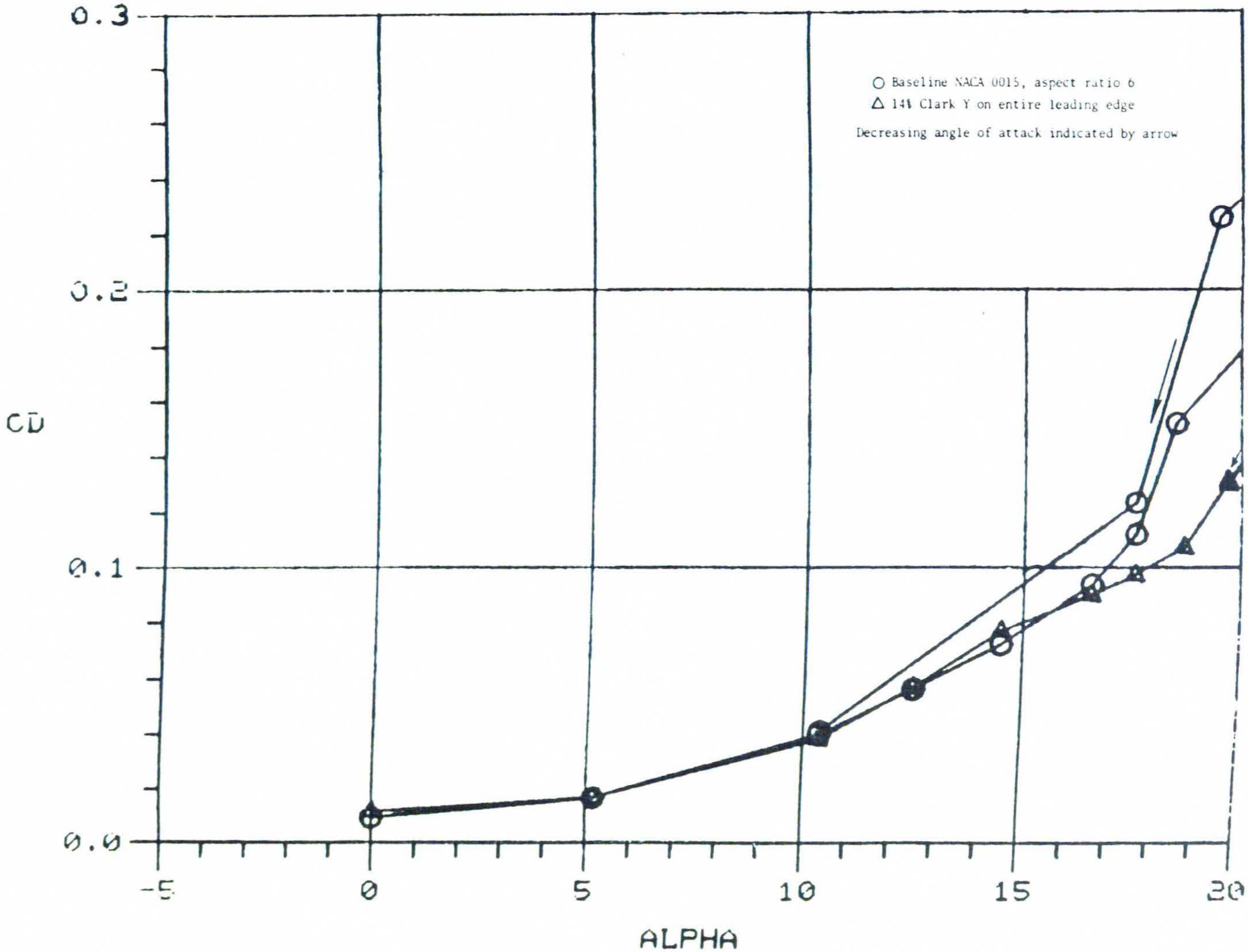

b) Data for $\alpha = 0^{\circ}$ to 20°

Figure 25 - Continued.

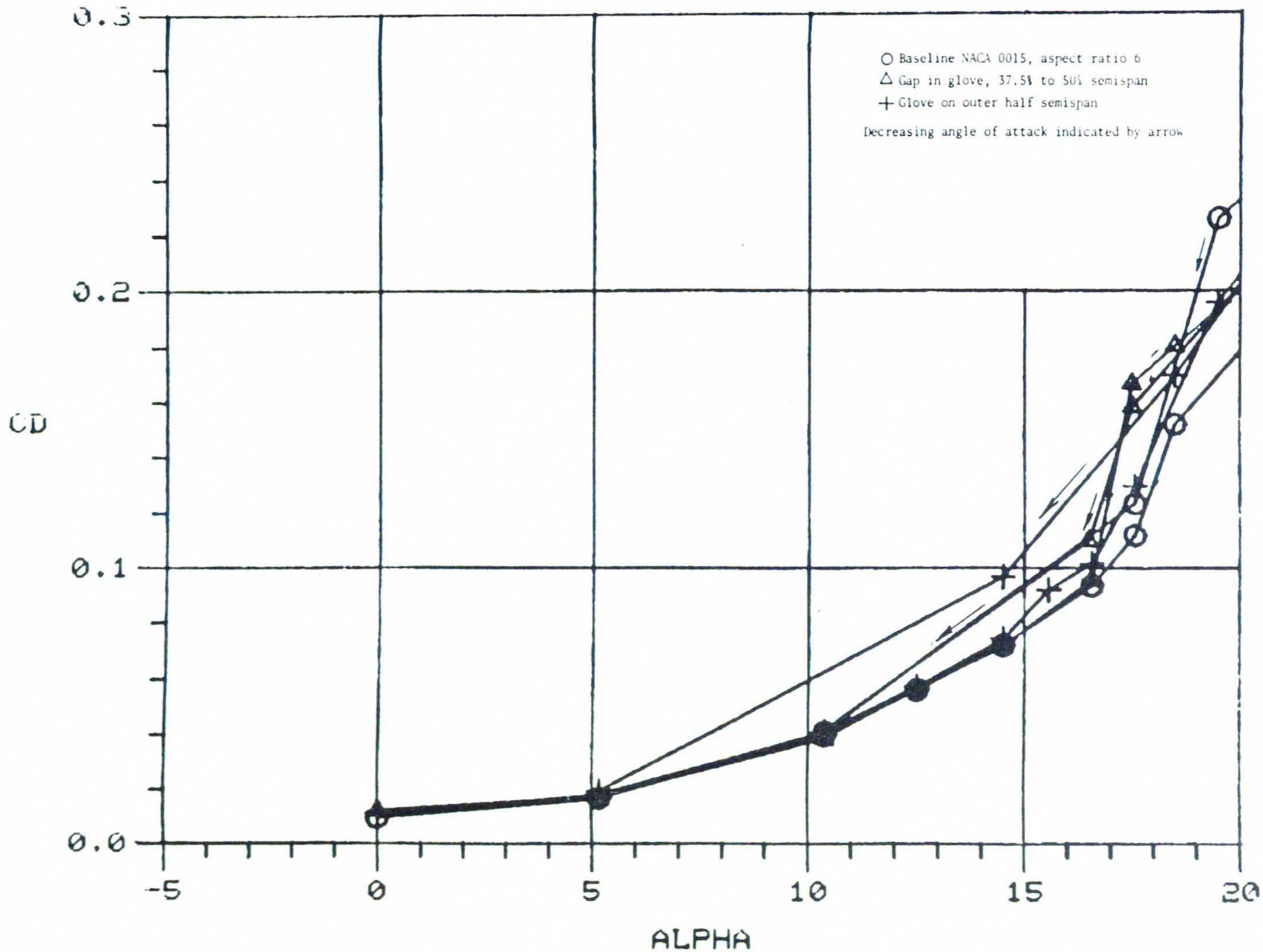

b) Concluded

Figure 25 - Concluded.

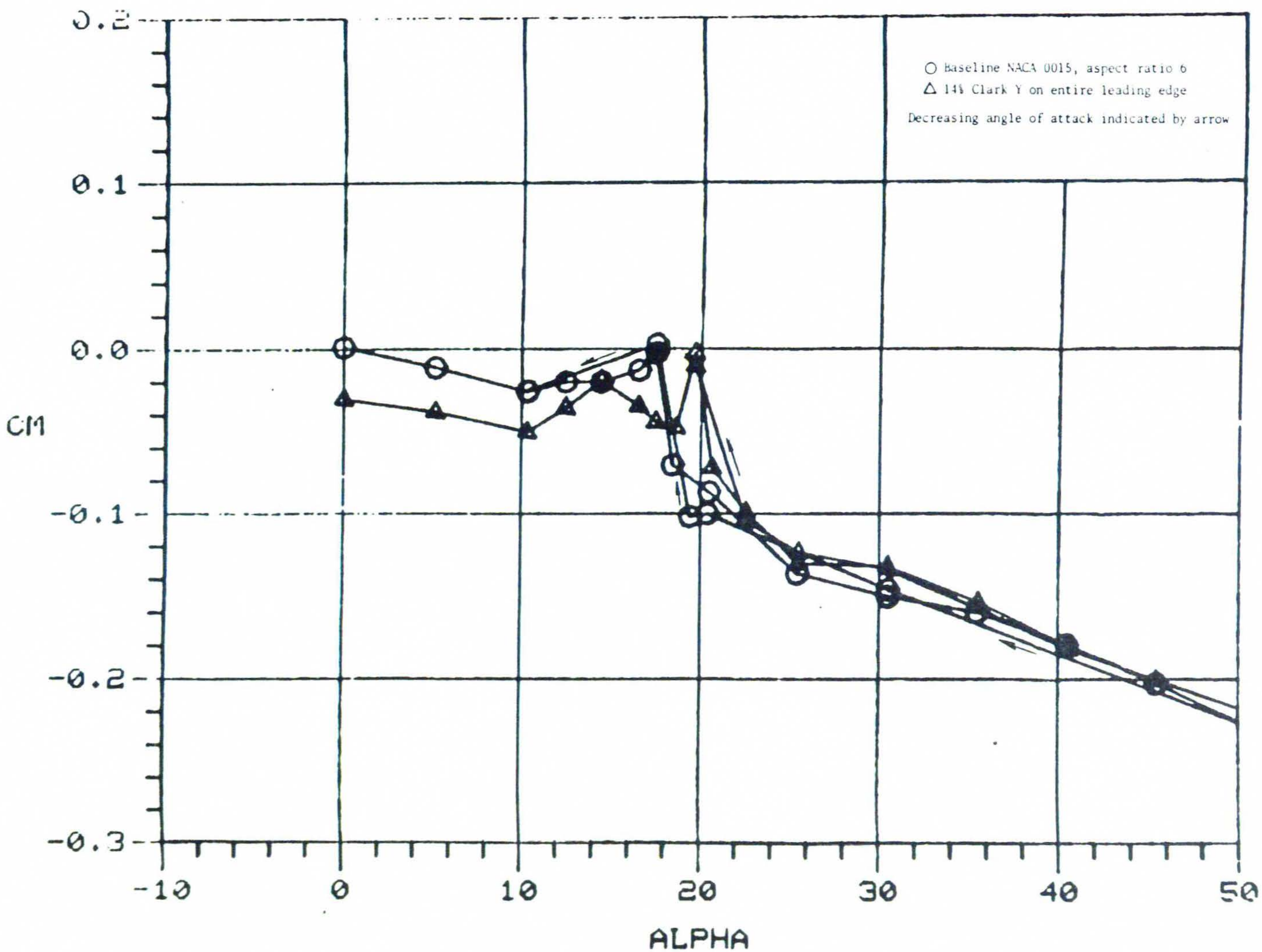

Figure 26 - Pitching moment coefficient vs. α (including hysteresis) for NACA 0015 wing with various leading edge modifications, $Re_c = 2.0 \times 10^6$.

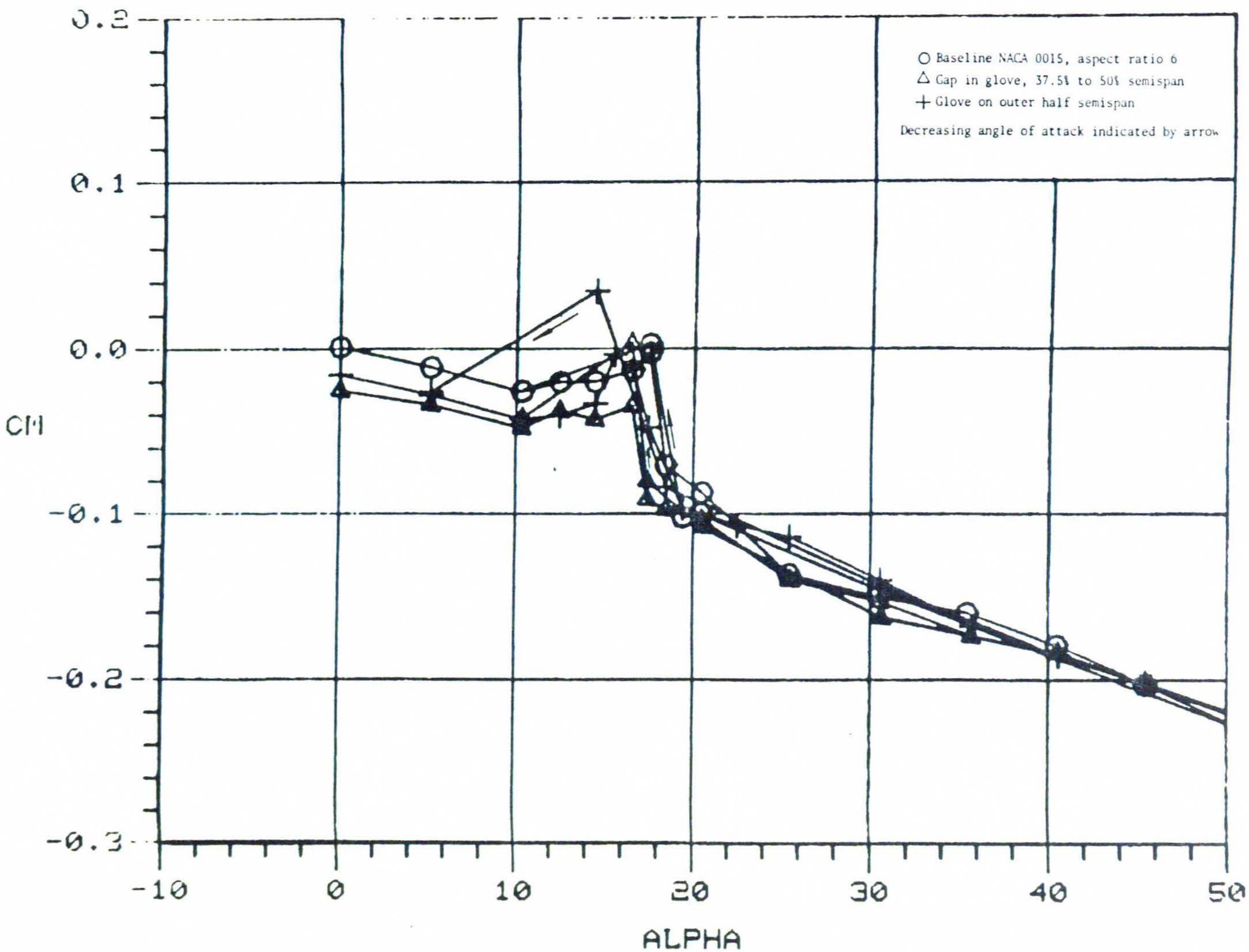

Figure 26 - Concluded.

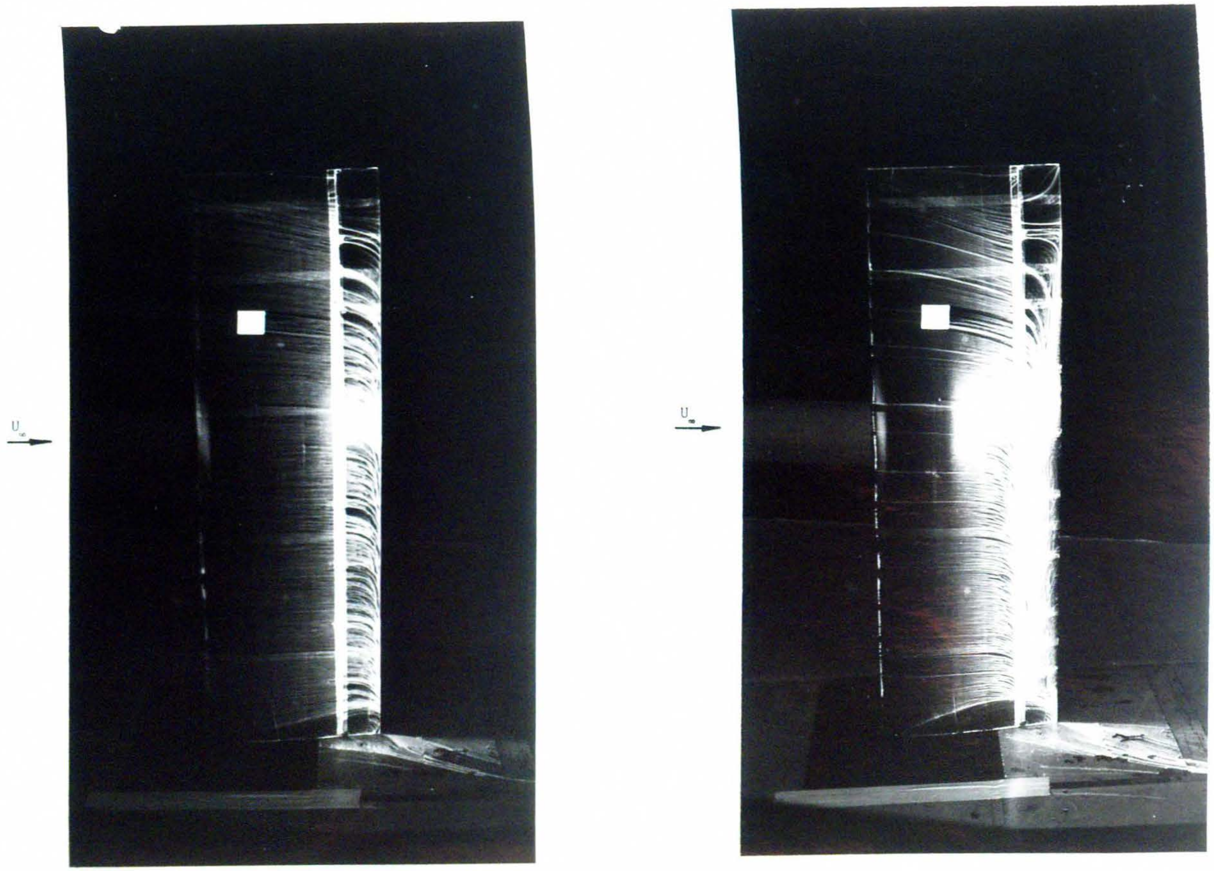

a) $\alpha = 10^{\circ}$

b) $\alpha = 16.5^{\circ}$

Figure 27 - Oil flow patterns on NACA 0015 wing at various angles of attack, $Re_c = 2.0 \times 10^6$.

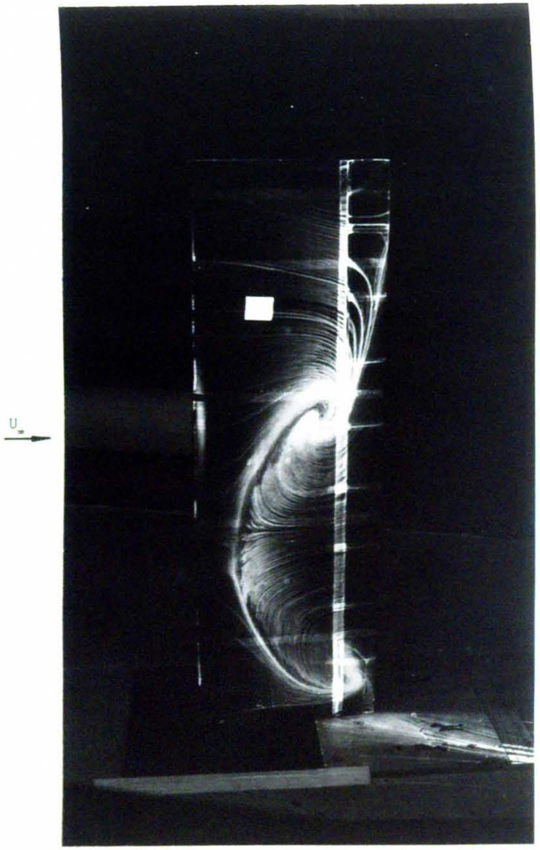

c) $\alpha = 18.5^{\circ}$

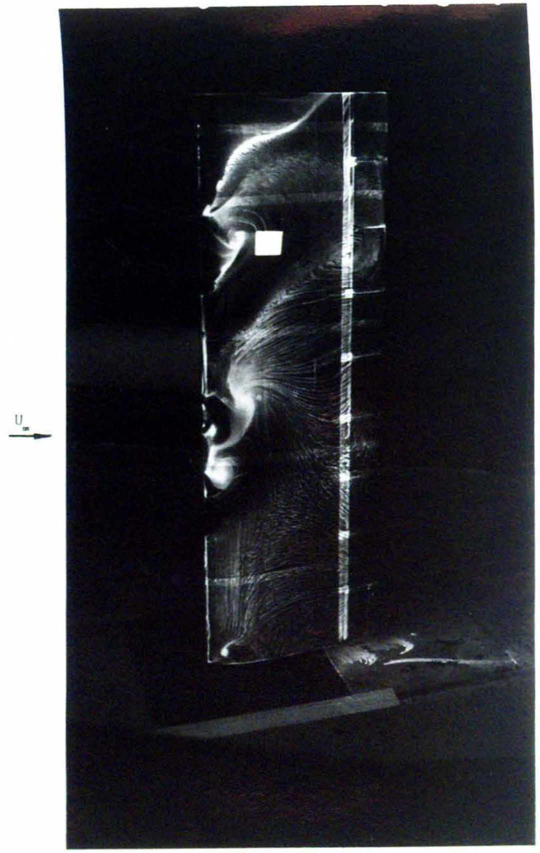

d) $\alpha = 30^{\circ}$

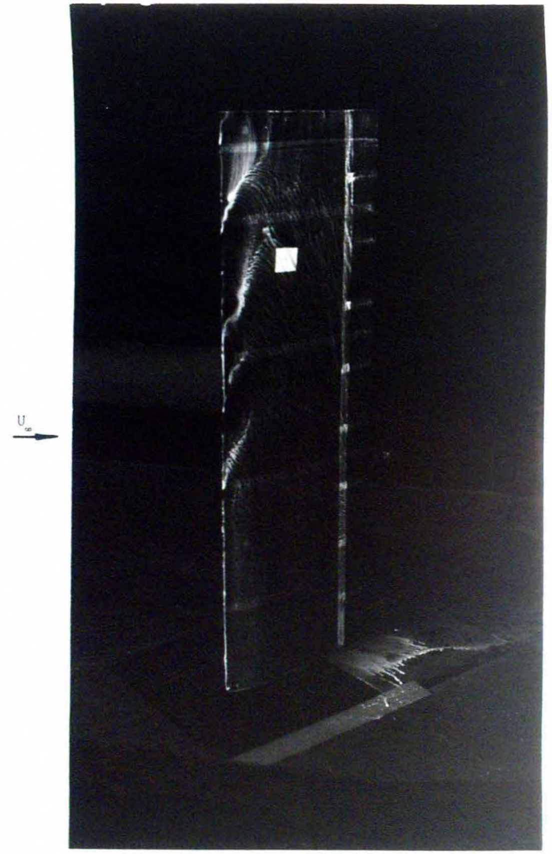

e) $\alpha = 50^{\circ}$

Figure 27 - Concluded.

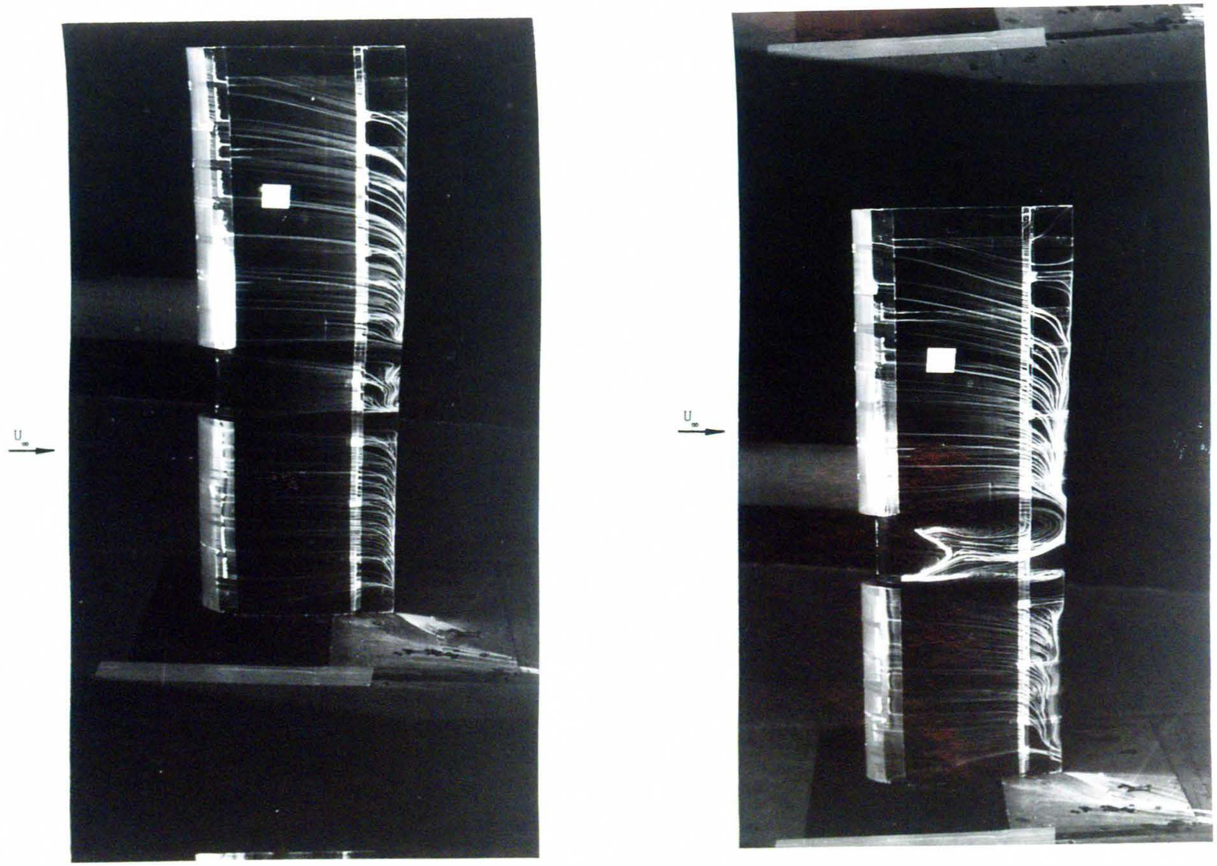

a) $\alpha = 10^{\circ}$

b) $\alpha = 16.5^{\circ}$

Figure 28 - Oil flow patterns on NACA 0015 wing with glove on entire leading edge except at 37.5% to 50% semispan, $Re_c = 2.0 \times 10^6$.

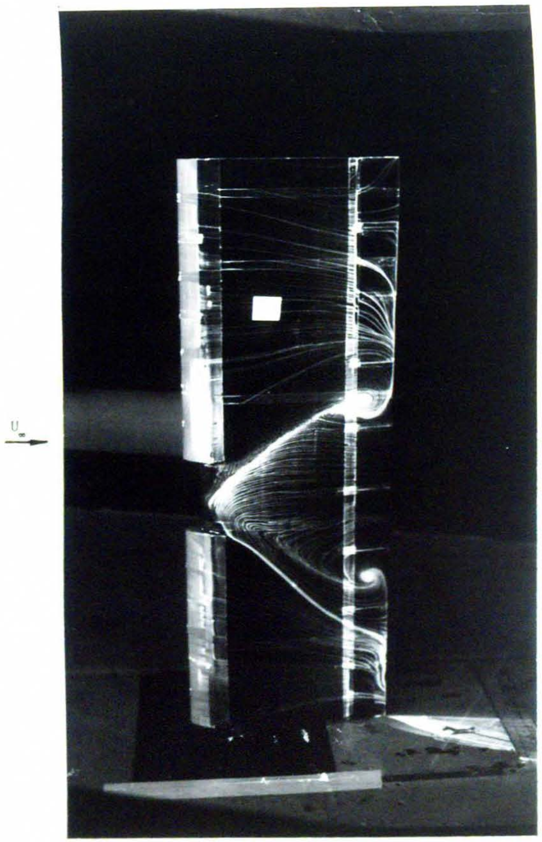

c) $\alpha = 18.5^\circ$

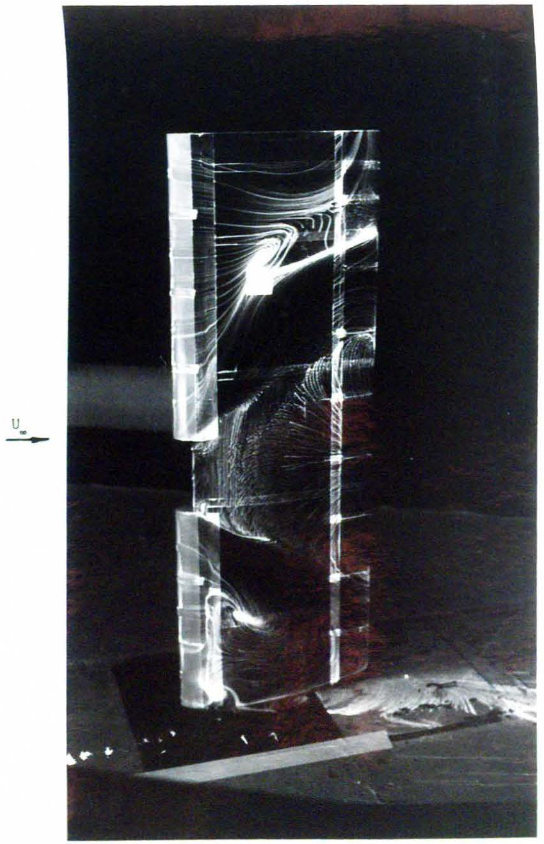

d) $\alpha = 30^\circ$

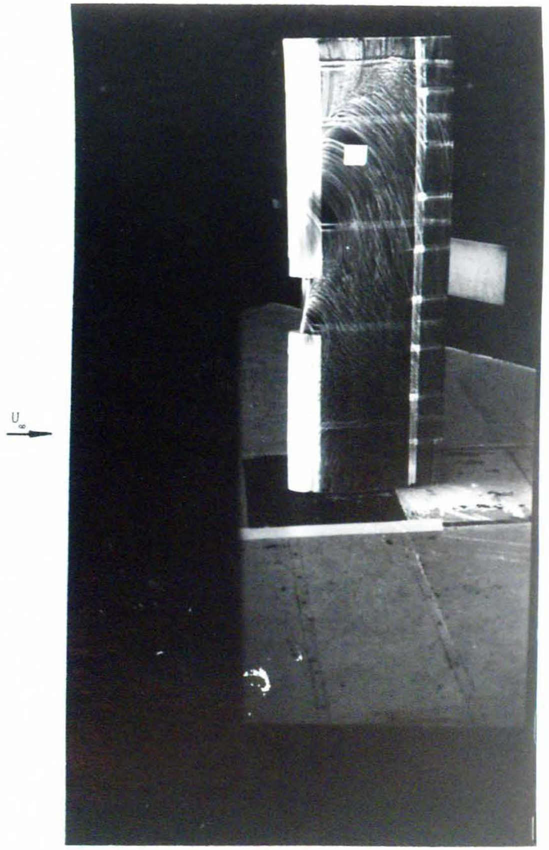

e) $\alpha = 50^\circ$

Figure 28 - Concluded.

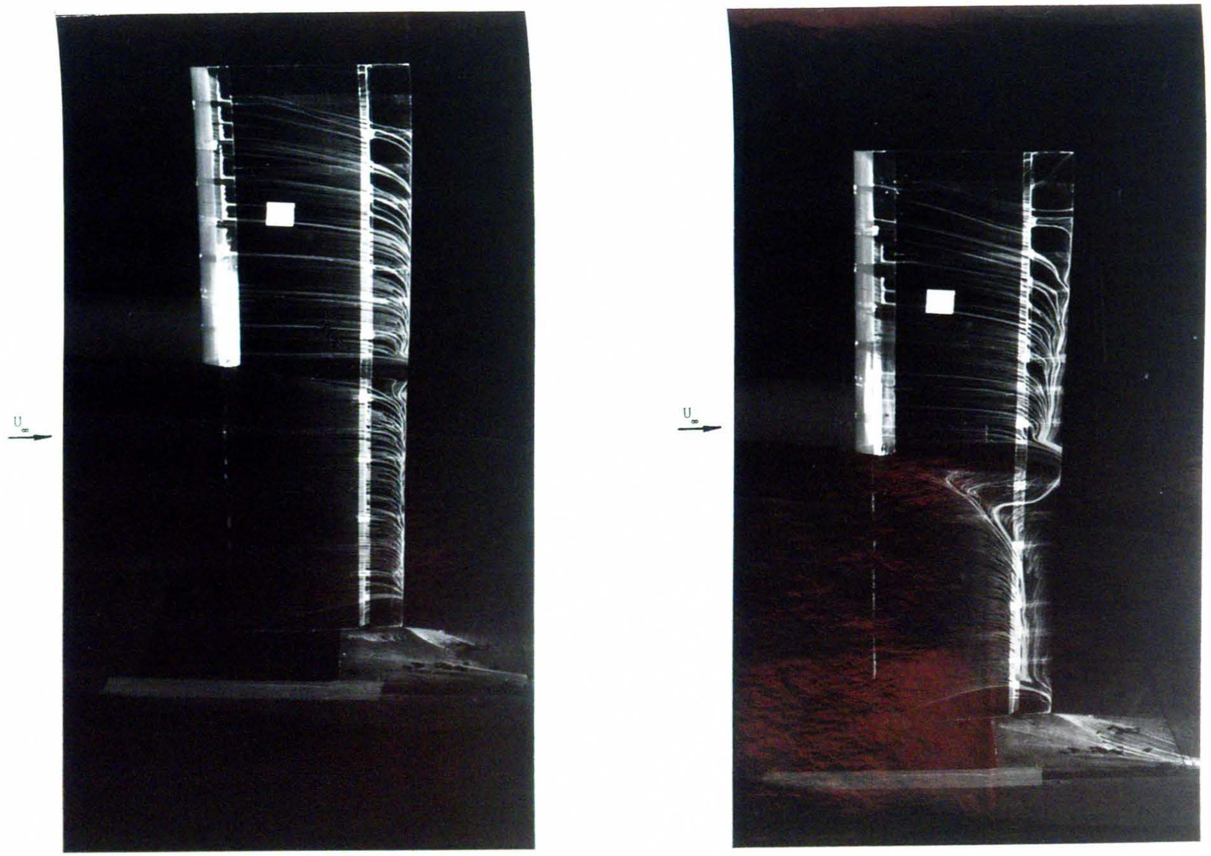

a) $\alpha = 10^\circ$ b) $\alpha = 16.5^\circ$

Figure 29 - Oil flow patterns on NACA 0015 wing with glove on outer half semispan, $Re_c = 2.0 \times 10^6$.

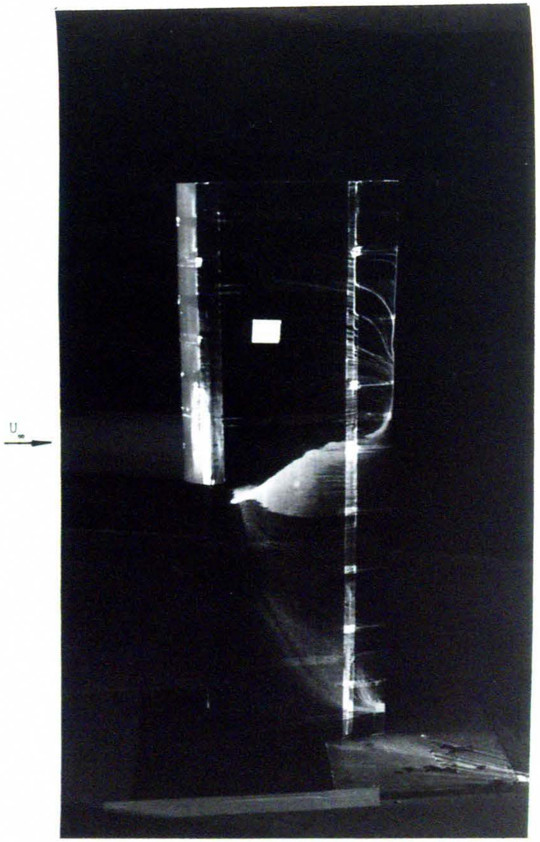

c) α = 18.5°

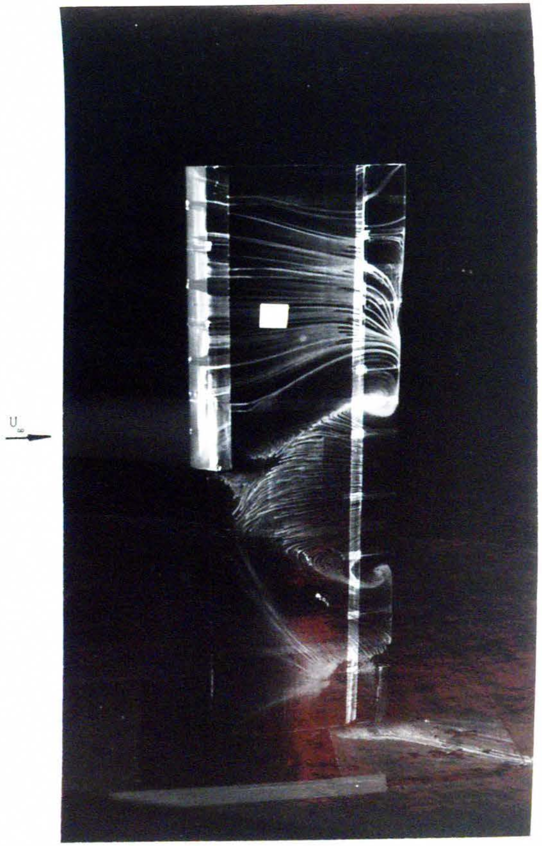

d) α = 20°

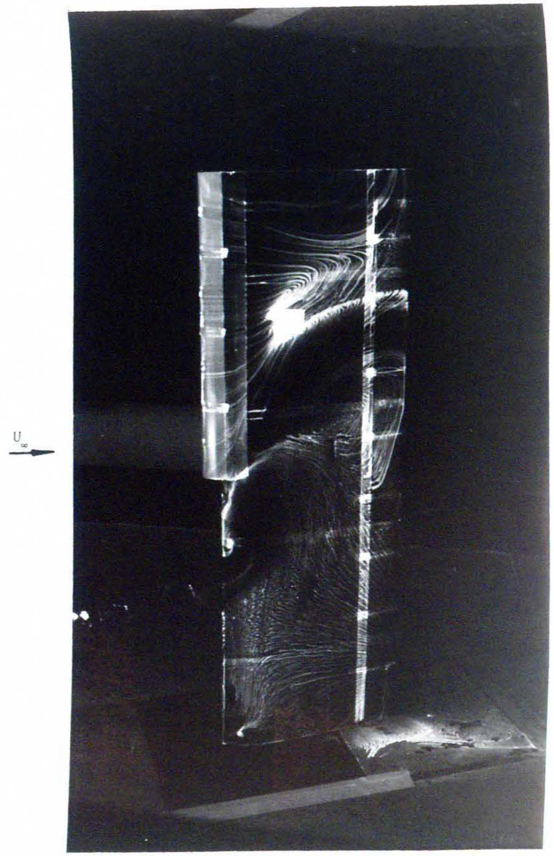

e) α = 30°

Figure 29 - Concluded.

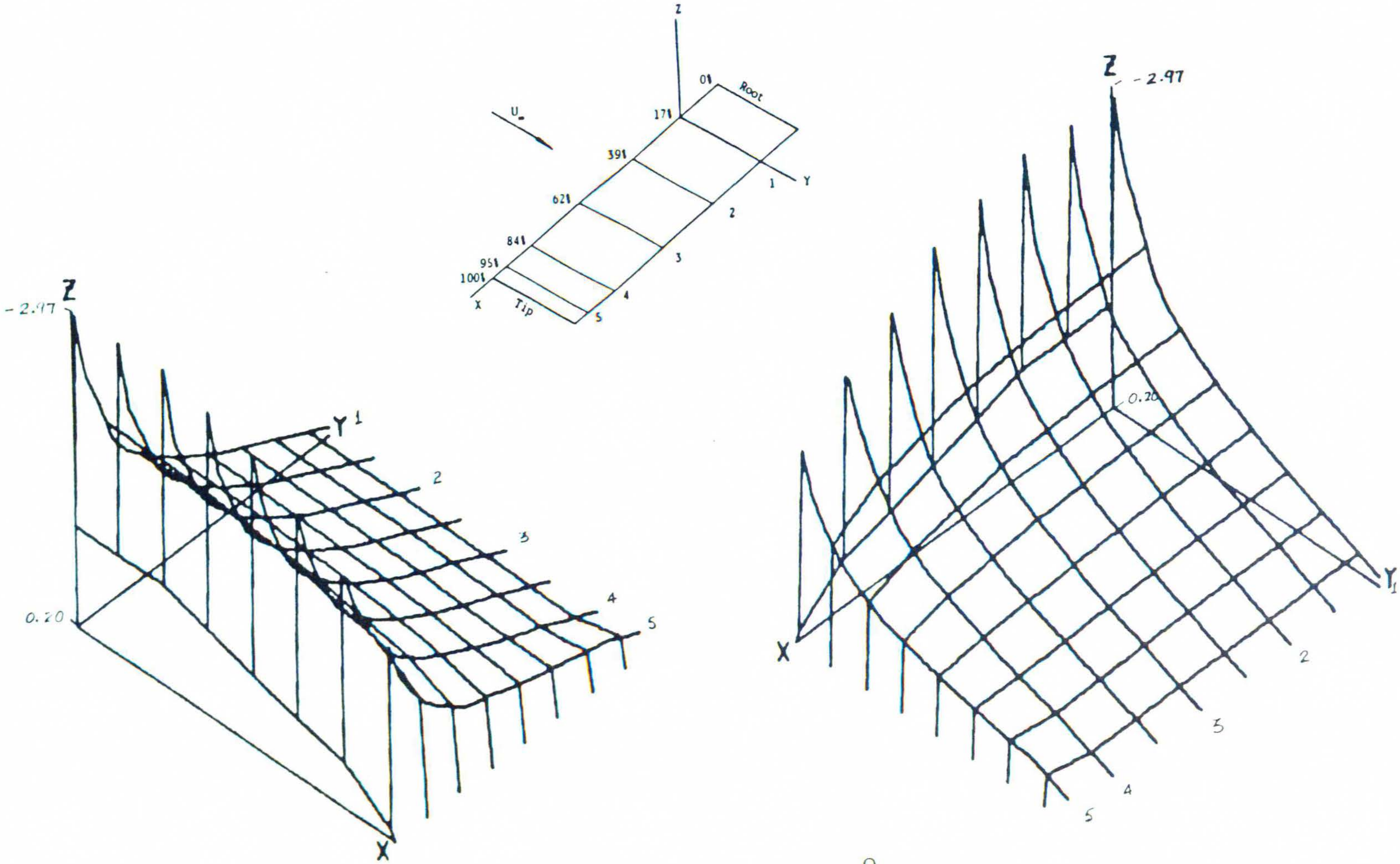

a) C_p on upper surface at $\alpha = 10^o$

Figure 30 - Three-dimensional plot of pressure distribution on NACA 0015 wing, aspect ratio 6, $Re_c = 2.0 \times 10^6$.

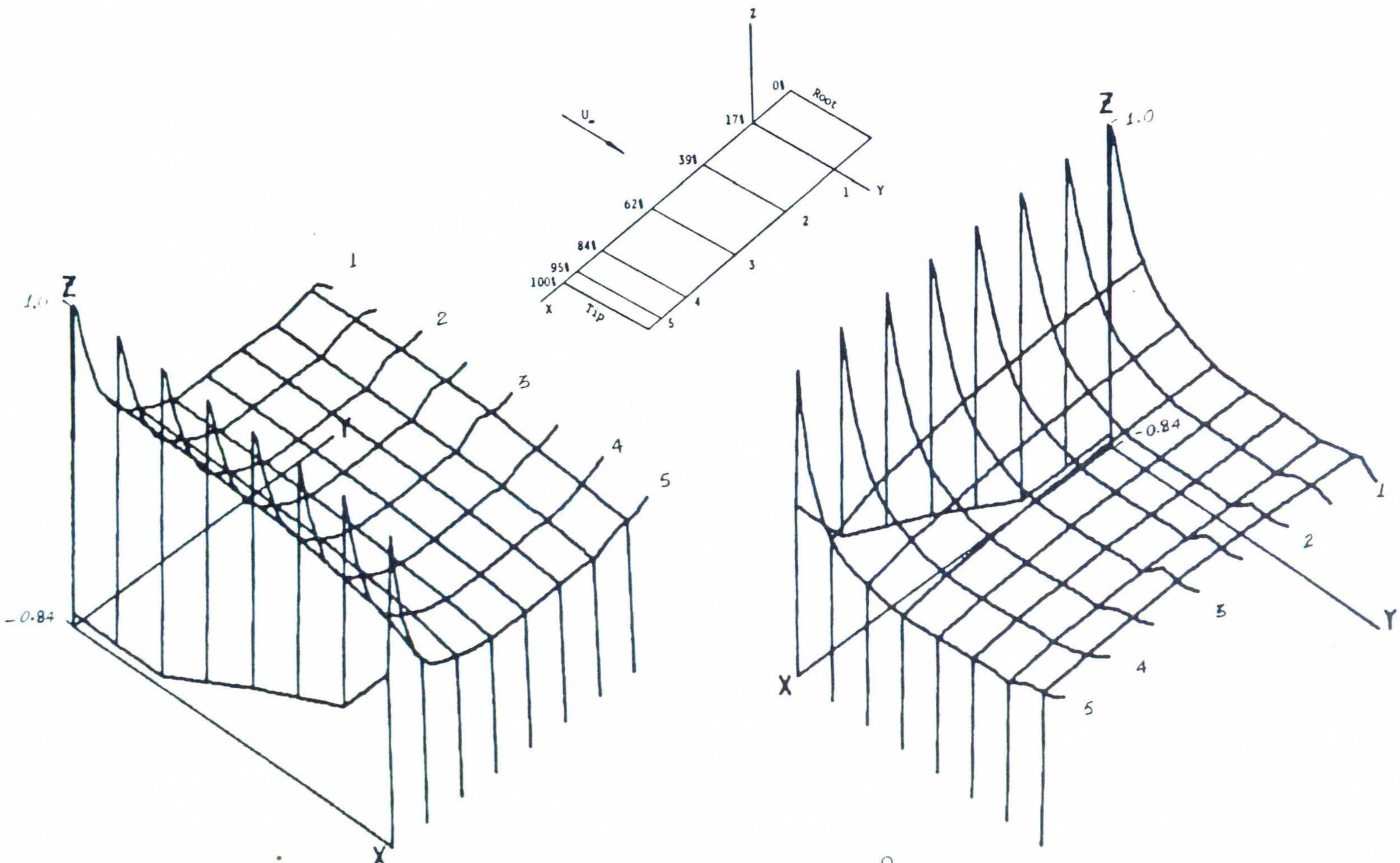

b) C_p on lower surface at α = 10°

Figure 30 - Continued.

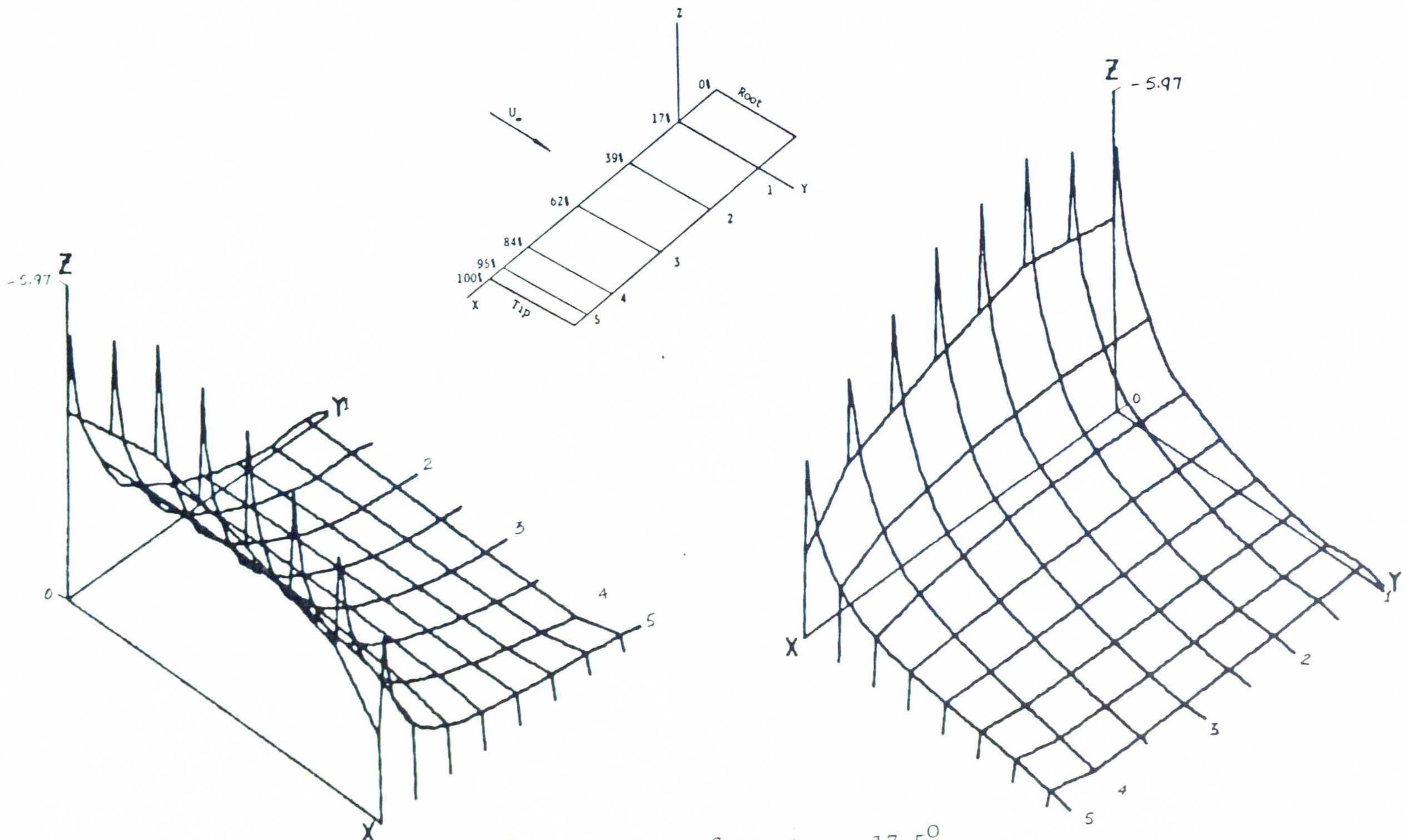

c) C_p on upper surface at $\alpha = 17.5^{\circ}$

Figure 30 - Continued.

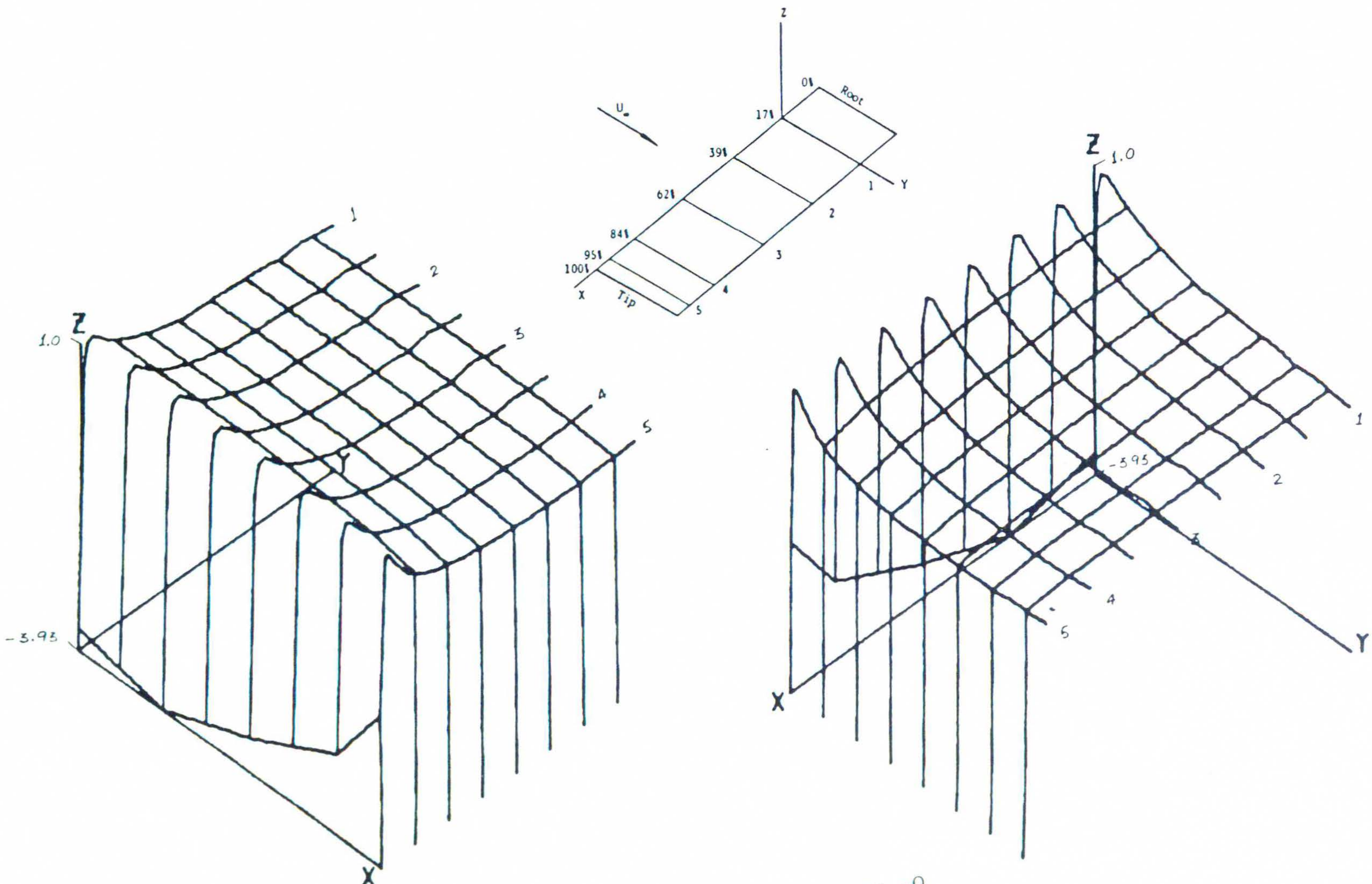

d) C_p on lower surface at α = 17.5°

Figure 30 - Continued.

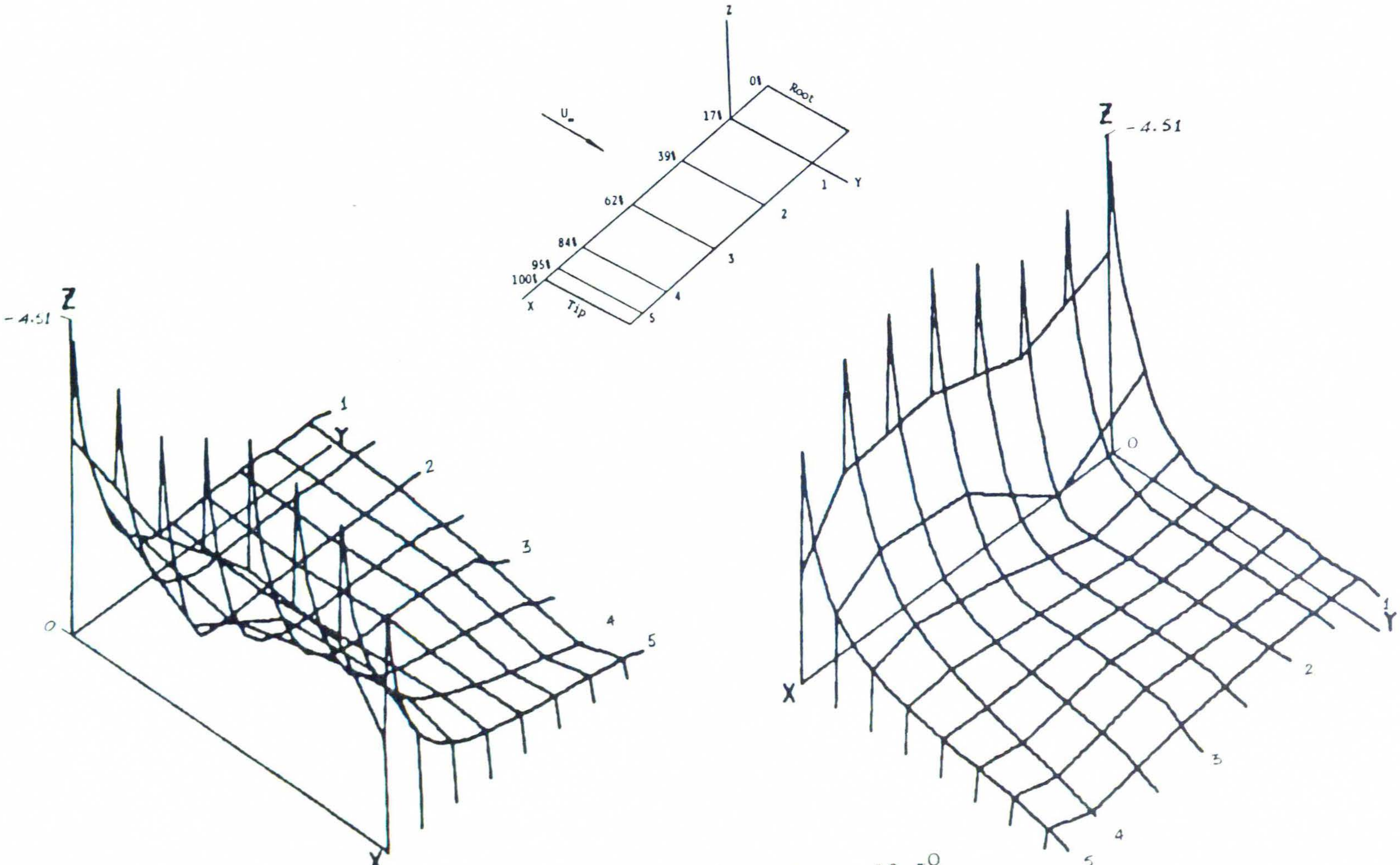

e) C_p on upper surface at $\alpha = 18.5^{\circ}$

Figure 30 - Continued.

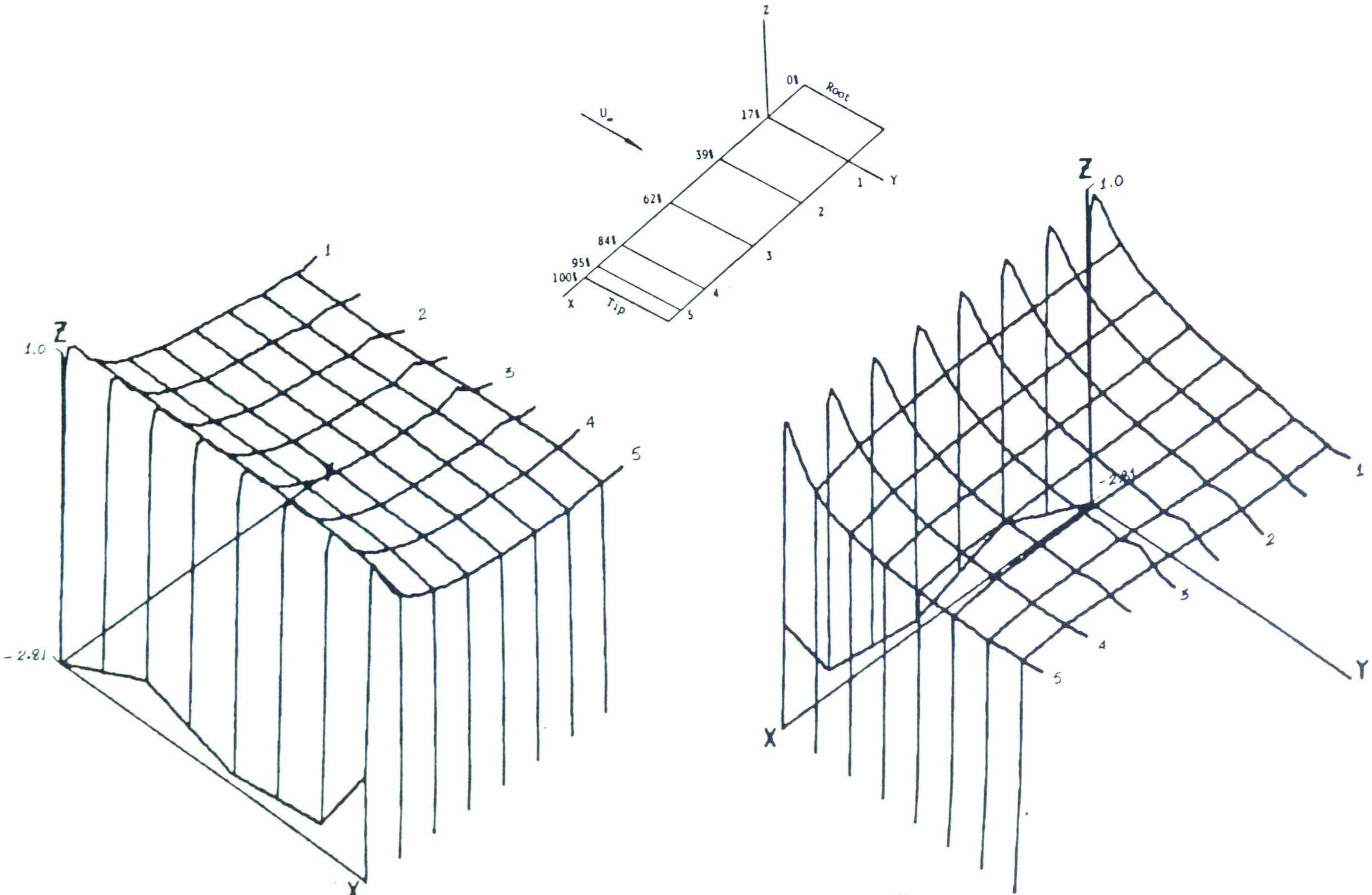

f) C_p on lower surface at $\alpha = 18.5^{\circ}$

Figure 30 - Continued.

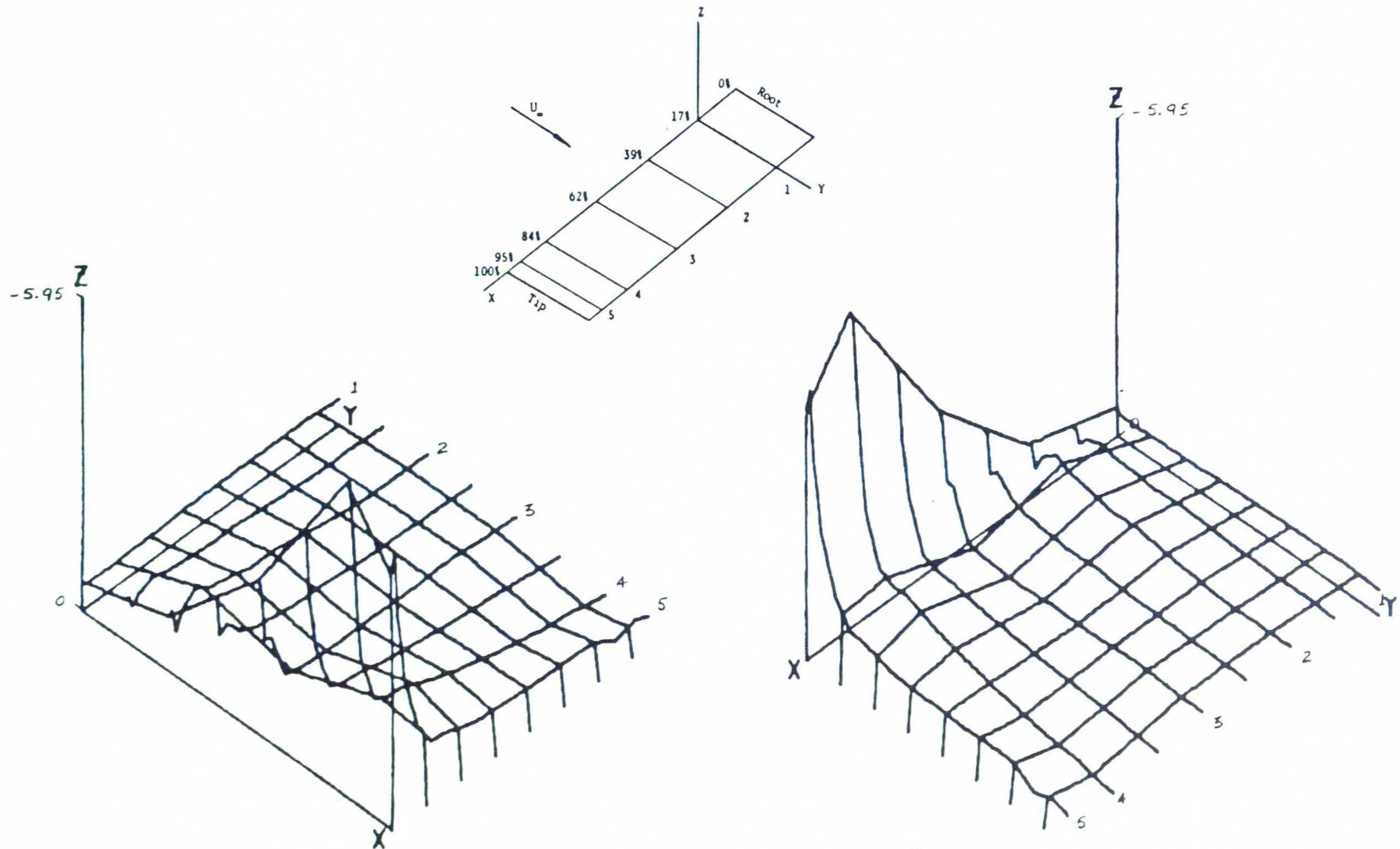

g) C_p on upper surface at $\alpha = 30^{\circ}$

Figure 30 - Continued.

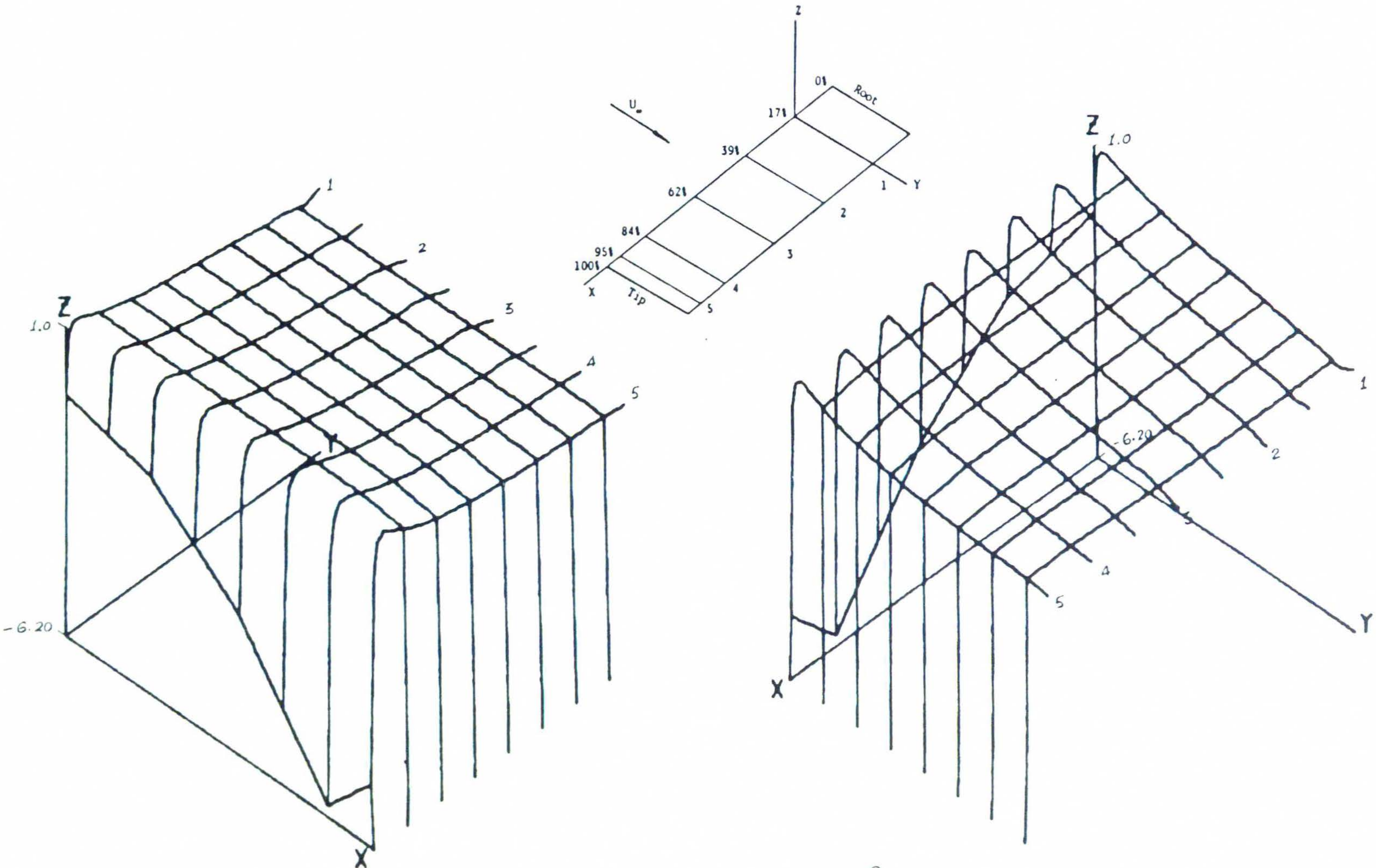

h) C_p on lower surface at $\alpha = 30^{\circ}$

Figure 30 - Continued.

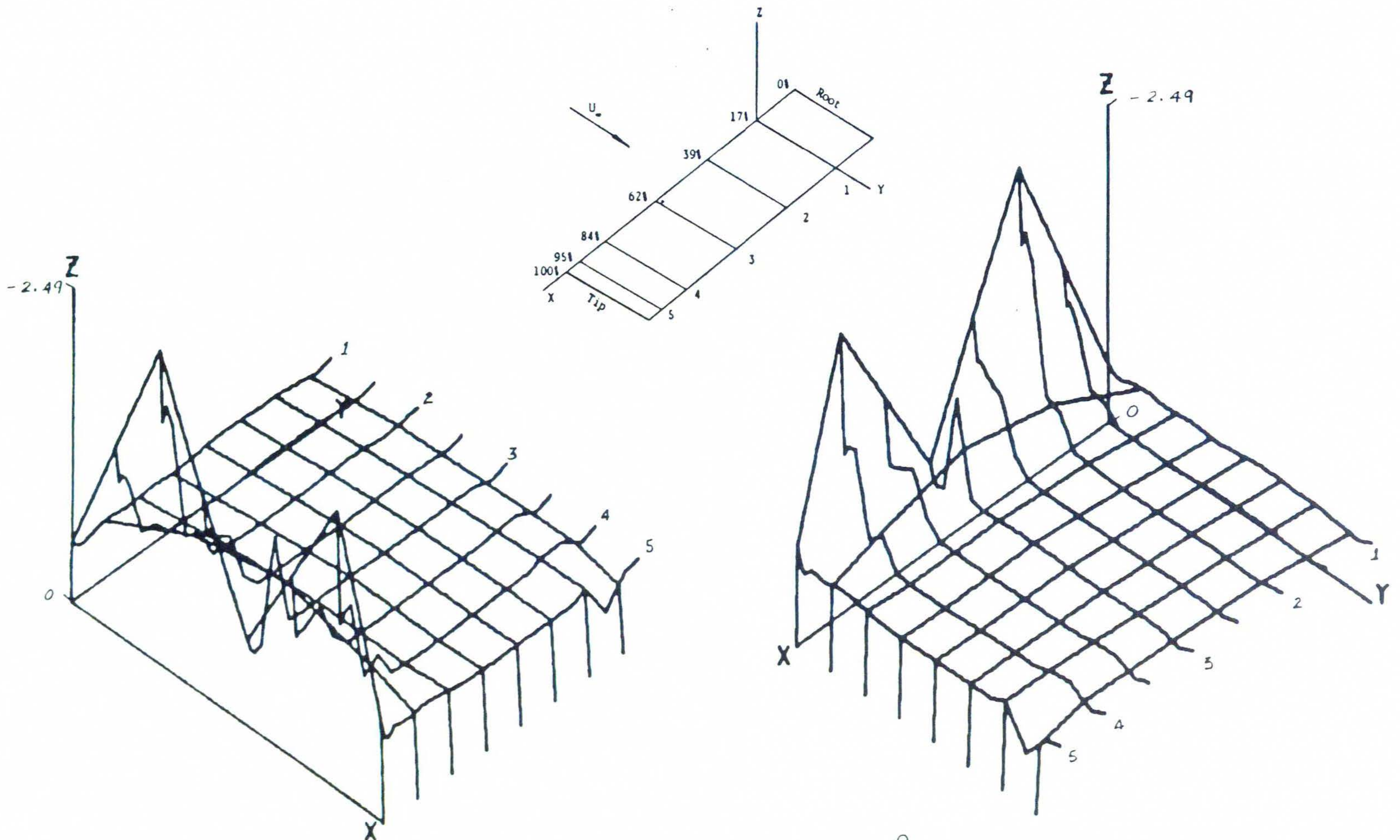

i) C_p on upper surface at $\alpha = 40^{o}$

Figure 30 - Continued.

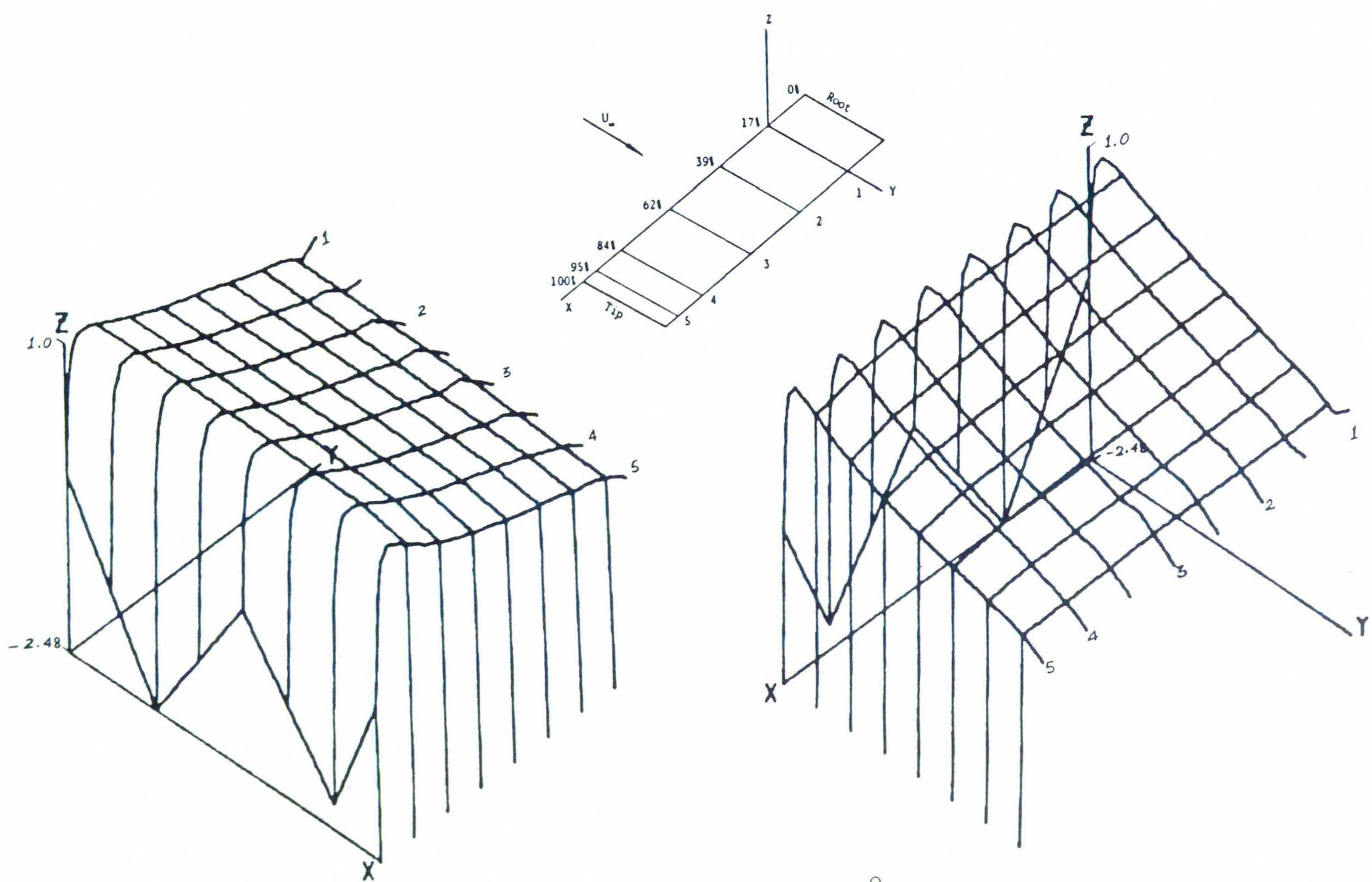

j) C_p on lower surface at $\alpha = 40^{o}$

Figure 30 - Continued.

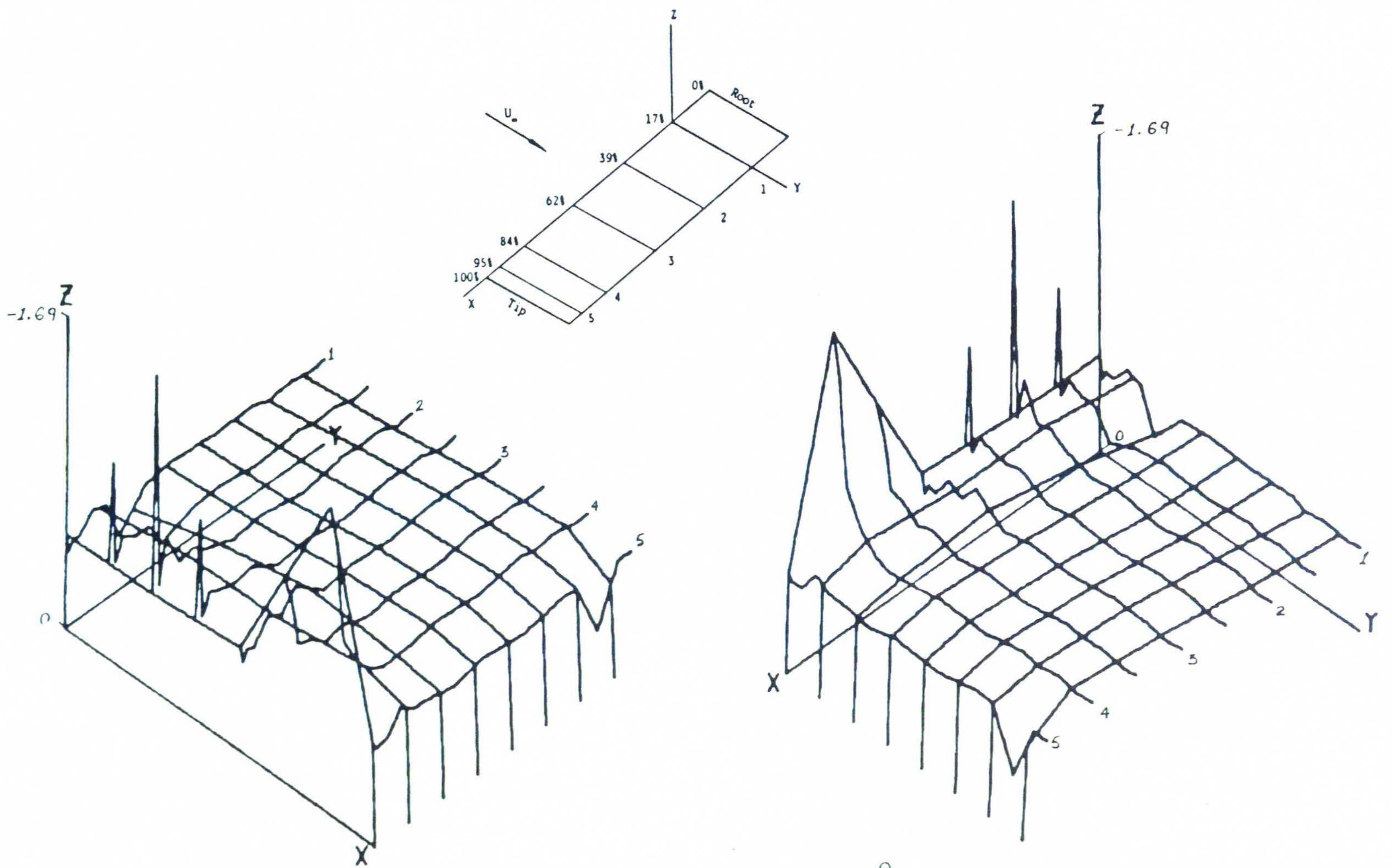

k) C_p on upper surface at $\alpha = 50^{\circ}$

Figure 30 - Continued.

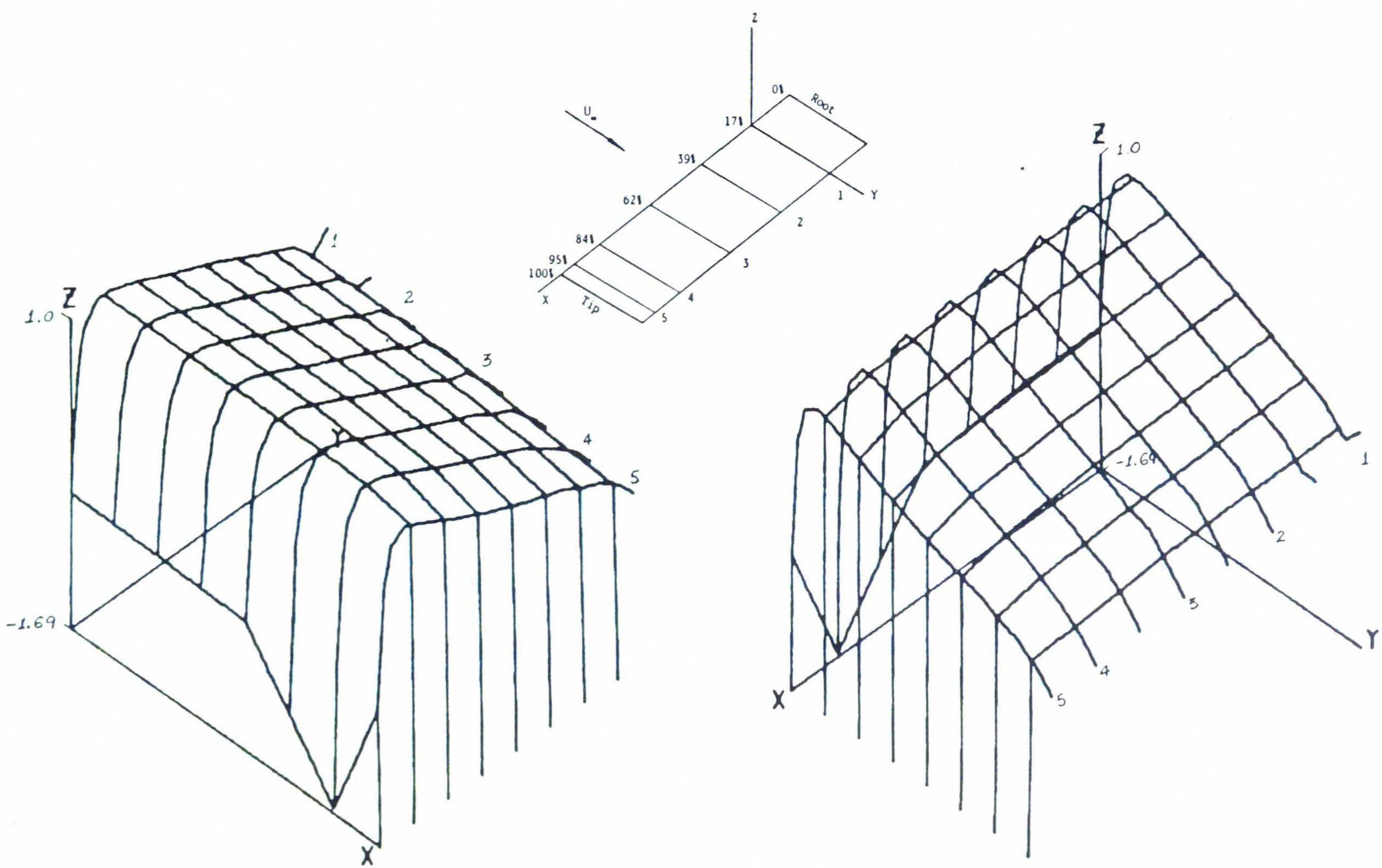

1) C_p on lower surface at $\alpha = 50^{\circ}$

Figure 30 - Concluded.

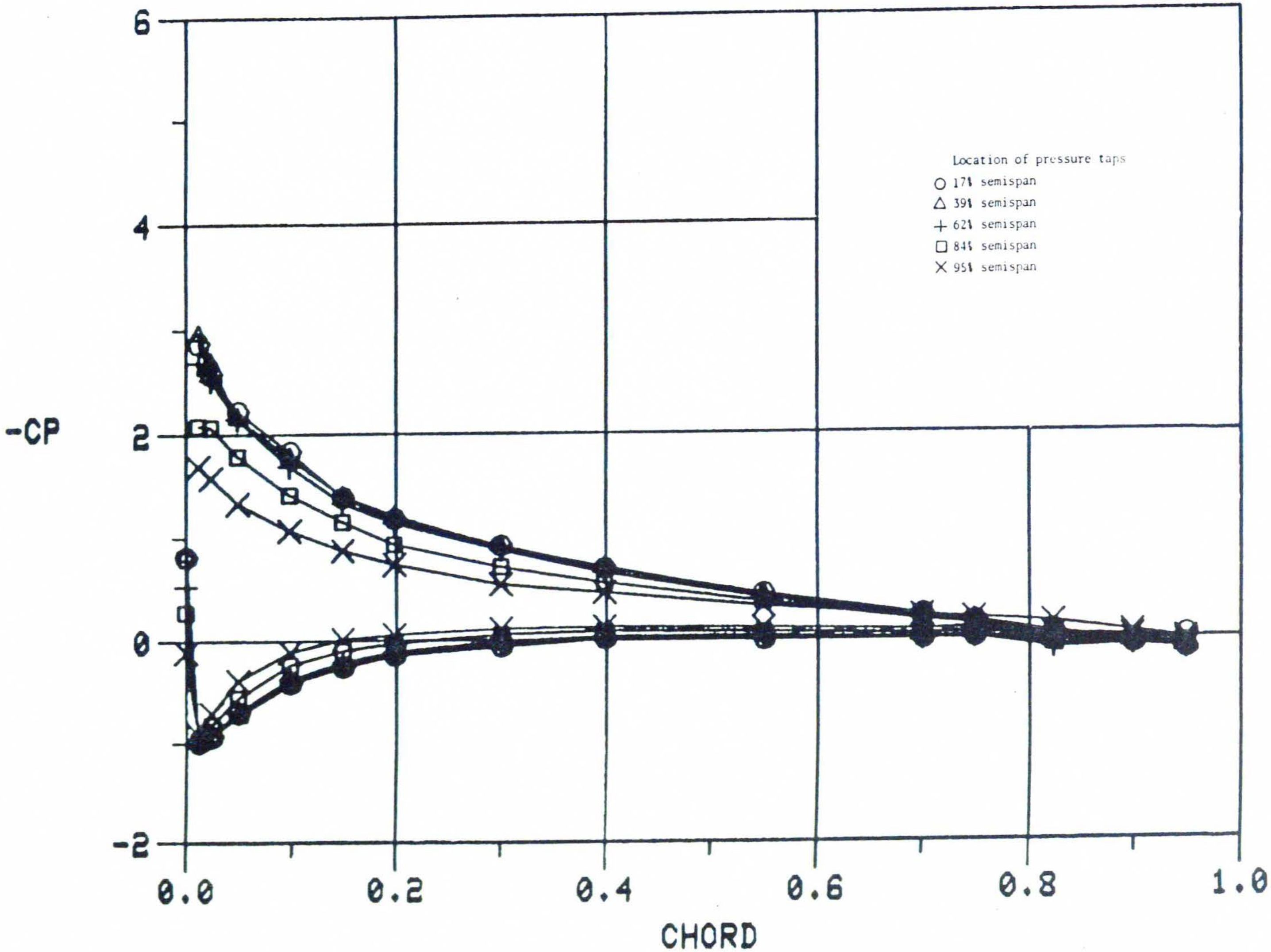

a) $\alpha = 10^{\circ}$

Figure 31 - Pressure distribution on NACA 0015 wing (aspect ratio 6) at various angles of attack, $Re_c = 2.0 \times 10^6$.

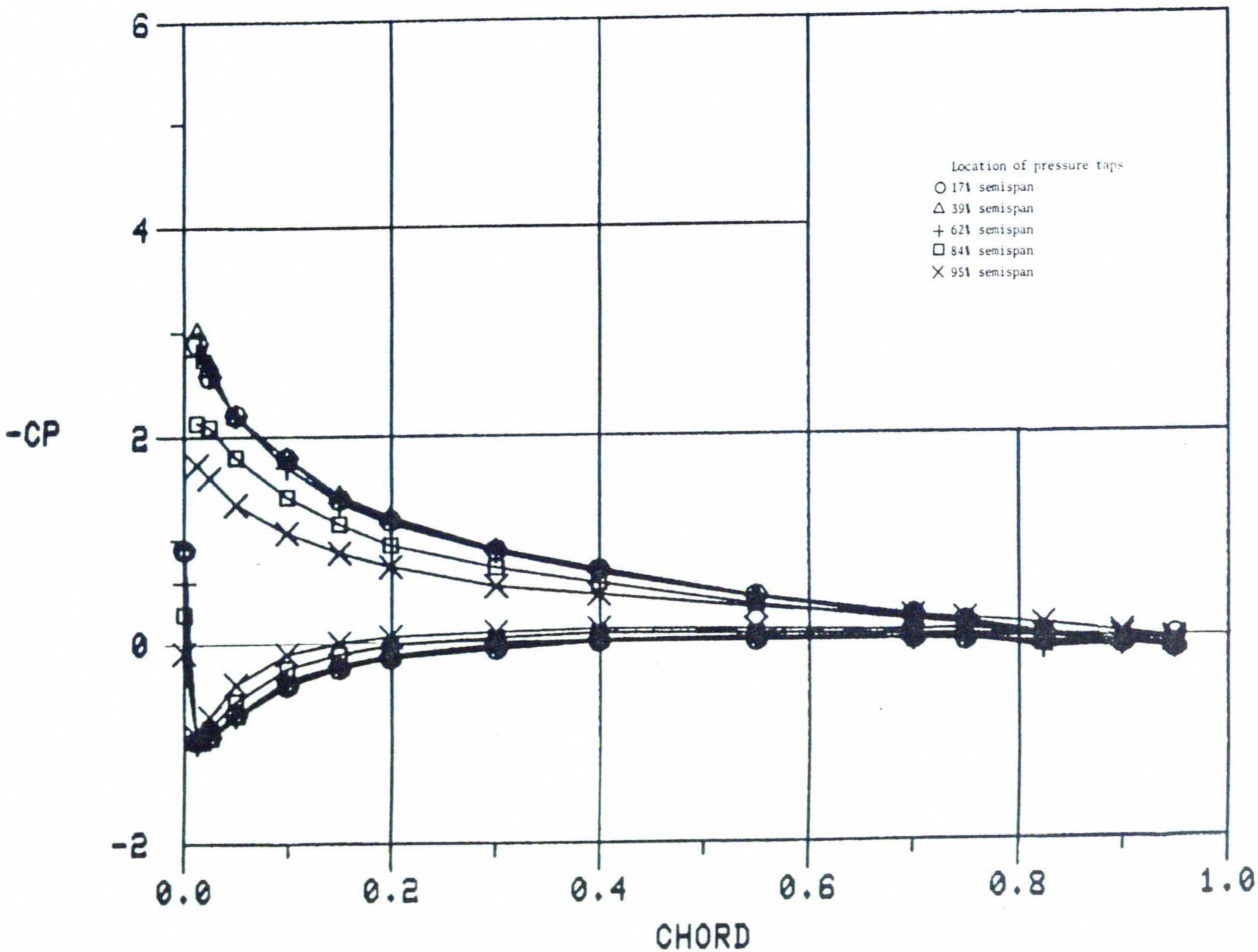

b) $\alpha = 10^{o}$ (decreasing angle)

Figure 31 - Continued.

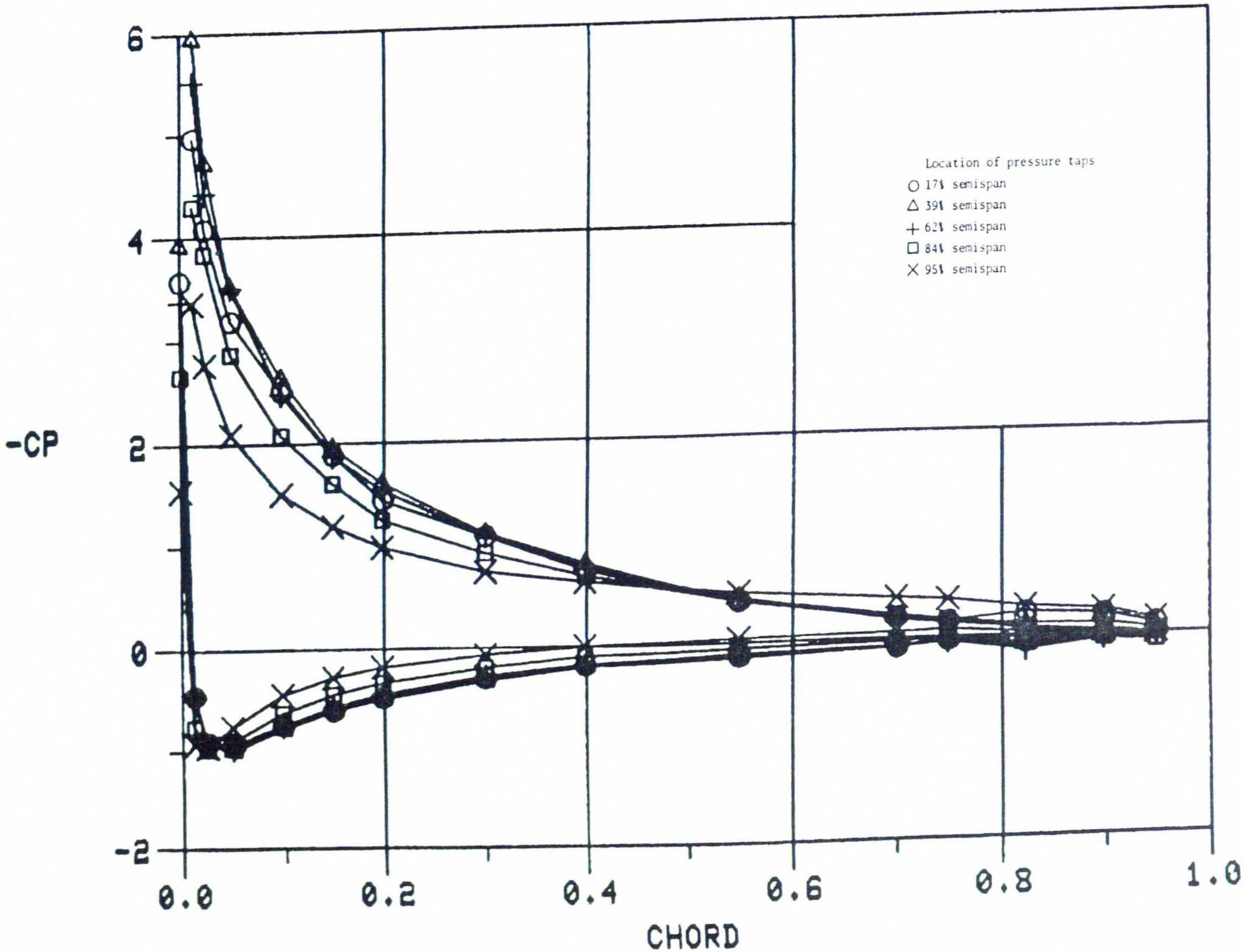

c) $\alpha = 17.5^{\circ}$

Figure 31 - Continued.

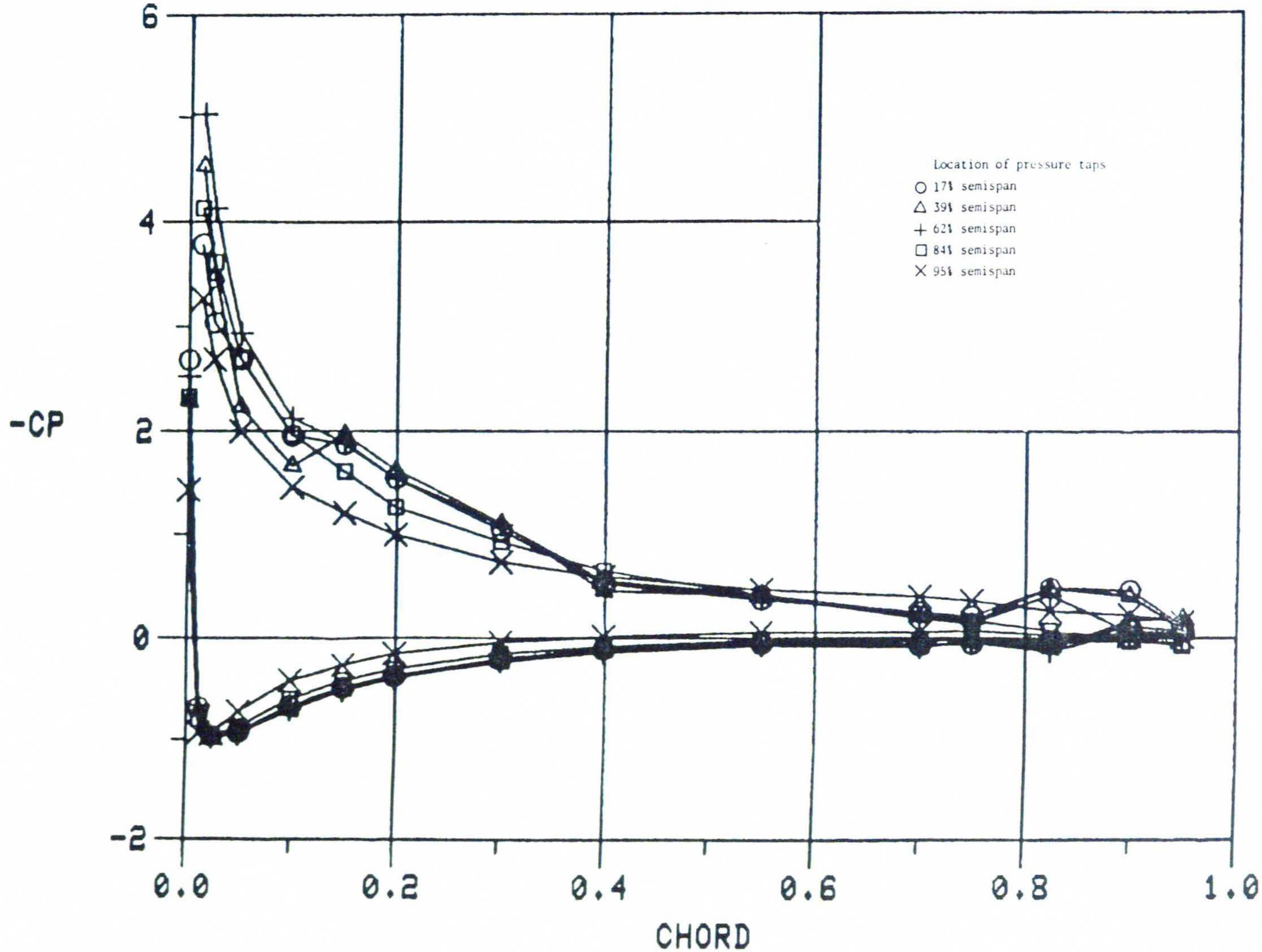

d) α = 17.5° (decreasing angle)

Figure 31 - Continued.

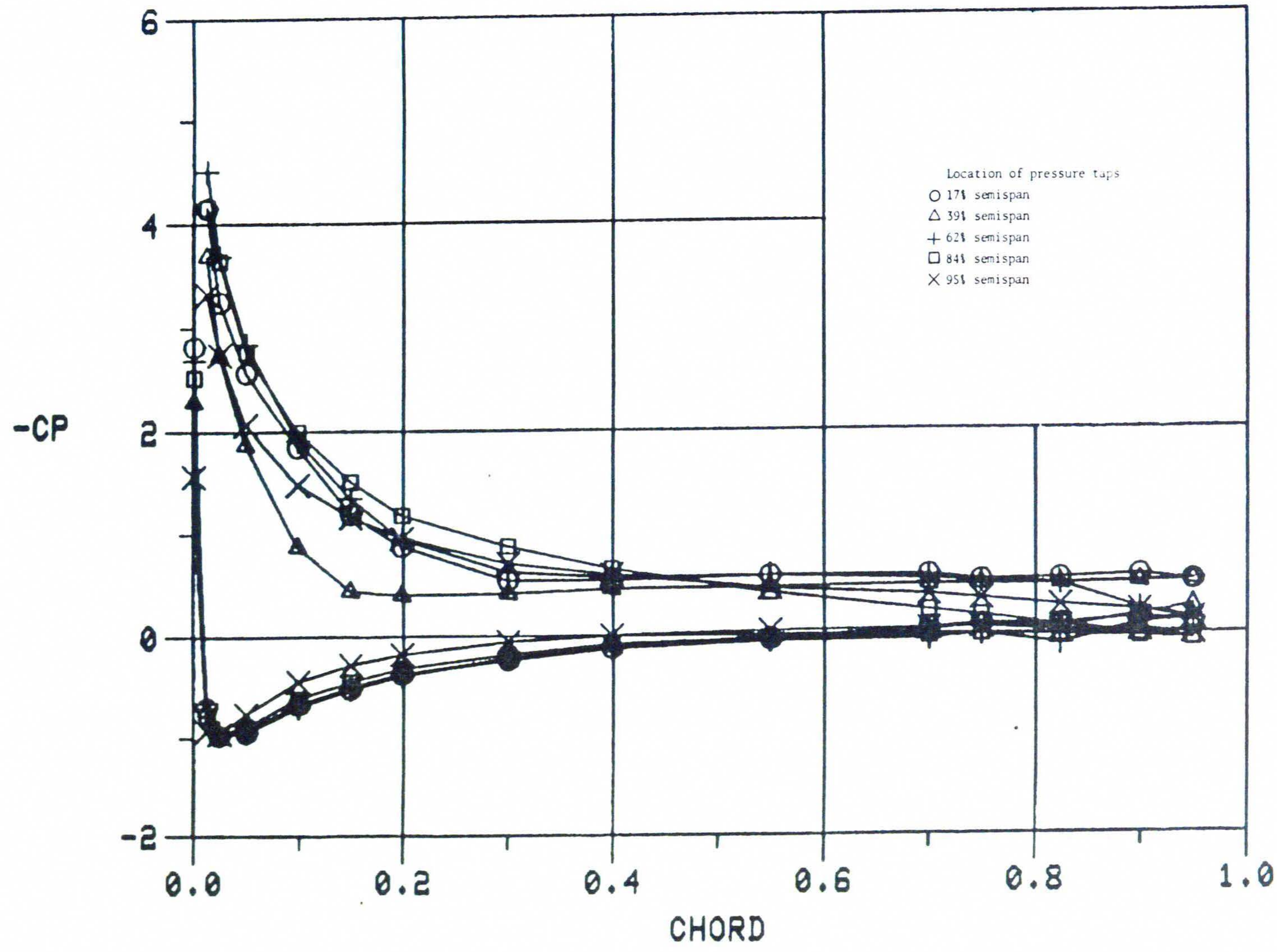

e) $\alpha = 18.5^{\circ}$

Figure 31 - Continued.

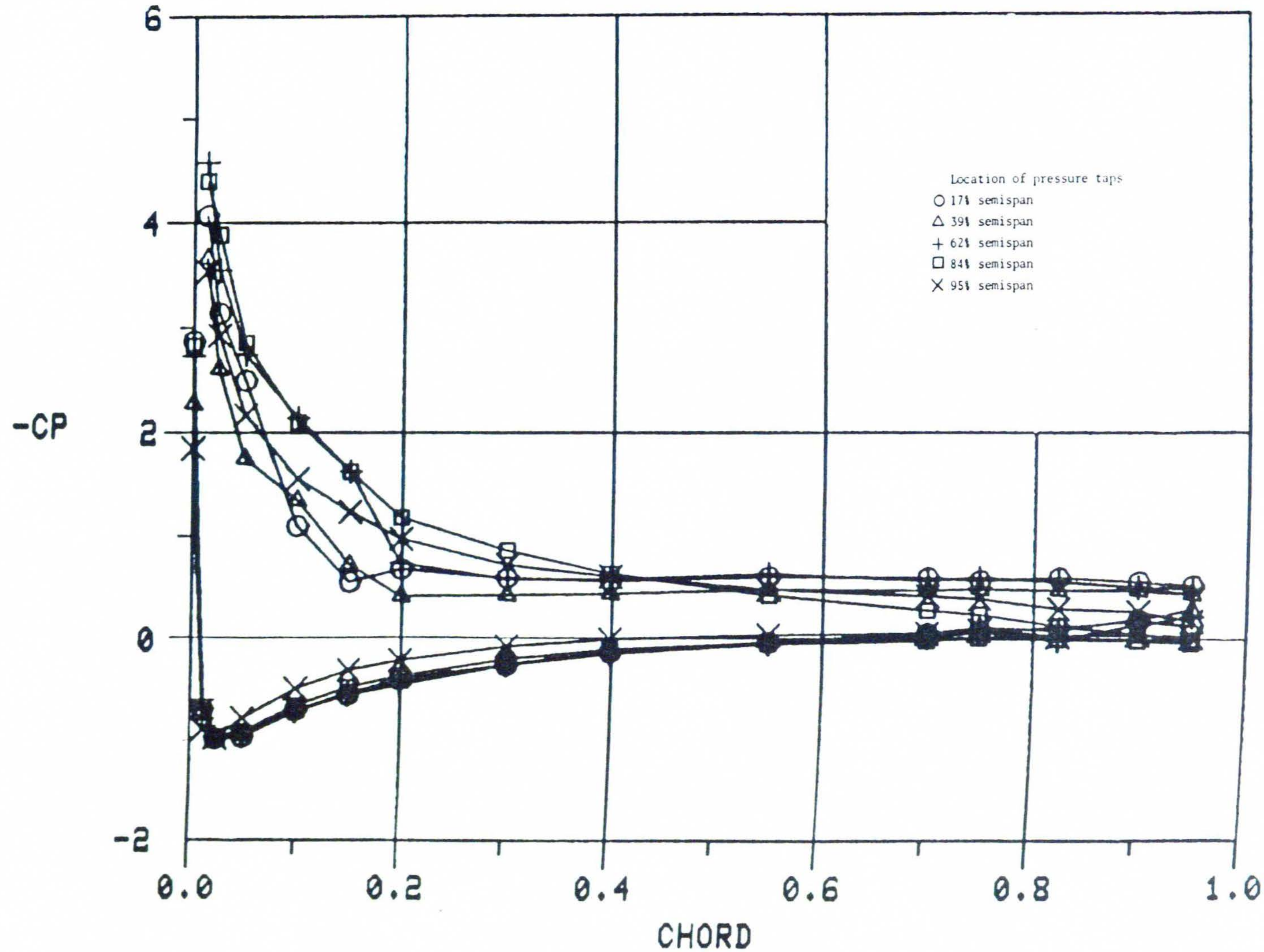

f) $\alpha = 18.5^{o}$ (decreasing angle)

Figure 31 - Continued.

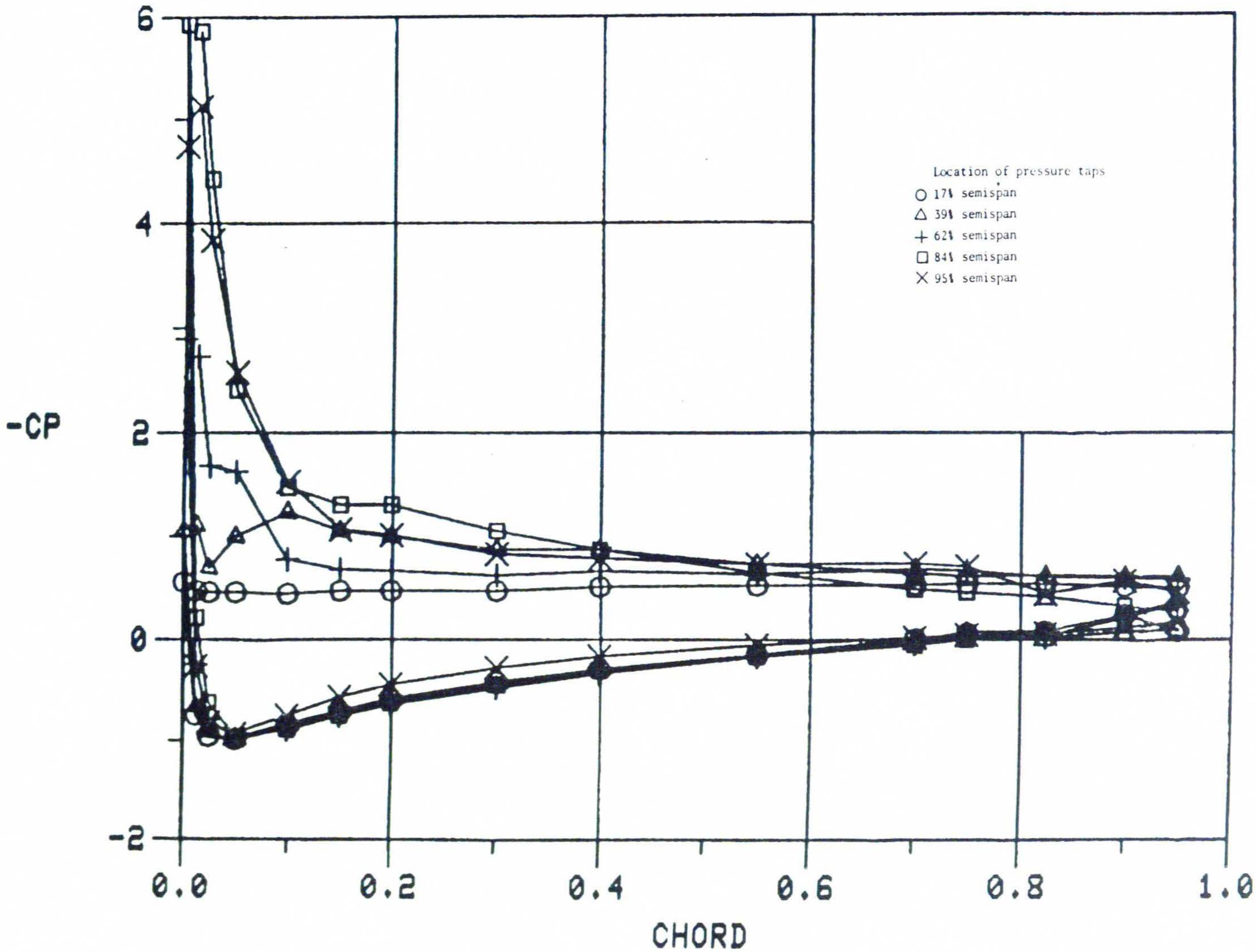

g) α = 30°

Figure 31 - Continued.

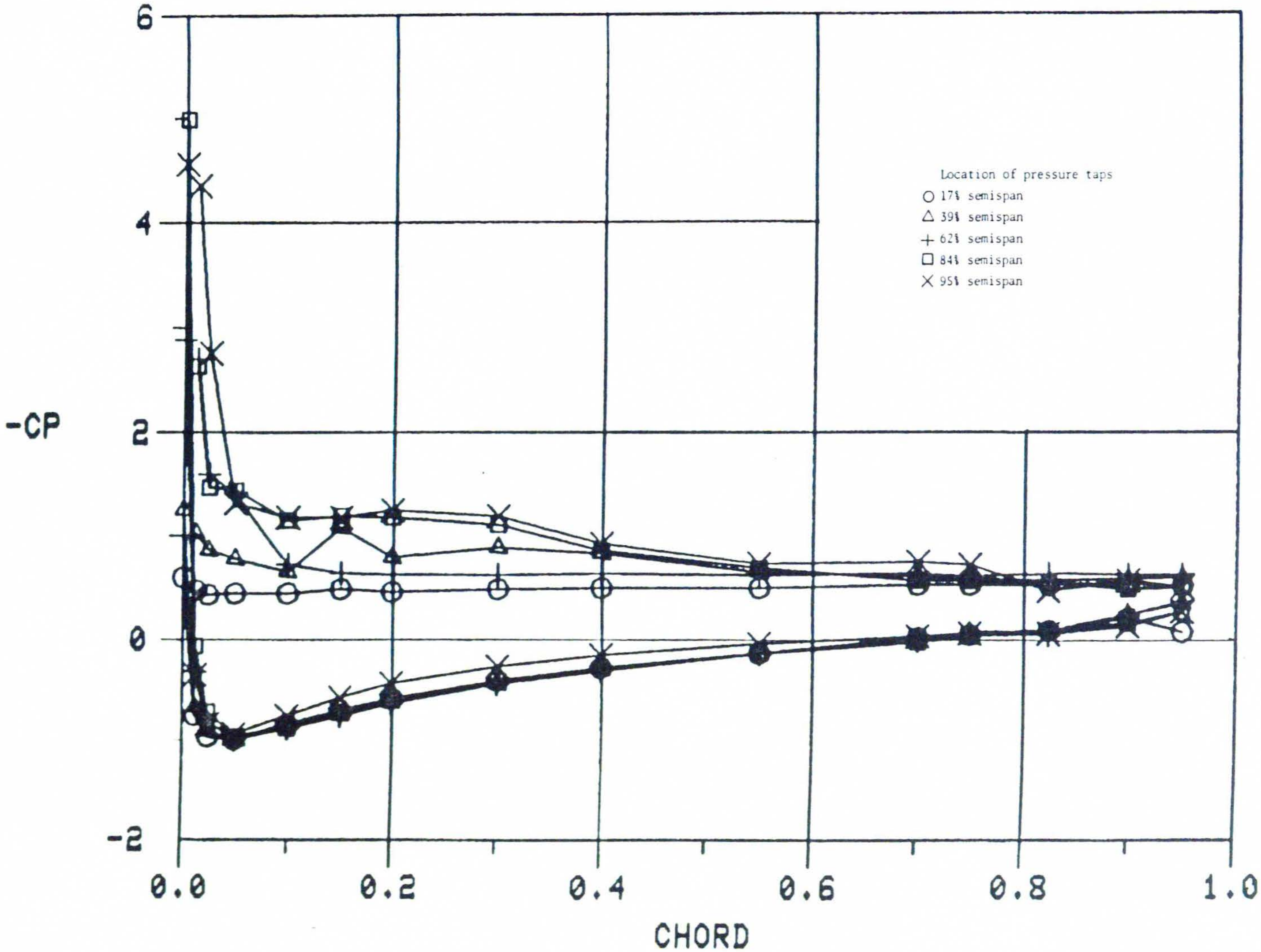

h) $\alpha = 30^{\circ}$ (decreasing angle)

Figure 31 - Continued.

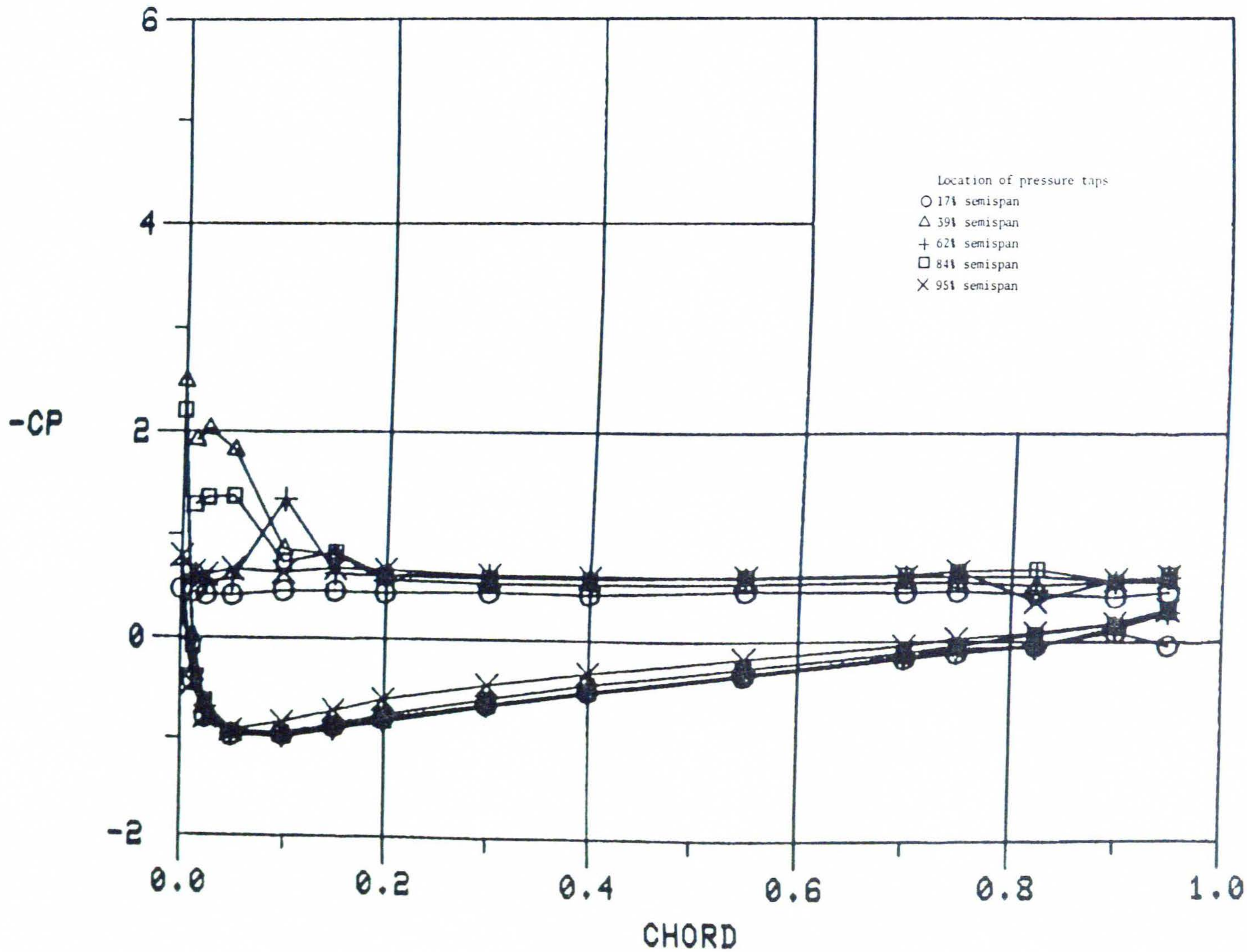

i) $\alpha = 40^{\circ}$

Figure 31 - Continued.

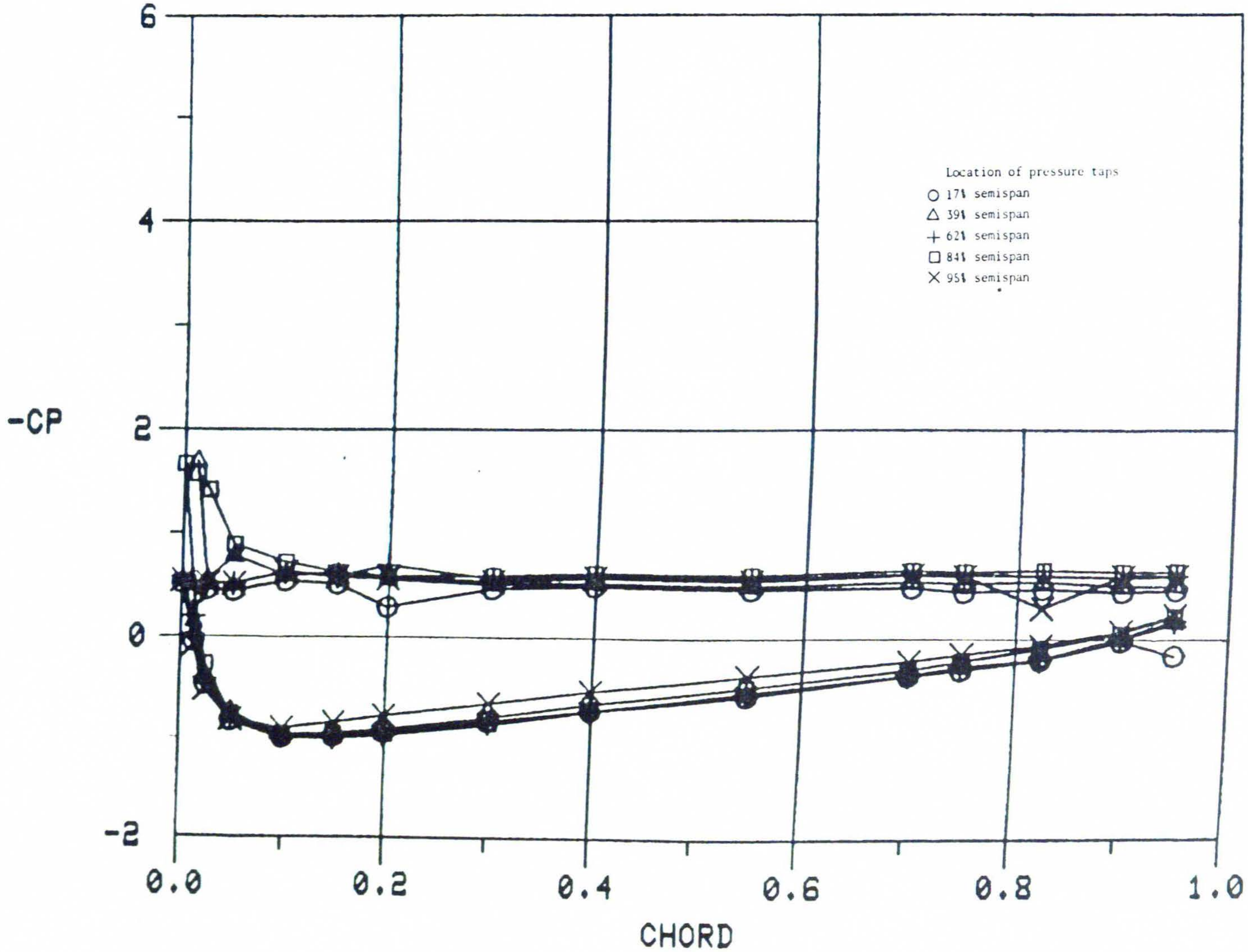

j) $\alpha = 50^{o}$

Figure 31 - Concluded.

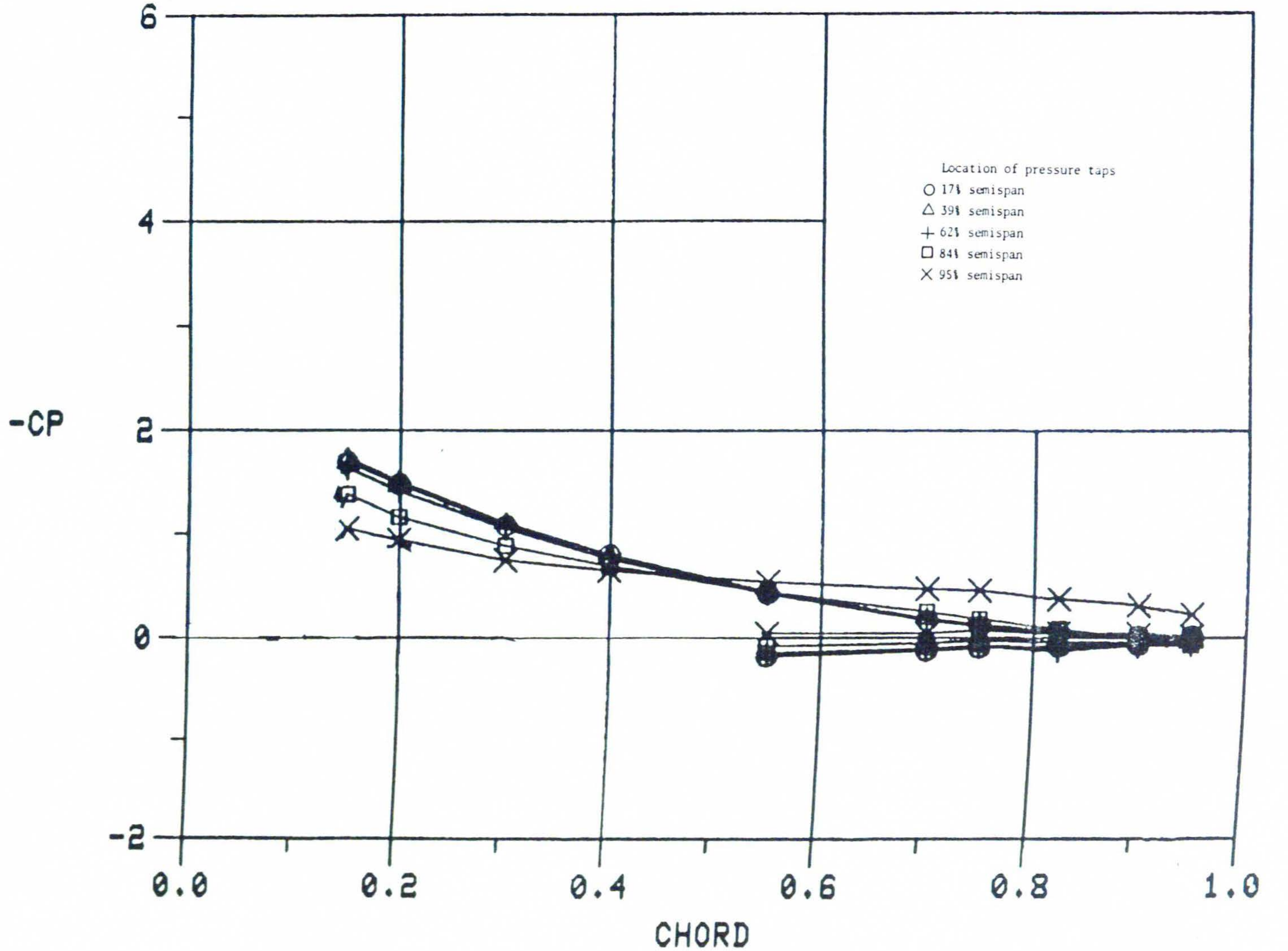

a) $\alpha = 18.5^{o}$

Figure 32 - Pressure distribution on NACA 0015 wing with 14% Clark Y glove on entire leading edge, $Re_c = 2.0 \times 10^6$.

115

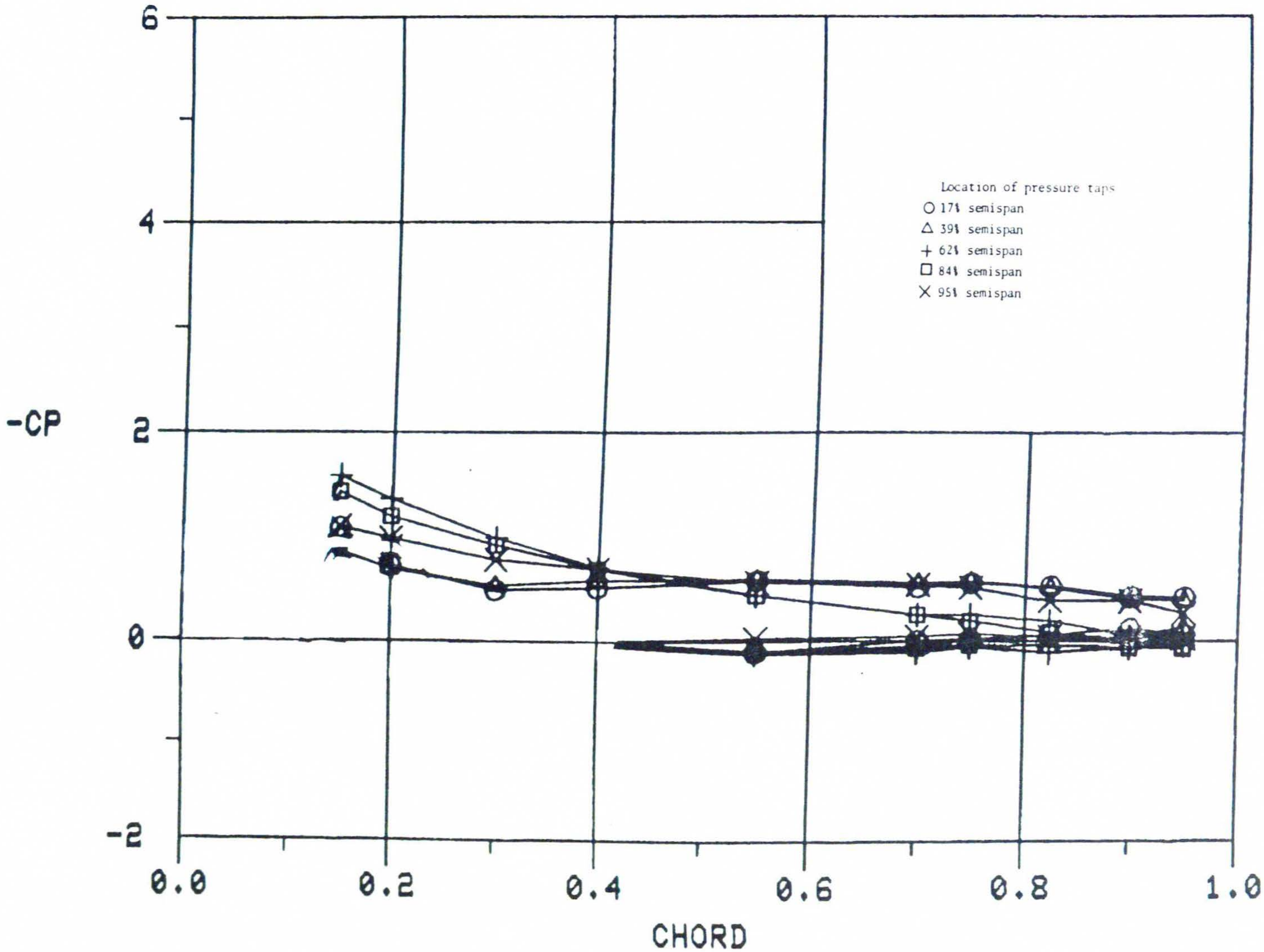

b) $\alpha = 20^{\circ}$

Figure 32 - Continued.

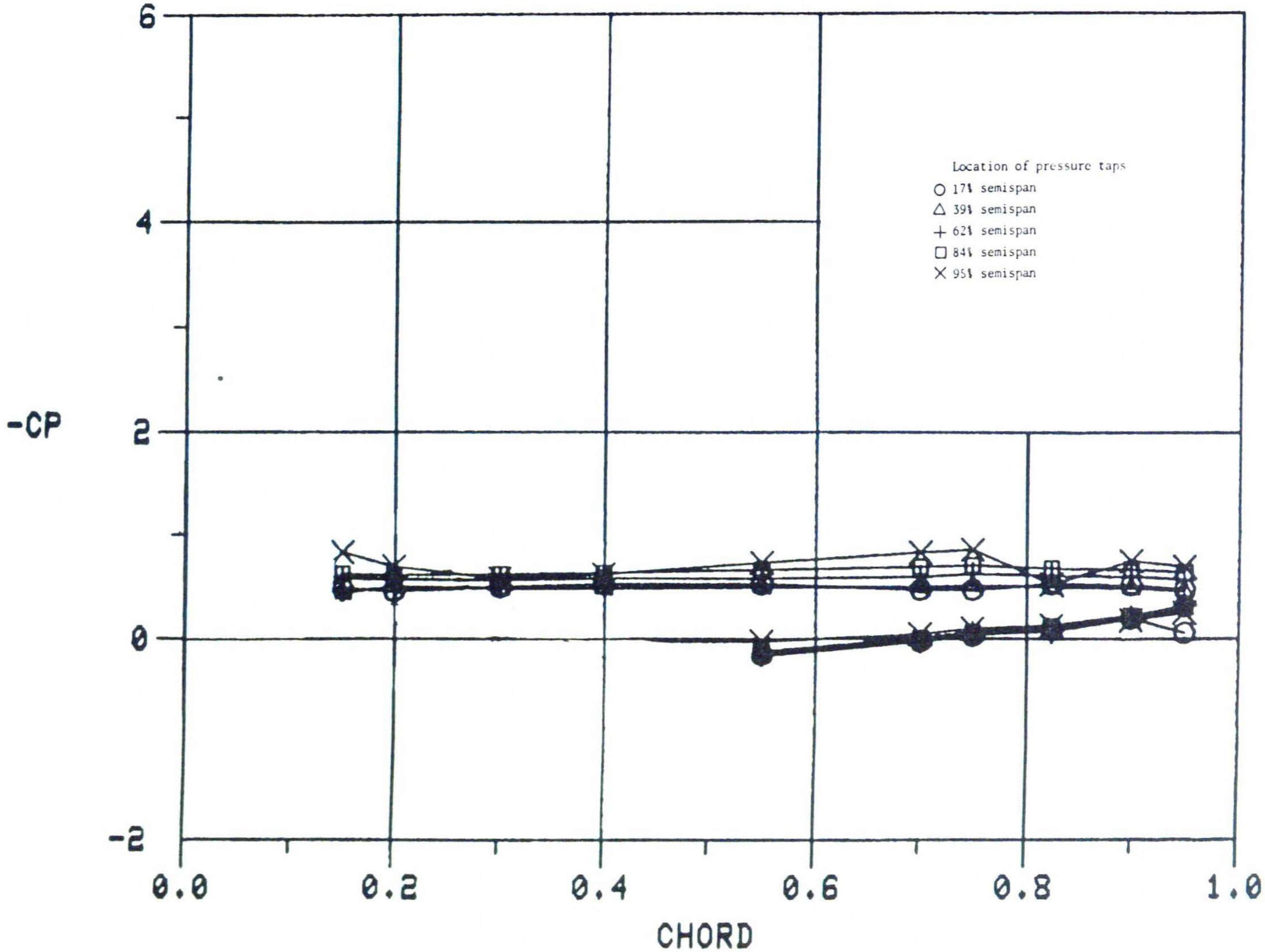

c) $\alpha = 30^{\circ}$

Figure 32 - Continued.

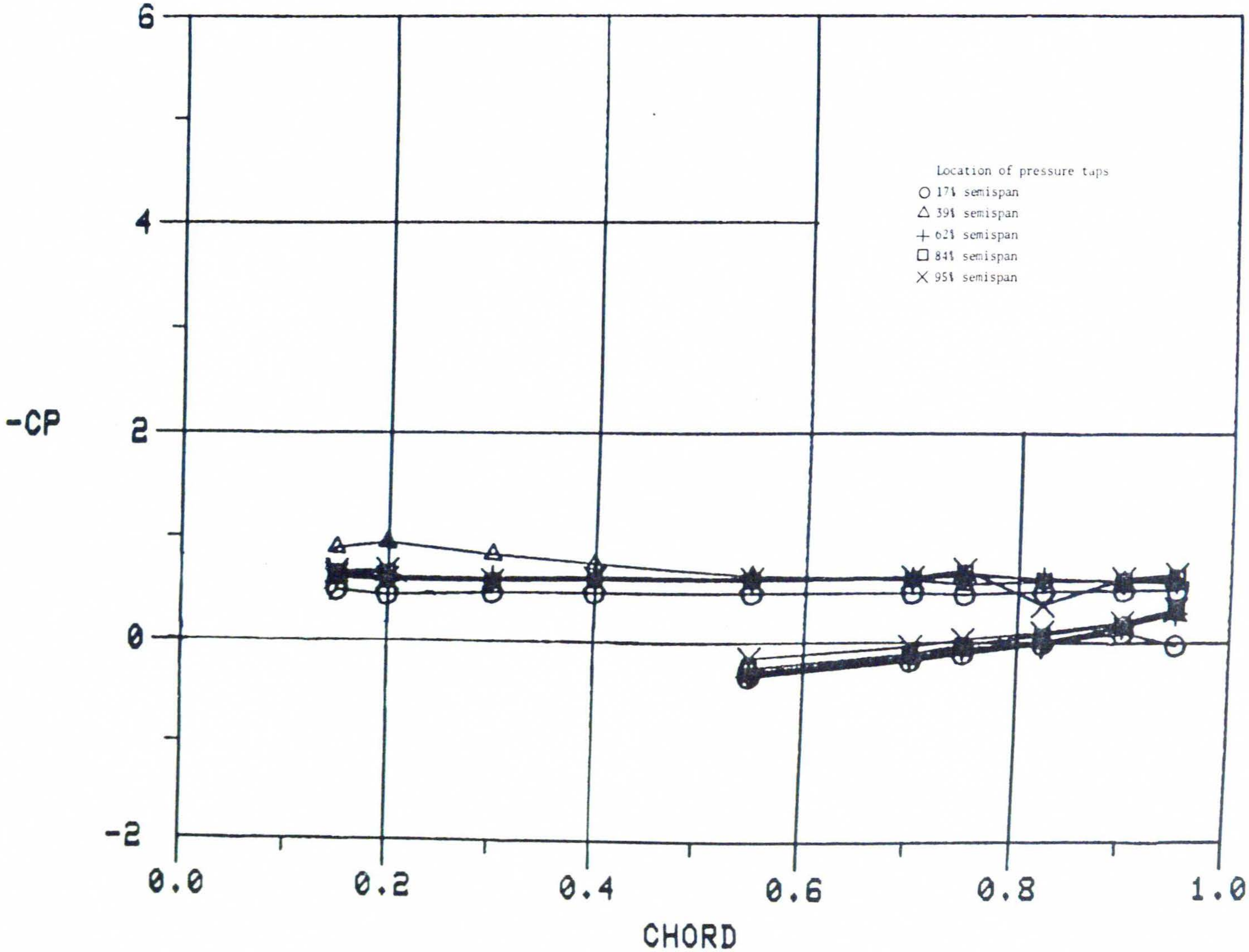

d) $\alpha = 40^{o}$

Figure 32 - Continued.

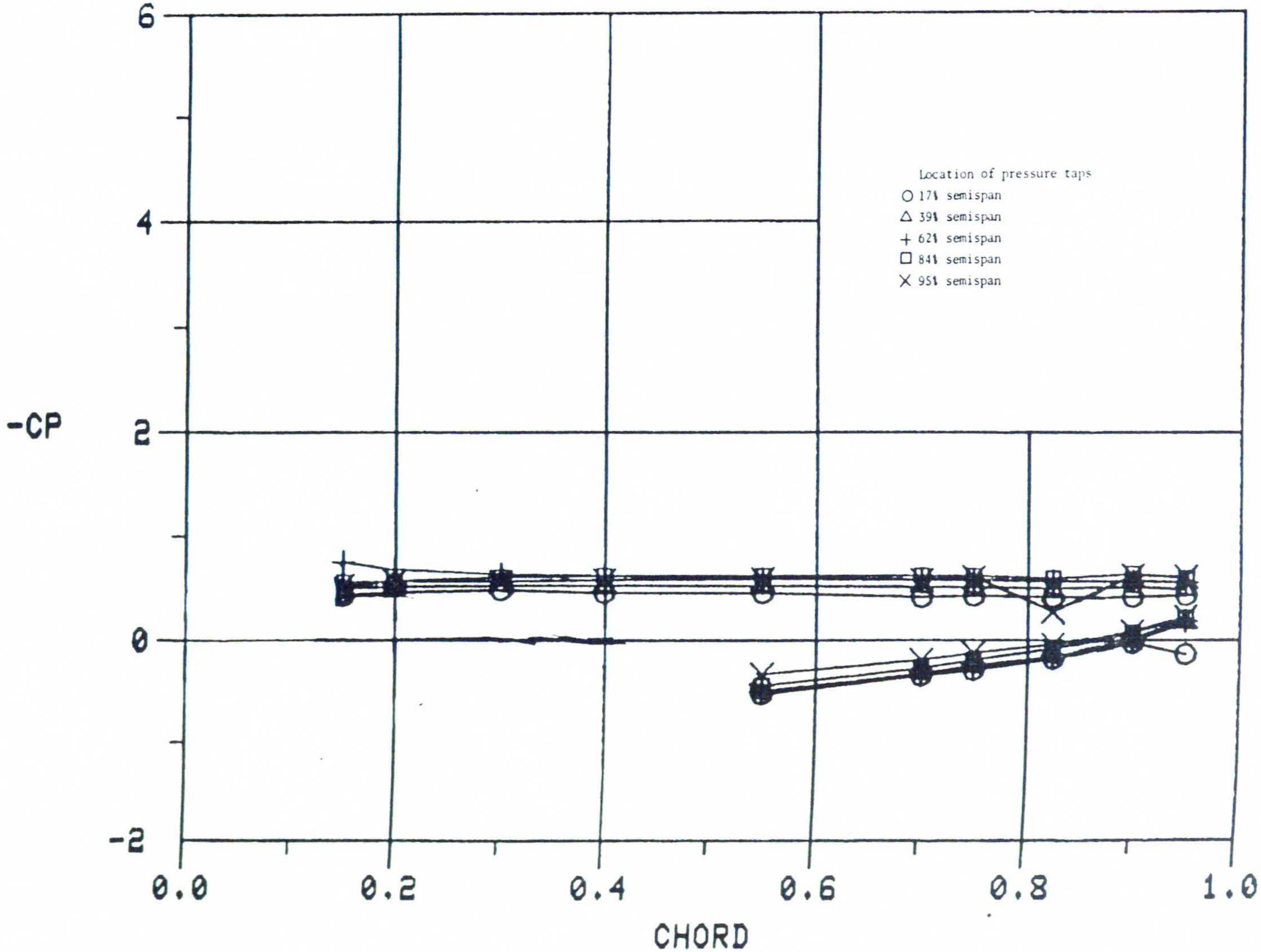

e) $\alpha = 50^{o}$

Figure 32 - Concluded.

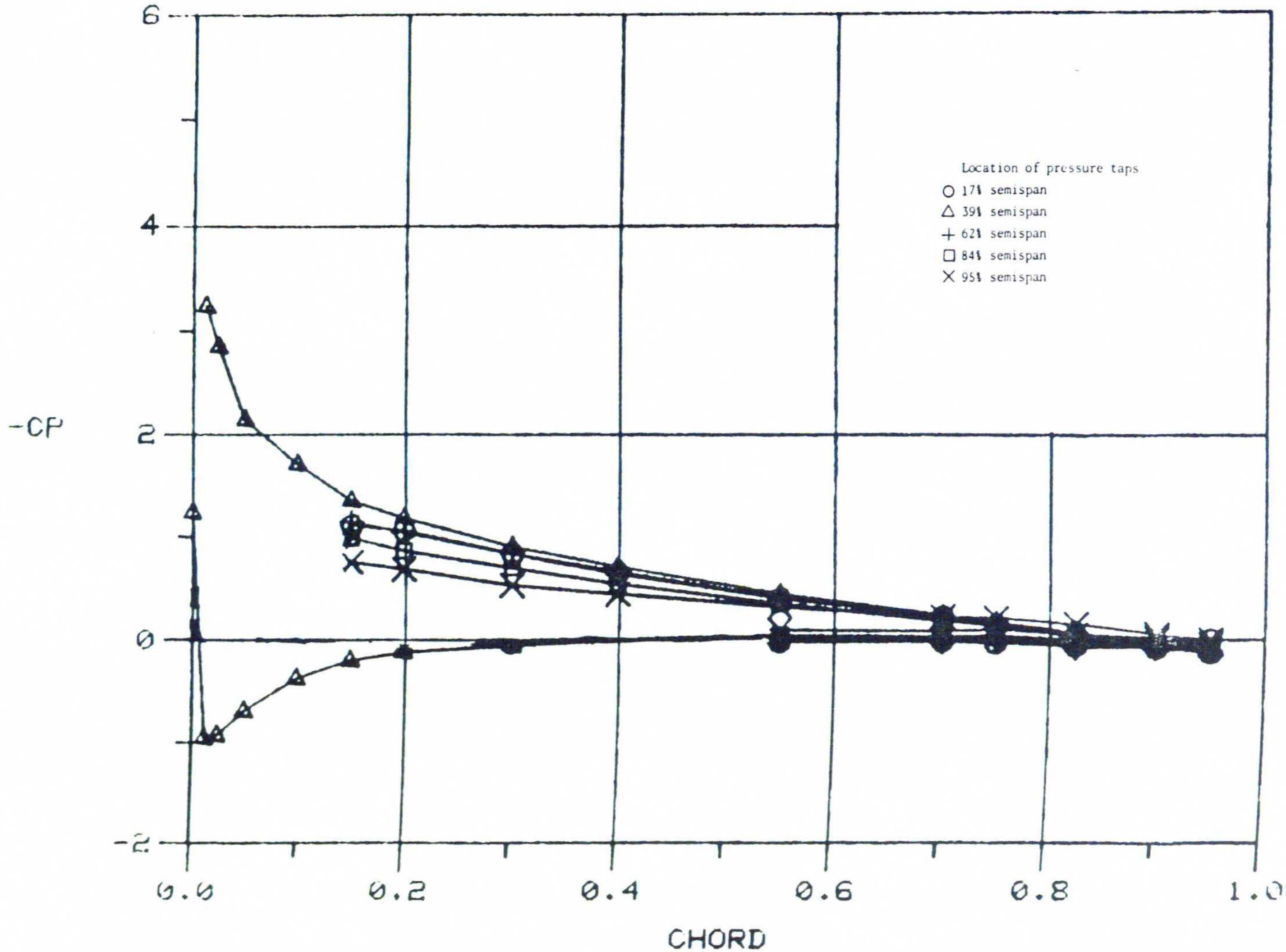

a) $\alpha = 10^{o}$

Figure 33 - Pressure distribution on NACA 0015 wing with glove on entire leading edge except at 37.5% to 50% semispan, $Re_c = 2.0 \times 10^6$.

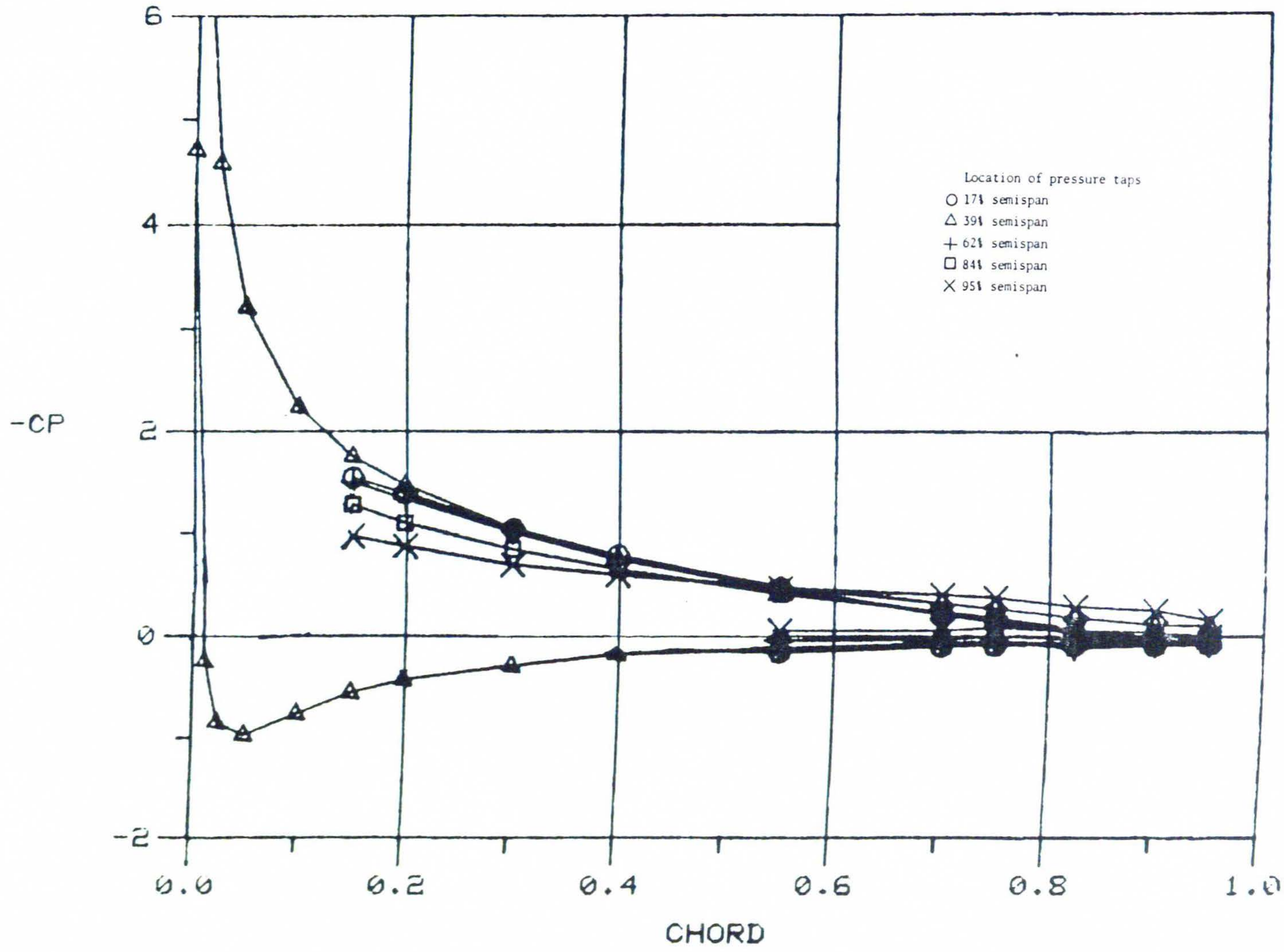

b) $\alpha = 16.5^{\circ}$

Figure 33 - Continued.

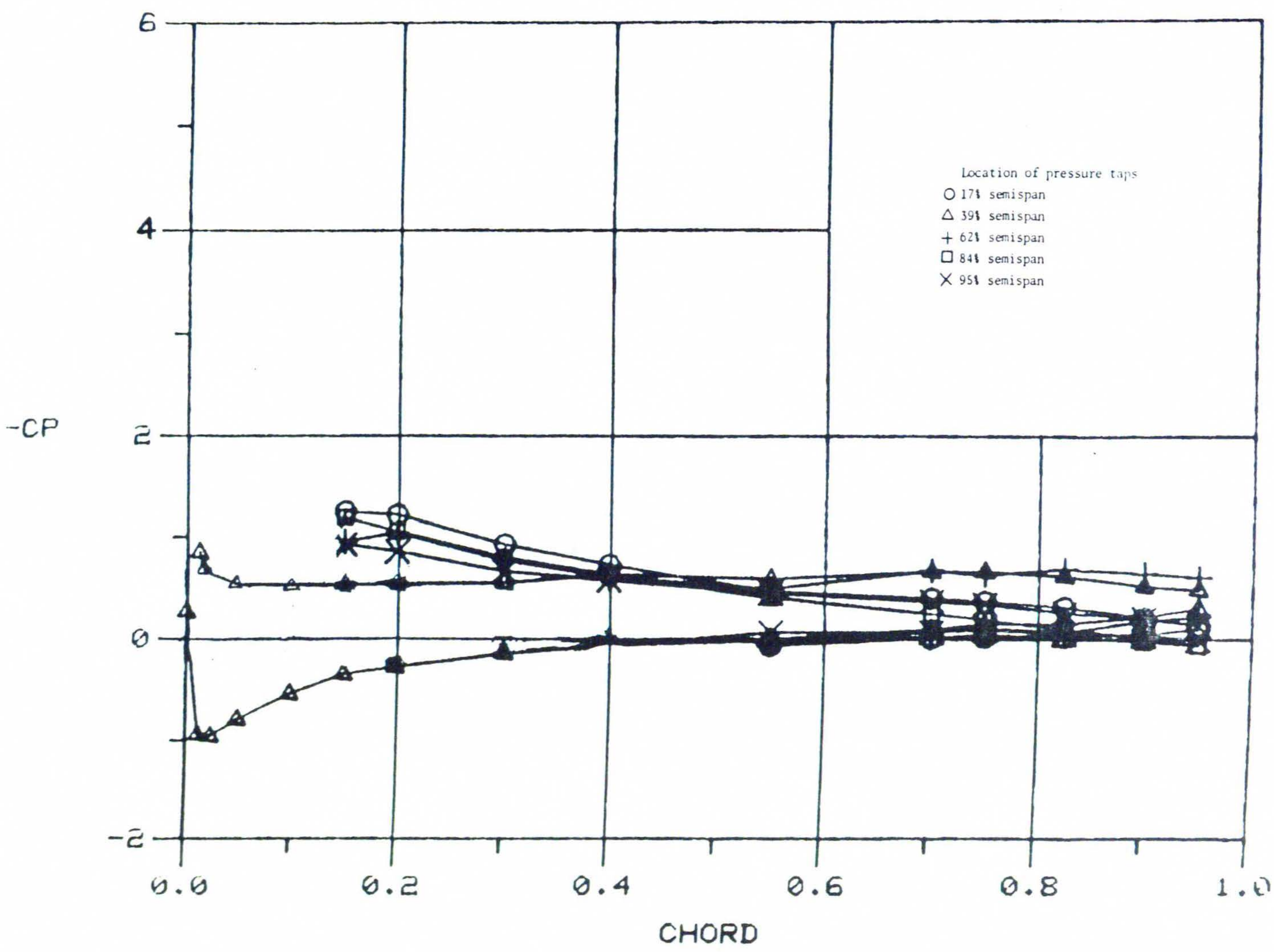

c) $\alpha = 17.5^{\circ}$

Figure 33 - Continued.

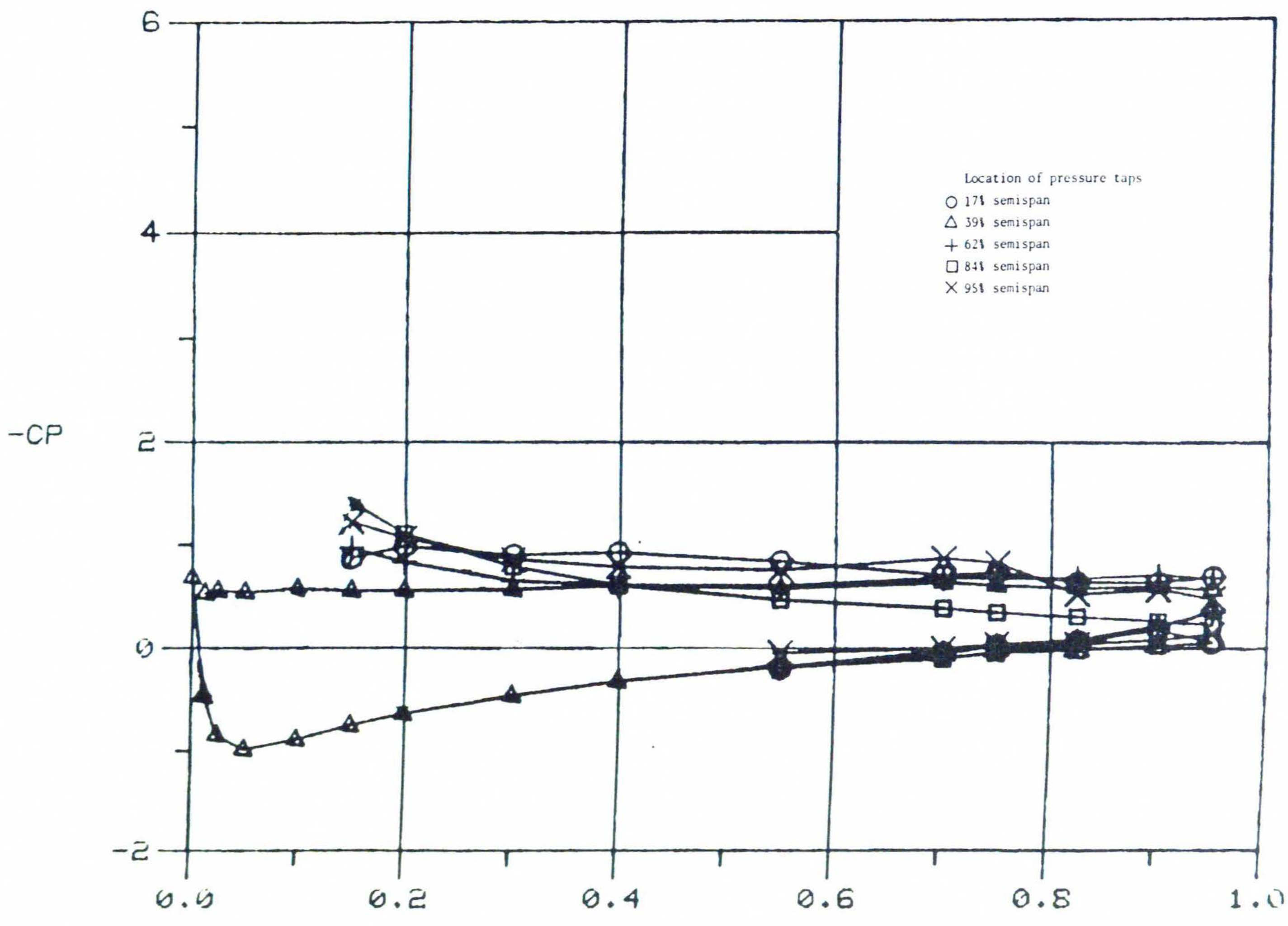

d) $\alpha = 30^{\circ}$

Figure 33 - Continued.

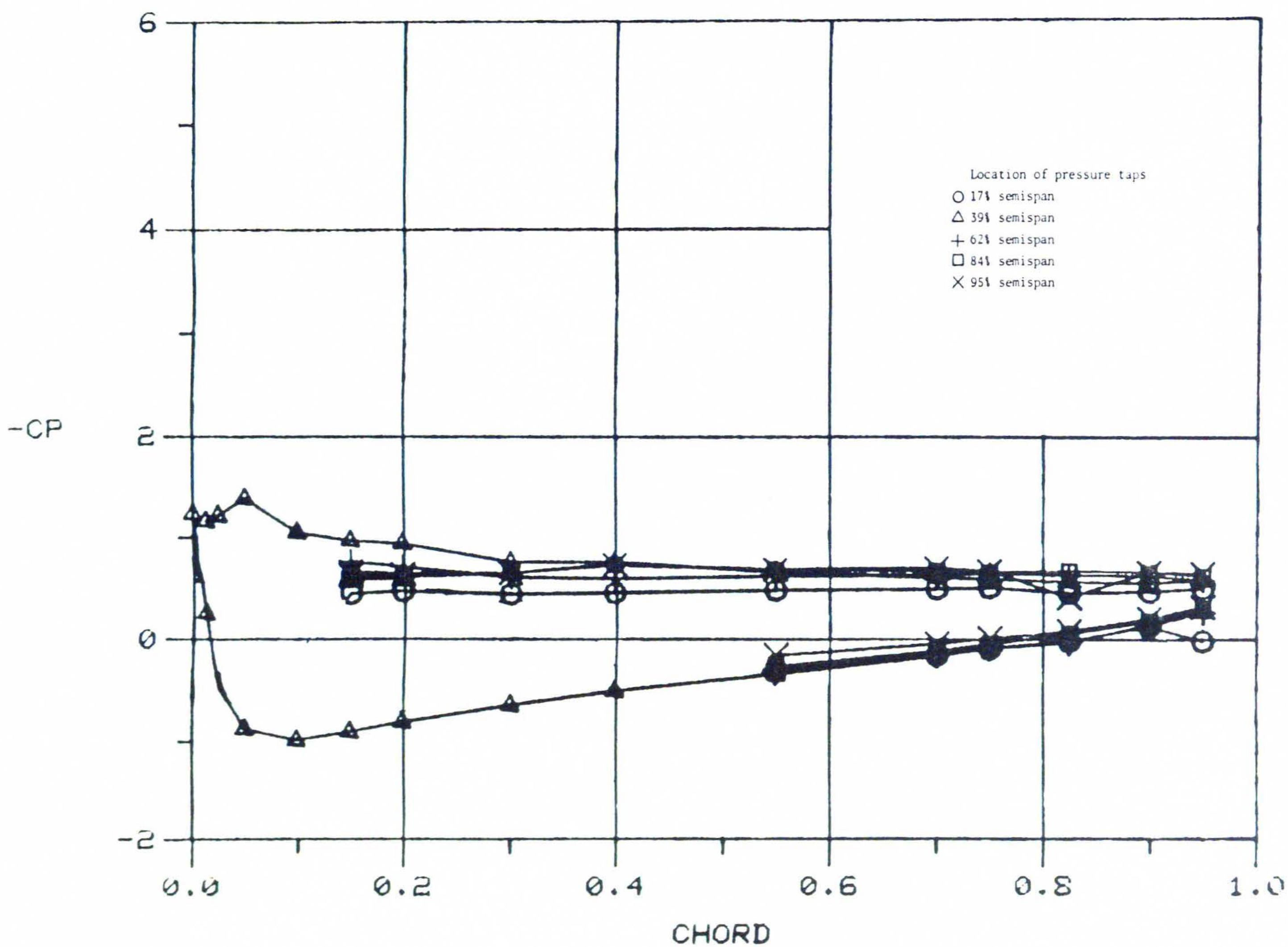

e) $\alpha = 40^{\circ}$

Figure 33 - Continued.

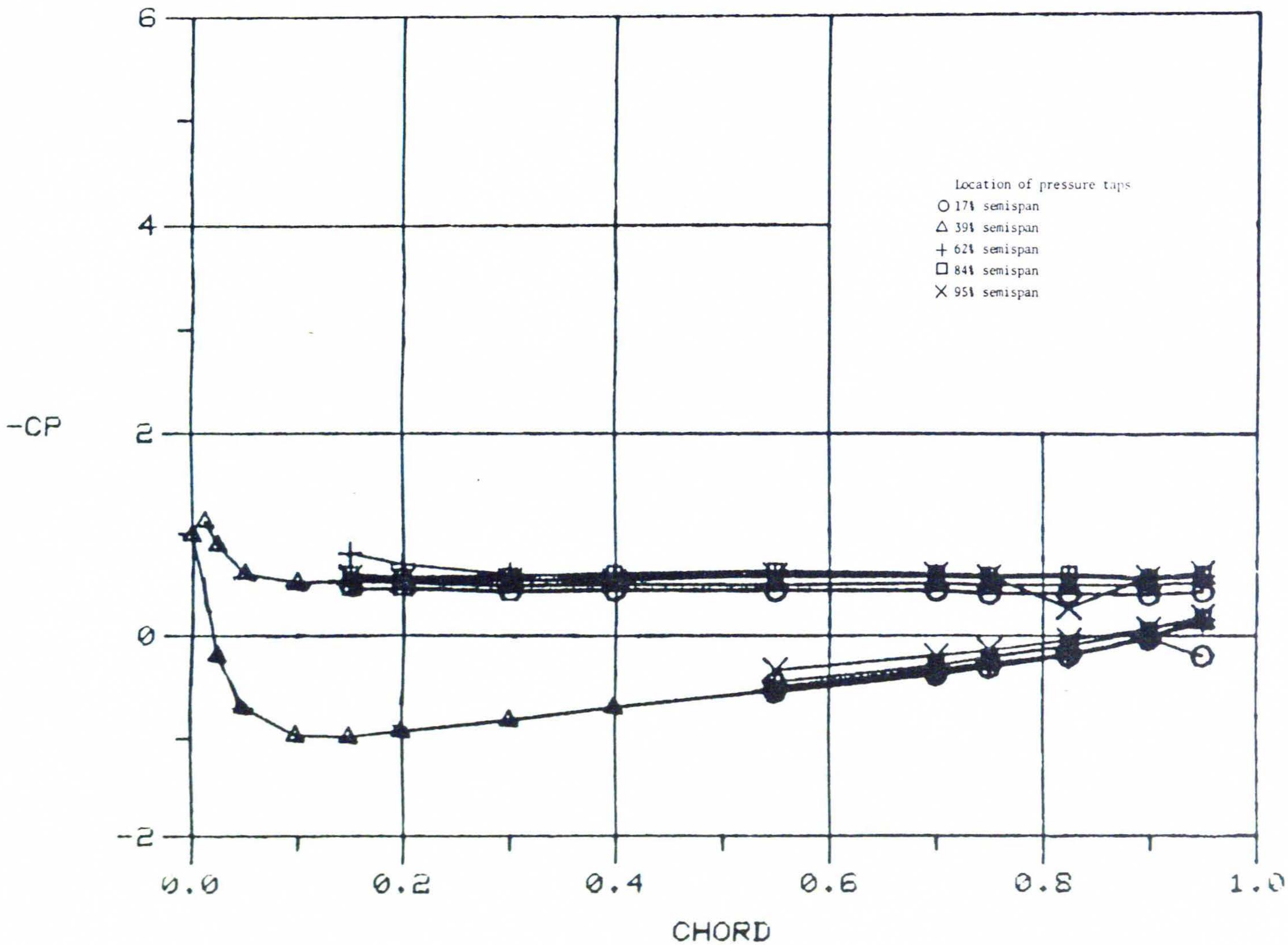

f) $\alpha = 50^{\circ}$

Figure 33 - Concluded.

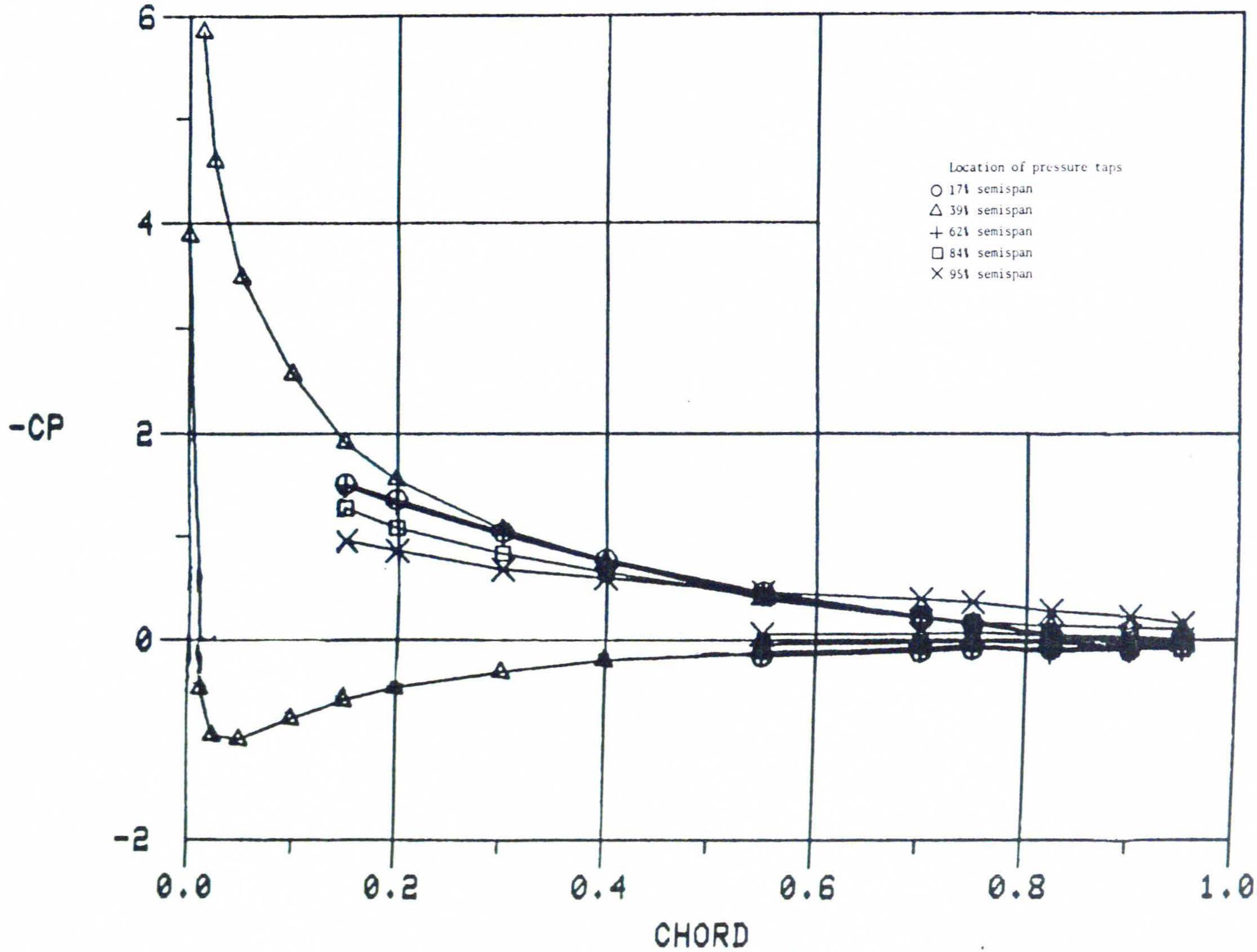

a) α = 16.5°

Figure 34 - Pressure distribution on NACA 0015 wing with glove on entire leading edge except at 25% to 50% semispan, $Re = 2.0 \times 10^6$

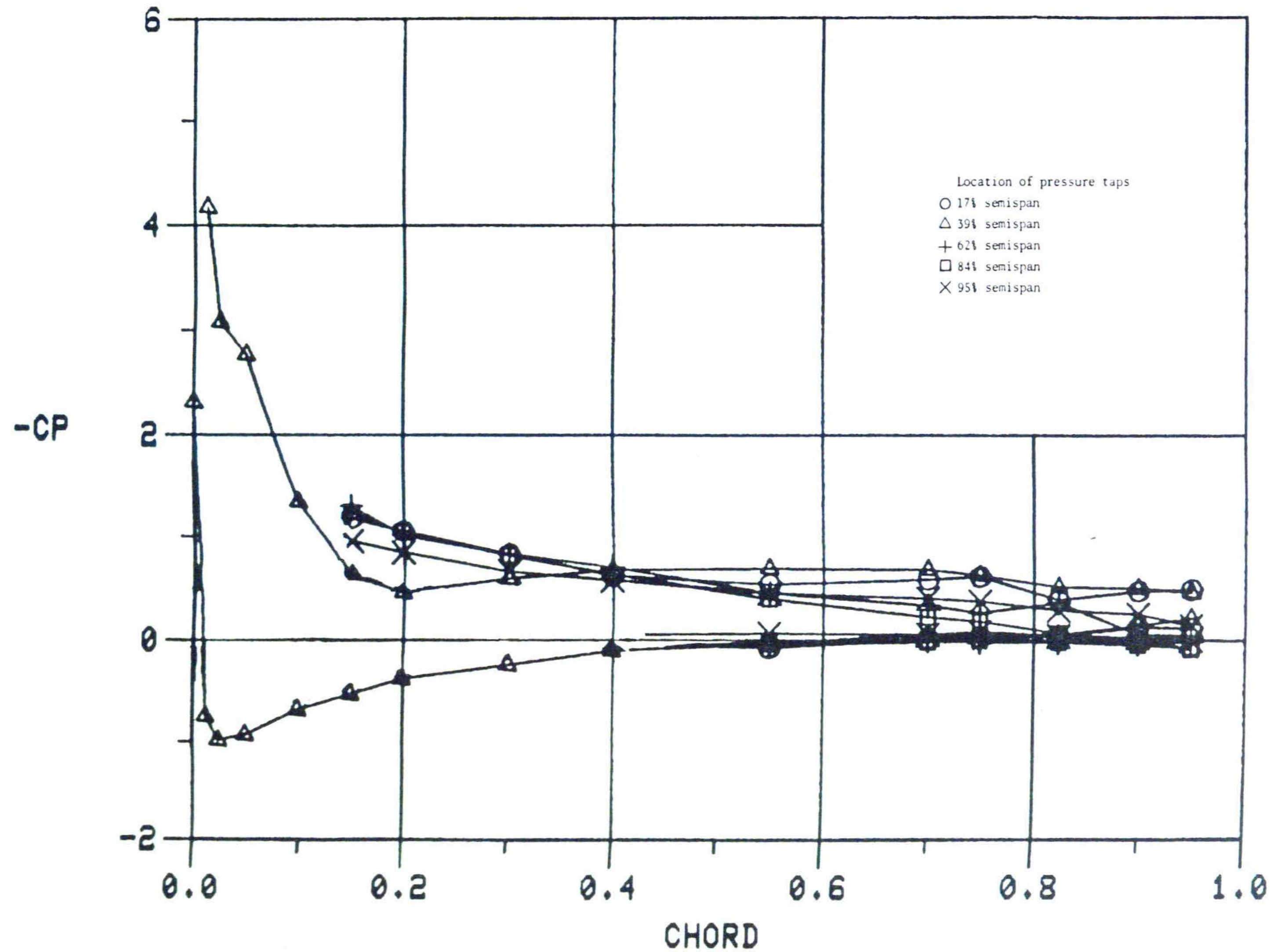

b) $\alpha = 17.5^{o}$

Figure 34 - Continued.

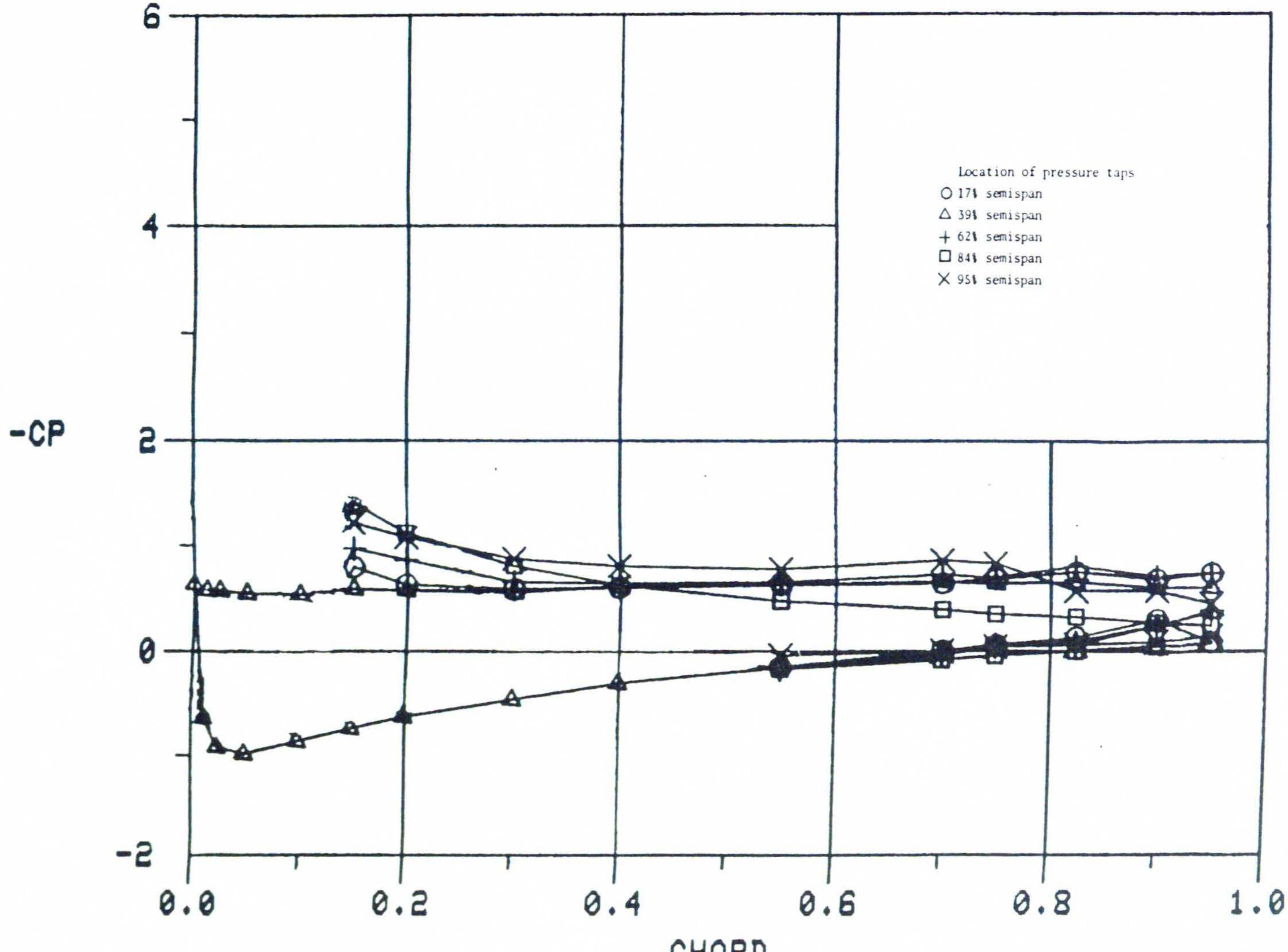

c) $\alpha = 30^{\circ}$

Figure 34 - Continued.

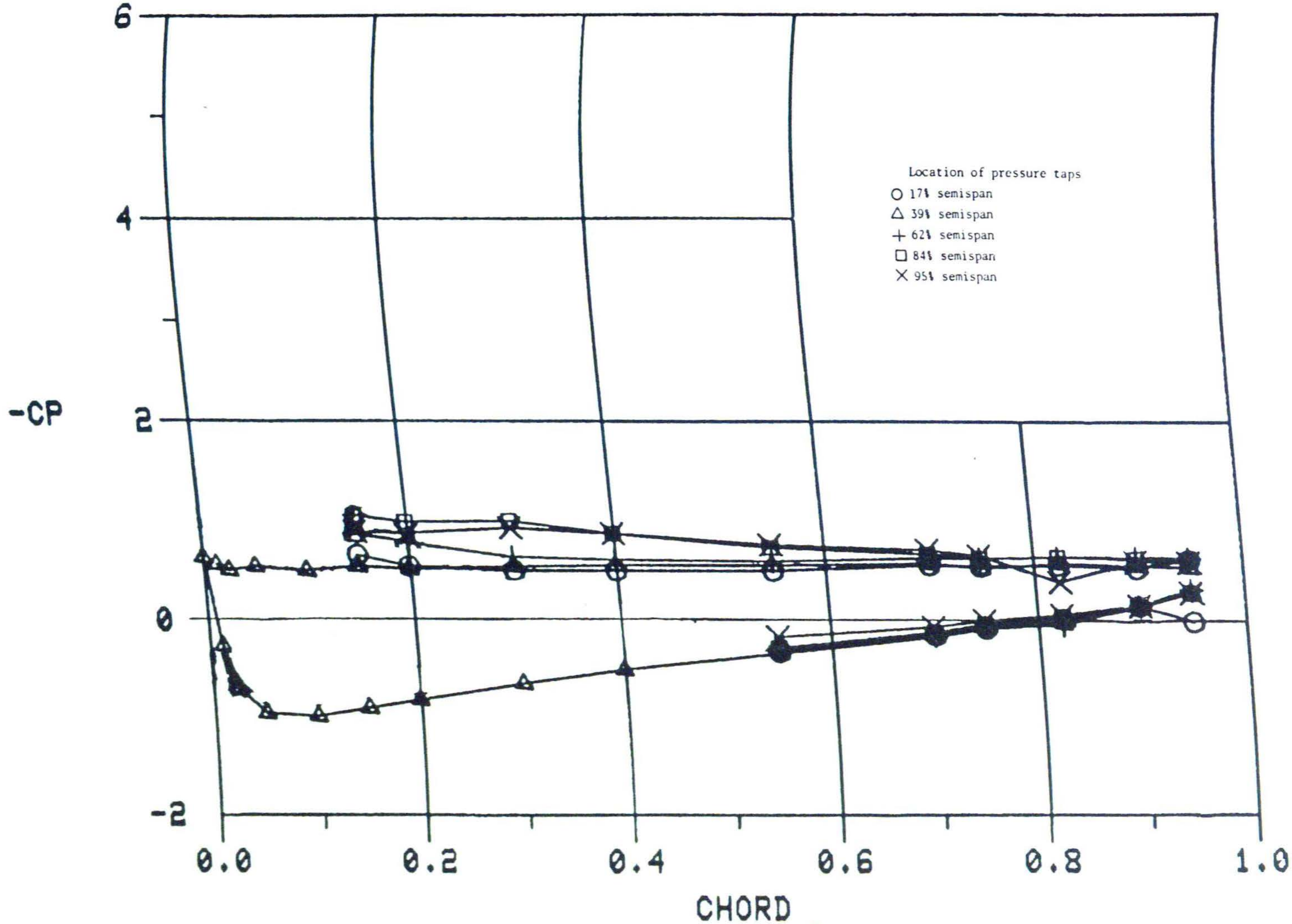

d) $\alpha = 40^{o}$

Figure 34 - Continued.

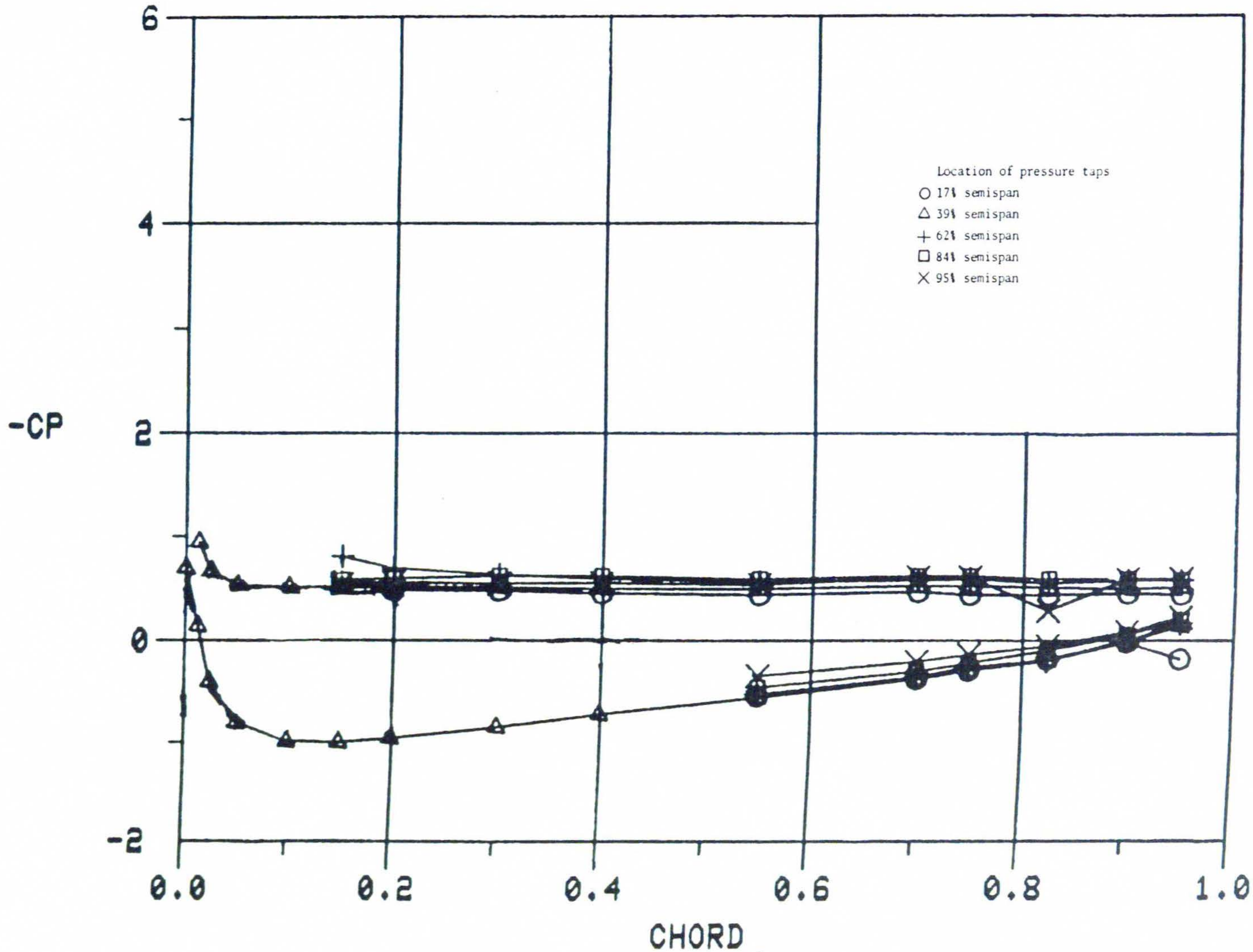

e) $\alpha = 50^{o}$

Figure 34 - Concluded.

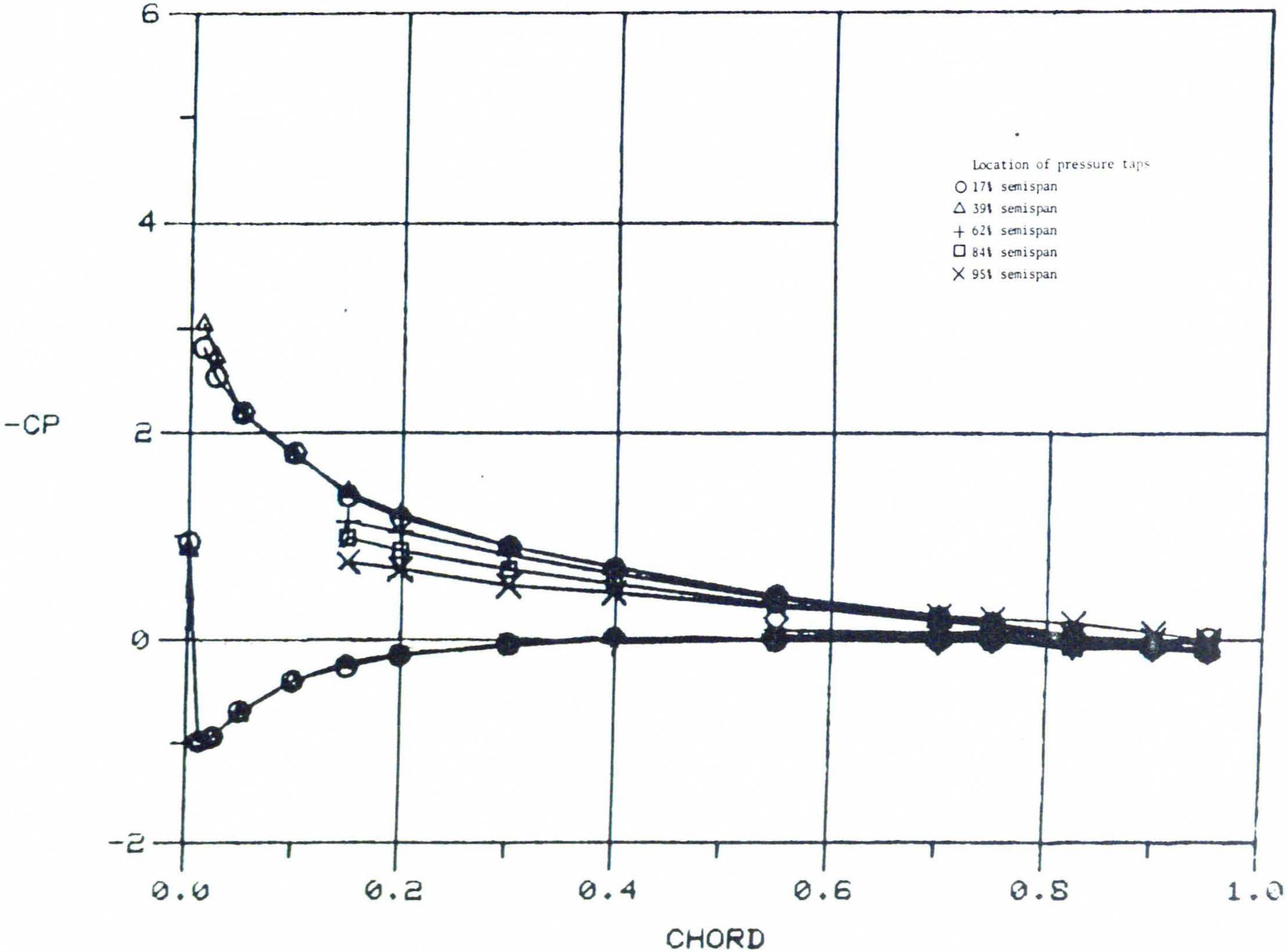

a) $\alpha = 10^{o}$

Figure 35 - Pressure distribution on NACA 0015 wing with glove on outer half semispan, $Re_c = 2.0 \times 10^6$.

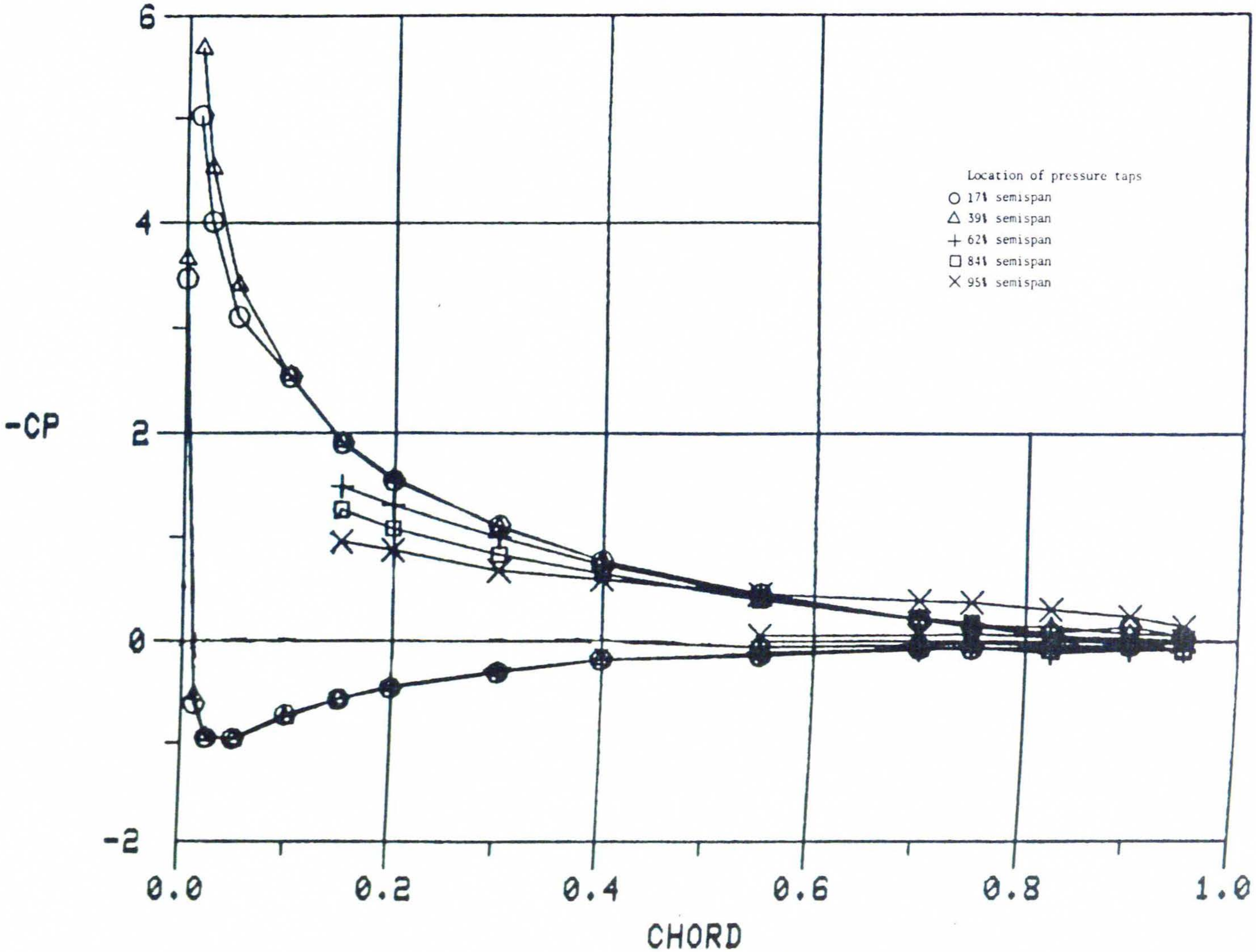

b) $\alpha = 16.5^{\circ}$

Figure 35 - Continued.

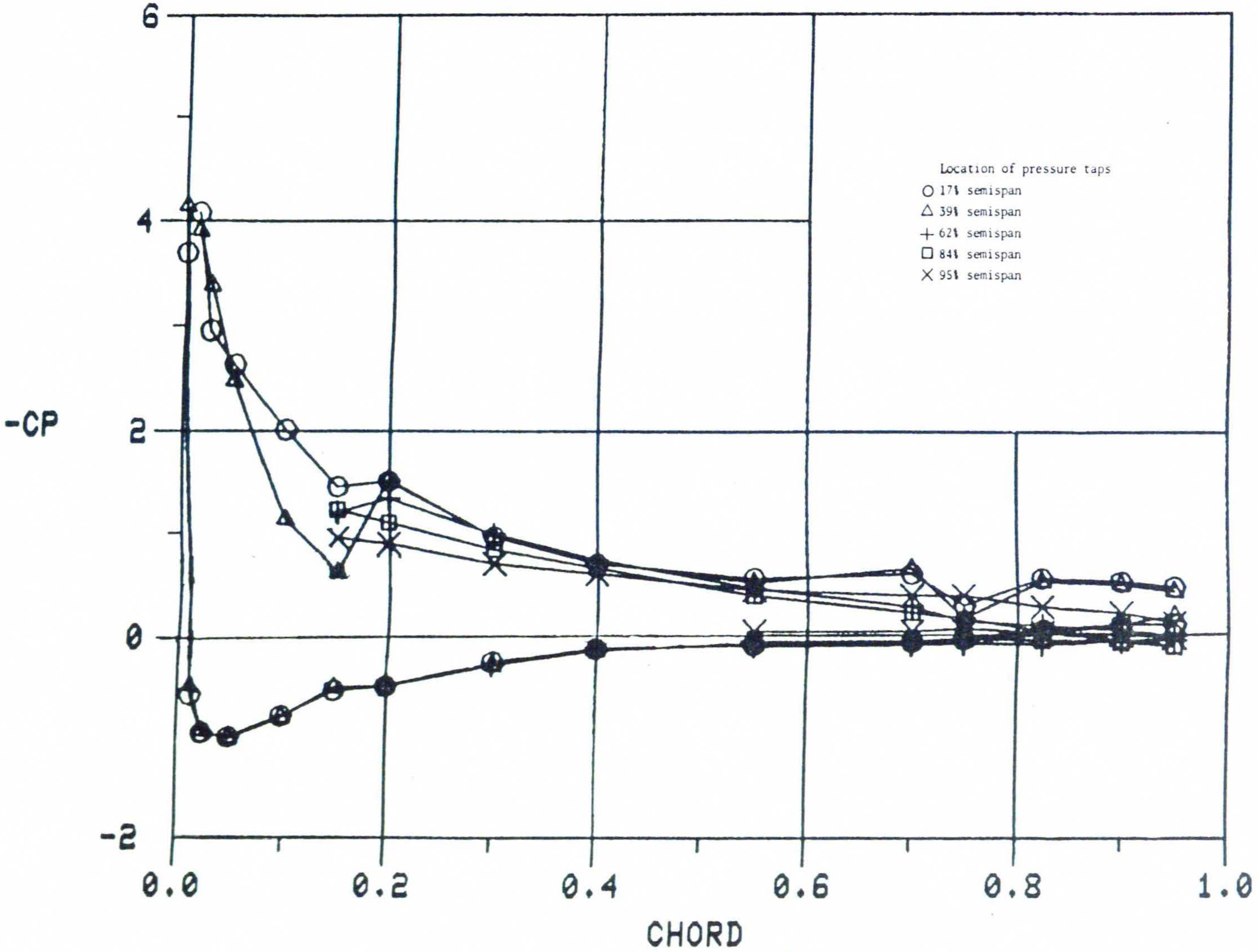

c) $\alpha = 17.5^{\circ}$

Figure 35 - Continued.

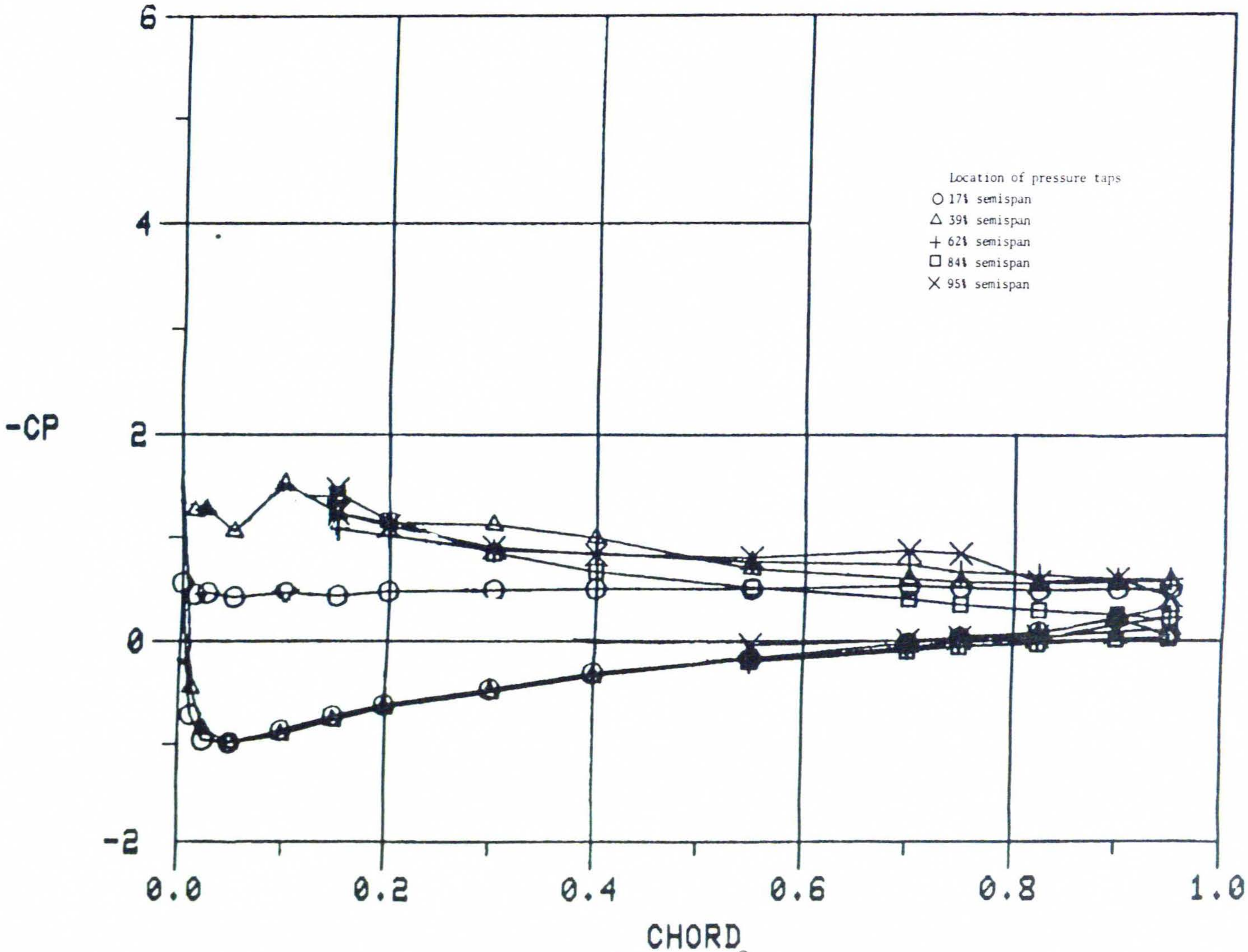

d) $\alpha = 30^{o}$

Figure 35 - Continued.

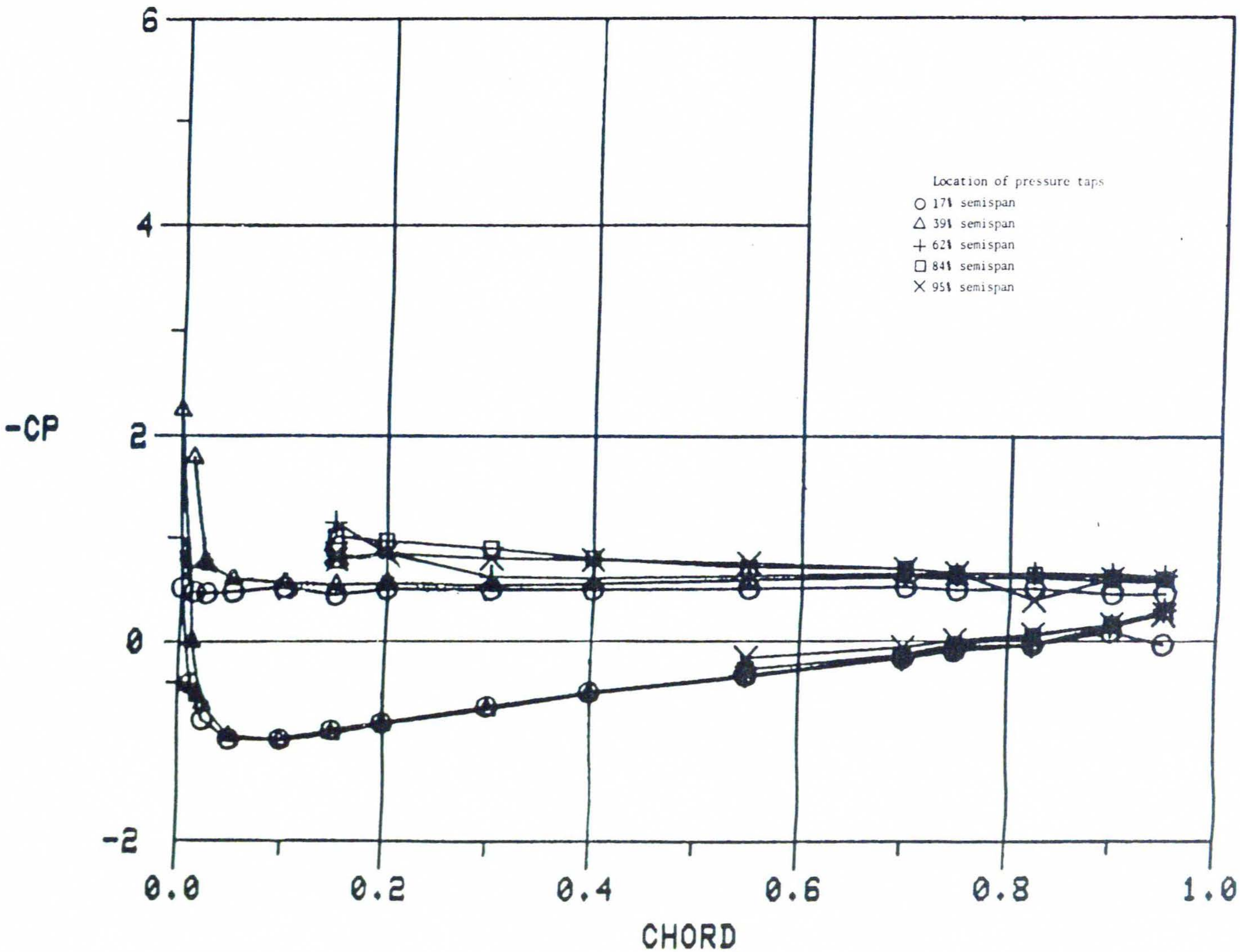

e) $\alpha = 40^{\circ}$

Figure 35 - Continued.

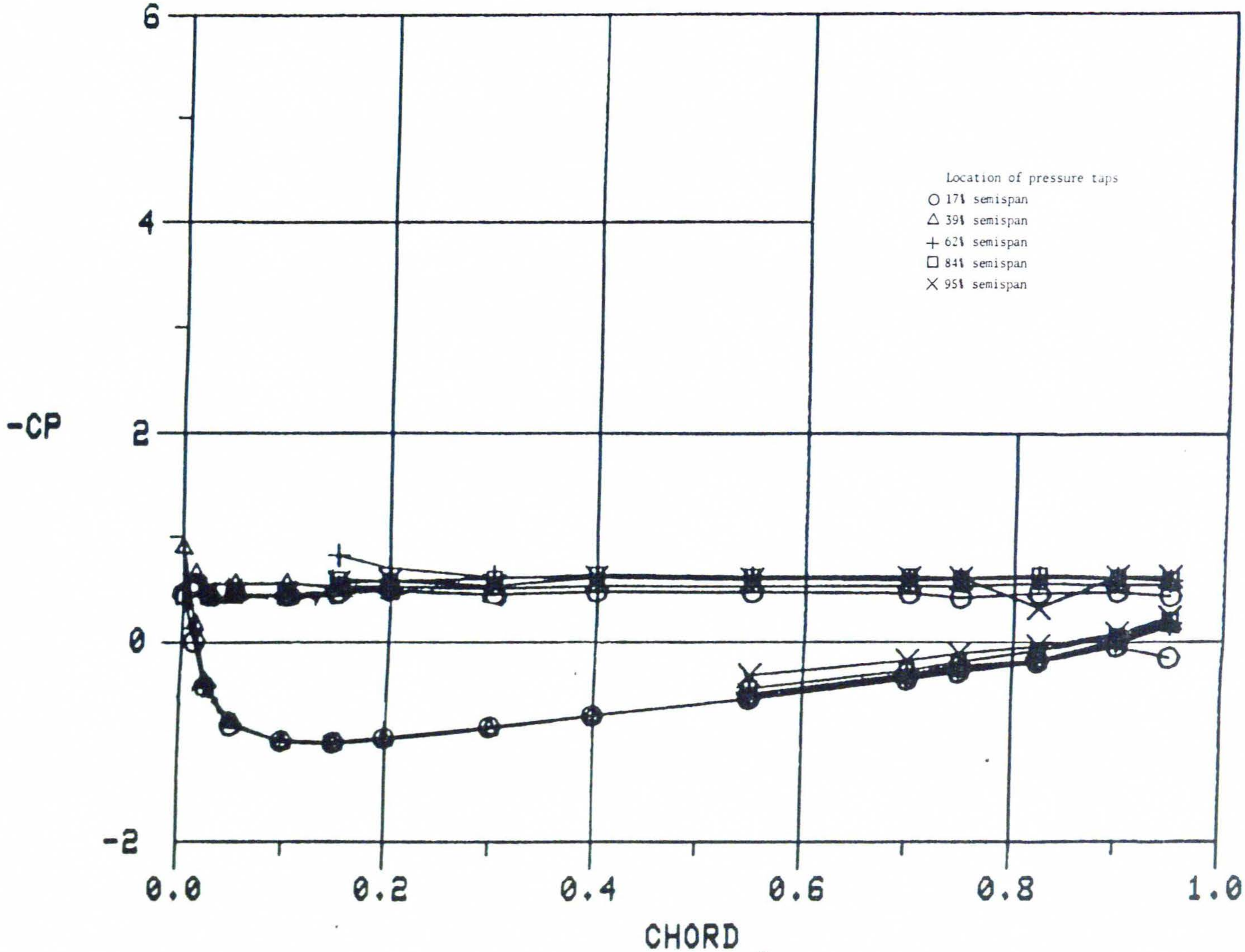

f) α = 50°

Figure 35 - Concluded.

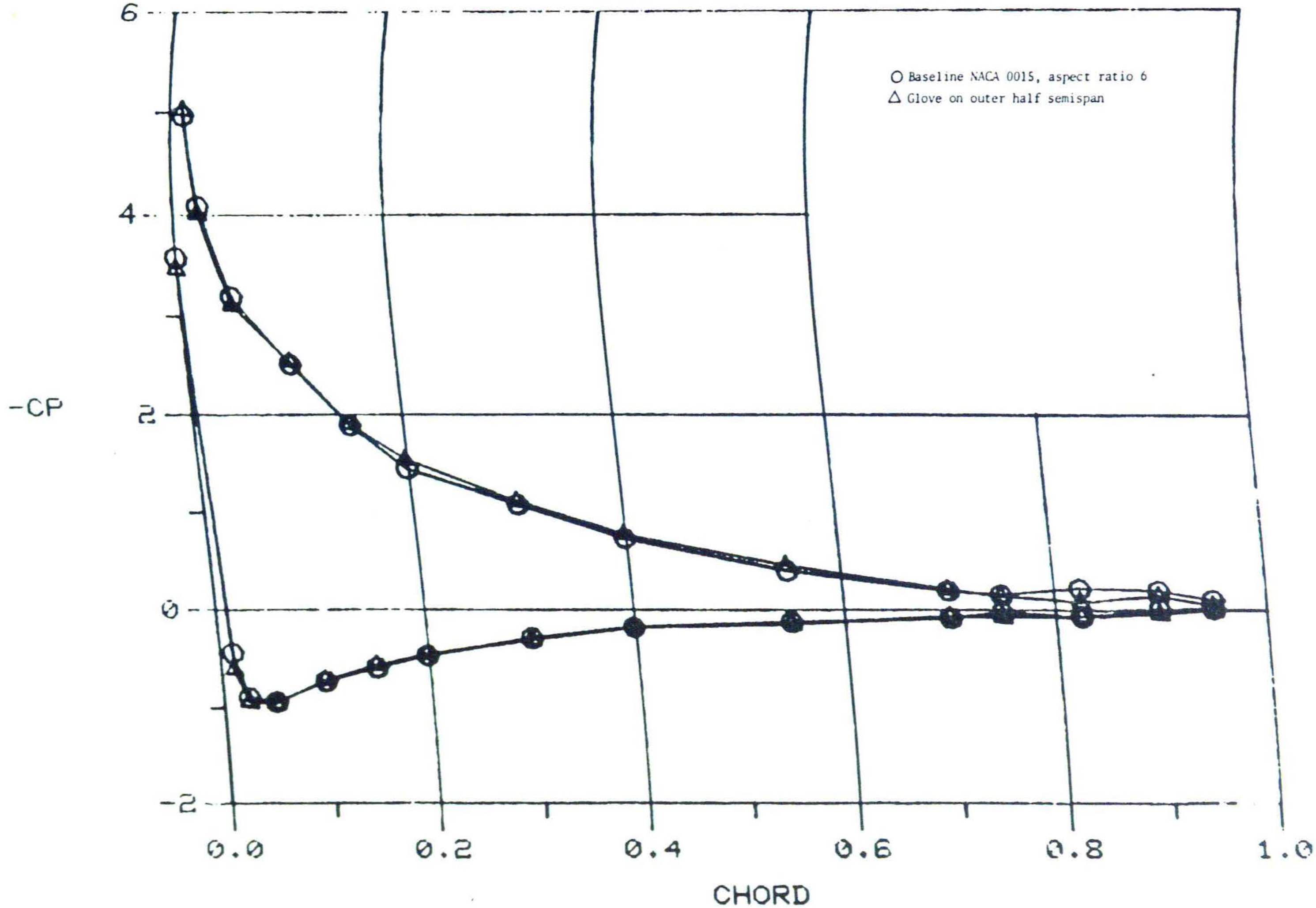

a) Maximum lift angle

Figure 36 - Pressure distribution at 17% semispan for various leading edge modifications, $Re_c = 2.0 \times 10^6$.

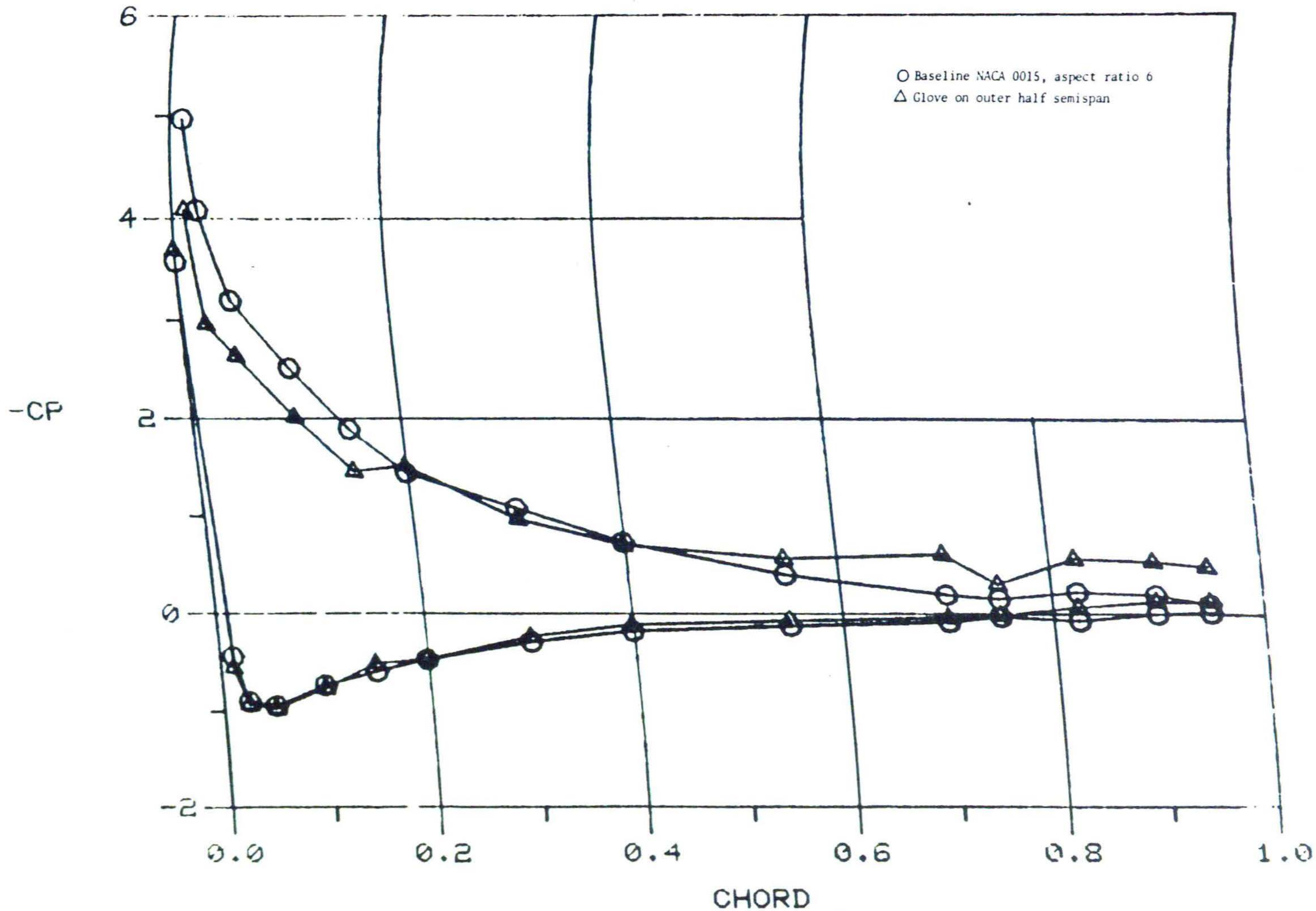

b) $\alpha = 17.5^{\circ}$

Figure 36 - Continued.

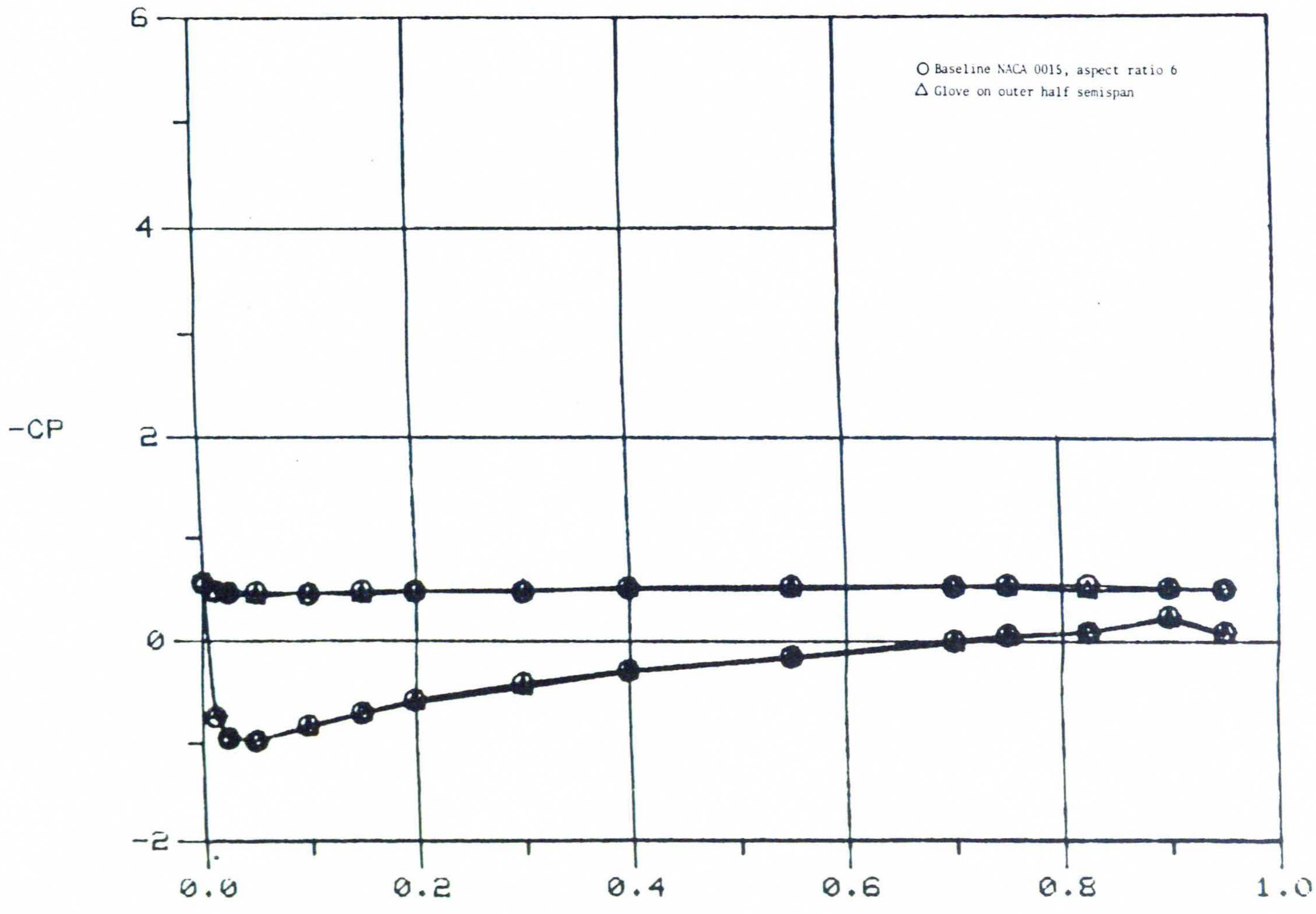

c) $\alpha = 30^o$

Figure 36 - Continued.

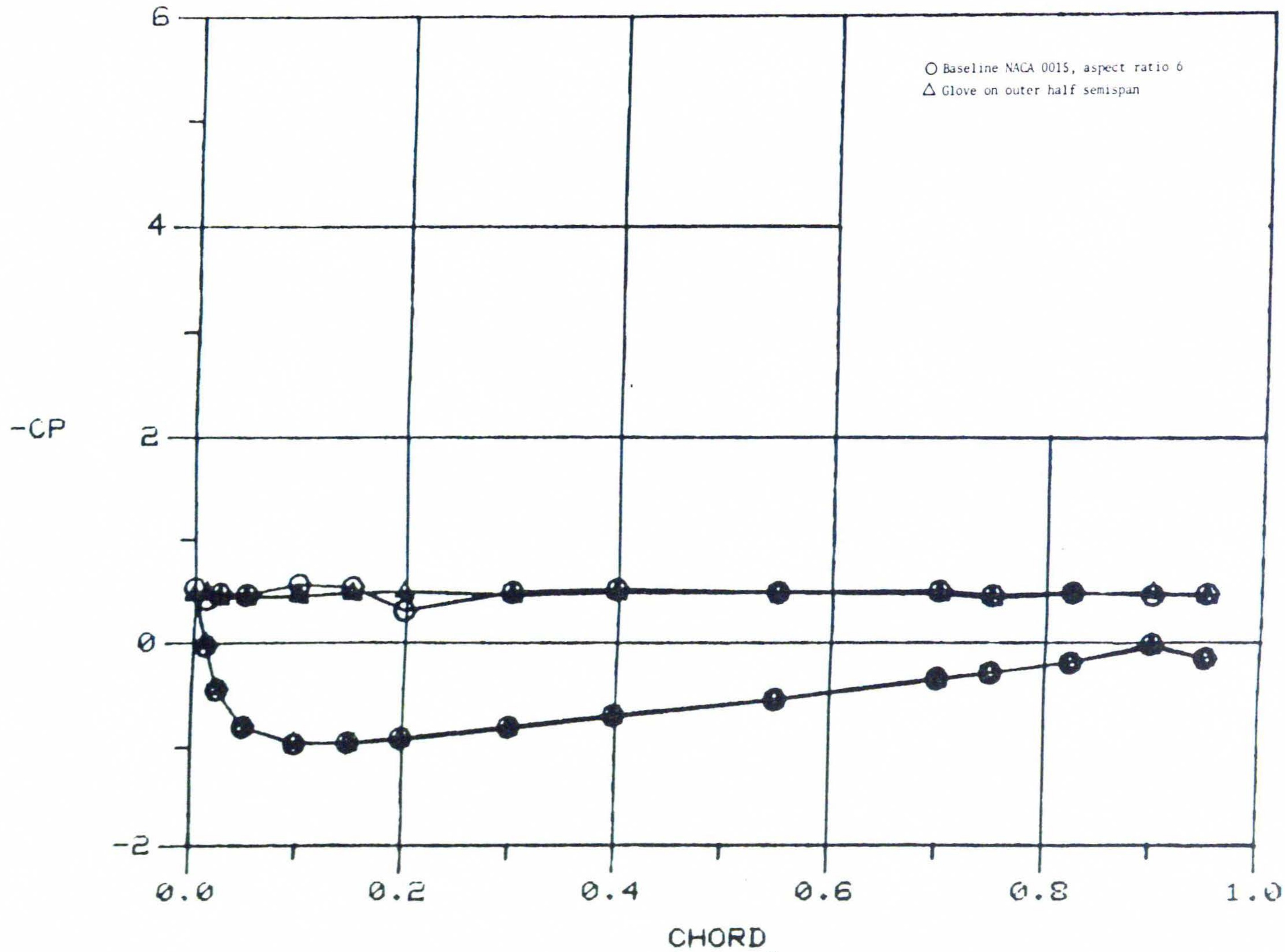

d) α = 50°

Figure 36 - Concluded.

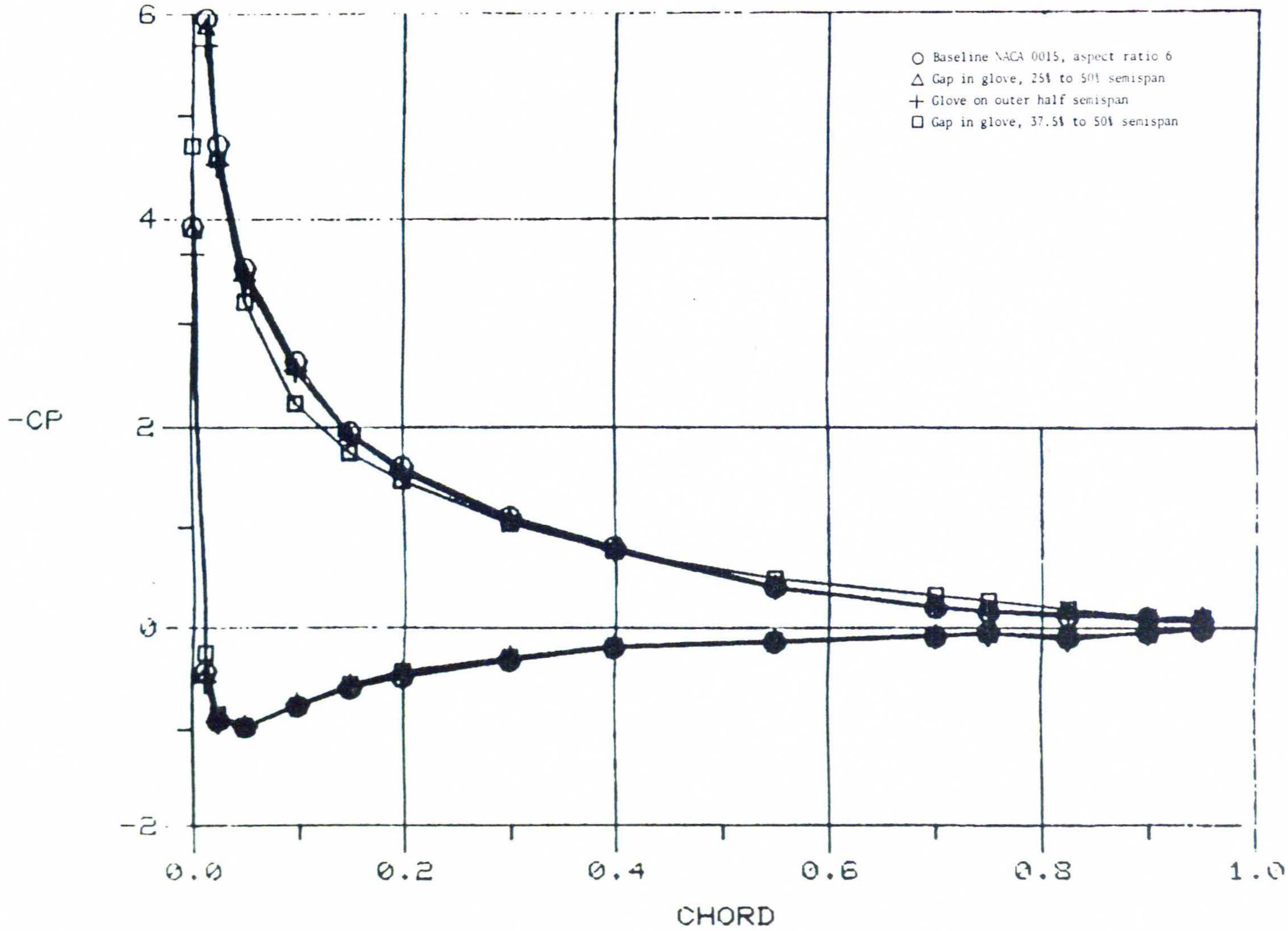

a) Maximum lift angle

Figure 37 - Pressure distribution at 39% semispan for various leading edge modifications, $Re_c = 2.0 \times 10^6$.

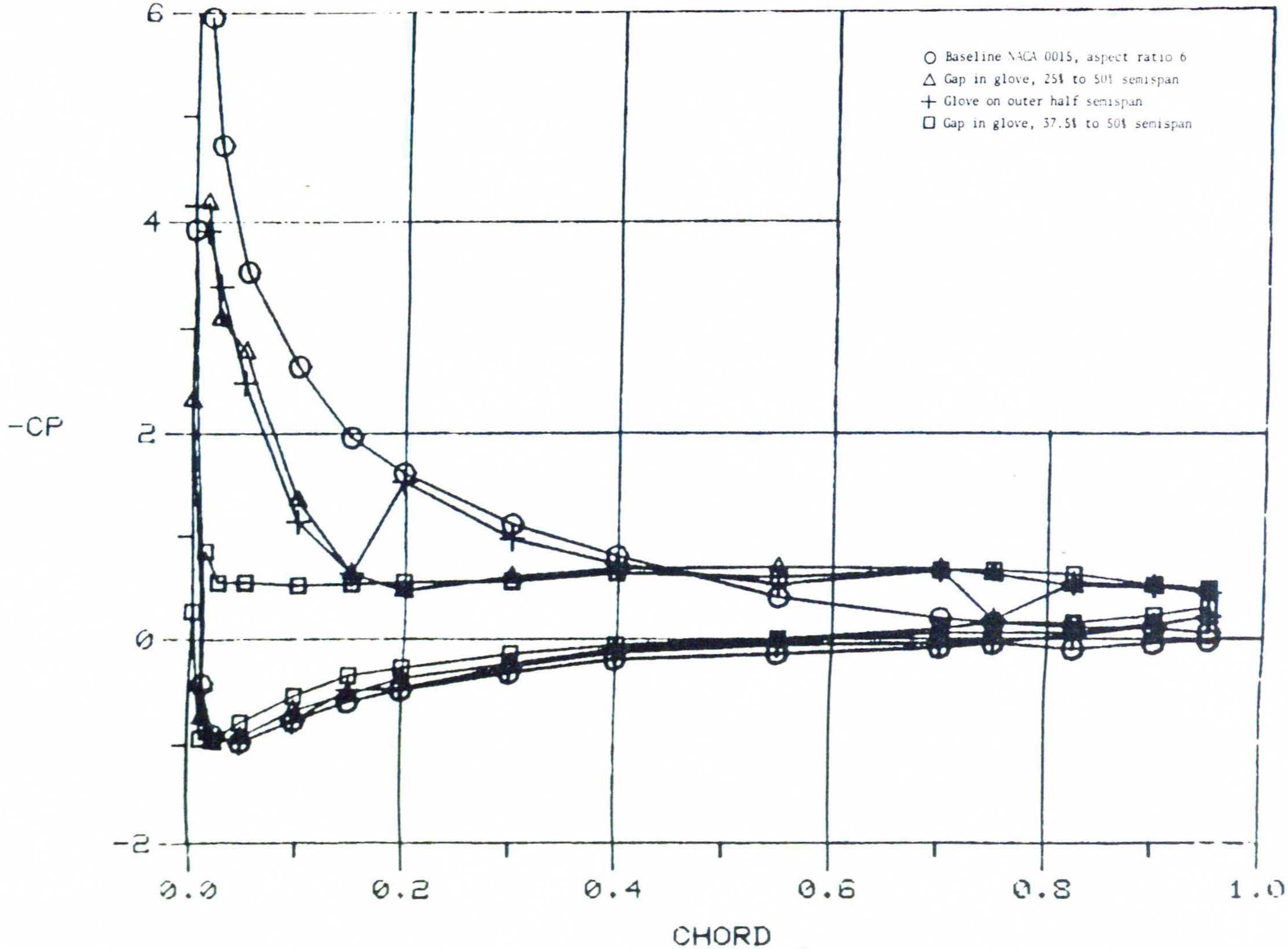

b) $\alpha = 17.5^{\circ}$

Figure 37 - Continued.

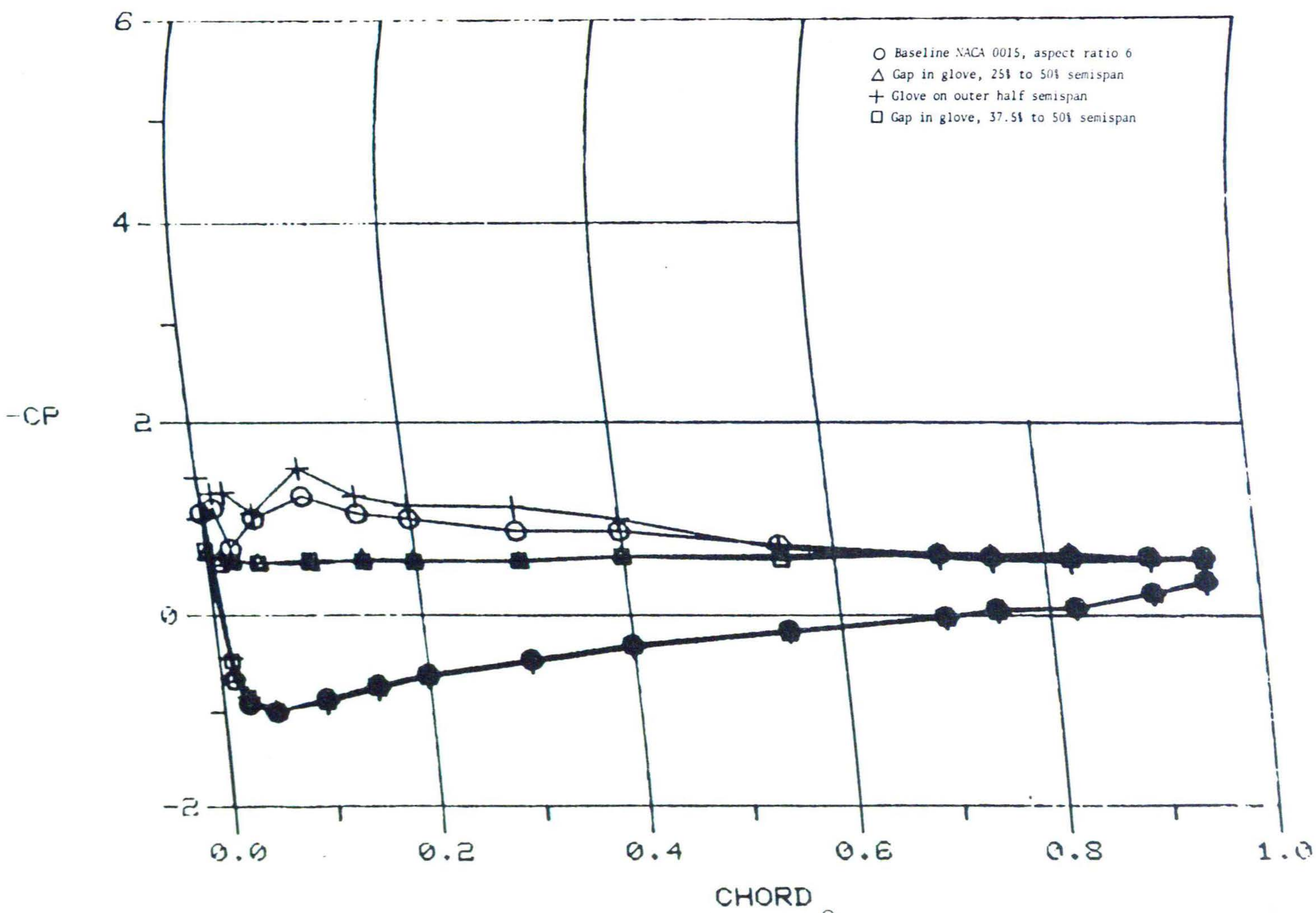

c) $\alpha = 30^{o}$

Figure 37 - Continued.

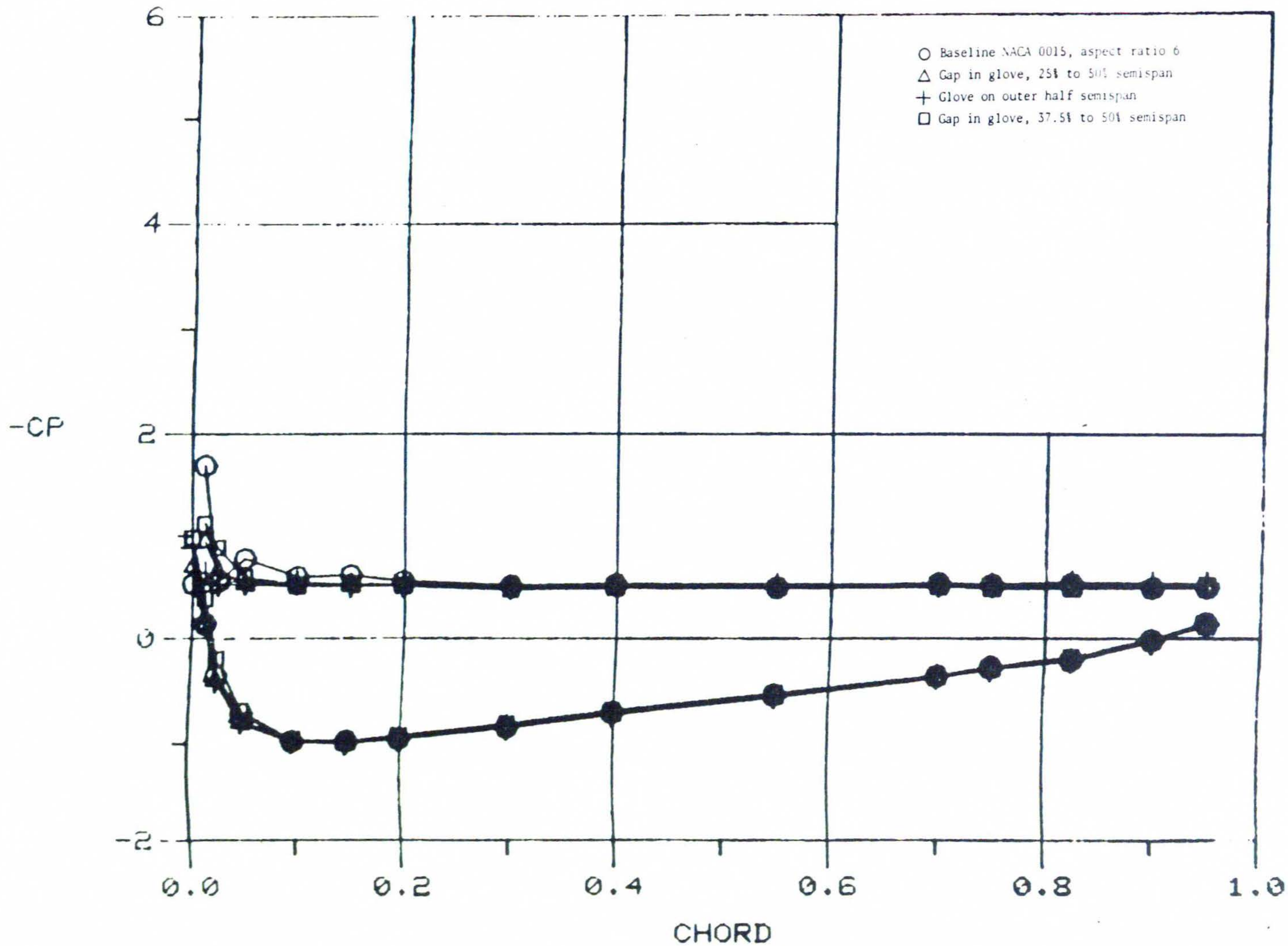

d) $\alpha = 50^{\circ}$

Figure 37 - Concluded.

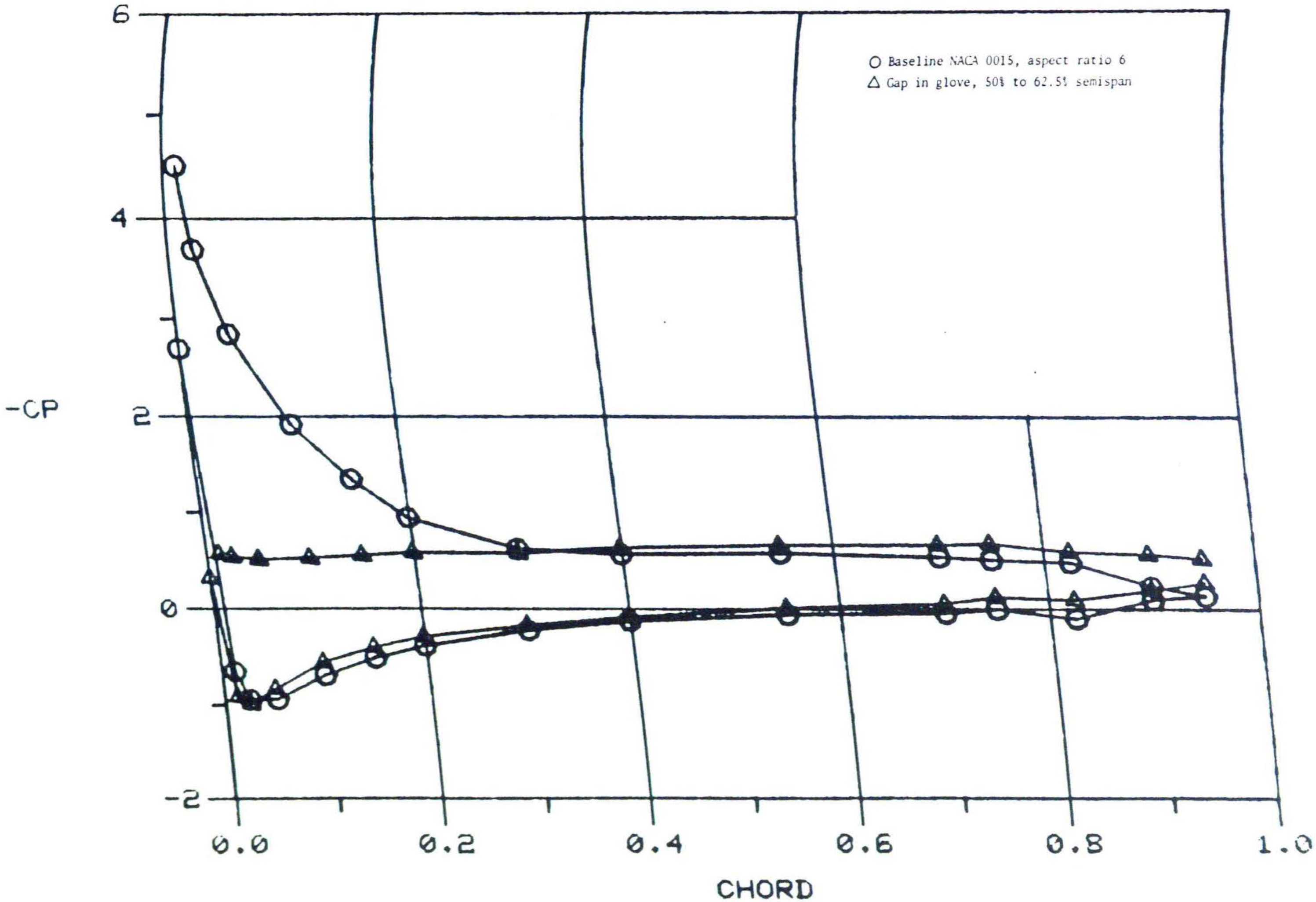

a) $\alpha = 18.5^{\circ}$

Figure 38 - Pressure distribution at 62% semispan for various leading edge modifications, $Re_c = 2.0 \times 10^6$.

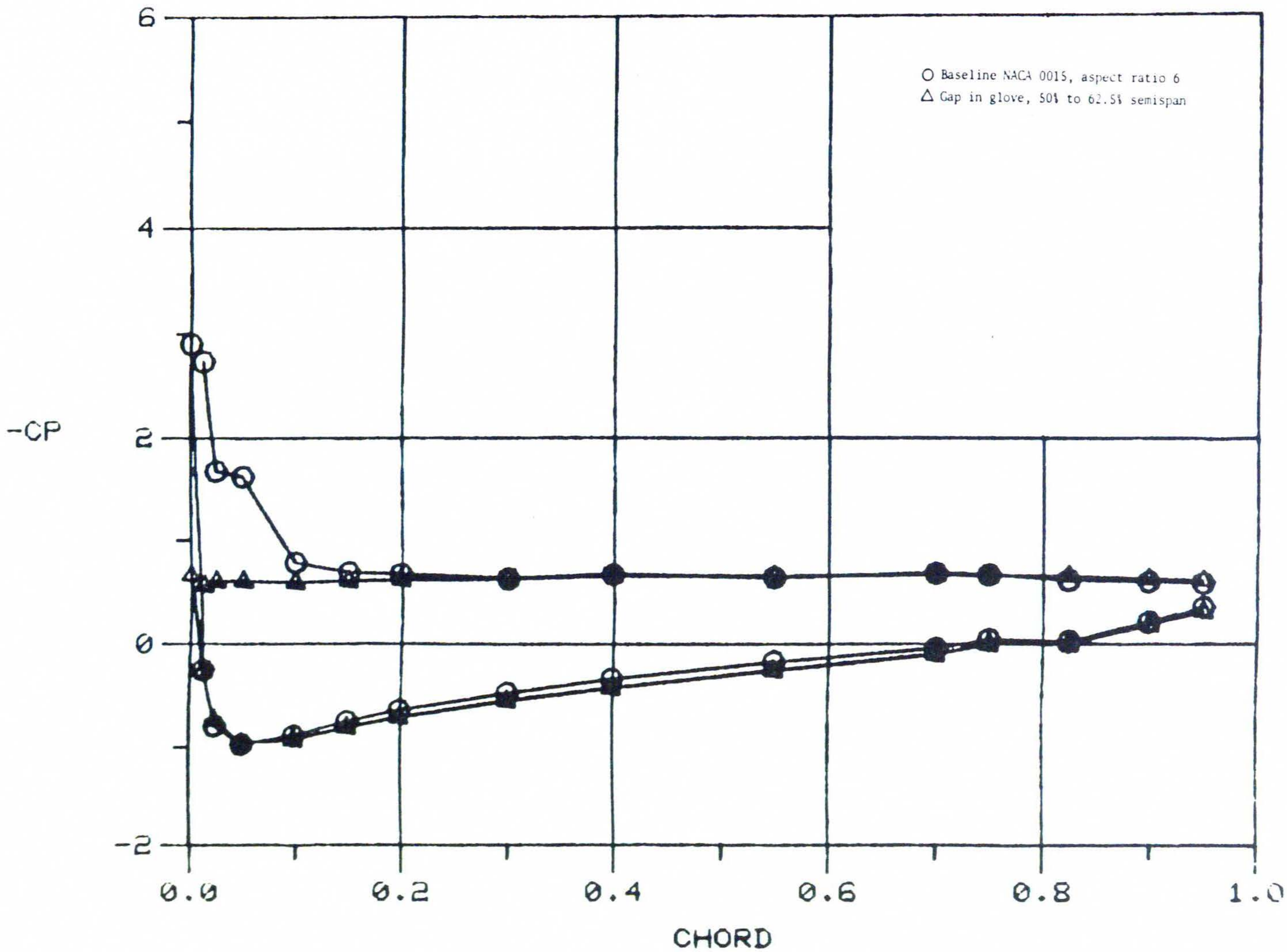

b) $\alpha = 30^{\circ}$

Figure 38 - Continued.

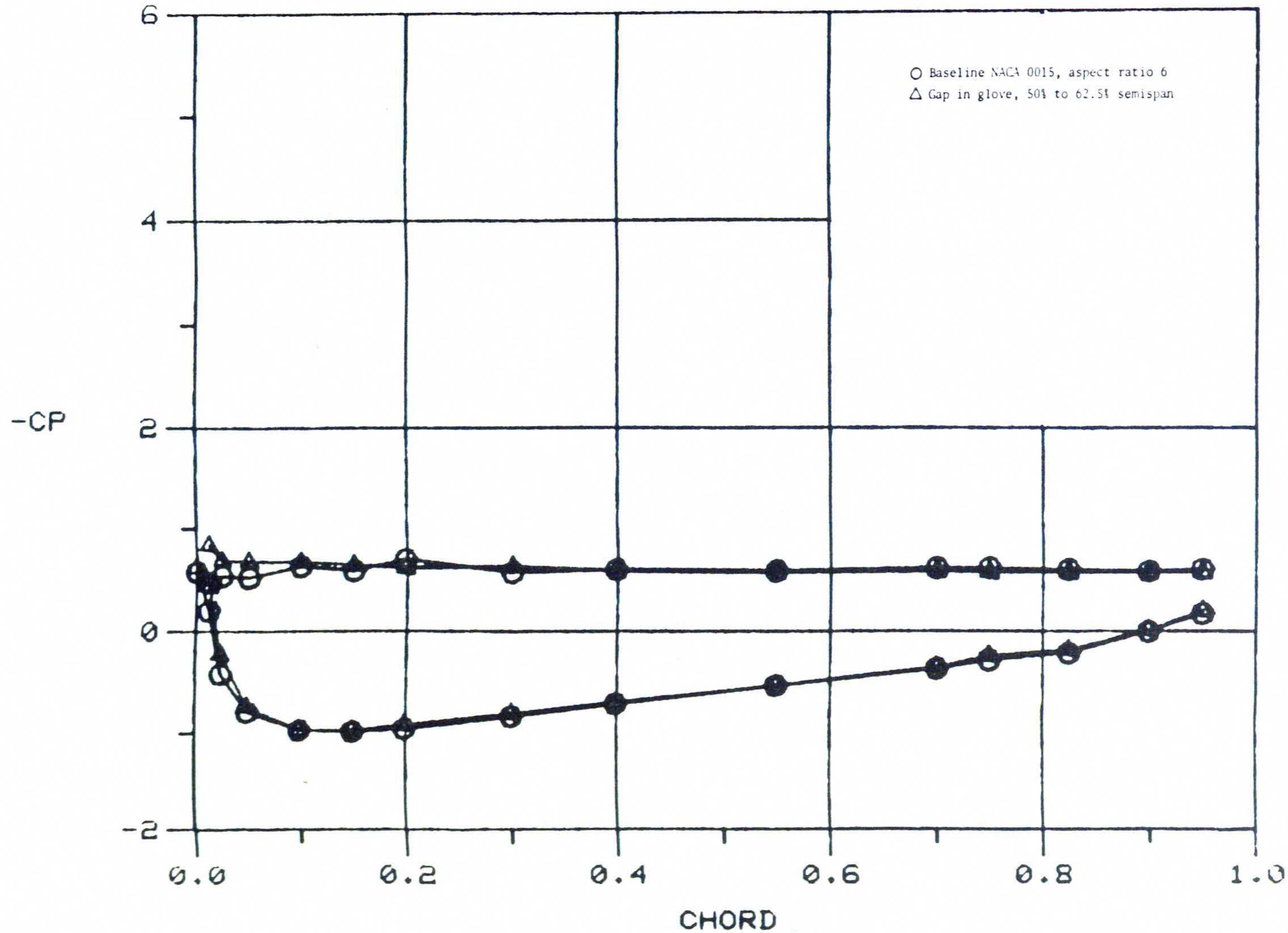

c) $\alpha = 50^{\circ}$

Figure 38 - Concluded.

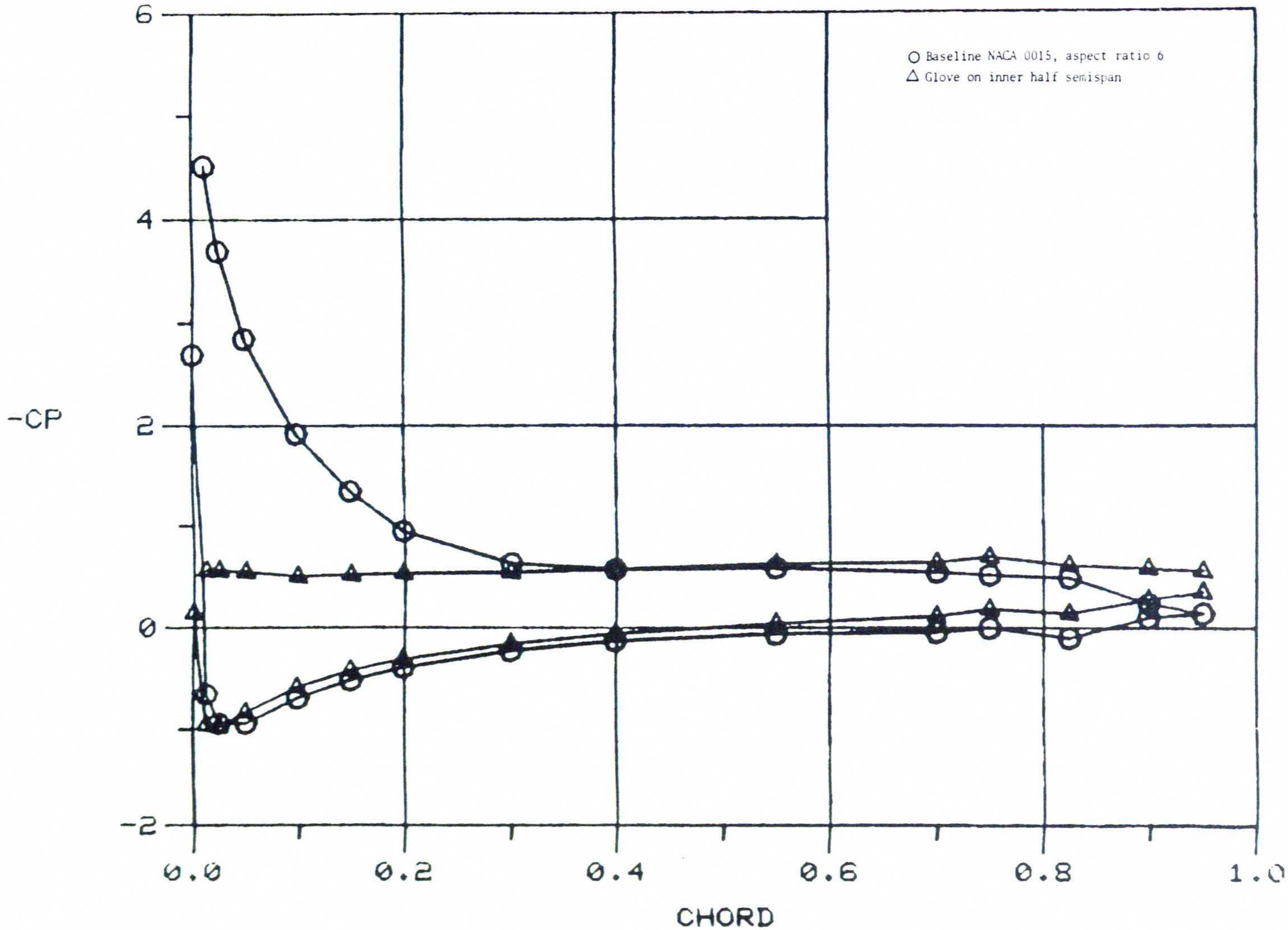

a) At 62% semispan

Figure 39 - Pressure distribution on NACA 0015 wing with and without modifications at $\alpha = 18.5^0$, $Re_c = 2.0 \times 10^6$.

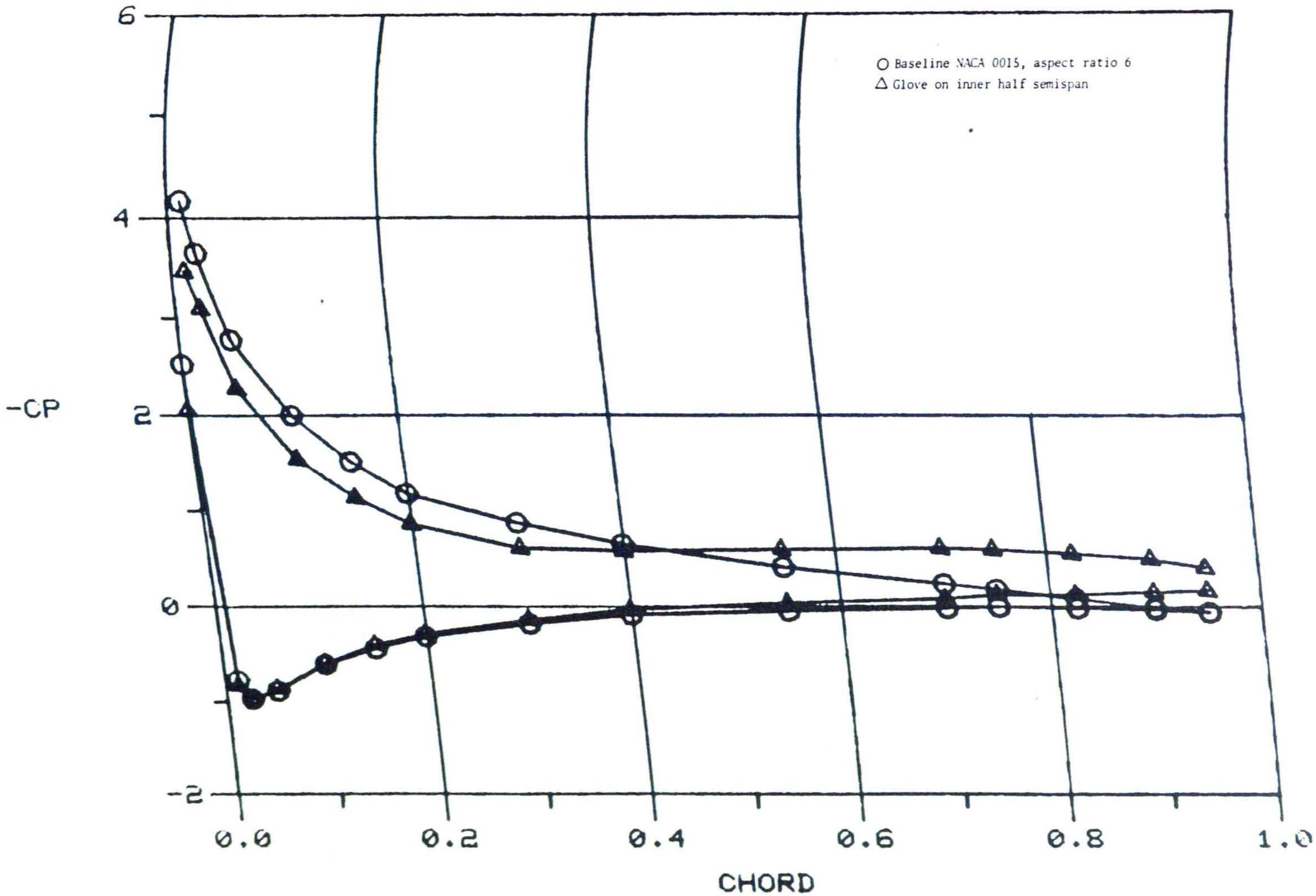

b) At 84% semispan

Figure 39 - Continued.

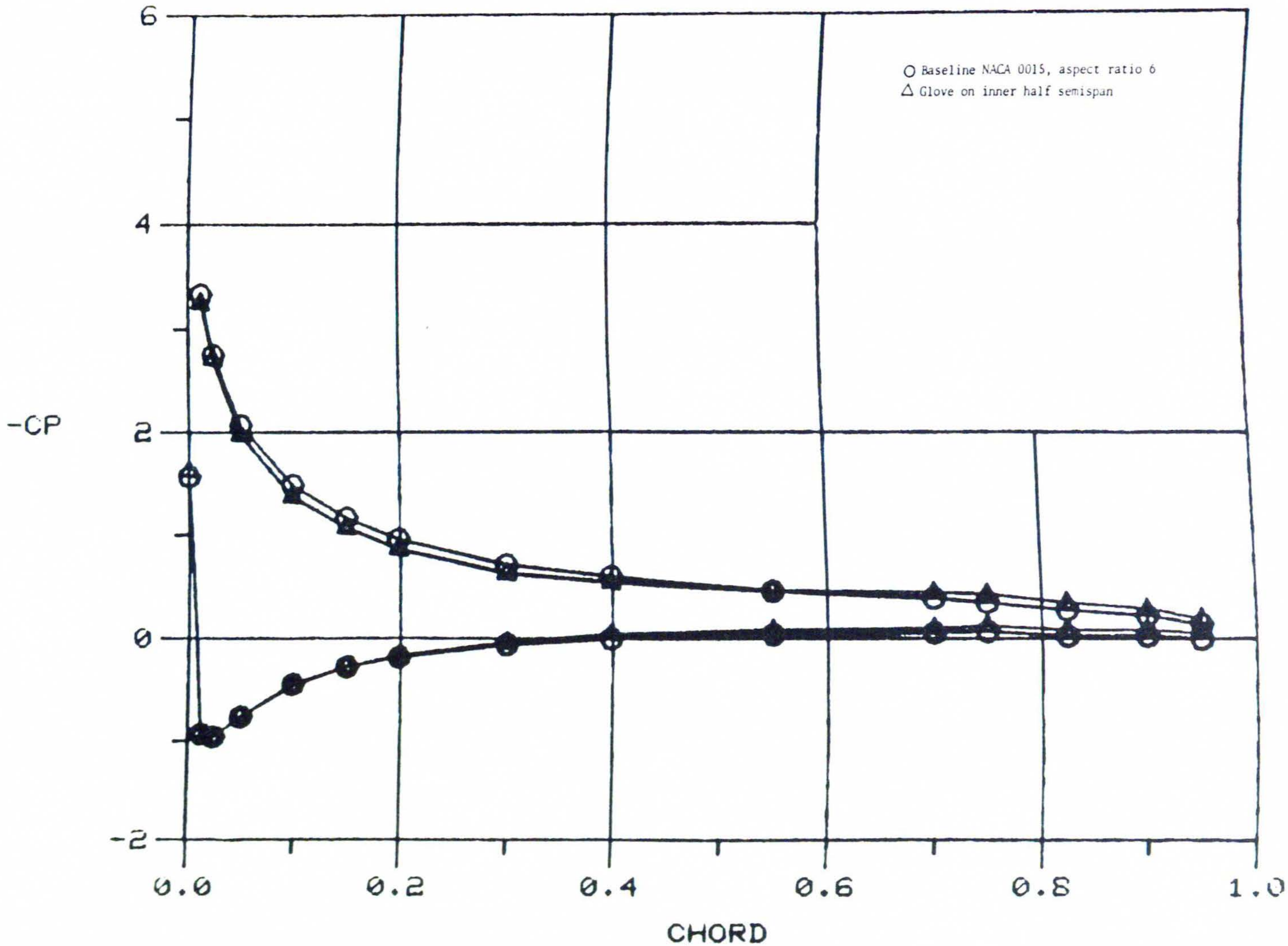

c) At 95% semispan.

Figure 39 - Concluded.

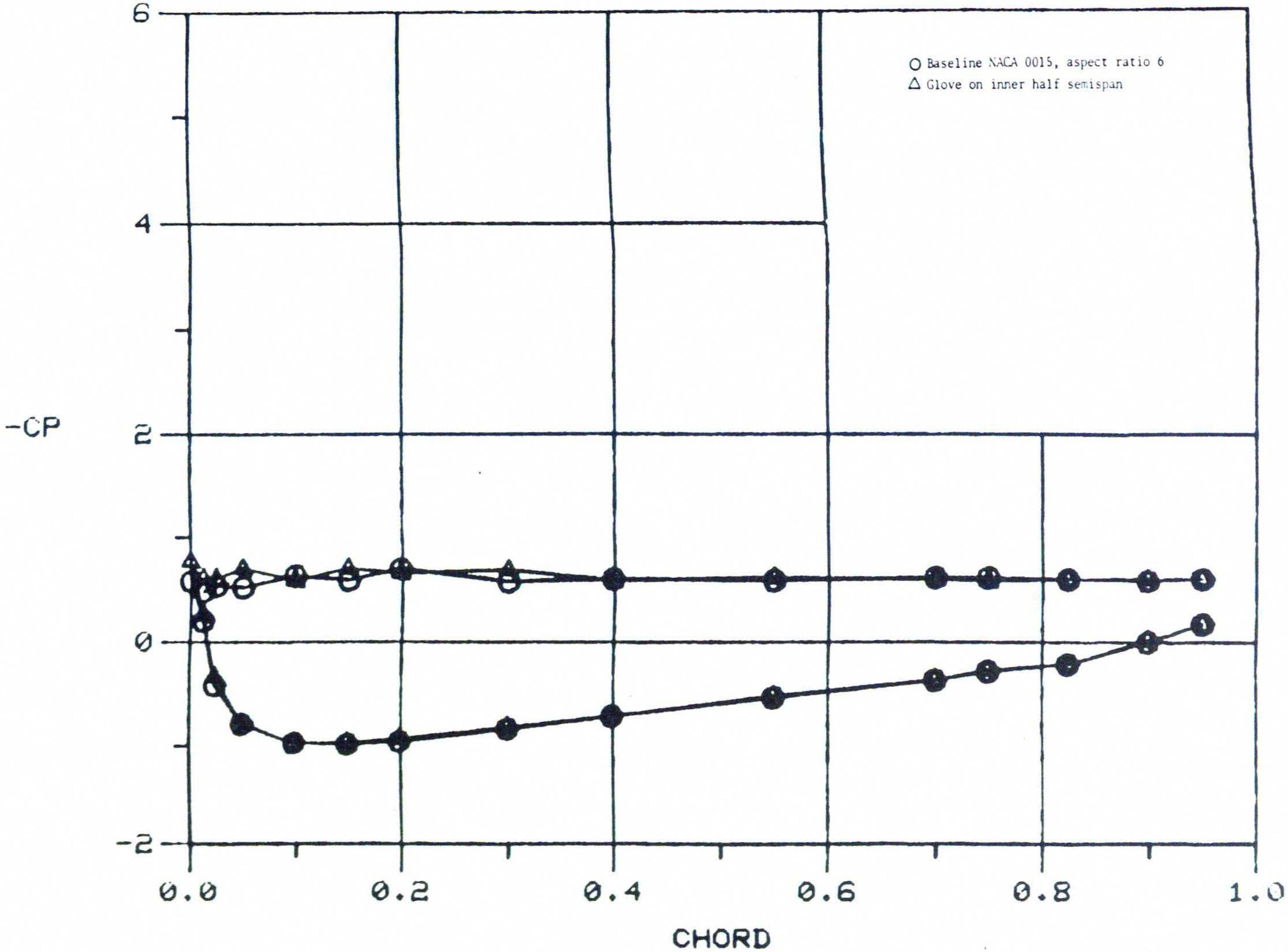

a) At 62% semispan

Figure 40 - Pressure distribution on NACA 0015 wing with and without modifications at $\alpha = 50^{0}$, $Re_c = 2.0 \times 10^{6}$.

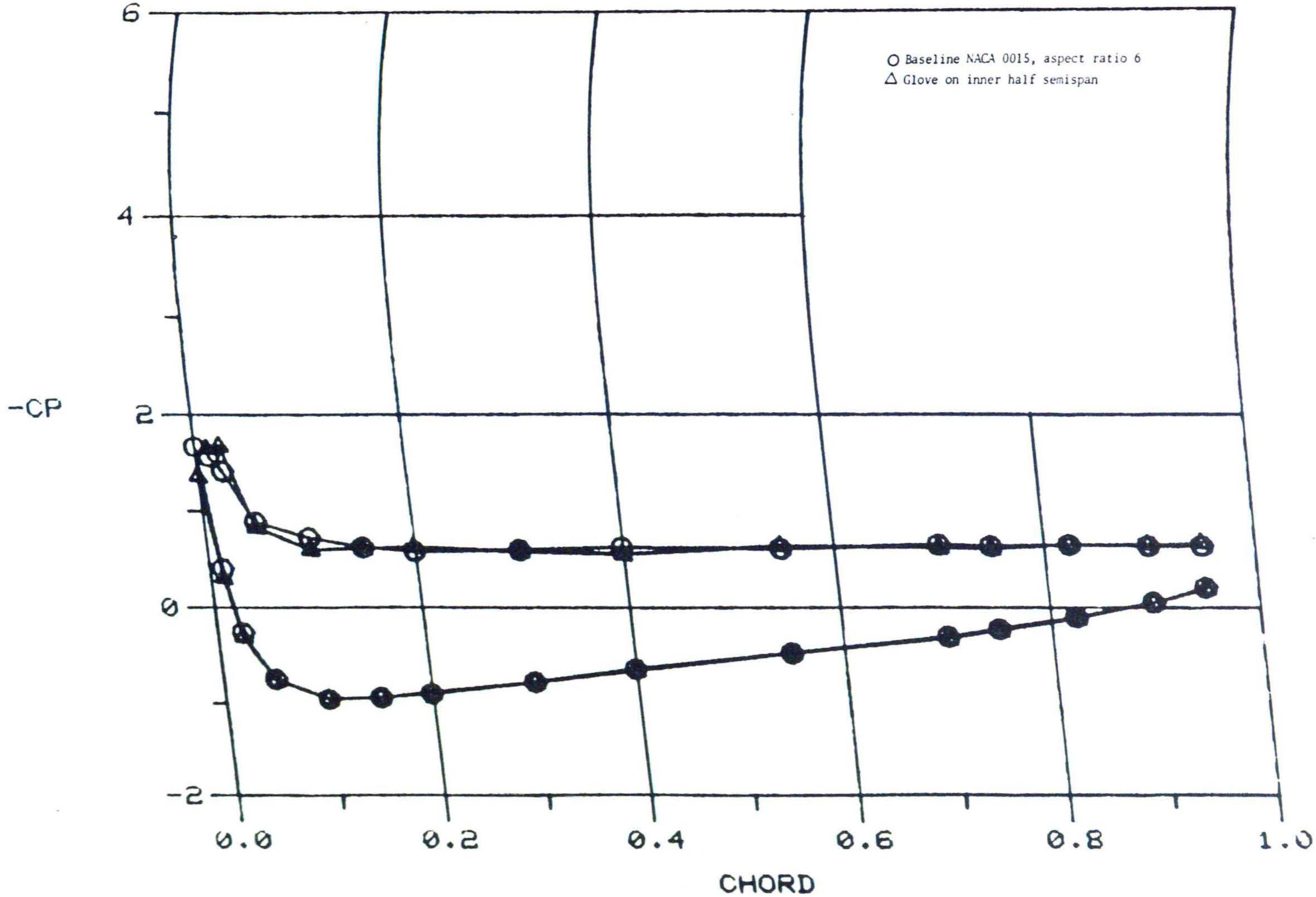

b) At 84% semispan

Figure 40 - Continued.

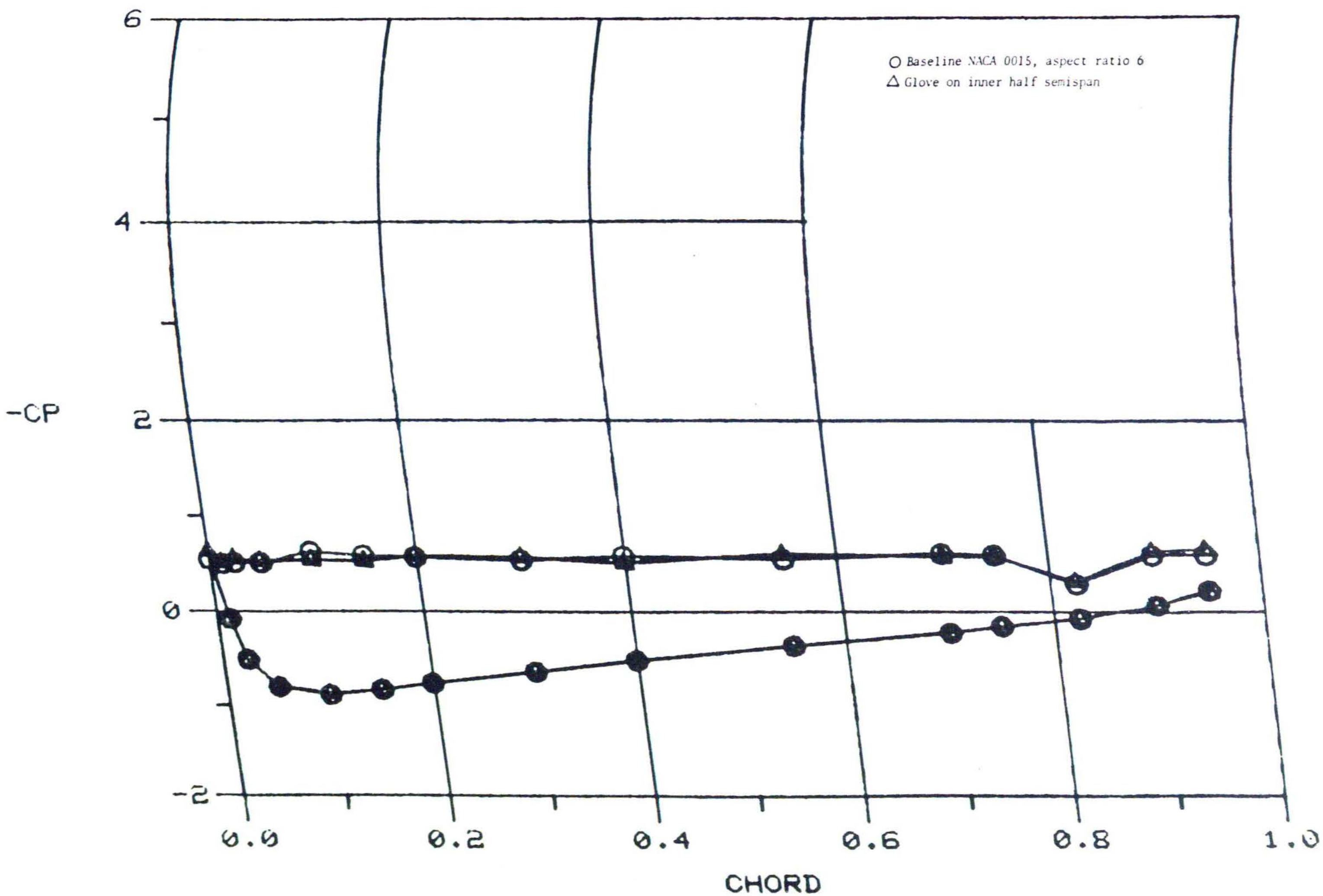

c) At 95% semispan

Figure 40 - Concluded.